

INFORMATION TO USERS

This manuscript has been reproduced from the microfilm master. UMI films the text directly from the original or copy submitted. Thus, some thesis and dissertation copies are in typewriter face, while others may be from any type of computer printer.

The quality of this reproduction is dependent upon the quality of the copy submitted. Broken or indistinct print, colored or poor quality illustrations and photographs, print bleedthrough, substandard margins, and improper alignment can adversely affect reproduction.

In the unlikely event that the author did not send UMI a complete manuscript and there are missing pages, these will be noted. Also, if unauthorized copyright material had to be removed, a note will indicate the deletion.

Oversize materials (e.g., maps, drawings, charts) are reproduced by sectioning the original, beginning at the upper left-hand corner and continuing from left to right in equal sections with small overlaps.

ProQuest Information and Learning
300 North Zeeb Road, Ann Arbor, MI 48106-1346 USA
800-521-0600

UMI[®]

NOTE TO USERS

This reproduction is the best copy available.

UMI

UNIVERSITY OF OKLAHOMA

GRADUATE COLLEGE

**DYNAMIC ADJUSTMENT IN AN IDEALIZED NUMERICALLY-
SIMULATED BOW ECHO**

A Dissertation

SUBMITTED TO THE GRADUATE FACULTY

in partial fulfillment of the requirements for the

degree of

Doctor of Philosophy

By

ERNANI DE LIMA NASCIMENTO

Norman, Oklahoma

2002

UMI Number: 3070630



UMI Microform 3070630

Copyright 2003 by ProQuest Information and Learning Company.

All rights reserved. This microform edition is protected against
unauthorized copying under Title 17, United States Code.

ProQuest Information and Learning Company
300 North Zeeb Road
P.O. Box 1346
Ann Arbor, MI 48106-1346

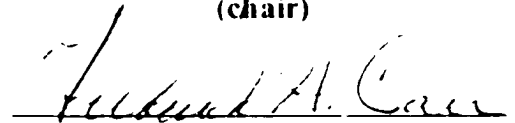
**DYNAMIC ADJUSTMENT IN AN IDEALIZED NUMERICALLY-SIMULATED
BOW ECHO**

**A Dissertation APPROVED FOR THE
SCHOOL OF METEOROLOGY**

BY



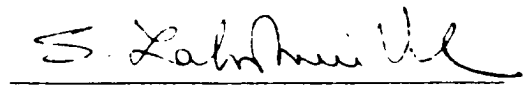
Dr. Kelvin K. Droegemeier
(chair)



Dr. Frederick H. Carr




Dr. Eugenia Kalnay



Dr. S. Lakshmivaran



Dr. Alan Shapiro



Dr. David J. Stensrud

© Copyright by Ermani de Lima Nascimento 2002
All Rights Reserved

Dedication

I dedicate this dissertation to my Family (parents, brother and sister) who *always* gave me invaluable support, even during the most difficult moments, while I sought to realize my own professional dreams thousands of miles away.

Acknowledgments

First of all I would like to thank Prof. Kelvin Droegemeier for being not only a great advisor but also a great friend, and for his invaluable and insightful guidance that kept my research on the right track, deviating from some rough obstacles. I must also thank Prof. Eugenia Kalnay for supporting me since the beginning of this journey, and for her inspirational ideas. I am highly grateful to both of you.

I am also particularly grateful to the Members of my Advisoral Committee, Profs. Frederick Carr, S. Lakshmivarahan, Alan Shapiro and David Stensrud for some very enlightening discussions and suggestions, addressing fundamental topics incorporated in this research. I ought to include Prof. Brian Fiedler in this acknowledgment, for his comments and feedback.

Special thanks also go to all the School of Meteorology faculty, in particular to Prof. Ming Xue for being very accessible in helping me with the numerical code, and to Prof. Evgeni Fedorovich, always willing to help during the writing of this dissertation, and for supporting my effort almost daily. I must also thank Drs. Daniel Webber, Yvette Richardson and Stephen Wevgandt, and Edwin Adlerman for “saving” me several times regarding the numerical code, and Mark Lauferweiller regarding crucial technical support. I wish to thank Prof. Peter Lamb for inviting me to participate in several international events organized by CIMMS. I am grateful to all SoM (Andrea, Celia, Marcia, Nancy) and CAPS (Deanna, Eileen, Luwanda, Brandon, Scott) staff, and in particular to CAPS College of Geosciences for delaying the decommissioning of CRAY-J90. Without this decision, the present research would have never been finished in a reasonable time.

I would like to thank my Professors in Brazil, who strongly supported my coming to the USA: Profs. Tércio Ambrizzi, Maria Assunção F. da Silva Dias, Augusto Pereira, Pedro L. Silva Dias, Cibele G. Picango, Maria G. Justi da Silva.

I am highly grateful to Conselho Nacional de Desenvolvimento Científico e Tecnológico (CNPq) from Brazil and the National Science Foundation (NSF) from the USA for funding this research.

Naturally, I owe a lot to my Family, to the ones who taught me the difficult lesson of life and who always supported me unconditionally. What else can I say? My accomplishment is also yours. This dissertation is dedicated to you. (Evidentemente, eu devo muito à minha Família, àqueles que me ensinaram a difícil lição da vida, e

que sempre me apoiaram de forma incondicional. O que mais posso dizer? A minha realização também é de vocês. Esta dissertação é dedicada a vocês.)

Last but not least, I must thank all my friends who became my “Family” in the USA. Paul and Elaine Nutter, Bill Martin, Jerry Brotzge, Bob Conzemius, Ken Hamm. Special thanks also go to Elicia Inazawa and Pierre Herckes for being such great friends. No word expresses my gratitude to all of you. Also Celia Jones, John Estherheld, Jennifer Ritterling, Frank Gallagher III, Rob Hale, Evgeni Fedorovich and Petra Kastner-Klein, Scott and Yvette Richardson. Thanks for the fun time we spent together. And thank you Isabel for the logistic support when I first arrived in the USA. It has been a pleasure meeting all of you.

Contents

Dedication	iv
Acknowledgments	v
Contents	vii
List of Tables	x
List of Figures	xi
List of Acronyms	xxvii
Abstract	xxix
1 Introduction	1
1.1 Numerical simulation and prediction of severe convective storms.....	1
1.2 The search for a stormscale initial condition.....	3
1.3 Motivation and goals.....	6
2 Theory of Atmospheric Adjustment	14
2.1 Geostrophic adjustment.....	15
2.2 Hydrostatic adjustment: an anelastic approach.....	19
2.3 Hydrostatic adjustment: an acoustic approach.....	23
2.3.1 Basic considerations of acoustic-gravity waves.....	23
2.3.2 Response of a stably-stratified atmosphere to impulsive heating: Lamb's problem.....	29
2.3.3 Transient adjustment in a non-hydrostatic regime: thermal compression waves.....	37
2.4 Pure acoustic adjustment.....	41
2.5 Implications for the present research.....	48

3	The Bow Echo	50
3.1	Pioneer investigations.....	50
3.2	Bow echoes and derechos.....	55
3.3	Mesoscale features in bow echoes.....	58
3.4	Environmental conditions conducive to long-lived bow echoes and derechos.....	64
4	Methodology and the Control Simulation	71
4.1	Methodology.....	71
4.2	The control simulation.....	75
4.2.1	Sensitivity of the control run to ice microphysics.....	90
5	Withdrawal of Kinematic Fields	97
5.1	General results.....	97
5.2	Analysis of the prognostic pressure equation: divergence forcing.....	108
5.3	Buoyancy effects.....	120
5.4	Analysis of advection terms in the pressure equation.....	124
5.5	Response of the wind field shortly after restart time.....	127
5.6	The aspect ratio of the convective flow and implications for dynamic adjustment.....	134
5.7	Summary and additional remarks.....	146
6	"Transient Evolution" in Experiments WVEL and UVVEL from a Wave Propagation Standpoint	150
7	Withdrawal of Thermodynamic Fields	173
7.1	Experiment THETA: General results.....	173
7.2	Experiment VAP: General results.....	180
7.3	Evolution of the surface cold pool and the role played by evaporation at low levels in experiments THETA and VAP.....	187
7.4	Dynamic adjustment aloft: experiment THETA.....	198
7.4.1	Early evolution of buoyancy, pressure and wind fields.....	201
7.4.2	Manifestation of IGWs in experiment THETA.....	216
7.4.2.1	Interpretation of the results.....	230
7.4.3	Manifestation of acoustic modes in experiment THETA.....	234
7.5	Dynamic adjustment aloft: experiment VAP.....	238
7.5.1	Evolution of buoyancy, pressure and wind fields in the first 10-min.....	240
7.5.2	Evolution of buoyancy, pressure and wind fields in the first 20-min.....	248
7.5.3	Impact upon the RIJ, inclination of the convective cells, and IGW and acoustic wave activity.....	262
7.6	Impact of the Coriolis force.....	272
7.7	Summary.....	273

8	Summary and Conclusions	275
8.1	Summary	275
8.2	Conclusions and final remarks.....	280
8.2.1	Relative importance of specific meteorological fields.....	280
8.2.2	Wave regime during dynamic adjustment.....	282
8.2.3	Representativeness of the results and future work.....	283
	Bibliography	288

List of Tables

2.1	Nomenclature adopted to label distinct wave regimes, and their corresponding dispersion relationship (DR).	28
4.1	Summary of the experiments restarting at 4-hr (withdrawal experiments): variables that are set back to the base state values. (The acronym referring to the control run is CTRL).	74
4.2	Physical and computational parameters used in the numerical simulations	79

List of Figures

1.1	Sketch of the typical sequence of events when examining (either analytically or numerically) atmospheric adjustment processes driven by balance relations. An initial condition that does not satisfy the balance relation is specified. This is followed by a transient solution (dominated by the propagation of high frequency waves), which eventually leads to the final solution that satisfy the balance relation.	8
1.2	Conceptual comparison between a numerical study of geostrophic adjustment using a shallow-water equation model (SWEM) and the study of dynamic adjustment processes in a convective storm using a non-hydrostatic fully compressible model (NHFCM). Geostrophic adjustment: an IC not geostrophically balanced is imposed in the SWEM. As soon as the model is started, high frequency inertia-gravity waves are triggered due to the initial imbalance, and acceleration is present. As the waves propagate out of the domain and/or are damped, a final solution in steady-state is obtained, where the geostrophic balance is satisfied. Dynamic adjustment in a convective system: an artificial IC violating the conservation equations is imposed in the NHFCM. This IC contains incomplete information about the inner structure of a simulated convective storm. As the model is started, strong accelerations (as well as time tendencies of scalar fields) are induced while the conservation equations are satisfied, and the simulated fields respond to the artificially-specified IC. The objective is to study how the withdrawal of information about the convective system affects its simulation, and how distinct meteorological fields respond to each other in the early stages of the numerical experiment. Note that no steady-state solution is obtained in this case.	10
2.1	Geostrophic adjustment of initial geopotential perturbation (a). Solutions at 1, 2, 3, and 6-hr are indicated by (b-e). Contoured field is geopotential, and arrows indicate speed and direction of wind field. (After Barwell and Bromley, 1988; adapted from Daley 1991).	17
2.2	Idealized sketch of the perturbation pressure field induced by a buoyancy source, as described by Equation (2.7). Double-headed arrows indicate layers of stronger variation of buoyancy with height.	21

2.3	Idealized sketches of the pressure perturbation field induced by a buoyancy source with (a) high aspect ratio, and (b) low aspect ratio (i.e., "infinite" horizontal layer). In (a) the response of the pressure field is non-hydrostatic with respect to the buoyancy source, while in (b) pressure is in hydrostatic balance with the buoyancy source. Arrows indicate direction of pressure gradient accelerations. VPGA (HPGA) vertical (horizontal) pressure gradient acceleration. (Based on Figures 7.1 and 7.2 of Houze (1993)).	22
2.4	Relation between intrinsic frequency (indicated by $\nu_a = u\tilde{k}$) and the zonal and squared vertical wavenumbers (\tilde{k}, \tilde{m}^2) for an isothermal atmosphere with buoyancy frequency of 0.0180 s^{-1} (indicated by N_{bc} in a dot-dashed line), acoustic cutoff frequency of 0.0198 s^{-1} (indicated by ν_c in a dashed line), and $c_s = 346 \text{ m s}^{-1}$. Regions of $\tilde{m}^2 > 0$ refer to vertically- and horizontally-propagating waves (i.e., internal waves), whereas $\tilde{m}^2 \leq 0$ refers to purely horizontally-propagating waves (i.e., external waves). The dotted line indicate the dispersion relationship for Lamb waves, connecting the point ($\tilde{k} = 0, \tilde{m}^2 = 0$) to the point ($\tilde{k} \rightarrow \infty, \tilde{m}^2 = 0$). (Adapted from Jacobson 1999).	28
2.5	Diagram of distinct perturbation fields as a function of height for the one-dimensional hydrostatic adjustment problem with instantaneous and horizontally-uniform heating source: (a) pressure (p'), (b) density (ρ') and vertical displacement (ζ'), (c) temperature (T'), and (d) potential temperature (θ'). Dashed lines indicate the initial hydrostatically-imbalanced state. Solid lines depict the final steady-state solution. (Adapted from Bannon 1995).	31
2.6	Time evolution of the perturbation vertical motion at the top ($z = a$), bottom ($z = -a$), and middle ($z = 0$) of the heated layer for the one-dimensional hydrostatic adjustment problem with instantaneous and horizontally-uniform heating source. (Adapted from Bannon 1995).	32
2.7	Dispersion relationship for three-dimensional mixed acoustic-gravity waves in an isothermal atmosphere. Dashed (solid) contours are isopleths of the scaled frequency of oscillation for acoustic (internal gravity) waves, where the scaling factor is the buoyancy frequency N . The ordinate (abscissa) refers to the scaled vertical (horizontal) wavenumber, where H_s is the scale height for an isothermal atmosphere. Typical horizontal and vertical wavelengths are indicated on the top and right sides of the diagram, respectively. Arrows show direction of group velocities. (Adapted from Bannon 1995)	34
2.8	Vertical cross section of the steady-state pressure perturbation field for the three-dimensional hydrostatic adjustment problem with instantaneous heating sources of distinct aspect ratios in an infinite isothermal atmosphere. Response for a heating source with (a) high aspect ratio, (b) low aspect ratio. Positive (negative) pressure perturbations indicated by solid (dashed) lines. Each field is normalized by its maximum amplitude. Vertical (horizontal) distance scaled by the scale height of an isothermal atmosphere H_s (Rossby radius of deformation L_R). (Adapted from Chagnon and Bannon 2001).	36

2.9	Vertical structure (xz-plane) of perturbation energy fields 40 min after a localized heating source of high aspect ratio and lasting 20 min is positioned in the center of the domain in a fully compressible two-dimensional mesoscale model. (a) Perturbation internal energy (contour increment of 12 J m^{-3}); (b) perturbation total energy (contour increment of 20 J m^{-3}). Top and bottom boundaries are rigid. (Adapted from Nicholls and Pielke 1994a).	40
2.10	Numerical solution (in a xz-plane) at 1 hr for a two-dimensional simulation of an idealized sea breeze circulation in a compressible mesoscale model. The heating source is prescribed at the central 20 grid-points, in the first level above surface, and lasts for 1 hr. (a) Horizontal mass flux (contour increment of $0.04 \text{ kg m}^{-2} \text{ s}^{-1}$); (b) perturbation pressure (contour increment of 16 Pa). Top boundary is "open" for sound waves (Adapted from Nicholls and Pielke 1994b).	41
2.11	Sketches of idealized convective flows confined within top and bottom rigid boundaries: (a) fully developed circulation cell; (b) initial specification of an artificial wind field that does not satisfy mass conservation (initial horizontal velocity being eliminated), and (c) a weakened (or "destroyed") convective cell. See text for details.	44
2.12	Idealized bounded vertical motion (updrafts and downdrafts), with distinct aspect ratios. (a) high aspect ratio; (b) low aspect ratio.	47
3.1	Schematic representation of typical hook and bow echoes (solid lines) and regions associated with strong straight-line winds at the surface (hatched areas). (From Fujita 1978).	52
3.2	Conceptual model for the life cycle of a typical bow echo. Stage A: tall echo; B and C: bow echo; D and E: comma echo. (From Fujita 1979).	52
3.3	Typical radar echo distributions observed in warm season bow echo-type MCSs, as classified by PD85: (a) type I convective system; (b) type II; (c) type III; (d) type IV. Contour lines are low level reflectivity contours in dBZ. The four diagrams shown are not in the same spatial scale (see text for details). (Adapted from PD85).	54
3.4	Schematic depiction of surface synoptic-scale features associated with the occurrence of (a) progressive derecho (warm season pattern), and (b) serial derecho (dynamic pattern). The hatched areas refer to the sectors affected by strong straight-line winds at the surface (derechos). Front and squall line symbols are conventional. Adapted from JH87.	57
3.5	Conceptual model of a linear MCS with trailing stratiform precipitation viewed in a vertical cross section oriented perpendicular to the line of convective cells. Medium and dark shadings denote areas associated with intermediate and strong radar reflectivity, respectively. Heavy solid (Light scalloped) line represents the boundaries of the storm as indicated from radar reflectivity (direct observation). Storm motion is toward the right of the figure. (Adapted from Houze et al. 1989).	59

- 3.6 Schematic representation of the upshear-tilted convective flow in an idealized bow echo during its mature stage with a (a) developing RIJ, and (b) well defined elevated RIJ. Thick, double-lined vector represents the updraft current; thick solid vector denotes the RIJ; thin, circular arrows indicate convective-scale circulations associated with horizontal vorticity generated either by the ambient vertical wind shear or by the convective system; shading denotes the surface cold pool; regions of lighter or heavier rainfall are indicated by the more sparsely or densely packed vertical lines, respectively; scalloped line denotes the outline of the cloud. (Adapted from Weisman 1993). 61
- 3.7 Low-elevation, plan-position indicator reflectivity analysis of the 19 July 1983 central Minnesota derecho-producing bow echo at 2112 UTC from Minneapolis-St. Paul, MN (MSP) radar. Reflectivity contours are 18, 30, 41 and 46 dBZ. Shaded region represents reflectivity values greater than 50 dBZ; vectors denote the rear inflow notch (i.e., the RIJ sector), and dashed, circular line indicates location of the mesoscale circulation. (From Przybylinski 1995). 63
- 3.8 Schematic of vertical vorticity generation through vortex tilting within bow echoes. In (a), ascending motion along the leading edge of the bow echo pushes the vortex lines up in the presence of convectively-generated easterly vertical wind shear, resulting in anticlockwise (clockwise) rotation on the north (south) end of the system. In (b), localized descent in an environment with westerly vertical wind shear produces the same line-end vertical vorticity pattern. (From Weisman and Davis 1998). 63
- 3.9 Idealized sketches of mid-latitude synoptic-scale situations favorable for development of severe thunderstorms including: (a) tornadic supercells, (b) derecho-producing bow echoes (dynamic pattern). Thin lines denote sea level isobars around a low pressure center with cold and warm fronts. Broad arrows represent low-level jet (LLJ), upper-level polar jet (PJ), and upper-level subtropical jet (SJ). (Panel (a) is after Barnes and Newton 1986; panel (b) is after Johns 1993; both panels are adapted from Johns 1993). 65
- 3.10 Typical mid-latitude synoptic conditions favorable for the development of progressive derecho-producing bow echoes (warm season pattern). The thin arrow, with a WNW-ESE orientation, indicates the main "damage axis" of the progressive derecho associated with the long-lived bow echo convective system (point "B" represents the beginning point of the MCS, "M" represents its mid-point and "E" its end point; the B-M-E path can be as long as 1400km). The broad arrows indicate the positioning of the low-level jet stream (LLJ) and the polar jet stream (PJ) aloft. The thin solid lines represent the sea level isobars, with the surface quasi-stationary thermal boundary and the mid-level ridge also being indicated. (Adapted from Johns et al. 1990) 67

4.1	Diagram showing the methodology employed to study the dynamic adjustment in an idealized bow echo. A 6-hr simulation of an idealized bow echo (control run) is followed by a series of withdrawal experiments in which selected variables in the control run are reset to their base state values at 4-hr. Each withdrawal experiment produce a 2-hr "forecast". The evolution of the simulated bow echo from 4 to 6-hr is examined for each case.	73
4.2	Skew-T diagram of the idealized thermodynamic sounding utilized at the initial time for CNTRL (environment sounding). Thick solid lines are temperature and dew point temperature profiles. Heavy dashed line depicts the moist adiabat along which a surface-based air parcel ascends. Values shown in the top of the diagram indicate dry adiabats (in Celsius). Wind profile is in m s^{-1} .	76
4.3	Time evolution of CNTRL simulation at the first model level ($z = 200$ m): (a) 4-hr, (b) 5-hr, (c) 6-hr. Thick solid line denotes the -2 K potential temperature perturbation indicating the boundary of the cold pool; pressure perturbation contours at each 100 Pa are indicated by thin solid (positive values) and dashed (negative values) lines. Vectors are ground-relative winds. A domain translation of 22 m s^{-1} in the x-direction is applied from 4 to 5-hr, while an additional domain speed of -1.67 m s^{-1} in the y-direction is applied from 5 to 6-hr.	80
4.4	Time evolution of CNTRL simulation at $z = 2600$ m: (a) 4-hr, (b) 5-hr, (c) 6-hr. Contours of vertical velocity perturbation indicated at each 2 m s^{-1} . Solid (dashed) lines are updrafts (downdrafts). Vectors are storm-relative winds. A domain translation of 22 m s^{-1} in the x-direction is applied from 4 to 5-hr, while an additional domain speed of -1.67 m s^{-1} in the y-direction is applied from 5 to 6-hr.	81
4.5	As in Fig. 4.4, but for rainwater and hail mixing ratios indicated at 1 g kg^{-1} intervals (contours).	82
4.6	Bow echo segment at $t = 4$ -hr: (a) $z = 2600$ m: ground-relative wind (vectors); rainwater and hail mixing ratio in g kg^{-1} (shaded); zonal component of the ground-relative wind (contour lines). Solid line encircles region with $u > 30 \text{ m s}^{-1}$; (b) $z = 200$ m: ground-relative wind (vectors) and its zonal component (contour lines). Solid contours indicate values of u greater than 25 m s^{-1} , plotted at each 2 m s^{-1} . Dotted line indicates -2 K potential temperature perturbation representing the boundary of the cold pool. Domain shown is: $104 \text{ km} \leq x \leq 192 \text{ km}$; $170 \text{ km} \leq y \leq 234 \text{ km}$.	83

4.7	Vertical cross section at $t = 4$ -hr across $y = 205$ km (segment \overline{AB} in Figure 4.3a), from surface to $z = 16$ km. All panels contain storm-relative wind vectors presented at every other vertical grid-point. Reference horizontal wind vector of 10 m s^{-1} is indicated on the lower-left corner of each panel. (a) potential temperature perturbation in K; contours plotted at each 1 K; (b) pressure perturbation in Pa; contours plotted at each 50 Pa; (c) rainwater (shaded) and hail (solid contours) mixing ratio plotted at each 1 g kg^{-1} ; (d) equivalent potential temperature presented at each 2 K; only values between $\theta_e = 326$ and 334 K are shown, with $\theta_e = 334\text{K}$ being the first contour in the top of the figure. In (a) and (b) positive (negative) perturbations are indicated by solid (dashed) contours	87
4.8	As in Figure 4.6b, but at $t = 6$ -hr, in a close-up view for the two main bow echo segments shown in Figures 4.4c, 4.5c.	88
4.9	As in Figure 4.7, but at $t = 6$ -hr, for (a) pressure perturbation and (b) equivalent potential temperature, along segment \overline{CD} ($y = 169$ km) in Figure 4.3c. Reference horizontal wind vector (bottom of panels) is 20 m s^{-1}	89
4.10	Time evolution of domain maximum updrafts and downdrafts for the 6-hr simulation of an idealized bow echo. NO_ICE: no ice microphysics; CNTRL: with ice microphysics.	91
4.11	Early evolution of the bow echo simulation with and without ice microphysics. Perturbation vertical velocity (w) and storm-relative winds at $z = 2600$ m. w plotted at each 2 m s^{-1} , with solid (dashed) lines representing updrafts (downdrafts). Only contours within $-10 \text{ m s}^{-1} \leq w \leq 10 \text{ m s}^{-1}$ are plotted. (a),(b): 1-hr; (c),(d): 2-hr; (e),(f): 3-hr. First column: NO_ICE, second column: CNTRL. In (a)-(d) the domain size shown is $128 \times 128 \text{ km}^2$; in (e),(f) is $128 \times 164 \text{ km}^2$.	92
4.12	Early evolution of the bow echo simulation with and without parameterization of ice microphysics. Surface cold pool, perturbation pressure, and ground-relative winds ($z = 200$ m). Thick solid line denotes the -2 K potential temperature perturbation indicating the boundary of the cold pool; pressure contours at each 100 Pa are indicated by thin solid (positive values) and dashed (negative values) lines. (a),(b): 1-hr; (c),(d): 2-hr; (e),(f): 3-hr. First column: NO_ICE; second column: CNTRL. In (a)-(d) the domain size shown is $128 \times 128 \text{ km}^2$; in (e),(f) is $128 \times 164 \text{ km}^2$.	93
4.13	NO_ICE simulation at 4-hr (first row) and 6-hr (second row). (a), (c) surface cold pool and outflow; vectors are ground-relative winds, thick solid line represents -2 K potential temperature perturbation indicating the boundary of the cold pool, thin solid (dashed) contours indicate positive (negative) pressure perturbations plotted at each 100 Pa. (b), (d) storm-relative winds (vectors) and vertical velocity contoured at 2 m s^{-1} intervals, at height $z = 2600$ m. Solid (dashed) lines are updrafts (downdrafts).	96

5.1	Bow echo simulation in WVEL. First row: 5-hr; second row: 6-hr. (a),(c) surface cold pool and outflow: vectors are ground-relative winds, thick solid line represents -2 K potential temperature perturbation indicating the boundary of the cold pool, thin solid (dashed) contours indicate positive (negative) pressure perturbations plotted at each 100 Pa. (b),(d) storm-relative winds (vectors) and magnitude of vertical velocity (contoured at 2 m s^{-1} intervals) at height $z = 2600 \text{ m}$. Solid (dashed) lines are updrafts (downdrafts). Domain translation is as in CNTRL (Figs. 4.3, 4.4).	98
5.2	As in Figure 5.1, but for experiment UVVEL.	100
5.3	Time evolution, from 4-hr to 5-hr (at 10-min increments), of system-averaged profiles of vertical momentum flux ($\overline{u'w'}$) in $\text{m}^2 \text{ s}^{-2}$: (a) CNTRL, (b) WVEL, (c) UVVEL. The averaging is applied for the region enclosed by a rectangle in Fig. 4.4b.	101
5.4	As in Figure 5.3, but for vertical heat flux ($\overline{u'\theta'}$) in $\text{m s}^{-1} \text{ K}$.	102
5.5	Vertical cross-sections in the xz -plane along $y = 205 \text{ km}$ (same y -coordinate of segment \overline{AB} in Fig. 4.3a) for the storm-relative wind field across the gust front. The domain shown is $18 \text{ km} \times 18 \text{ km}$. First column: $t = 4:00:00\text{-hr}$ (restart time for withdrawal experiments); second column: $t = 4:01:04\text{-hr}$; third column: $t = 4:10:00\text{-hr}$ (also refer to CNTRL); (d)-(f) to WVEL; and (g)-(i), to UVVEL. Vectors represent the xz -component of the system-relative wind in m s^{-1} , and contours indicate magnitude of the vertical velocity in m s^{-1} (contoured at 2 m s^{-1} increments, with the zero line being suppressed). Solid (dashed) lines indicate updrafts (downdrafts).	104
5.6	As in Fig. 5.5, but only for WVEL, at (a) $t = 4:00:08\text{-hr}$, (b) $t = 4:00:24\text{-hr}$, (c) $t = 4:00:40\text{-hr}$.	106
5.7	Evolution of the simulated gust front for the sector indicated by a rectangle in Fig. 4.4b: (a)-(c) CNTRL; and (d)-(f) UVVEL. First column: 4:20:00 hr; second column: 4:40:00 hr; third column: 5:00:00 hr. Dashed lines (referring to negative values) are contours of potential temperature perturbation, plotted at -2 K increments. The first contour from right to left is the -2 K line, indicating the leading edge of the advancing cold pool. Vectors are ground-relative winds in m s^{-1} , with a reference vector of 10 m s^{-1} indicated on the lower left corner of each panel. Note that solution from UVVEL deviates significantly from CNTRL.	107
5.8	Solution at 4-hr for CNTRL along same vertical cross section shown in Fig. 5.5. First three terms on the right-hand-side of the pressure equation (Eq. 5.5): (a) term I: $\bar{\rho}qa$, contoured at 10.0 Pa s^{-1} intervals, (b) term II: $-\bar{V}^2 \cdot \nabla p'$, contoured at 0.2 Pa s^{-1} intervals, (c) term III: $-\rho c_p^2 \nabla \cdot \bar{V}$, contoured at 25.0 Pa s^{-1} intervals. Zero lines are suppressed.	111
5.9	Idealized sketch of the upward branch of a convective cell.	112
5.10	Idealized sketch of the pressure perturbation induced shortly after the elimination of the updraft in Figure 5.9. (Proxy for experiment WVEL).	112

5.11	Cross-sections in the xz-plane across the gust front (same domain as in Fig. 5.5), for (a) perturbation pressure (Pa): CNTRL; (b) perturbation pressure (Pa): WVEL, both at $t = 4:00:08$ hr; (c) horizontal divergence ($\cdot 10^{-3} \text{ s}^{-1}$): WVEL, at $t = 4:00:00$ hr. In (a) and (b) the fields are contoured at 50 Pa intervals; in (c) the contour interval is $2 \cdot 10^{-3} \text{ s}^{-1}$. In all figures, solid (dashed) lines indicate positive (negative) values, with zero lines being suppressed. All panels show storm-relative winds in m s^{-1} (vectors), with a reference vector of 10 m s^{-1} indicated on the lower left corner of each panel.	113
5.12	Idealized sketch of the pressure perturbation induced shortly after the elimination of the horizontal motion in Figure 5.9. (Proxy for experiment UVVEL).	116
5.13	As in Figure 5.11, but with (b) referring to UVVEL, and (c) indicating the initial vertical divergence ($(\partial w / \partial z) \cdot 10^3 \text{ s}^{-1}$) for UVVEL.	117
5.14	Vertical cross sections of pressure gradient acceleration (PGA) in m s^{-2} at $t = 4:00:08$ -hr: (a)-(c) CNTRL, (d)-(f) WVEL; (g)-(i) UVVEL. First column: zonal PGA (XPGA); second column: meridional PGA (YPGA); third column: vertical PGA (VPGA). For CNTRL the contour interval is 0.025 m s^{-2} , while for WVEL and UVVEL it is 0.2 m s^{-2} . Solid (dashed) lines indicate positive (negative) values, with the zero line being suppressed. Storm-relative wind vectors for CNTRL are also shown in (a), with a reference vector of 10 m s^{-1} indicated in the lower-left corner of the panel. The xz-domain shown is the same as in Figs. 5.11 and 5.13.	118
5.15	Cross sections of vertical acceleration due to buoyancy (first column), and due to vertical pressure gradient <i>and</i> buoyancy (second column) in m s^{-2} at $t = 4:00:08$ -hr: (a),(b) WVEL, and (c),(d) UVVEL. Buoyancy field is contoured at 0.05 m s^{-2} intervals; $A_{p\&B}$ field is contoured at 0.2 m s^{-2} intervals. Solid (dashed) lines indicate positive (negative) values, with the zero line being suppressed. The domain shown is the same as in Figs. 5.11 and 5.13.	121
5.16	As in Figs. 5.15a,c, but for CNTRL.	123
5.17	Terms of the prognostic pressure equation (Eq. 5.5) at $t = 4:00:00$ -hr (restart time) for: (a)-(c) WVEL; and, (d)-(g) UVVEL. (a),(d): term I (vertical advection of base-state pressure), contoured at 10.0 Pa s^{-1} intervals; (b),(e): term 2 (advection of perturbation pressure), at 0.2 Pa s^{-1} intervals; (c),(f): term III (divergence term), at 100.0 Pa s^{-1} intervals. (g): term I plus term III for UVVEL, at 100.0 Pa s^{-1} intervals. Solid (dashed) lines represent positive (negative) values. Zero lines are suppressed. The xz-domain shown is the same as in Figs. 5.11 and 5.13.	126

- 5.18 Terms of the prognostic pressure equation (Eq. 5.5) at $t = 4:00:08$ -hr for WVEL (first row) UVVEL (second row). First column: term I (vertical advection of base-state pressure), contoured at 10.0 Pa s^{-1} intervals; second column: term 2 (advection of perturbation pressure), at 0.2 Pa s^{-1} intervals; third column: term III (divergence term), at 100.0 Pa s^{-1} intervals. Solid (dashed) lines represent positive (negative) values. Zero lines are suppressed. The xz-domain shown is the same as in Figs. 5.11 and 5.13. 128
- 5.19 Vertical cross sections of horizontal ($\nabla_H \cdot \vec{V}$) and vertical ($\partial w / \partial z$) components of velocity divergence (contours) in 10^{-3} s^{-1} at $t = 4:00:08$ -hr for: (a),(b) CNTRL; (c),(d) WVEL; (e),(f) UVVEL. Contour interval is $1 \cdot 10^{-3} \text{ s}^{-1}$. Solid (dashed) lines indicate positive (negative) values, with zero line being suppressed. Storm-relative wind vectors are in m s^{-1} , with a reference vector of 10 m s^{-1} indicated on the lower-left corner of each panel. The xz-domain shown is the same as in Figs. 5.11 and 5.13. 130
- 5.20 Vertical cross sections of three-dimensional velocity divergence (contours) at $t = 4:00:00$ hr (first column) and $t = 4:00:08$ hr (second column): (a),(b) WVEL; (c),(d) UVVEL. Contour interval is $0.5 \cdot 10^{-3} \text{ s}^{-1}$. Solid (dashed) lines indicate positive (negative) values, with zero lines being suppressed. Storm-relative wind vectors are in m s^{-1} , with a reference vector of 10 m s^{-1} indicated on the lower-left corner of each panel. The xz-domain shown is the same as in Figs. 5.11 and 5.13. 132
- 5.21 Storm-relative winds (vectors) and magnitude of vertical velocity (contours) at $z = 2600 \text{ m}$ and $t = 4:00:00$ -hr for CNTRL. Vectors are in m s^{-1} , with a 10 m s^{-1} (5 m s^{-1}) reference vector indicated on the lower-left corner of (a) (b) and (c). Vertical motion is contoured at each 2 m s^{-1} , with solid (dashed) lines indicating updrafts (downdrafts). Zero lines are suppressed. (a) is just like Fig. 4.1a, but indicates (with rectangles) sectors where vertical cross sections are taken. (b) and (c) are close-up views for the northern and southern rectangle, respectively. Numbers label cross sections, and line segments indicate their zonal extent (all equal to 18 km): [1]: $y = 219 \text{ km}$, $x = 158$ to 176 km ; [2]: $y = 197 \text{ km}$, $x = 162$ to 180 km ; [3]: $y = 139 \text{ km}$, $x = 162$ to 180 km ; [4]: $y = 135 \text{ km}$, $x = 164$ to 182 km ; [5]: $y = 129 \text{ km}$, $x = 162$ to 180 km ; [6]: $y = 241 \text{ km}$, $x = 152$ to 170 km ; [7]: $y = 108 \text{ km}$, $x = 184$ to 202 km ; [8]: $y = 105 \text{ km}$, $x = 176$ to 194 km . 136
- 5.22 Vertical motion field (w) (contours; first column) and vertical component of divergence ($\partial w / \partial z$) (contours; second column) at $t = 4:00:00$ -hr for CNTRL for the vertical cross sections indicated in Figs. 5.21b,c. Solid (dashed) lines indicate positive (negative) values, with zero line being suppressed. Vectors depict the storm-relative wind field in the xz-plane, with a 10 m s^{-1} reference vector indicated on the lower-left corner of each panel. The domain size in all panels is $18 \text{ km} \times 18 \text{ km}$. 137

5.23	Idealized sketch in a xz -plane of the pressure response to an imposed divergence field, as governed by Eq.5.5 (prognostic pressure equation). In (a) the divergence forcing is vertically oriented, displaying a high aspect ratio. Accordingly, the pressure response is also vertically oriented. For this case the induced XPGA is stronger than the corresponding VPGA. In (b) the divergence forcing is oblate, with considerable horizontal orientation and low aspect ratio. The pressure response displays features that are also horizontally oriented, i.e., with considerable horizontal extent. In this case, the induced VPGA is stronger than XPGA.	142
5.24	Vertical cross sections for storm-relative wind field and pressure perturbation (first column), XPGA (second column) and VPGA (third column) for WVFL at 8 s after restart time. The sectors shown correspond to the same eight vertical cross sections indicated in Fig. 5.22 (Figs. 5.24a,b indicate their position in the simulated MCS). In the first column, storm-relative wind vectors are shown in m s^{-1} , with a reference vector of 10 m s^{-1} indicated on the lower-left corner of the panel; perturbation pressure is contoured in Pa, at 50 Pa increments. Second and third columns display pressure gradient accelerations in 0.2 m s^{-2} contour intervals. In all panels, solid (dashed) lines refer to positive (negative) values, with zero lines being suppressed.	143
6.1	Early evolution of the difference field of perturbation pressure in WVFL with respect to CNTRL (i.e., WVFL minus CNTRL) at $z = 200 \text{ m}$. The entire horizontal domain is shown: (a) $t = 4.01\text{-hr}$, (b) 4.02-hr , (c) 4.03-hr , (d) 4.04-hr , (e) 4.05-hr , (f) 4.06-hr , (g) 4.07-hr , (h) 4.08-hr , (i) 4.09-hr , (j) 4.10-hr . Contour interval is 20 Pa in all panels. Solid (dashed) lines indicate positive (negative) values.	152
6.2	As in Fig. 6.1, but for UVVEL minus CNTRL.	155
6.3	First 10-min evolution of perturbation pressure (Pa) and perturbation potential temperature (K) at grid-point $(x, y, z) = (140.0, 204.0, 0.2) \text{ km}$: (a) WVFL, (b) UVVEL.	158
6.4	As in Fig.6.3, but for perturbation pressure (Pa) and zonal component of the wind (m s^{-1}).	159
6.5	Time series for the first 15-min after restart time ($t = 4\text{-hr}$) of perturbation pressure (in Pa) at grid-point $(x, y, z) = (140.0, 204.0, 0.2) \text{ km}$ for WVFL, UVVEL and CNTRL: (a) 0 to 5-min, (b) 5 to 10-min, (c) 10 to 15-min. The perturbation pressure field is sampled at each big time step (4 s).	161
6.6	As in Figure 6.5, but at grid-point $(x, y, z) = (140.0, 204.0, 5.0) \text{ km}$.	162
6.7	Vertical profiles of buoyancy frequency (given by Eq. 2.13) and acoustic cutoff frequency (given by Eq. 2.19) for the base-state environment used in CNTRL and withdrawal runs — associated with the thermodynamic profile depicted in Fig. 4.2.	164
6.8	As in Fig. 6.5, but for neutral simulation (constant potential temperature = 303 K). The time series are extracted from the same two grid-points analyzed in Figs. 6.5 and 6.6 [i.e., $(x, y, z) = (140.0, 204.0, 0.2\text{-}5.0) \text{ km}$]. Time zero refers to the initialization time with a thermal bubble.	165

6.9	As in Fig. 6.8, but for the first 20-min of integration of a neutral simulation with horizontal domain extent that is half of that used in simulations CNTRL, WVCL and UVVEL. The grid-points from which the time series are extracted are $(x, y, z) = (70.0, 108.0, 0.2-5.0)$ km. In (d) (which refers to the last 5-min of the 20-min window) only the time series for $z = 200$ m is shown, with the vertical scale zoomed in for a 2 Pa range. Time zero refers to the initialization time with a thermal bubble.	167
6.10	As in Fig. 6.8, but for the first 20-min of integration of a neutral simulation with horizontal and vertical domain extents that are half of those used in simulations CNTRL, WVCL and UVVEL. The grid-points from which the time series are extracted are the same as in Fig. 6.9. In (d) (which refers to the last 5-min of the 20-min window) only the time series for $z = 200$ m is shown, with the vertical scale zoomed in for a 4 Pa range. Time zero refers to the initialization time with a thermal bubble.	170
7.1	Skew-T diagrams for thermodynamic profiles within the simulated bow echo at restart time. Location: $(x, y) = (160, 200)$ km; just upstream of the main bow echo segment at 4-hr (see Fig. 4.6a). (a) CNTRL, (b) THETA.	176
7.2	Bow echo simulation in experiment THETA. First row: 5-hr; second row: 6-hr. (a),(c) surface cold pool and outflow: vectors are ground-relative winds, thick solid line represents -2 K potential temperature perturbation indicating the boundary of the cold pool, thin solid (dashed) contours indicate positive (negative) pressure perturbations plotted at each 100 Pa. (b),(d) storm-relative winds (vectors) and magnitude of vertical velocity (contoured at each 2 m s^{-1}) at height $z = 2600$ m. Solid (dashed) lines are updrafts (downdrafts).	177
7.3	Structure of the simulated bow echo at 6-hr at height $z = 2600$ m, zoomed in for the area indicated by a rectangle in Figure 4.4c. (a) CNTRL, (b) THETA. Vectors are storm-relative winds in m s^{-1} , with a 10 m s^{-1} reference vector indicated at the bottom of each panel. Solid lines are magnitude of zonal component of the wind (storm-relative), contoured at each 5 m s^{-1} . Only values equal to or above 10 m s^{-1} are plotted. Storm motion is approximately 26 m s^{-1} in the zonal direction. Shading indicates rainwater mixing ratio in g kg^{-1} .	179
7.4	Time evolution, from 4-hr to 5-hr (at 10-min increments), of system-averaged profiles of vertical momentum flux ($\overline{u'w'}$) in $\text{m}^2 \text{ s}^{-2}$ (first row), and of vertical heat flux ($\overline{w'\theta'}$) in $\text{m s}^{-1} \text{ K}$ (second row). (a),(c) CNTRL, (b),(d) THETA. The averaging is applied for the region enclosed by a rectangle in Fig. 4.4b.	181
7.5	As in Fig. 7.1, but comparing thermodynamic profiles from experiments (a) CNTRL and (b) VAP.	183
7.6	As in Fig. 7.2, but for VAP.	184
7.7	As in Fig. 7.4, but with (b),(d) referring to experiment VAP.	186

- 7.8 Evolution of the simulated gust front ($z = 200$ m) for the sector indicated by a rectangle in Fig. 4.4b: (a)-(c) CNTRL; (d)-(f) THETA; and, (g)-(i) VAP. First column: 4:20-hr; second column: 4:40-hr; third column: 5:00-hr. Dashed lines (referring to negative values) are contours of potential temperature perturbation, plotted at -2 K increments. The first contour from right to left is the -2 K line, indicating the leading edge of the advancing cold pool. Vectors are ground-relative winds in m s^{-1} , with a reference vector of 10 m s^{-1} indicated on the lower left corner of each panel. A line segment along $x = 176.0$ km is indicated in all panels as a reference to compare the eastward progression of the gust front from both experiments. 188
- 7.9 As in Fig. 7.8, but for the perturbation pressure field. Contour interval is 50 Pa. 190
- 7.10 Time series of evaporation rate of rainwater (E_r) averaged for the first two model levels within the domain enclosed by a box in Fig. 4.4b for simulations CNTRL, THETA and VAP. Units: $10^{-4} \text{ g kg}^{-1} \text{ s}^{-1}$. (a) time evolution in the first 10-min after restart time, with E_r sampled at every 1-min; in (b) E_r is indicated from 4:10 to 5:00-hr, sampled at every 10-min. 192
- 7.11 Time evolution, from 4-hr to 5-hr (at 10-min increments), of system-averaged profiles of perturbation water vapor mixing ratio (in g kg^{-1}). (a) CNTRL, (b) THETA, (c) VAP. The averaging is applied for the region enclosed by a rectangle in Fig. 4.4b. 195
- 7.12 Time series of mean surface perturbation potential temperature error for withdrawal experiments in Weygandt et al. (1999). Time zero refers to restart time. (Adapted from Weygandt et al. 1999). 197
- 7.13 Vertical cross sections (xz-plane), from surface to $z = 12$ km, of equivalent potential temperature (θ_e ; solid lines) and storm-relative wind field (vectors) at distinct times ($t = 4:10$, $4:30$ and $4:50$ -hr) for experiments CNTRL (first column) and THETA (second column). Only the 326 K (thin solid line) and 334 K (thick solid line) isentropes are plotted. At $4:10$ and $4:30$ -hr (a-d) the vertical cross section is along $y = 205$ km, while at $4:50$ -hr (e-f) it is along $y = 197$ km (following the gradual southward displacement of the apex of the main bow echo segment in CNTRL). The horizontal extent of the domain shown is 80 km long, from $x = 120$ km to $x = 200$ km. Domain translation is eastward at 22.0 m s^{-1} . 199
- 7.14 Vertical cross sections from surface to $z = 16$ km (along $y = 205$ km) of acceleration due to buoyancy (given by Eq. 5.8), contoured at 0.05 m s^{-2} intervals. (a) solution from CNTRL simulation at $t = 4:05$ -hr (reference for comparison); (b)-(g) first 10-min evolution in experiment THETA, with solutions shown at 2-min intervals. Solid (dashed) lines indicate positive (negative) values, with zero lines being suppressed. The horizontal extent of the domain shown is 80 km long, and is the same as in Fig. 7.13. Domain translation is eastward at 22.0 m s^{-1} . 202

- 7.15 As in Fig. 7.14, but for the acceleration induced by distinct terms
composing the buoyancy field (given by Eq. 5.8) for CNTRL simulation
at 4:05-hr: (a) thermal buoyancy; (b) perturbation pressure buoyancy;
(c) perturbation water vapor mixing ratio term; (d) condensate loading
term. In (a) the contour interval is 0.05 m s^{-2} , while in (b),(c),(d) a
 0.0125 m s^{-2} contour interval is used. The domain shown is the same
as in Fig. 7.14. 204
- 7.16 As in Fig. 7.14, but for perturbation pressure (contours; Pa) and
storm-relative winds (vectors, m s^{-1}). Pressure field is contoured at
50 Pa intervals, with solid (dashed) lines indicating positive (negative)
values, and zero lines being suppressed. Areas with downdrafts equal
to or stronger than -1 m s^{-1} are shaded (single color shading). 206
- 7.17 As in Fig. 7.14, but for: cloud water (q_c) and cloud ice (q_i) mixing
ratios (solid lines); condensate loading term of the acceleration due
to buoyancy $-(g(q'_c + q'_i)/(1 + \bar{q}_v))$ (dashed line); and downdraft areas
(single shading). Only the 0.1 g kg^{-1} mixing ratio line is indicated
for q_c and q_i , with the lower (upper) contour referring to q_c (q_i). The
dashed line encloses areas with condensate loading term equal to or less
than -0.025 m s^{-2} . Areas with downdrafts equal to or stronger than -1
 m s^{-1} are shaded (single color shading). (a)-(f) first 10-min evolution
in experiment THETA, with solutions shown at 2-min intervals. 210
- 7.18 Force field in the xz -plane of the buoyancy pressure gradient accel-
eration (BPGA) induced by a homogeneous and positively buoyant air
parcel (or layer) of finite dimensions. Lines of BPGA are shown as
streamlines. This field is obtained analytically from Eq. 2.7. Plus and
minus signs indicate the sign of the buoyancy forcing (r.h.s. of 2.7).
Adapted from Wakimoto (2001) (originally from Houze 1993, Yuter
and Houze 1995b). Note: our Fig. 2.3a is based on the figure above). 212
- 7.19 Vertical acceleration due to buoyancy and vertical pressure gradient
(dashed lines) at 4:02-hr for simulations (a) CNTRL and (b) THETA,
contoured at 0.01 m s^{-2} intervals. Only negative values are shown.
Areas with downdrafts equal to or stronger than -1 m s^{-1} are shaded
(single shading). Domain shown is same as in Fig. 7.14. 214
- 7.20 Vertical cross sections along $y = 205 \text{ km}$ of (a) $[-\partial B/\partial x]$ ($\times 10^3 \text{ s}^{-2}$)
contoured at 0.005 s^{-2} intervals, and (b) acceleration due to buoyancy
(given by Eq. 5.8), contoured at 0.05 m s^{-2} intervals, for experiment
THETA 10-min after restart time. Dashed (Thin solid) lines represent
negative (positive) values. In (a), zero lines are plotted as thick solid
contours, while in (b) zero lines are suppressed. The cross section
shown covers only the lower western portion of the domain in Fig.
7.14 (from the surface to $z = 9.6 \text{ km}$, and $120 \text{ km} \leq x \leq 170 \text{ km}$). In
both panels, areas with downward motion stronger than or equal to -1
 m s^{-1} are shaded (single shading). 215
- 7.21 As in Fig. 7.14, but for the zonal component of the storm-relative flow
in m s^{-1} (contours), from $t = 4:06$ to 4:20-hr in experiment THETA.
Only contours for $u = -12 \text{ m s}^{-1}$ (dashed line) and 8 m s^{-1} (solid line)
are shown. Vectors are storm-relative winds in m s^{-1} , and shading
indicates areas with downdrafts stronger than -1 m s^{-1} . 217

7.22	First 20-min evolution of vertical motion field at $z = 4.8$ km in experiment THETA, starting at $t = 4:02$ -hr. Solid (dashed) lines denote updrafts (downdrafts) contoured at 0.5 m s^{-1} intervals, with zero lines being suppressed. Only vertical motions between $\pm 4 \text{ m s}^{-1}$ are plotted. In all panels, light shading indicates areas with hail mixing ratio greater than 1 g kg^{-1} , and an E-W oriented line segment along $y = 205$ km illustrates the location of vertical cross sections studied in previous plots. The horizontal domain shown is the same as in Fig. 4.6, and translates eastward at 22 m s^{-1} .	220
7.23	As in Fig. 7.14, but for the vertical motion field at $t = 4:18$ -hr. Only contours for $w < -1 \text{ m s}^{-1}$ (dashed lines) and $w > 1 \text{ m s}^{-1}$ (solid lines) are plotted. Vectors are storm-relative winds in m s^{-1} .	222
7.24	As in Fig. 7.22, but for a larger horizontal domain, enclosing $104 \text{ km} \leq x \leq 260 \text{ km}$, $146 \text{ km} \leq y \leq 262 \text{ km}$.	224
7.25	Time sequence from $t = 4:12$ to $4:20$ -hr of vertical motion at $z = 4.8$ km along $y = 205$ km (line segment in Fig. 7.22) in experiment THETA for a horizontal domain covering $112 \text{ km} \leq x \leq 168 \text{ km}$ (the abscissa in the panels above). The domain moves eastwards at 22 m s^{-1} which is approximately the propagation speed of the bow echo, such that the phase speed indicated above is storm-relative.	225
7.26	Vertical profiles of: (a) buoyancy frequency squared (N^2 ; $\times 10^{-4} \text{ s}^{-2}$), and (b) zonal component of ground-relative winds (\bar{u} ; m s^{-1}), in experiment THETA at 4:10-min averaged for the area enclosed by a rectangle in Fig. 7.22e.	227
7.27	Time series of vertical velocity in m s^{-1} at $(x, y) = (160, 205) \text{ km}$ and $z = 1.8 \text{ km}$, 4.6 km , 7.8 km , for the first 20-min of experiment THETA. The vertical velocity field is sampled at each 4s.	228
7.28	As in Fig. 7.27, but for simulation CNTRL.	234
7.29	Time series for the first 20-min after the restart time ($t = 4$ -hr) of perturbation pressure (in Pa) at $(x, y) = (160, 205) \text{ km}$ and $z = 1.8 \text{ km}$, 4.6 km , 7.8 km (just upstream of the bow echo in Fig. 7.22) for experiment THETA, (a) 0 to 5-min, (b) 5 to 10-min, (c) 10 to 15-min, (d) 10 to 15-min. The perturbation pressure is sampled at each big time step (4 s).	235
7.30	As in Fig. 7.13, but comparing experiments CNTRL and VAP.	239
7.31	As in Fig. 7.14, but for experiment VAP.	241
7.32	Vertical acceleration induced by thermal buoyancy (first column) and condensate loading (second column) terms of the total buoyancy field at $t = 4:00$ -hr (first row) and $4:02$ -hr (second row) for experiment VAP. In (a),(c) the contour interval is 0.05 m s^{-2} , while in (b),(d) a 0.0125 m s^{-2} contour interval is used. The domain shown is the same as in Fig. 7.31.	244
7.33	As in Fig. 7.16, but for experiment VAP.	245
7.34	As in Fig. 7.14, but for experiment VAP, from $t = 4:12$ -hr to $4:20$ -hr.	249
7.35	As in Fig. 7.16, but for experiment VAP, from $t = 4:12$ -hr to $4:20$ -hr.	251
7.36	As in Fig. 7.26, but for experiment VAP at $t = 4:15$ -min.	254
7.37	As in Fig. 7.21, but for experiment VAP, from $t = 4:10$ -hr to $4:20$ -hr.	255

7.38	Vertical cross sections of the magnitude of downward motion (dashed lines) and storm-relative winds (vectors) in m s^{-1} for (a) experiment THETA at 4:08-hr, and (b) experiment VAP at 4:16-hr. Contour interval is 2 starting at -2 m s^{-1} . The domain shown is the same as in Fig. 7.14.	258
7.39	Vertical cross sections of the ratio q_v/q_{vs} at 0.2 dimensionless intervals. Thick solid line in the center of the domain encloses areas with q_v/q_{vs} equal to 1, while thin solid line indicates areas with q_v/q_{vs} equal to or less than 0.6. Vectors are storm-relative winds in m s^{-1} . The domain shown is the same as in Fig. 7.14.	259
7.40	Vertical cross sections of total water mixing ratio (solid lines) along $y = 205 \text{ km}$ for (a) experiment THETA at $t = 4:08\text{-hr}$, and (b) experiment VAP at $t = 4:16\text{-hr}$. Contour interval is 1 g kg^{-1} . Vectors are storm-relative winds in m s^{-1} , and shading indicates areas with downward motion equal to or stronger than -1 m s^{-1} . Domain shown is the same as in Fig. 7.14.	260
7.41	Time series, from 3 to 6-hr, of domain maximum updrafts (m s^{-1}) sampled at 5-min intervals. Comparison between simulations CNTRL, THETA and VAP.	262
7.42	As in Fig. 7.19, but comparing solutions from simulation CNTRL at $t = 4:10\text{-hr}$ (panel (a)) and simulation VAP at $t = 4:08\text{-hr}$, 4:10-hr and 4:12-hr (panels (b)-(d)).	263
7.43	As in Fig. 7.19, but for experiment VAP at $t = 4:16\text{-hr}$. Positive (solid lines) and negative (dashed lines) values of $A_{p/B}$ are plotted at 0.02 m s^{-2} intervals. Storm-relative winds (in m s^{-1}) are indicated by vectors.	265
7.44	Vertical cross sections in the xz -plane along $y = 205 \text{ km}$ for the storm-relative wind field across the gust front in experiment VAP, from $t = 4:14\text{-hr}$ to 4:20-hr. The domain shown is $18 \text{ km} \times 18 \text{ km}$. Vectors represent system-relative winds in m s^{-1} , and contours indicate magnitude of the vertical velocity in m s^{-1} (contoured at 2 m s^{-1} increments, with the zero line being suppressed). Solid (dashed) lines indicate updrafts (downdrafts).	267
7.45	As in Fig. 7.24, but for THETA (panel (a)) and VAP (panel (b)) at $t = 4:30\text{-hr}$.	268
7.46	As in Fig. 7.27, but for experiment VAP.	270
7.47	As in Fig. 7.29 but for the first 10-min in experiment VAP.	271
7.48	As in Fig. 7.14, but comparing the solutions from simulations CNTRL and THETA at 4:30-hr.	273

- 8.1 Diagrams summarizing the response among meteorological fields early in the withdrawal experiments (i.e., during “transient evolution”). Panel (a) indicates the response in simulations WVVEL and UVVEL (dynamic adjustment induced by kinematic fields). Violation of mass conservation, associated with incomplete specification of the three-dimensional divergence field, leads to strong (but short-lived) pressure perturbations. In turn, the induced pressure gradient acceleration (PGA) leads to responses in the velocity field. The response from the vertical component of the wind is stronger due to a more intense PGA in the vertical during the adjustment process, which translates into the vertical motion adjusting to the horizontal wind field specified in the initial condition. Panel (b) indicates the response in simulations THETA and VAP (dynamic adjustment induced by the thermodynamic fields). Water vapor and condensate fields modulate the rates of latent heating and cooling, which, in turn, affect the temperature field. Variations in temperature affect buoyancy, while the pressure field responds to the distribution of buoyancy. This overall response emphasizes the importance of an adequate specification of the meteorological variables that control the magnitude of latent heating and cooling within convective storms. 279

List of Acronyms

AGW:	acoustic gravity wave
ARPS:	Advanced Regional Prediction System
B95:	Bannon (1995)
BPGA:	buoyancy pressure gradient acceleration
CAPE:	convective available potential energy
CFL:	Courant-Friedrichs-Lewy
CIN:	convective inhibition
DMU:	domain-maximum updraft
DPMCS:	derecho-producing mesoscale convective system
DR:	dispersion relationship
ED01:	Evans and Doswell (2001)
HIGW:	hydrostatic internal gravity wave
HP:	high precipitation
HPGA:	horizontal pressure gradient acceleration
IC:	initial condition
IGW:	internal gravity wave
JH87:	Johns and Hirt (1987)
LEWP:	line echo wave pattern
MARC:	mid-altitude radial convergence
MCS:	mesoscale convective system
MCV:	mesoscale convective vortex
MLSRW:	mid-level storm-relative wind
NHFCM:	non-hydrostatic fully compressible model

NP94a: Nicholls and Pielke (1994a)
NP94b: Nicholls and Pielke (1994b)
PD85: Przybylinski and DeCaire (1985)
PD96: Pandya and Durran (1996)
PDE: partial differential equation
PGA: pressure gradient acceleration
PGF: pressure gradient force
RIJ: rear inflow jet
RKW: Rotunno-Klemp-Weisman
SWEM: shallow water equation model
TCW: thermal compression wave
TKE: turbulent kinetic energy
VPGA: vertical pressure gradient acceleration
WEC: weak echo channel
WSR-88D: Weather Surveillance Radar - 1988 Doppler
XPGA: zonal pressure gradient acceleration
YPGA: meridional pressure gradient acceleration

Abstract

While the large-scale atmosphere is governed by relatively simple dynamic balance relations that describe the mutual adjustment between the mass and wind fields (e.g., hydrostatic and geostrophic balances), no simple relation is known to govern flow adjustments on the convective scale. To gain better insight into this issue, a set of identical-twin numerical experiments are performed in the present work. A control simulation of an idealized long-lived bow echo, which serves as "truth", is compared against forecasts in which selected variables in the control run are reset to their undisturbed base state values during the mature stage of the convective system. The goal is to understand how, and at what rates, the unperturbed meteorological fields adjust to the variable that is withdrawn impulsively (and vice versa).

Our results indicate that withdrawal of the perturbation horizontal wind field has a major impact on storm morphology, while elimination of the vertical motion has virtually no impact. This behavior can be explained by the response of the pressure field to incomplete specification of the three-dimensional divergence, associated with which is the creation of high-amplitude mixed acoustic-gravity waves. A strong squall line, sharing many of the characteristics of bow echoes, results from the simulation in which perturbation potential temperature is withheld, with the water vapor and condensate fields regenerating the main thermal structure of the convective system through diabatic effects. Withdrawal of perturbation water vapor mixing ratio leads to a storm system whose evolution deviates significantly from the control simulation, owing to a delay in the restoration of the thermal field and to substantial modification in rates of latent heating and cooling.

These results suggest that if a choice exists regarding which variables can be specified in a stormscale model in the presence of a mature convective system (particularly, squall lines and bow echoes), the horizontal wind, water vapor and condensate species should be given the highest priority. On the other hand, information contained in the pressure, temperature and vertical motion fields tend to be redundant.

Chapter 1

Introduction

1.1 Numerical simulation and prediction of severe convective storms

The investigation of the structure and evolution of severe convective storms is motivated by the fact that their associated weather — flash floods, damaging hail, strong surface winds, severe turbulence and tornadoes — poses a threat to life, property, the economy, and even national security. Therefore, the continuous improvement of mesoscale operational weather prediction (especially applied to convective systems), and the assessment of the feasibility of numerical weather forecasting at the storm-scale¹, are of both scientific importance and practical relevance to society.

Historically, numerical modeling has played an important role in improving our knowledge of the dynamics and physics of thunderstorms and severe weather phenomena. In contrast to large-scale meteorology, where the first applications of numerical

¹Even though no universally accepted definition for “*stormscale*” exists, this term is used throughout the text for time and space scales in which convective storms and their main inner structures can be explicitly resolved by numerical models and/or detected by observing systems. That is, from few hundred meters (and few minutes) to several kilometers (and several hours), encompassing, basically, the micro- and meso- scales as defined by Orlanski (1975) or, alternatively, the meso- and meso- scales defined in Tulus and Bornstein (1996). Whenever the term *convective scale* or *cloud scale* is used, it should be interpreted as having the same meaning as *stormscale*.

models were closely associated with operational prediction (e.g., Charney et al. 1950), the numerical approach at the stormscale was primarily applied to basic research motivated by the need for improving our understanding about the dynamic intricacies of cumulus convection and thunderstorms (Ogura 1963, Soong and Ogura 1973, Steiner 1973, Schlesinger 1975, Klemp and Wilhelmson 1978, Clark 1979, among others).

The relevance of numerical studies at this scale of motion is evident if we consider that thunderstorms are more difficult to observe than synoptic-scale patterns. Their localized nature and high intermittency, and the existence of very fine structures, make the planning of adequate observing systems a difficult task. The mathematical modeling of convective storms in the 1970's and early 1980's allowed the investigation of the morphology and dynamics of storm structures (such as strong downdrafts and mesocyclones) and their relation with the synoptic scale environment. These models represented the backbone for the development of the first theories to explain the observed behavior of severe storms (e.g., Wilhelmson and Klemp 1978, Rotunno and Klemp 1982, 1985, Wilhelmson and Wicker 2001).

The development of more sophisticated numerical techniques and physical parameterizations suitable for mesoscale and stormscale applications, combined with continuous advances in computing power, led to a rapid evolution of mesoscale and cloud modeling during the 1980's. This rapid development, as well as progress in technology applied to observing systems (most notably, the Doppler weather radar), allowed a better understanding of thunderstorm dynamics. As a natural evolution, the challenge proposed for the 1990's and beyond was the translation of such evolving knowledge into specific applications toward a large goal: operational stormscale weather forecasting (Lilly 1990, Droegemeier 1990, 1997). In this new context, numerical solutions from convective-scale models would be used as *forecasting tools*, rather than serve as idealized or post-event simulations of thunderstorms.

Lilly (1990) pointed out that if operational weather *prediction* on the convective scale is to become a reality, major efforts should be focused in the areas of thunderstorm predictability, numerical model design, stormscale data acquisition, and initialization of stormscale models. Although significant progress has been made in these areas in the last decade, including real time numerical prediction of convective storms with varying degrees of sophistication (Xue et al. 1996, Droegemeier 1997, Wicker et al. 1997, Wilson et al. 1998), several issues still need to be addressed.

One of these refers to the identification of stormscale processes that are most important to the prediction of convective systems, and their impact on model initialization. For example, if a given variable or storm feature that plays a crucial role in the maintenance of the convective system is badly initialized in a stormscale model, the forecast may be poor. Thus, *what atmospheric fields and features within convective storms are most relevant? Which variables should be initialized best? Is the information content of every variable equally important to the specification of the atmospheric flow in a convective system? Or are there variables that contain redundant information? How do errors in a given atmospheric field affect other fields, and how does this response influence the capability to predict the evolution of a convective storm? What fields must be observed (or retrieved) with higher accuracy?* ***The present research aims to gain insight into these issues by assessing the influence of specific atmospheric fields in the numerical simulation of an idealized long-lived convective system.***

1.2 The search for a stormscale initial condition

While the operational initialization of large-scale models in meteorology has a fifty-year history (e.g., Daley 1991), only recently have initialization procedures been

specifically developed for stormscale models (Shapiro et al. 1995b, Droegemeier 1997, Sun and Crook 2001a, Weygandt 2002a,b). Several topics unique to the initialization of such models have been studied during the past ten years, regarding the specification of both environmental conditions and fields describing the inner structure of convective storms.

Many investigations have sought to evaluate the sensitivity of simulated thunderstorm evolution and/or related features to different meteorological fields (e.g., Yang and Houze 1995b, Crook 1996, Gilmore and Wicker 1998, Pandya et al. 2000, McCaul and Cohen 2002, among several others²). For instance, Crook (1996) discussed the sensitivity of moist convection to some thermodynamic parameters in the planetary boundary layer in the absence of strong large-scale forcing. He showed that convective initiation can be very sensitive to temperature and moisture differences between the surface and the well mixed boundary layer, and that once a deep convective cell is well developed, the strength of the storm is most sensitive to the boundary layer moisture field, compared to the temperature field.

Other studies have investigated *explicitly* the sensitivity of thunderstorm simulations/predictions to the initial conditions (ICs) (e.g., Weygandt et al. 1993, Elmore et al. 2002b). This includes the determination of ICs suitable for the stormscale (e.g., Ducrocq et al. 2000, Elmore et al. 2002a), and the analysis of error growth associated with initial perturbations applied to specific parameters and/or meteorological variables in cloud models (e.g., Li et al. 1995, Park and Droegemeier 2000).

Park and Droegemeier (2000) studied the sensitivity of a simulated supercell thunderstorm to errors applied to input parameters, especially moisture fields, using the tangent linear approach. Moisture perturbations inserted in the storm and in the background environment had a great impact on the storm features, such as the up-

²These studies do not necessarily address the model initialization problem directly, but their results have important implications to it.

draft and rainfall amount. The perturbations inside the storm generally had a greater influence on the forecast error than the ones applied in the environment. The pressure field was the variable with greatest impact on forecast error right after the perturbations were inserted in the storm, but overall, the temperature field inside the storm was the one with greatest influence over forecast errors.

Finally, investigations also have focused on data retrieval and assimilation techniques applied to the convective scale. In this respect, Doppler weather radar, such as the Weather Surveillance Radar-1988 Doppler (WSR-88D), represents the most powerful observing system available for the remote sensing of convective storms. While mesoscale surface observing networks, wind profilers and satellites can provide very useful observations of thunderstorms and/or related features, Doppler radars go a step further and monitor the inner structure of such systems. However, the information provided by Doppler radars is limited to the reflectivity, radial component of the wind with respect to the radar location, and spectrum width (Klazura and Imy 1993).

Therefore, the development of techniques to retrieve the unobserved fields, like the cross-beam velocity, temperature and microphysical quantities, is an area that has received much attention, especially in the last decade (Tuttle and Foote 1990, Sun et al. 1991, Verlinde and Cotton 1993, Laroche and Zawadzki 1994, Crook and Tuttle 1994, Shapiro et al. 1995a, Qiu and Xu 1996, Sun and Crook 1998, 2001a, Gao et al. 2001, Lazarus et al. 2001, Xu et al. 2001, Weygandt et al. 2002a,b, and others). In general, the performance of the retrieval/assimilation techniques has been tested with both simulated and real radar data, with emphasis on the operational aspect of the problem. These studies indicate that the capability to estimate/retrieve information about the inner structure of convective systems does exist. However, *having this capability does **not** mean that we know which fields should be best estimated*

(or retrieved) and initialized in a model to obtain a good forecast on the stormscale. To determine that, it is necessary to assess what meteorological variables contain the most crucial information describing the atmospheric flow within a convective storm, which represents the specific topic of our research.

1.3 Motivation and goals

Our experience with large-scale flow shows that knowledge of the physical laws governing the atmosphere, and of atmospheric balances (e.g., geostrophic, hydrostatic), are useful for determining which meteorological fields are most important in the initialization of numerical models (Smagorinski et al. 1970, Daley 1980, 1991). This is because *one state described by a given variable may constrain the behavior of another variable*. Thus, under some circumstances, the information provided by a certain variable can be redundant. Or, quoting Smagorinski (1969) (from Daley 1980): “First of all, not all data are equal in their information-yielding capacity. Some are more equal than others. This tells us that if there is a choice as to what can be measured, then one variable may be preferable over another”.

Geostrophic adjustment, for example, was the main motivation for Charney et al. (1969) to assess the impact of satellite-derived temperature observations on the initialization of a global circulation model — given that temperature and pressure (i.e., mass field) can be hydrostatically related. They indicated that the wind field could be inferred from the “satellite”-derived temperature profile (if the surface pressure is known), and that, by inserting temperature corrections to the model at 12h intervals, the forecast could be significantly improved. This is an example of how knowledge of the dynamic constraints that govern atmospheric motion can be used to assess the relative importance of meteorological fields in the context of numerical weather

prediction.

Although no simple dynamic balance relation exists on the stormscale³, investigations of geostrophic adjustment (e.g. Blumen 1972), and, more recently, the revisiting of the hydrostatic adjustment problem (e.g., Bannon 1995), serve as a conceptual basis for the examination of the mutual adjustment of atmospheric variables at smaller spatial scales.

The general idea in large-scale studies which examine adjustment mechanisms under balanced dynamics, is that the specification of an unbalanced IC leads to a transient response, manifested as propagating waves, after which the balance relation being considered (e.g., geostrophic, hydrostatic) is restored and a final solution in steady-state is attained. Figure 1.1 indicates this general concept, valid for both analytical and numerical approaches. By understanding how the system evolves from the initial imbalance to a final balanced state implies an understanding of the *dynamic adjustment process*.

Now, let us draw our attention back to the simulation (or explicit prediction) of convective storms. No balance relation exists to define a strictly “unbalanced IC” or a “final balanced solution in steady state”. The full conservation equations must be used for the explicit numerical modeling of convective systems (e.g., Xue et al. 2000). So how can we examine dynamic adjustment mechanisms on the stormscale? To address this important topic, we define an *artificial* IC containing incomplete information about the inner structure of an idealized convective storm, i.e., *an IC that does not satisfy one or more of the conservation equations*. This is accomplished by impulsively eliminating (the information contained in) certain variables on the

³The cyclostrophic flow, which is a form of balanced dynamics, is mostly restricted to tornadic vortices (Davies-Jones et al. 2001), i.e., to a smaller scale than the one to be considered here. Long-lived mesoscale convective vortices, on the other hand, may approach the definition of a balanced flow (e.g., Davis and Weisman 1994), but such features do not account for the maintenance of the entire convective system that generated them.

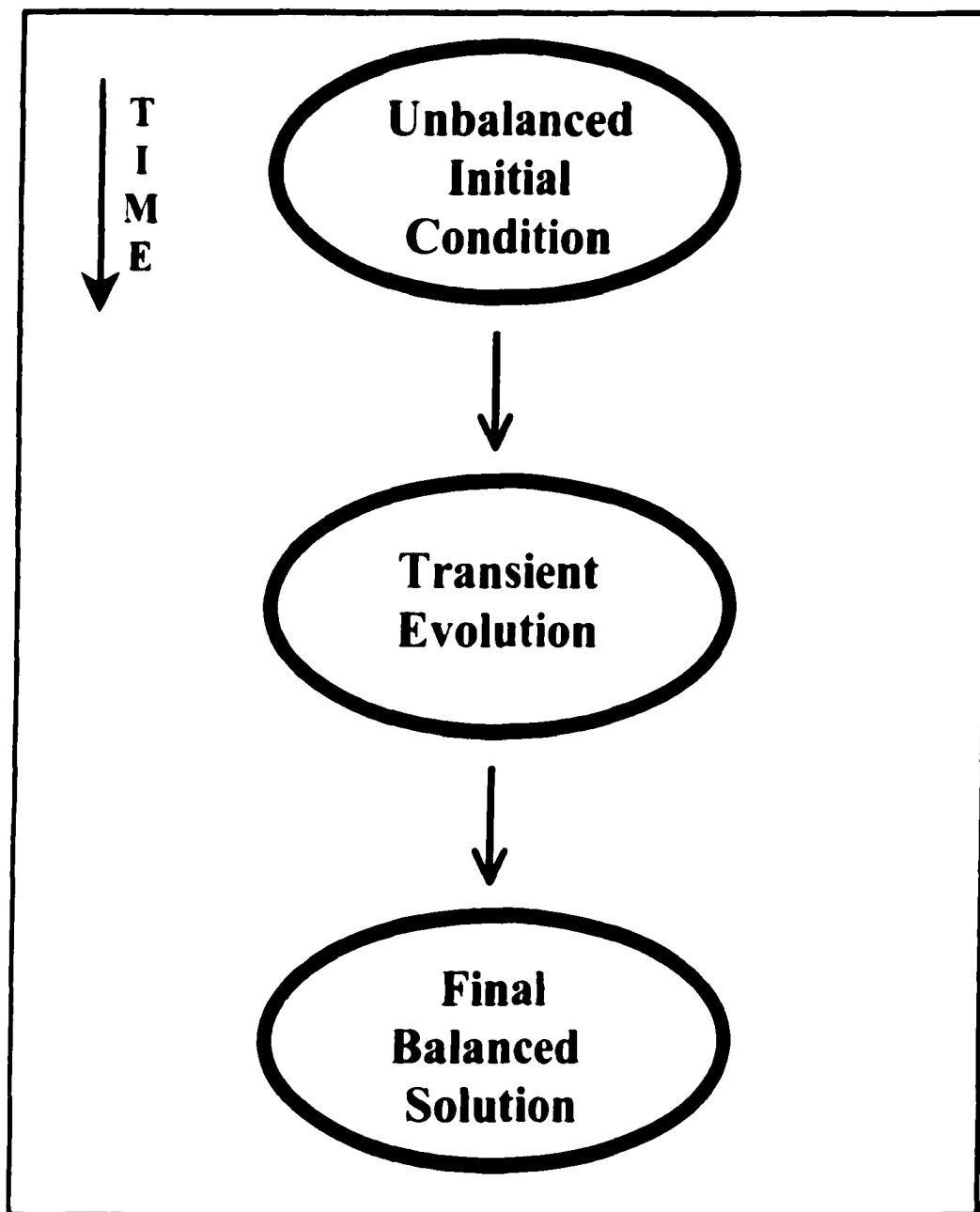


Figure 1.1: Sketch of the typical sequence of events when examining (either analytically or numerically) atmospheric adjustment processes driven by balance relations. An initial condition that does not satisfy the balance relation is specified. This is followed by a transient solution (dominated by the propagation of high frequency waves), which eventually leads to the final solution that satisfy the balance relation.

numerical simulation of a long-lived convective system¹, while maintaining other fields unchanged, and restarting the simulation with incomplete description of the state of the convective storm. *This artificial IC will be the stormscale-equivalent of the unbalanced IC depicted in Fig. 1.1.*

This approach has been investigated before by Weygandt et al. (1999), who studied the impact of the impulsive withdrawal of perturbation values of selected variables on the simulation of an idealized supercell. In that study, the withdrawal of vertical motion, for example, violated mass conservation because regions of horizontal convergence and divergence were not compensated by vertical motion. Thus, local variations in the mass (density) field were not consistent with the kinematic structure owing to the incorrect specification of the three-dimensional divergence. Our research follows similar approach and extends the work by Weygandt et al. (1999).

The generation of an IC that does not satisfy the conservation laws is not supposed to represent a realistic initialization of a convective-scale model, but rather a methodology for studying an intentionally-created transient response through an approach that is conceptually analogous to that used in large-scale dynamic adjustment processes (Fig. 1.1). Figure 1.2 summarizes this analogy by comparing the study of geostrophic adjustment using a shallow water equation model and the examination of adjustment processes in convective storms using a non-hydrostatic fully compressible model.

Because the model will force the restoration of conservation laws after the elimination of a given variable (though with significant errors in time derivatives), one should expect the perturbed and unperturbed fields to undergo some kind of adjustment, or response, under the stringent control of the conservation laws. This is the main aspect to be explored in the present research.

¹In practice this means that we reset variables back to the unperturbed base state representing the environment.

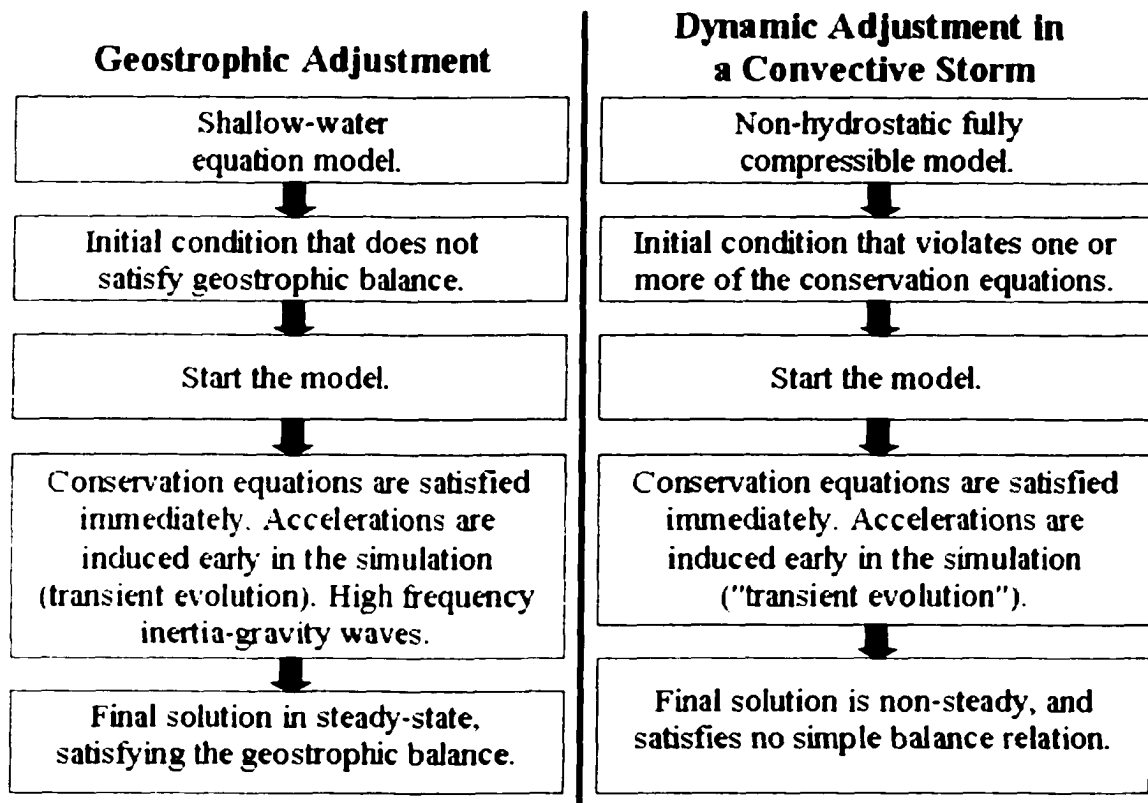


Figure 1.2: Conceptual comparison between a numerical study of geostrophic adjustment using a shallow-water equation model (SWEM) and the study of dynamic adjustment processes in a convective storm using a non-hydrostatic fully compressible model (NHFCM). **Geostrophic adjustment:** an IC not geostrophically balanced is imposed in the SWEM. As soon as the model is started, high frequency inertia-gravity waves are triggered due to the initial imbalance, and acceleration is present. As the waves propagate out of the domain and/or are damped, a final solution in steady-state is obtained, where the geostrophic balance is satisfied. **Dynamic adjustment in a convective system:** an artificial IC violating the conservation equations is imposed in the NHFCM. This IC contains incomplete information about the inner structure of a simulated convective storm. As the model is started, strong accelerations (as well as time tendencies of scalar fields) are induced while the conservation equations are satisfied, and the simulated fields respond to the artificially-specified IC. The objective is to study how the withdrawal of information about the convective system affects its simulation, and how distinct meteorological fields respond to each other in the early stages of the numerical experiment. Note that no steady-state solution is obtained in this case.

The questions that arise are: *How do the mass and thermodynamic fields respond to the elimination of one or more of the wind components? How does the wind field respond to the elimination of the thermal structure within the convective system? What is the impact of eliminating information about moisture field? Are the withdrawn variables restored to the same value they would have if no perturbation had been applied? If so, how fast is this accomplished, and what processes control them? If not, what mechanisms prevent them from being correctly restored? Does wave propagation play any relevant role during the adjustment process? Among the variables being eliminated, which ones have the greatest impact on the simulated convective storm? Does any variable contain redundant information (as considered by Smagorinski 1969), such that its elimination does not pose any significant "threat" to the quality of the simulation?*

By addressing these questions we focus on the mechanisms that control the *equivalent* of a transient evolution toward the final solution on the stormscale (conceptually similar to the sequence indicated in Fig. 1.1), except that the "final solution" is not a balanced one. In other words, the transient regime considered here no more represents a step toward the fulfillment of a simple dynamic relation, but rather to a non-steady solution. In this context, it is important to note that, while the conservation equations are satisfied as soon as the model is started, early in the simulation the time tendency terms in the equations will be larger than expected in the real atmosphere. This is the regime representing dynamic adjustment on the stormscale, and is *conceptually equivalent* to the early generation of accelerations in a shallow water equation model started with a geostrophically unbalanced IC.

It should be emphasized that no investigation has studied explicitly the problem of dynamic adjustment within convective storms, even though this is a subject with potential implications for model initialization and data assimilation on the stormscale.

For example, Weygandt et al. (1999) and Sun and Crook (2001b), employing different methodologies on the study of numerically-simulated supercells, found that simulations in which the horizontal wind field within the storm was completely eliminated (or not well initialized) resulted in major changes in the storm behavior. Conversely, the elimination, or bad initialization, of the vertical motion field still allowed a good simulation of the supercell, given that the horizontal velocity was well represented at the initial time. Nascimento and Droegemeier (2002) found similar results for a numerically-simulated bow echo, and Fiedler (2002) discussed some of the characteristics of the simulated flow that lead to such behavior (to be described in chapter 2). Nevertheless, none of these studies fully explores the physical and dynamical mechanisms driving the adjustment process.

Given these points, *the main goal of the present research is to closely examine the processes behind the mutual adjustment among specific variables when an impulsive perturbation is applied in the three-dimensional stormscale simulation of an idealized mesoscale convective system.*

The storm system chosen is the *bow echo* squall line. Similar to supercells, bow echoes often display the remarkable characteristic of sustaining coherent mesoscale structures for several hours, even under weak mid-tropospheric forcing situations (Johns 1993). This characteristic indicates the prospect for considerable predictability, and makes the bow echo an interesting system to be studied under the context of dynamic adjustment processes. Because bow echoes usually display a strong surface outflow and cold pool, mesoscale convective vortices and a rear-inflow-jet (Weisman 2001), the sensitivity of the simulation of these features to different variables will be addressed.

One may view the present work as a sensitivity study to ICs, as in a predictability investigation. However, an important difference exists from predictability research in

that the ICs defined here intentionally violate the conservation equations. Thus, our investigation does not represent an explicit study of atmospheric predictability on the convective scale; rather, it aims at understanding the response among meteorological variables in convective storms.

Nevertheless, results from the present research will provide at least further insight into some relevant issues in several research areas in convective scale meteorology, which includes predictability, ensemble forecasting (e.g., better dynamic understanding of mechanisms leading to error growth in convective scale models), and model initialization with Doppler radar data retrieval (e.g., which retrieved variables are most crucial from an initialization standpoint?). The degree of generality expected for our results is discussed later in the text.

Chapter 2

Theory of Atmospheric Adjustment

An understanding of how meteorological variables mutually respond in atmospheric models is critical for avoiding IC imbalances that can quickly ruin a forecast (Daley 1991). One example is the generation of large amplitude inertia-gravity waves in primitive equation models when no initial balance is imposed, or when the initialization procedure fails to adequately filter high-frequency waves.

In the present research, the mutual *response* of meteorological fields to one another is referred to as *dynamic adjustment*. It is not necessary, for our purposes, that the final state — achieved after the adjustment process is realized — be steady. *We are using the expression “dynamic adjustment” in a broader sense given the lack of simple balance relations on the stormscale.*

We describe below a few atmospheric adjustment processes. Although geostrophic adjustment may have a secondary impact on most of the processes of interest at the stormscale, its well-known implication to model initialization serves as an important conceptual motivation for the present research. Hydrostatic and acoustic adjustments are more pertinent to our study, and thus will be described in detail.

2.1 Geostrophic adjustment

Geostrophic adjustment is the most well-known dynamic adjustment process in the atmosphere, and the one identified long ago as having a significant impact on model initialization (Phillips 1960, Blumen 1972). It can be examined, for example, by imposing an unbalanced geopotential height field as an IC in a simple shallow water system of equations

Such a system, discussed in standard textbooks (e.g., Gill 1982), consists of a shallow rotating layer of fluid that is homogeneous, incompressible and inviscid. It is the most simple system capable of reproducing the general aspects of high- and low-frequency dynamics of the large-scale atmosphere. In its linearized form (around a base state at rest), the shallow water system can be written as:

$$\frac{\partial u'}{\partial t} = f v' - \frac{\partial \phi}{\partial x} \quad (2.1)$$

$$\frac{\partial v'}{\partial t} = -f u' - \frac{\partial \phi}{\partial y} \quad (2.2)$$

$$\frac{\partial \phi}{\partial t} + \Phi \left(\frac{\partial u'}{\partial x} + \frac{\partial v'}{\partial y} \right) = 0 \quad (2.3)$$

In (2.1)-(2.3) standard notation is used, and $\phi = gh$ and $\Phi = gH$ are, respectively, the perturbation and base-state geopotential, where H is the (unperturbed) mean height of the free surface and h is the deviation from H .

It can be shown (Daley 1991) that, from the vorticity and divergence equations derived from (2.1)-(2.3), the shallow water system leads to a set of coupled linear partial differential equations (PDEs) which admit wave-type solutions of the form of two inertia-gravity modes and one Rossby mode.

An unbalanced IC in this system implies that an initial geopotential height field is not in geostrophic balance with the wind field through the pressure gradient term in

Eqs. (2.1) and (2.2). Figure 2.1 shows the time evolution of the solution obtained from a linearized shallow-water model when an initially unbalanced geopotential height field is imposed (Fig. 2.1a). The initial wind field is at rest. The imbalance triggers inertia-gravity waves that move away from the imposed geopotential field, and perturbations in both geopotential and wind fields are generated.

After 6 hours (Fig. 2.1e), the inertia-gravity waves have propagated out of the domain and a steady-state solution is obtained. The final amplitude of the geopotential height is just a small fraction of the that in the IC, and a weak wind field is maintained in geostrophic balance with the geopotential perturbation. In this case, most of the adjustment was performed by the mass field (indicated by the geopotential height), while the wind field was only slightly modified.

A distinct behavior can be obtained with the final solution being composed of a wind field that responds strongly to the initially unbalanced geopotential height. In this case, most of the adjustment is performed by the winds, while the final geopotential field maintains the initial structure. An important parameter for the identification of the field that tends to control geostrophic adjustment is the Rossby radius of deformation L_R , given by:

$$L_R = \frac{\sqrt{gH}}{f} \quad (2.4)$$

L_R defines a characteristic length scale at which rotational effects (i.e., associated with earth's rotation) become as important as buoyancy effects (i.e., associated with gravity waves) (Gill 1982). If the characteristic length scale L_D of the initial field (a wave) is small compared with L_R , then the final steady-state solution from an unbalanced IC will be determined by the initial wind field, which is the case in Figure 2.1. Conversely, if L_D is large compared with L_R , then the final steady-state solution will be determined by the initial mass field.

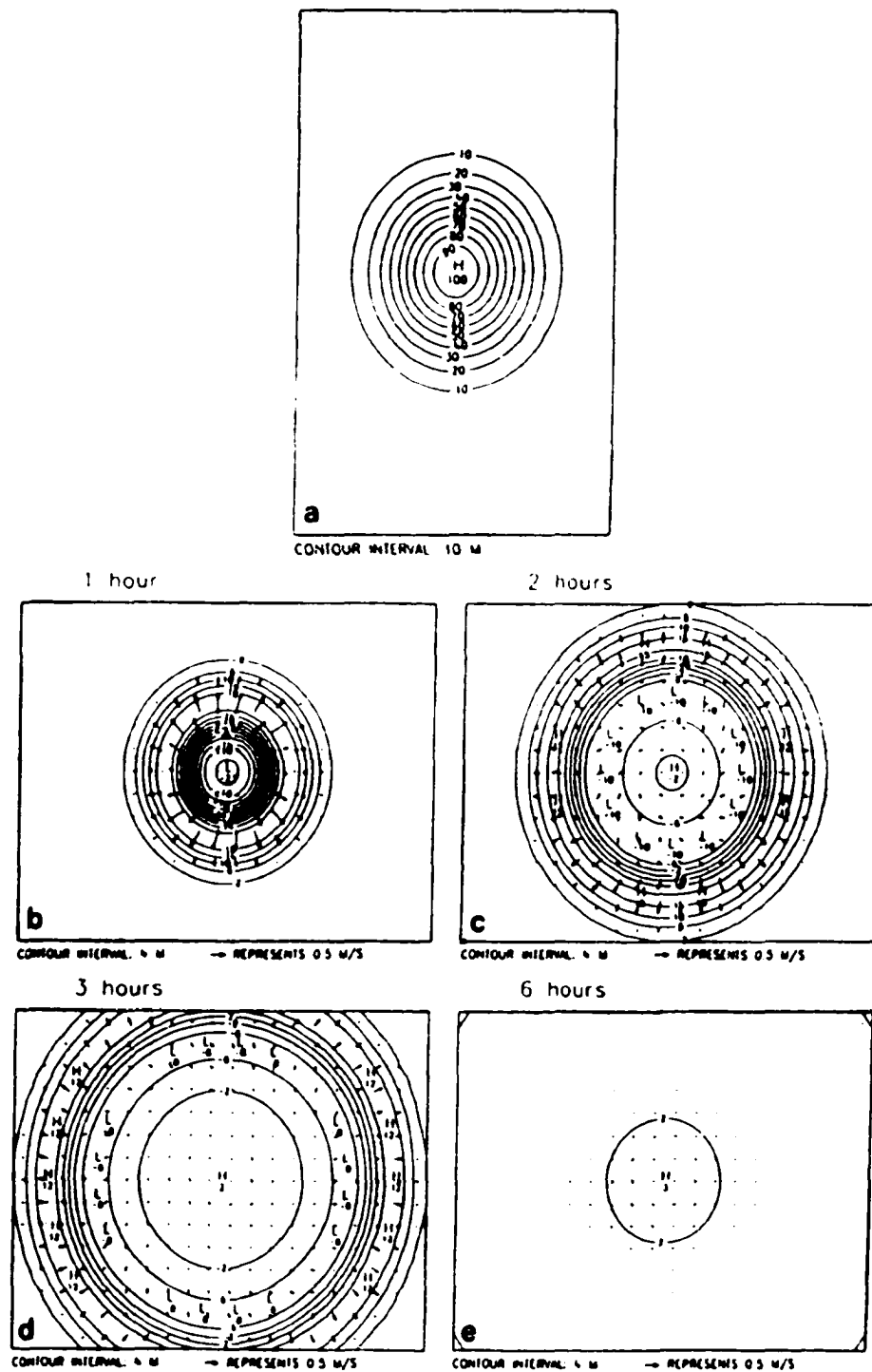


Figure 2.1. Geostrophic adjustment of initial geopotential perturbation (a). Solutions at 1, 2, 3, and 6-hr are indicated by (b-e). Contoured field is geopotential, and arrows indicate speed and direction of wind field. (After Barwell and Bromley, 1988, adapted from Daley 1991).

In mid-latitudes, where f is relatively large and, therefore, L_R is relatively small, the wind field tends to adjust to the mass field. In this case, it is possible to obtain a good approximation for the mid-latitude wind field from pressure (geopotential height) observations alone (e.g., Phillips 1963, Holton 1992). This is a nice example of one variable constraining the behavior of another, through a dynamic relation. It is, conceptually, the type of dynamic adjustment process that we also are interested in on the stormscale.

Significant effort in formulating initialization procedures for large-scale atmospheric models was stimulated by the relatively simple adjustment discussed above. Normal mode initialization (e.g., Williamson and Temperton 1981, Daley 1991), for example, is a method in which the component of a given wave amplitude associated with inertia-gravity waves is filtered from the observations (analysis in normal mode space¹), such that, when projected back to the physical space, the primitive equation model is free from spurious high-frequency waves during the entire model integration. In other words, the IC is balanced.

The clear implication of geostrophic adjustment for model initialization is a major motivation for analogous studies on the stormscale. As discussed in chapter 1, we do not expect to find a simple balance mechanism on the convective scale. However, if we understand how meteorological fields mutually adjust at this scale of motion (similar in concept to the mass and wind field adjustment under geostrophic balance), we can assess the relative importance of distinct variables and fields when initializing stormscale models, and also the impact of assimilating specific meteorological fields from observations without adjusting or constraining the remaining model variables.

¹i.e., the space where the observed analyzed field is decomposed into one Rossby mode and two fast moving inertia-gravity waves (Daley 1991)

2.2 Hydrostatic adjustment: an anelastic approach

Although geostrophic balance plays a role in the dynamics of some long-lived mesoscale features produced by thunderstorms (e.g., anvil-level dynamics; Fulton et al. 1994), atmospheric adjustment processes associated with fast moving gravity and sound waves are the ones more evidently related to the intermittent nature of severe convective systems.

Before studying these adjustment mechanisms from the wave theory standpoint, it is useful to understand some simple processes regarding the response of the atmosphere to a localized heating (or buoyancy) source-sink, following the approach used by Houze (1993) and Yuter and Houze (1995b). It is shown below that buoyancy and pressure fields adjust to each other as the atmosphere tends to attain hydrostatic balance (not always achieved). This process has important application to dynamic adjustment within convective systems.

As in Houze (1993), consider the momentum conservation equation (multiplied by the base-state density $\bar{\rho}$, that is function only of height) for an anelastic, and inviscid atmosphere in a non-rotating reference frame:

$$\frac{\partial}{\partial t}(\bar{\rho}\vec{V}) = -\bar{\rho}(\vec{V} \cdot \nabla \vec{V}) - \nabla p' + \bar{\rho}B\hat{k} \quad (2.5)$$

In (2.5), standard notation is used (\vec{V} is the *three-dimensional* wind), and B is the buoyancy term, defined as $B = -g\frac{\rho'}{\bar{\rho}}$, where ρ' is the perturbation density. Note that, in contrast to the shallow water system discussed previously, we now refer to a non-hydrostatic system (with buoyancy representing the gravitational effects).

By taking the three-dimensional divergence of (2.5), and noting that $\nabla \cdot \bar{\rho}\vec{V} = 0$ for an anelastic system, we obtain the following diagnostic equation for perturbation pressure:

$$\nabla^2 p' = \frac{\partial}{\partial z} (\bar{\rho} B) - \nabla \cdot (\bar{\rho} \vec{V} \cdot \nabla \vec{V}) \quad (2.6)$$

The first term on the right-hand-side of (2.6), which is associated with the vertical gradient of B , is called the *buoyancy source* for pressure perturbation. The second term, associated with the three-dimensional divergence of the advection field, is called the *dynamic source* (Houze 1993). Equation (2.6) indicates that pressure perturbations in a non-hydrostatic system can be affected by (i.e., respond to) buoyancy and wind fields². One example of the latter case is the generation of negative pressure perturbations within mesocyclones/mesoanticyclones in supercell thunderstorms (e.g., Klemp 1987). However, to study hydrostatic adjustment, it is sufficient to analyze the relation between the pressure and buoyancy fields, such that only the buoyancy source is retained. Hence, (2.6) reduces to:

$$\nabla^2 p' = \frac{\partial}{\partial z} (\bar{\rho} B) \quad (2.7)$$

Equation (2.7) is an elliptic PDE (Poisson's equation) for the pressure perturbation field. Recall that, for wavelike disturbances (away from boundaries), the Laplacian of a given quantity is proportional to the negative of the deviation of this quantity with respect to its mean. Thus, from (2.7) one would expect to find negative (positive) pressure perturbations where $\frac{\partial}{\partial z}(\bar{\rho} B) > 0$ ($\frac{\partial}{\partial z}(\bar{\rho} B) < 0$).

Consider, now, an idealized positively buoyant air parcel, as depicted in Figure 2.2. On the upper portion of the parcel, where $\frac{\partial}{\partial z}(\bar{\rho} B) < 0$, a positive pressure perturbation is induced, while on its lower portion, where $\frac{\partial}{\partial z}(\bar{\rho} B) > 0$, a negative pressure perturbation forms³. Therefore, as the positively buoyant air parcel tends to

²Equation (2.6) describes a diagnostic relation derived from a non-hydrostatic and anelastic system. For a non-hydrostatic and fully compressible system of equations, this diagnostic relation does not hold. However, because the anelastic system can be considered a "sub-system" (or special case) of the fully compressible equations, the processes described in (2.6) are also present in solutions obtained from compressible models.

³Actually, the negative vertical variation of the base-state density in the lower portion of the air parcel induces a positive pressure perturbation, competing with the contribution from the positive vertical variation of buoyancy. In describing Figure 2.2, we assume that the vertical variation of base-state density is much less than the vertical

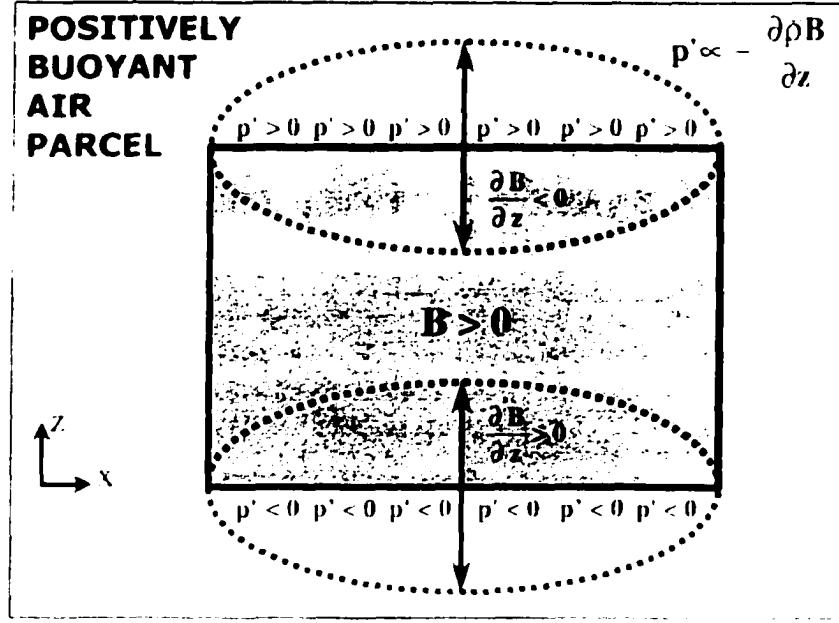


Figure 2.2: Idealized sketch of the perturbation pressure field induced by a buoyancy source, as described by Equation (2.7). Double-headed arrows indicate layers of stronger variation of buoyancy with height.

rise, the atmosphere responds by generating a vertical pressure gradient acceleration (VPGA) that counteracts the effects of buoyancy. This is a response that weakens the net vertical acceleration

Whether or not the induced pressure field is capable of hampering the vertical motion depends upon the aspect ratio of the buoyancy perturbation, as indicated in Figure 2.3. The pressure response to a buoyant parcel of high aspect ratio (i.e. “tall and narrow” region of positive buoyancy; Fig. 2.3a) generates not only the VPGA described in Figure 2.2, but also a significant *horizontal* pressure gradient acceleration (HPGA) that is consistent with a rising air parcel. In Figure 2.3a, horizontal air motion tends to diverge (converge) at the top (bottom) of the air parcel, which is a mass adjustment required for a rising air parcel. In this case, the system tends to be

variation in buoyancy, such that the net effect is the generation of a negative pressure perturbation just below the buoyant air parcel

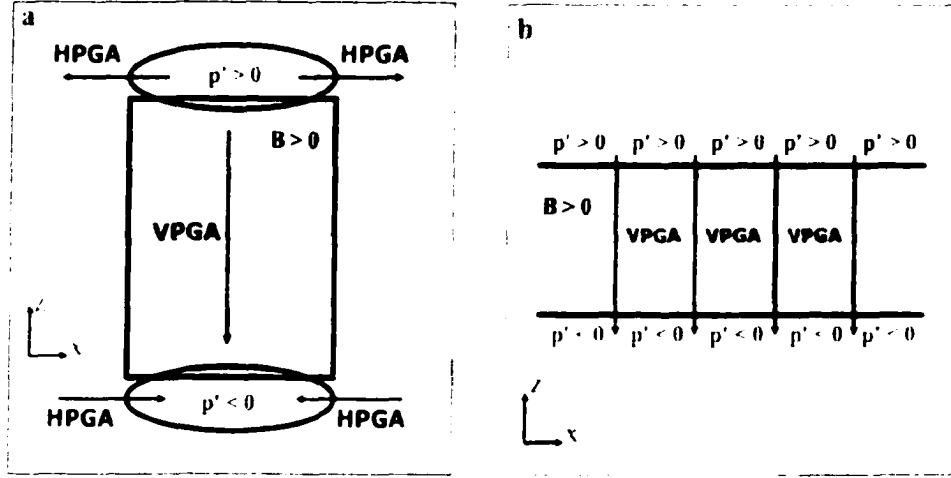


Figure 2.3. Idealized sketches of the pressure perturbation field induced by a buoyancy source with (a) high aspect ratio, and (b) low aspect ratio (i.e., “infinite” horizontal layer). In (a) the response of the pressure field is non-hydrostatic with respect to the buoyancy source, while in (b) pressure is in hydrostatic balance with the buoyancy source. Arrows indicate direction of pressure gradient accelerations (VPGA, HPGA) = vertical, horizontal, pressure gradient acceleration. (Based on Figures 7.1 and 7.2 of Houze (1993)).

non-hydrostatic.

In contrast, if the buoyant parcel is actually an entire layer of “infinite” horizontal dimension (i.e., a low aspect ratio “pancake” of air; Fig. 2.3b), then the pressure response will be horizontally homogeneous – assuming that the buoyancy perturbation is uniform. No significant HPGA (which would be required for rising motion, from mass conservation considerations) is generated, and the pressure response tends to be in hydrostatic balance with the buoyancy perturbation. *This is the mechanism of hydrostatic adjustment.*

Note that this entire discussion simply states the conditions in which hydrostatic balance is valid, i.e., situations in which the flow has a horizontal length scale much greater than the vertical length scale (e.g., Holton 1992).

2.3 Hydrostatic adjustment: an acoustic approach

2.3.1 Basic considerations of acoustic-gravity waves

The discussion above describes, in a relatively simple way, how the pressure field responds to buoyancy in the atmosphere. It has important implications for our research because this response is common within convective systems (e.g., Lafore and Moncrieff 1989) and, thus, will be addressed in our numerical experiments. To understand such basic adjustment mechanisms, it is sufficient to assume that the response of the pressure field is instantaneous. This assumption is in agreement with the employment of the anelastic system of equations, for which sound waves propagate “infinitely” fast, leading to instantaneous response in the pressure field.

However, for a complete description of the processes related to hydrostatic adjustment, it is necessary to take into account wave theory in an explicit way. This is because, in reality, the adjustment described in the previous section does not occur instantaneously, but is performed by the propagation of waves over finite intervals of time.

Note that when buoyancy effects are examined, we study perturbations in density on atmospheric motion (recall that $B = -g\frac{\rho'}{\bar{\rho}}$). In a stably stratified atmosphere, both sound and gravity waves *can* be triggered by perturbations in density because, for an ideal gas in a dry atmosphere, we have (from the equation of state; see, for example, Emanuel 1994):

$$\frac{\rho'}{\bar{\rho}} = \frac{p'}{\bar{p}} - \frac{T'}{\bar{T}} \quad (2.8)$$

Following Hooke (1986), consider an air parcel that, at its initial position, is in pressure and thermal equilibrium with the environment (i.e., no initial density perturbation according to (2.8)). Suppose this air parcel is vertically displaced in a rapid

manner, such that neither pressure nor thermal equilibrium is attained in the parcel just after its displacement. In this case, both terms on the right-hand-side of (2.8) contribute to the density perturbation. As the restoration of pressure equilibrium is realized, sound waves propagate, “communicating” the pressure disequilibrium to the surroundings⁴. Moreover, *in a stably stratified atmosphere*, the thermal component of the perturbation in density also generates waves: internal gravity waves. This is because, in its new position, the air parcel is denser than its surroundings, leading to an oscillatory regime.

Therefore, to fully examine hydrostatic adjustment and its implication to the modeling of convection, it is necessary to analyze systems that allow the propagation of both acoustic and gravity waves. Thus, consider a two-dimensional (xz-plane), adiabatic, inviscid and fully compressible flow where the effects of earth’s rotation are neglected. The set of *linearized* equations relevant for the study of acoustic-gravity waves is:

$$\left(\frac{\partial}{\partial t} + \bar{u} \frac{\partial}{\partial x} \right) u' = - \frac{1}{\rho_o} \frac{\partial p'}{\partial x} \quad (2.9)$$

$$\left(\frac{\partial}{\partial t} + \bar{u} \frac{\partial}{\partial x} \right) w' = - \frac{1}{\rho_o} \frac{\partial p'}{\partial z} - g \frac{\rho'}{\rho_o} \quad (2.10)$$

$$\left(\frac{\partial}{\partial t} + \bar{u} \frac{\partial}{\partial x} \right) \rho' - \frac{\rho_o}{g} N^2 w' = \frac{1}{c_s^2} \left(\frac{\partial}{\partial t} + \bar{u} \frac{\partial}{\partial x} \right) p' \quad (2.11)$$

$$\frac{\partial u'}{\partial x} + \frac{\partial w'}{\partial z} + \frac{1}{\rho_o c_s^2} \left(\frac{\partial}{\partial t} + \bar{u} \frac{\partial}{\partial x} \right) p' - \frac{g}{c_s^2} w' = 0 \quad (2.12)$$

Standard notation is used above. Expressions (2.9) and (2.10) are, respectively, the zonal and vertical momentum equations; (2.11) is the thermodynamic equation; and (2.12) is the mass conservation equation. These equations are linearized around a flow state defined by: $\rho = \rho_o(z) + \rho'(x, z, t)$; $p = \bar{p}(z) + p'(x, z, t)$, where $\bar{p}(z)$ is in

⁴Recall that sound waves are a manifestation of density variations due to pressure effects (Granger 1995).

hydrostatic balance with $\rho_o(z)$: $u = \bar{u} + u'(x, z, t)$: $w = w'(x, z, t)$. In (2.11), N^2 is the square of the *buoyancy frequency* (or *Brunt-Väisälä frequency*) for a compressible flow, given by:

$$N^2 = -g \left(\frac{1}{\rho_o} \frac{d\rho_o}{dz} + \frac{g}{c_s^2} \right) \quad (2.13)$$

where c_s^2 is the square of the adiabatic speed of sound, defined as:

$$c_s^2 = \gamma p / \rho \quad (2.14)$$

with γ being the ratio between specific heats at constant pressure and volume.

Equations (2.9)-(2.12) can be combined to yield two coupled hyperbolic PDEs for w' and p' (see sections 6.4 and 6.14 of Gill (1982) for a detailed derivation):

$$\left(\frac{\partial}{\partial t} + \bar{u} \frac{\partial}{\partial x} \right) \left(\frac{\partial W}{\partial t} - \Gamma W \right) = \frac{\partial^2 P}{\partial x^2} - \frac{1}{c_s^2} \left(\frac{\partial}{\partial t} + \bar{u} \frac{\partial}{\partial x} \right)^2 P \quad (2.15)$$

$$\left(\frac{\partial}{\partial t} + \bar{u} \frac{\partial}{\partial x} \right)^2 W + N^2 W = - \left(\frac{\partial}{\partial t} + \bar{u} \frac{\partial}{\partial x} \right) \left(\frac{\partial P}{\partial z} + \Gamma P \right) \quad (2.16)$$

where $W = \sqrt{\rho_o} w'$, and $P = (1/\sqrt{\rho_o}) p'$, and the parameter Γ is given by:

$$\Gamma = \frac{1}{2\rho_o} \frac{d\rho_o}{dz} + \frac{g}{c_s^2} \quad (2.17)$$

For an isothermal atmosphere, (2.15) and (2.16) have constant coefficients, with wave-type solutions for W and P that yield the dispersion relationship (DR) for *mixed acoustic-gravity waves*:

$$\frac{(\varpi - \bar{u}k)^2}{c_s^2} - (k^2 + m^2 + N_a^2/c_s^2) + \frac{N^2 k^2}{(\varpi - \bar{u}k)^2} = 0 \quad (2.18)$$

In (2.18), ϖ is the frequency of oscillation [$(\varpi - \bar{u}k)$ is the intrinsic or Doppler-shifted frequency of oscillation], k and m are the zonal and vertical wavenumbers, respectively, and N_a is the *acoustic cutoff frequency*, given by:

$$N_a = (N^2 + c_s^2 \Gamma^2)^{1/2} \quad (2.19)$$

N_a is the frequency below which vertically-propagating acoustic waves are not possible, while the buoyancy frequency (N) is the upper limit frequency for internal gravity waves, with N_a always exceeding N .

As in Jacobson (1999), it is useful to examine particular wave regimes from (2.18) by considering specific ranges of frequency and wavenumbers. For $\varpi^2 \ll N_a^2$, the purely acoustic component of (2.18) can be neglected, and the DR reduces to that of *internal gravity waves*:

$$(\varpi - \bar{u}k)^2 = \frac{N^2 k^2}{(k^2 + m^2 + N_a^2/c_s^2)} \quad (2.20)$$

Note that in (2.20) the effects of compressibility are not completely eliminated since for a pure internal gravity wave, the term N_a^2/c_s^2 vanishes.

On the other hand, for $\varpi^2 \gg N^2$ the gravity-wave component of (2.18) becomes unimportant, such that the DR can be written as:

$$(\varpi - \bar{u}k)^2 = c_s^2(k^2 + m^2) + N_a^2 \quad (2.21)$$

This is the DR for *internal acoustic waves* modified by stability effects — due to the presence of term N_a^2 , which does not appear for pure sound waves.

The degree with which these waves are influenced by gravity depends upon their wavenumber. As discussed in Sotack and Bannon (1999), for large wavenumbers, the second term on the right-hand-side of (2.21) becomes comparatively small, and (2.21) tends to a DR for pure sound waves, which are non-dispersive. On the other hand, for small wavenumbers, N_a^2 cannot be neglected, and (2.21) describe dispersive “sound” waves that are strongly affected by stable stratification effects. This is the wave regime referred to as *acoustic-gravity waves*.

Another regime of interest for the present investigation is the one obtained when no vertical propagation is allowed (i.e., $m^2 = 0$) and $\varpi^2 \ll N_a^2$ for long waves ($k \rightarrow 0$).

or $\varpi^2 \gg N^2$ for short waves ($k \rightarrow \infty$), yielding:

$$(\varpi - \bar{u}k)^2 = (c_s k)^2 \quad (2.22)$$

Expression (2.22) is the DR for external sound waves, or *Lamb waves*, which essentially have the frequency of pure sound waves. These waves propagate only horizontally, with their *energy* decreasing exponentially with height (Lindzen and Blake 1972).

Figure 2.4 summarizes the different wave regimes discussed above, with a graphical representation of the DR given by (2.18)⁵. To avoid confusion, the following nomenclature is adopted here (see Table 2.1): *mixed acoustic-gravity waves* refer to the most general wave regime indicated by the full expression (2.18). *Acoustic-gravity waves* (AGWs) refer to the specific regime described by (2.21) — i.e., with non-negligible N_d^2 . *High frequency sound acoustic waves* refer to non-dispersive sound waves, for which Na^2 is negligible in (2.21). If the expression *sound acoustic waves* is used without specification of frequency, then we refer to a more general acoustic regime that includes both AGWs and high frequency sound waves. If Lamb waves are to be included in *sound acoustic waves* we will make a clear reference in the text; otherwise, they will be referred to separately. *Internal gravity waves* (IGWs) are used for waves described by DR (2.20) — either in their compressible or incompressible forms.

To correctly interpret the adjustment processes to be described in the next subsections, it is important to recall the basic characteristic that IGWs have group velocity perpendicular to their phase velocity, while high frequency sound waves have group velocities in the same direction of their phase velocity.

⁵Equation (2.18) also includes the DR for mountain waves, but this regime is not addressed here.

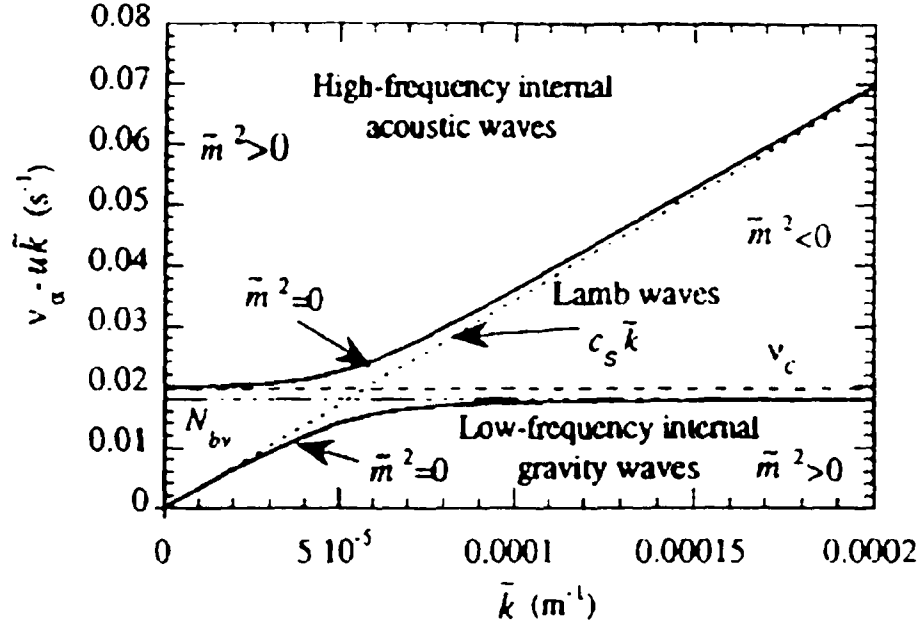


Figure 2.4: Relation between intrinsic frequency (indicated by $v_a - u\bar{k}$) and the zonal and squared vertical wavenumbers (\bar{k}, \bar{m}^2) for an isothermal atmosphere with buoyancy frequency of 0.0180 s^{-1} indicated by N_{bv} in a dot-dashed line, acoustic cutoff frequency of 0.0198 s^{-1} indicated by v_c in a dashed line, and $c_s = 346 \text{ m s}^{-1}$. Regions of $\bar{m}^2 > 0$ refer to vertically- and horizontally-propagating waves (i.e., internal waves), whereas $\bar{m}^2 \leq 0$ refers to purely horizontally-propagating waves (i.e., external waves). The dotted line indicate the dispersion relationship for Lamb waves, connecting the point ($\bar{k} = 0, \bar{m}^2 = 0$) to the point ($\bar{k} \rightarrow \infty, \bar{m}^2 = 0$). (Adapted from Jacobson 1999)

Table 2.1: Nomenclature adopted to label distinct wave regimes, and their corresponding dispersion relationship (DR).

<i>Nomenclature for wave regime</i>	<i>Two-dimensional DR expression</i>
mixed acoustic-gravity	Equation (2.18)
internal gravity (IGW)	Equation (2.20)
acoustic-gravity (AGW)	Equation (2.21), with non-negligible N_a^2
high frequency sound acoustic	Equation (2.21), with negligible N_a^2
sound acoustic	Equation (2.21)
Lamb	Equation (2.22)

2.3.2 Response of a stably-stratified atmosphere to impulsive heating: Lamb's problem

The role played by IGWs in the response of the airflow to a source/sink of heating, and even its potential implication to thunderstorm maintenance, have been the subject of several studies such as Lin and Li (1988), Bretherton and Smolarkiewicz (1989), Raymond and Rotunno (1989), Schmidt and Cotton (1990), Nicholls et al. (1991), Mapes (1993), Young and Houze (1995a), and Fovell (2002). However, in this subsection, we focus on the problem of the linear response of a stably stratified atmosphere to an impulsive heating source (or sink), as, for example, studied analytically by Lamb (1932). In that original one-dimensional approach, Lamb showed that, for an isothermal and compressible atmosphere, the transient response to a horizontally-uniform impulsive heating with no vertical extent (i.e., with aspect ratio tending to zero) consists of AGWs, with the final solution being in hydrostatic balance. This physical configuration is sometimes called *Lamb's problem* (Bannon 1995a, hereafter referred to as B95), and is considered a prototype for hydrostatic adjustment.

This problem has been revisited and extended in a series of papers by Peter R. Bannon and contributors since the mid-1990s, and deserves careful attention in our analysis because deep convective storms represent a form of impulsive and localized thermal perturbation in the atmosphere.

B95 analyzes the impact of a vertically-uniform instantaneous heating source with finite vertical extension — instead of the infinitesimally thin layer considered by Lamb (1932) — on an isothermal atmosphere where compressibility effects are included. The unperturbed state is hydrostatic and at rest. As in Lamb (1932), only the response in an infinitely long vertical dimension is considered in B95 (i.e., no horizontal dependence exists, being consistent with a horizontally-uniform heating source).

The initial and instantaneous heating is applied to a layer confined within $-a \leq z \leq a$, as shown by the dashed lines in Figures 2.5c,d, which indicate the initial temperature and potential temperature perturbations, respectively⁶. The initial pressure perturbation is represented by a dashed line in Figure 2.5a, while no initial perturbation in density or in vertical displacement is defined (Figure 2.5b), characterizing a system in hydrostatic *imbalance*. The main question is: How is hydrostatic balance restored in such simplified system? Since density is unbalanced with respect to the pressure field, AGWs are expected in this compressible system.

B95 describes the adjustment process as follows: upward (downward) motion is excited starting at the top (bottom) of the heated layer, in agreement with the initial vertical pressure gradient acceleration. These wave fronts, associated with high-frequency sound waves, propagate upwards and downwards (i.e., each boundary of the heated layer triggers two wave fronts). Oscillatory wakes trail the initial wave fronts, as indicated in Figure 2.6, in association with the arrival of the wave fronts triggered by the opposite boundary of the heated layer. With time, the frequency of oscillation approaches $N\alpha$. In other words, referring back to Figure 2.4, the regime gradually migrates from $(\tilde{k} = 0, \tilde{m}^2 > 0)$, associated with high-frequency sound waves, to $(\tilde{k} = 0, \tilde{m}^2 \ll 1)$, which implies AGWs, to $(\tilde{k} = 0, \tilde{m}^2 = 0)$, meaning that no acoustic mode remains in the domain and characterizing a final steady-state solution in hydrostatic balance — see also section 3a of Sotack and Bannon (1999).

The steady-state solution⁷ for different variables is indicated by *solid lines* in Figure 2.5. By comparing Figures 2.5a and 2.5b for the final solutions of pressure and density, it is possible to note a mutual adjustment between these two variables. That is,

⁶Although the heating is uniformly distributed within $-a \leq z \leq a$, the temperature response is vertically asymmetric due to the exponential decrease in density in such isothermal “atmosphere”

⁷This final *unique* solution is made possible by the conservation of the quantity *specific stability* for an adiabatic flow (see Equations 4.4 and 4.5 of B95). It eliminates the hydrostatic degeneracy in an analogous way with which the conservation of potential vorticity eliminates geostrophic degeneracy when studying the geostrophic adjustment

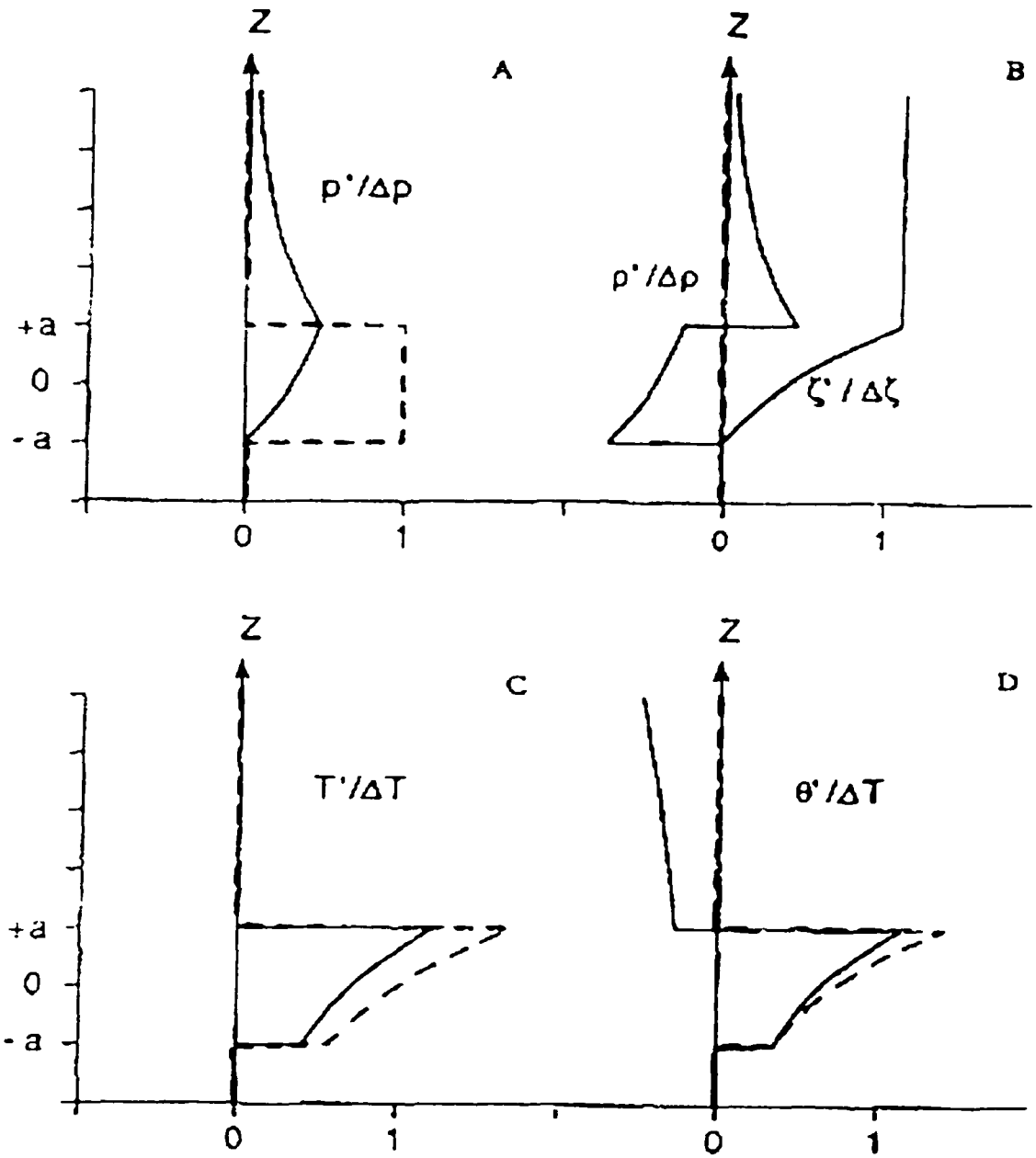


Figure 2.5: Diagram of distinct perturbation fields as a function of height for the one-dimensional hydrostatic adjustment problem with instantaneous and horizontally-uniform heating source: (a) pressure (p'), (b) density (ρ') and vertical displacement (ζ'), (c) temperature (T'), and (d) potential temperature (θ'). Dashed lines indicate the initial hydrostatically-imbalanced state. Solid lines depict the final steady-state solution. (Adapted from Bannon 1995).

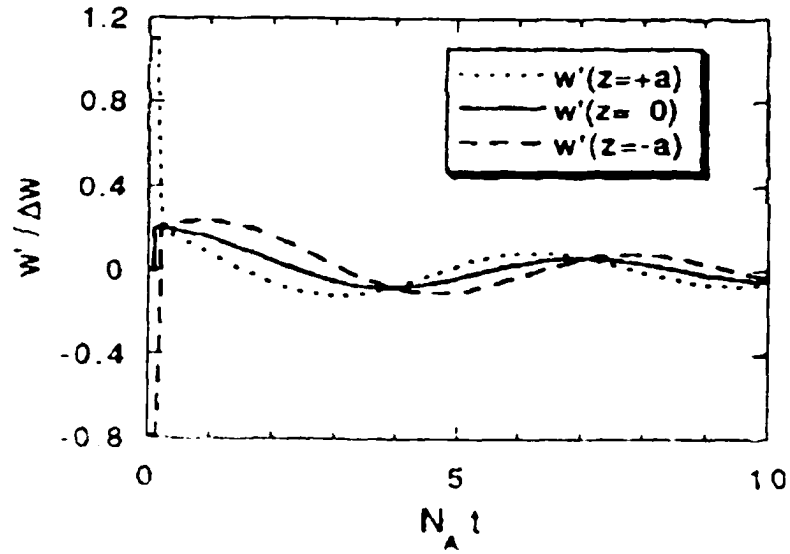


Figure 2.6 Time evolution of the perturbation vertical motion at the top ($z = +a$), bottom ($z = -a$), and middle ($z = 0$) of the heated layer for the one-dimensional hydrostatic adjustment problem with instantaneous and horizontally-uniform heating source. (Adapted from Bannon 1995).

neither pressure nor density retained its initial value. B95 found, for this idealized system, that only for very shallow heated layers does the pressure field respond to the initial density field, yielding a pressure perturbation equal or close to zero. This is because of the nature of the steady-state solution obtained for pressure (Eq. 1.8 of B95)⁵.

For the purposes of our research, the most relevant discussions in B95 are the inferences made about hydrostatic adjustment in three dimensions, and its sensitivity to the aspect ratio of the impulsive warming. One important question that can be addressed in this context is: What is the expected response from a fully compressible system when a heating source of relatively high aspect ratio is impulsively inserted in or removed from the domain of interest? This is the kind of perturbation to be induced in our numerical simulations of the bow echo.

⁵Another result evident in Figure 2.5, but that cannot be extrapolated to more realistic situations, is that layers below the heating source were not altered from their initial value. As discussed in B95 and Chagnon and Bannon (2001), this is a consequence of restricting the analysis to an one-dimensional (vertical) domain for which horizontal homogeneity is assumed. We will briefly revisit this point later in this subsection.

As discussed in section 2.2, a “tall and narrow” heating source yields a non-hydrostatic response, while an oblate heating source favors a hydrostatic response. Now this behavior can be re-addressed in the context of the dispersion relationship for mixed acoustic-gravity waves, and the adjustment process described in B95.

Following B95, consider Figure 2.7, which is a graphical representation (analogous to Fig. 2.4) of the DR for three-dimensional mixed acoustic-gravity waves. Frequencies of oscillation scaled by N are plotted as a function of the vertical (m) and horizontal (K_H) wavenumbers scaled by the scale height H , for an isothermal atmosphere. In the discussion that follows, it is important to keep in mind that IGWs are part of the solution “left behind” as the acoustic modes move rapidly out of the domain and/or are damped.

For an oblate heating source, the low aspect ratio implies low values of $K_H H$, and high values of $m H_s$. In this case, vertically-propagating acoustic modes promote hydrostatic adjustment because they are the ones with a large vertical component of group velocity (arrows in Figure 2.7). In other words, as sound waves move out of the domain, they leave behind a solution where IGWs have low frequency, which means that they are predominantly hydrostatic — i.e., parcel displacements induced by them are mostly horizontal. This is a different way of stating that the remaining solution is predominantly hydrostatic, and this process simply represents *the* hydrostatic adjustment described in B95’s results.

Conversely, a “tall and narrow” heating source is associated with high values of $K_H H$, and low values of $m H_s$. Under this condition, Figure 2.7 shows that acoustic modes propagate mostly in the horizontal, while the group (phase) velocities for IGWs are predominantly in the vertical (horizontal). This is a regime in which IGWs display higher frequency, associated with parcel displacements that are mostly in the vertical. These are non-hydrostatic IGWs. Hence, as sound waves move out of the domain,

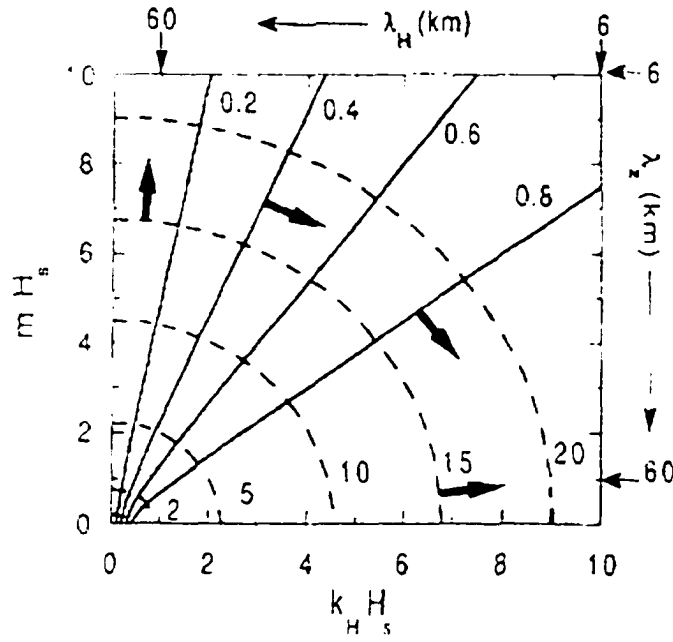


Figure 2.7: Dispersion relationship for three-dimensional mixed acoustic-gravity waves in an isothermal atmosphere. Dashed (solid) contours are isopleths of the scaled frequency of oscillation for acoustic (internal gravity) waves, where the scaling factor is the buoyancy frequency N . The ordinate (abscissa) refers to the scaled vertical (horizontal) wavenumber, where H_s is the scale height for an isothermal atmosphere. Typical horizontal and vertical wavelengths are indicated on the top and right sides of the diagram, respectively. Arrows show direction of group velocities. (Adapted from Bannon 1995)

the remaining solution is non-hydrostatic, as already expected from the anelastic approach presented by Houze (1993).

The processes just analyzed describe the basic mechanism behind hydrostatic adjustment. However, some of the considerations made by B95 in his one-dimensional approach are significantly restrictive. Bannon (1996a) expanded the analysis to include nonlinear effects and a non-isothermal atmosphere, while Sotack and Bannon (1999) studied the solution for heating of finite duration. The inclusion of top and bottom rigid boundaries in a three-dimensional framework, and with a horizontally-confined heating source of distinct aspect ratios, were addressed in Chagnon and Bannon (2001). Here are the most relevant findings:

(i) In the nonlinear version of B95's 1-dimensional analysis, Bannon (1996a) found that the fluid below the heated/cooled layer remains unaltered in the steady-state solution, just like in the linear approach (Fig. 2.5). For small amplitude heating, the total upward displacement of the top of the heated layer and the layers aloft (Fig. 2.5b for ζ') is relatively insensitive to the lapse rate. However, for heating or cooling of finite amplitude — for which non-linearities come into play — the vertical displacement is reduced as the atmosphere becomes more statically stable.

(ii) For any given lapse rate and finite amplitude initial perturbation in temperature, cooling the layer yields stronger vertical displacements for the top of the layer than does heating. In addition, more energy is dissipated into acoustic modes as static stability increases (Bannon 1996a).

(iii) The longer the heating source lasts, the broader and smaller amplitude are the acoustic wave fronts produced, with less energy going into such waves (Sotack and Bannon 1999) (i.e., more energy remains in the heated layer). For durations around and beyond the acoustic cutoff period, almost all energy produced remains in the final balanced state. On the other hand, the deeper the horizontally-uniform heated layer (for finite durations), the more energy that goes into acoustic modes (Sotack and Bannon 1999).

(iv) With a localized (i.e., not horizontally homogeneous) heating source in a three-dimensional atmosphere with rotation (Chagnon and Bannon 2001), the final steady-state solution consists of a vertical pressure dipole (high-over-low; Figs. 2.8a,b). This structure is related to a dipole in potential vorticity — i.e., anticyclone aloft and cyclone below. This dipole is not obtained for Lamb's original horizontally-uniform heating approach (Fig. 2.5a; B95, Bannon 1996a), but is the solution consistent with the analysis carried out in section 2.2.

(v) When prescribing a heating source with high aspect ratio, the final solution

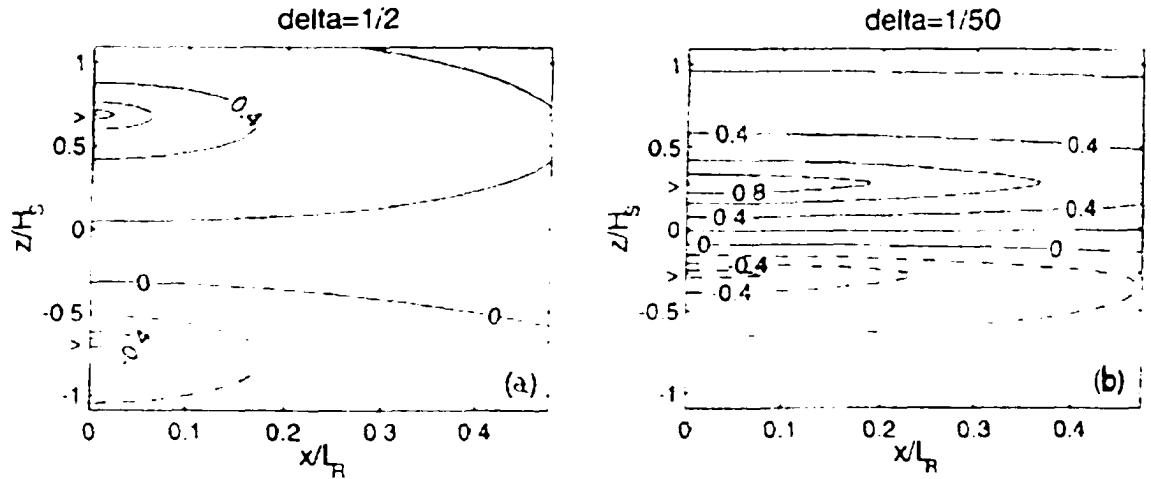


Figure 2.8: Vertical cross section of the steady-state pressure perturbation field for the three-dimensional hydrostatic adjustment problem with instantaneous heating sources of distinct aspect ratios in an infinite isothermal atmosphere. Response for a heating source with (a) high aspect ratio, (b) low aspect ratio. Positive (negative) pressure perturbations indicated by solid (dashed) lines. Each field is normalized by its maximum amplitude. Vertical (horizontal) distance scaled by the scale height of an isothermal atmosphere H_s (Rossby radius of deformation L_R). (Adapted from Chagnon and Bannon 2001).

for pressure tends to be less oblate, for which the pressure perturbation is more (less) horizontally (vertically) confined (see Fig. 2.8a). In other words, stronger horizontal pressure gradients are obtained for a “tall” heating source, associated with a non-hydrostatic regime (section 2.2). Moreover, a greater amount of energy goes into acoustic waves during the adjustment process (Chagnon and Bannon 2001), with these waves being predominantly horizontal (Fig. 2.7).

(vi) For a heated layer of low aspect ratio, the steady-state solution for pressure is more horizontally uniform and vertically confined (Fig. 2.8b), implying a condition closer to the hydrostatic regime. Thus, as expected, weaker horizontal pressure gradients are obtained for this case, and less energy is dissipated into vertically propagating acoustic waves (the modes favored in this condition; Fig 2.7).

(vii) Chagnon and Bannon (2001) found that, in the presence of a rigid boundary, stronger and broader pressure perturbations are obtained in the steady-state solution,

and less energy is dissipated by acoustic waves when both top and bottom rigid boundaries are present. This is because the boundaries limit the vertical expansion of the heated air column.

Other important discussion involves the differences in examining the energetics of hydrostatic adjustment through Lagrangian and Eulerian approaches, and the implication of hydrostatic adjustment on the behavior of numerical solutions under distinct compressibility assumptions (anelastic, pseudo-incompressible, modified compressible). The reader should refer to Bannon (1995b, 1996a,b), Sotack and Bannon (1999) and Chagnon and Bannon (2001) for further details.

2.3.3 Transient adjustment in a non-hydrostatic regime: thermal compression waves

Although B95 and Chagnon and Bannon (2001) expanded the discussion of Lamb’s adjustment problem to three-dimensions and localized heating sources (which can be considered a proxy for convective storms), most of their analysis serves as a prototype to better understand how hydrostatic adjustment is realized in a fully compressible *large-scale* atmosphere.

On the other hand, Nicholls and Pielke (1994a,b) — henceforth referred to as NP94a and NP94b, respectively — examined the role played by IGWs and acoustic modes in mass adjustment and total-energy transfer for the specific case of localized heating sources associated with mesoscale circulations and thunderstorms. In NP94a,b, the horizontal extent of the (two-dimensional) model atmosphere is not infinite as in the Lamb-Bannon approach, but has lateral boundaries. However, NP94a,b were only interested in how mass adjustment and energy transfer occur in the compressible model before the fastest waves, i.e., acoustic modes, reach the lateral boundaries. In other words, NP94a,b addressed the behavior of the early

transient response of a two-dimensional (xz-plane) compressible mesoscale model to a prescribed heating source of high aspect ratio.

The analysis by NP94a,b can be considered a special approach to the more general hydrostatic adjustment, in which one is mostly interested in examining horizontally-propagating acoustic waves (high aspect ratio limit in Fig. 2.7) and IGWs during the dynamic adjustment forced by a heating source. However, some subtle differences in the treatment of the system of equations yield discernible conceptual distinction between the two approaches, which deserves some comments before carrying the discussion any further.

In the derivation of the wave equation that governs the acoustic waves of interest, NP94a *neglected the effects of gravity*. Among the momentum conservation equations, only the zonal component was necessary to close the system of equations in NP94a's one-dimensional analytical approach. One may argue that this could still be considered a particular case of the Lamb-Bannon approach, for the situation in which the DR given by (2.21) reduces to that of a Lamb wave (Eq. 2.22). However, a conceptual difference still persists, because NP94a derive the *non-homogeneous* form of the wave equation to study the transient solution under *continuous* diabatic forcing. This equation is:

$$\frac{\partial^2 p'}{\partial t^2} - c_s^2 \frac{\partial^2 p'}{\partial x^2} = \frac{\gamma \bar{p}}{c_p \bar{T}} \frac{\partial Q_m}{\partial t} \quad (2.23)$$

where Q_m is the heating function, representing the forcing for the hyperbolic PDE.

The transient solutions studied in Lamb-Bannon's approach were mostly for instantaneous heating functions, for which a *homogeneous* wave equation (in terms of w') derived from an adiabatic system was necessary. Sotack and Bannon (1999) studied the case of a non-homogeneous equation (see their Eq. 2.12) when examining the transient solution for heating of finite duration. But in that case the authors

were interested in vertically-propagating acoustic modes associated with horizontally-uniform heating sources, which deviates from NP94a.

NP94a.b called the wave-type solutions for (2.23) *thermal compression waves* (TCWs), in order to discriminate from one-dimensional mechanically forced sound waves that can be described by the homogenous version of (2.23) (Holton 1992, Jacobson 1999). With these conceptual distinctions in mind, we proceed to describe the main results from NP94a.b.

NP94a found that systems allowing only IGWs (e.g., anelastic system) cannot represent, in a complete manner, the transport of total energy⁹ away from a source of latent heating, such as that associated with a thunderstorm. Thus, despite the specification of a source of heating in the model — which should lead to a net increase in internal and potential energies — NP94a described a net *decrease* in total energy within the domain.

NP94a showed that a system of linearized equations with solutions of TCWs does conserve energy. In this case, TCWs are responsible for propagating total energy away from the heating source, which is not completely performed by IGWs. This process is depicted in Figure 2.9, which shows the numerical solution for internal and total energies at 40 min for a fully compressible two-dimensional (xz-plane) model forced by a 20 min long localized heating source positioned at the center of the domain ($x = 0$ km). The contours of internal and total energies confined at the center of the domain are associated with the IGW component of the solution. However, off the center, the horizontally propagating acoustic waves (TCWs) are responsible for the transport of energy away from the heating source. This second component of the solution is not present in anelastic models.

NP94b expanded the discussion to include the mass adjustment problem, including

⁹By total energy we mean the sum of internal energy, gravitational potential energy and kinetic energy

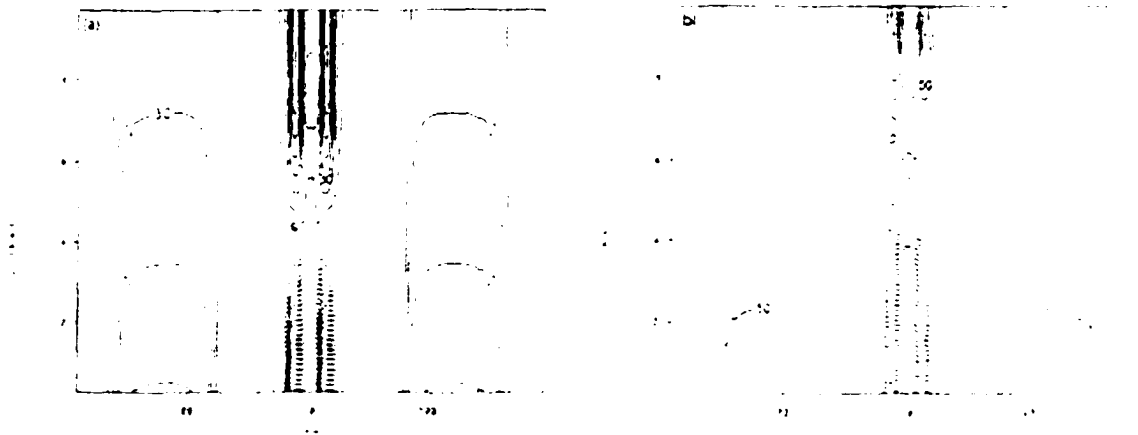


Figure 2.9: Vertical structure (xz-plane) of perturbation energy fields 40 min after a localized heating source of high aspect ratio and lasting 20 min is positioned in the center of the domain in a fully compressible two-dimensional mesoscale model. (a) Perturbation internal energy (contour increment of 12 J m^{-3}); (b) perturbation total energy (contour increment of 20 J m^{-3}). Top and bottom boundaries are rigid. (Adapted from Nicholls and Pielke 1994a).

the role played by vertically-propagating acoustic waves not emphasized in NP94a¹⁹. NP94b indicated that, similar to the total energy transfer issue, IGWs do not account for the entire process of mass adjustment in the presence of thunderstorms or significant mesoscale circulations, such as a sea breeze. Thus, analytic or numerical systems that do not resolve TCWs may not conserve mass.

The two-dimensional numerical simulation of an idealized sea breeze with a fully compressible model, carried out by NP94b, highlighted the importance of TCWs in adjusting the mass field, as indicated in Figure 2.10. The thick solid line at the bottom of the figure indicates the “heated island” — which behaves as a continuous heating source. The solution for horizontal mass flux (Fig. 2.10a) shows a stronger circulation at the “coasts”, but “offshore”, flow propagating outwards at the speed of sound is also present. The positive pressure perturbations in the “offshore” areas (Fig. 2.10b) represent wave fronts propagating at the speed of sound (TCWs). Thus,

¹⁹The numerical solutions in NP94a refer to a model with rigid top and bottom boundaries. In NP94b, the top boundary is “open” for sound waves.

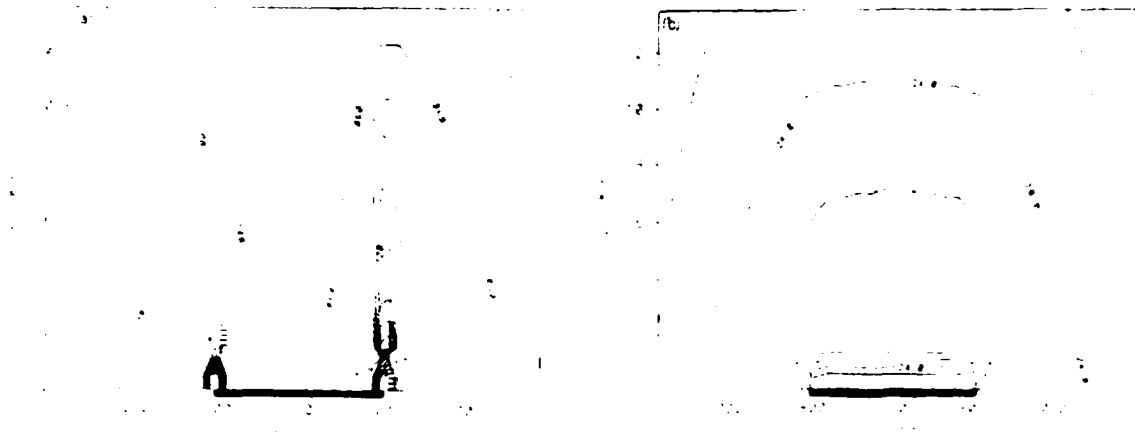


Figure 2.10: Numerical solution (in a xz -plane) at 1 hr for a two-dimensional simulation of an idealized sea breeze circulation in a compressible mesoscale model. The heating source is prescribed at the central 20 grid-points, in the first level above surface, and lasts for 1 hr. (a) Horizontal mass flux (contour increment of $0.04 \text{ kg m}^{-2} \text{ s}^{-1}$); (b) perturbation pressure (contour increment of 16 Pa). Top boundary is “open” for sound waves (Adapted from Nicholls and Pielke 1994b)

as mass is removed from the heated land, compensation occurs outside the “island”.

This compensation in mass adjustment is performed mostly by TCWs. The vertical mass flux (not shown) is much weaker, but TCWs also play a discernible role on it.

NP94b indicated that TCWs performing the mass adjustment have a vertical structure similar to that of Lamb waves, with maximum amplitude in pressure close to the ground, with the mass flux occurring almost exclusively in the horizontal. This result is consistent with some of the points discussed earlier in this subsection.

The mechanisms described above are a good example (actually, a prototype) of a dynamic adjustment process associated with the “initialization” of meso- and convective-scale circulations in fully compressible numerical models, and are particularly pertinent to our research.

2.4 Pure acoustic adjustment

Another dynamic adjustment process relevant for fully compressible convective-scale

models is one associated with the specification of the initial three-dimensional (3D) wind field, and is called simply *acoustic adjustment* (Fiedler 2002)¹¹.

In contrast to geostrophic and hydrostatic adjustments, acoustic adjustment refers to a “less realistic” type of dynamic adjustment (from an observational standpoint) related to artificial imbalances between the wind and mass fields in the initialization of a compressible numerical model. Under such conditions, high frequency acoustic waves are triggered in the model. The examination of acoustic adjustment is relevant for model initialization because it provides insight into how vertical and horizontal wind fields tend to adjust to each other in a stormscale numerical model when a convective storm is represented in the domain.

Following Fiedler (2002), consider a two-dimensional (xz-plane), adiabatic, inviscid and fully compressible flow, where the effects of earth’s rotation and gravity are neglected¹², and the base state is hydrostatic and motionless. It is possible to derive the following wave equation for perturbation pressure p' :

$$\frac{\partial^2 p'}{\partial t^2} - c_s^2 \nabla^2 p' = 0 \quad (2.24)$$

where $\nabla^2 p' = (\partial^2 p' / \partial x^2) + (\partial^2 p' / \partial z^2)$, and c_s^2 is the square of the adiabatic speed of sound, defined earlier.

By inspection, it can be shown that the following wave-type solution satisfies (2.24):

$$p' = P \cos(kx) \cos(mz) \sin(\varpi t) \quad (2.25)$$

In (2.25), P is the amplitude, k and m are, respectively, the horizontal and vertical wavenumbers, and ϖ is the frequency of oscillation, given by $\varpi^2 = c_s^2(m^2 + k^2)$ (which is a particular case of the DR (2.21)).

¹¹Not to be confused with the acoustic component of the hydrostatic adjustment, nor with processes involving FCWs.

¹²The effects of gravity are neglected in this case *not* because they can be ignored in the xz-plane, but because it is a convenient choice in order to obtain solutions of the form of *pure acoustic waves*, i.e., without the influence of buoyancy forces.

The linearized zonal and vertical equations of motion consistent with the system being described here are, respectively:

$$\frac{\partial u'}{\partial t} = -\frac{1}{\rho_0} \frac{\partial p'}{\partial x} \quad (2.26)$$

$$\frac{\partial w'}{\partial t} = -\frac{1}{\rho_0} \frac{\partial p'}{\partial z} \quad (2.27)$$

These equations are linearized around a base state at rest. Again, note that effects of gravity are not taken into account. Note also that the flow described by (2.26) and (2.27) is irrotational, i.e., for which $(\partial u'/\partial z - \partial w'/\partial x)$ is zero. After substituting (2.25) into (2.26) and (2.27), and respectively solving for u' and w' , we find:

$$u' = A k \sin(kx) \cos(mz) \cos(\nu t) \quad (2.28)$$

$$w' = A m \cos(kx) \sin(mz) \cos(\nu t) \quad (2.29)$$

where:

$$A = -P/(\nu \rho_0) \quad (2.30)$$

As in Fiedler (2002), consider now a two-dimensional (xz-plane) velocity field for an adiabatic flow confined within rigid boundaries at $z = 0$ and $z = H$ — i.e., an idealized local circulation cell, as indicated in Figure 2.11a. From the first theorem of Helmholtz (Granger 1995), the velocity field (U, W) can be decomposed into irrotational (or divergent) and incompressible (or nondivergent) parts:

$$U = u_{irr} + u_{inc} \quad (2.31a)$$

$$W = w_{irr} + w_{inc} \quad (2.31b)$$

such that:

$$\frac{\partial u_{irr}}{\partial z} - \frac{\partial w_{irr}}{\partial x} = 0 \quad (2.32)$$

$$\frac{\partial u_{inc}}{\partial x} + \frac{\partial w_{inc}}{\partial z} = 0 \quad (2.33)$$

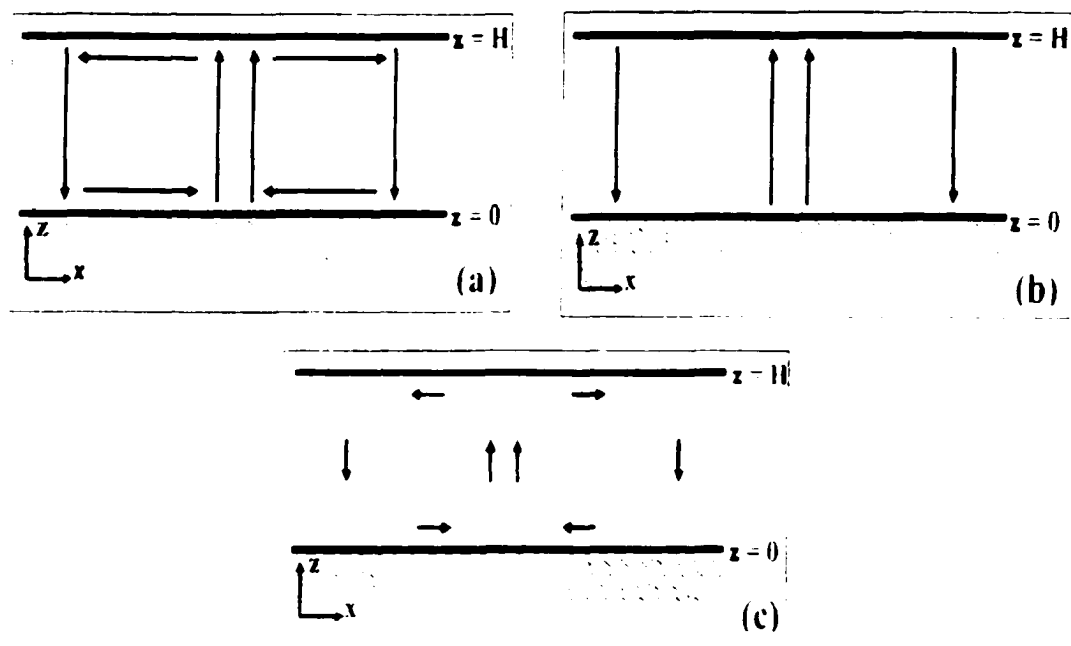


Figure 2.11: Sketches of idealized convective flows confined within top and bottom rigid boundaries: (a) fully developed circulation cell; (b) initial specification of an artificial wind field that does not satisfy mass conservation (initial horizontal velocity being eliminated), and (c) a weakened (or "destroyed") convective cell. See text for details.

For the purpose of examining acoustic adjustment, we consider the incompressible component of velocity as the *convective mode*, as in a Boussinesq system (where the flow is incompressible). It is the mode of meteorological relevance associated with an idealized steady convective circulation described by:

$$u_{conv} = -B m \sin(kx) \cos(mz) \quad (2.34)$$

$$w_{conv} = B k \cos(kx) \sin(mz) \quad (2.35)$$

where the vertical wavenumber is limited by $m = \pi/H$.

Expressions (2.34) and (2.35) satisfy the vorticity equation $D\eta/Dt = 0$ (where η is the meridional component of vorticity) obtained from the Euler equations in an xz -plane. Note that there is no time dependence in (2.34)-(2.35).

The irrotational field, on the other hand, refers to the transient regime (the *acoustic mode*) associated with the compressible component of the flow. Hence, solutions (2.28) and (2.29) are suitable to describe components u_{irr} and w_{irr} , respectively.

The problem posed in this simple analysis is the one in which an initial velocity field violates the incompressibility condition associated with the Boussinesq approximation (which describes the convective mode). Because of the initial deviation from incompressibility, high frequency sound waves are triggered, and a transient evolution promotes an acoustic adjustment until the final steady velocity field is obtained¹³. Thus, it is a dynamic adjustment conceptually similar to the ones discussed in the previous sections.

An IC that does not satisfy the incompressibility condition can be defined by setting $U(t = 0) = 0$. To this end (Fiedler 2002), we take $B = Ak/m$, where A is given by (2.30), such that:

¹³However, this is only true if we **assume** that high amplitude sound waves move out of the domain of interest and/or are damped. This characteristic is not stated in the original formulation of the problem (Fiedler 2002, and as described in this section) since the flow being considered in the analytic approach displays a periodic behavior with no friction and no divergence damping.

$$\begin{aligned}
U(0) &= u_{irr}(0) + u_{inc}(0) = \\
&= Ak \sin(kx) \cos(mz) \cos(0) - (Ak/m) m \sin(kx) \cos(mz) = 0
\end{aligned} \tag{2.36}$$

$$\begin{aligned}
W(0) &= w_{irr}(0) + w_{inc}(0) = \\
&= \frac{Bm^2}{k} \cos(kx) \sin(mz) + Bk \cos(kx) \sin(mz) = \\
&= B \frac{(m^2 + k^2)}{k} \cos(kx) \sin(mz)
\end{aligned} \tag{2.37}$$

So (2.36) and (2.37) are the IC's for U and W , respectively. From a physical perspective, this implies that the initial horizontal velocity is not consistent with the vertical velocity, as indicated in Figure 2.11b. If we *assume* that the high frequency sound waves propagate away and/or are dissipated (an assumption that is not clearly stated in the formulation of the problem by Fiedler 2002), then the amplitude of the acoustic mode vanishes, leaving only the convective mode. Therefore, at the final time, the steady vertical motion field has amplitude Bk only (see Eq. 2.35). In this case, the ratio between the final and initial amplitudes for W is (the ratio between (2.35) and (2.37)):

$$\frac{W(t \rightarrow \infty)}{W(t=0)} = Bk / (B \frac{(m^2 + k^2)}{k}) = \frac{k^2}{m^2 + k^2} \tag{2.38}$$

In other words, the final amplitude Bk is equal to the ratio (2.38) times the initial amplitude (Fiedler 2002)¹⁴. If, during acoustic adjustment, the horizontal wind field is to respond to the vertical motion and restore the convective cell (Fig. 2.11a), then the ratio (2.38) should be close to unity — i.e., the magnitude of the updrafts and downdrafts are not significantly changed. This is only possible if $k^2 \gg m^2$, implying that the characteristic length scale of the horizontal wind field is smaller than that of the vertical wind field. In this case, the updrafts and downdrafts are “tall and narrow”, characterizing a flow with high aspect ratio (Fig. 2.12a).

¹⁴This result should be seen as an hypothesis, rather than a solved problem

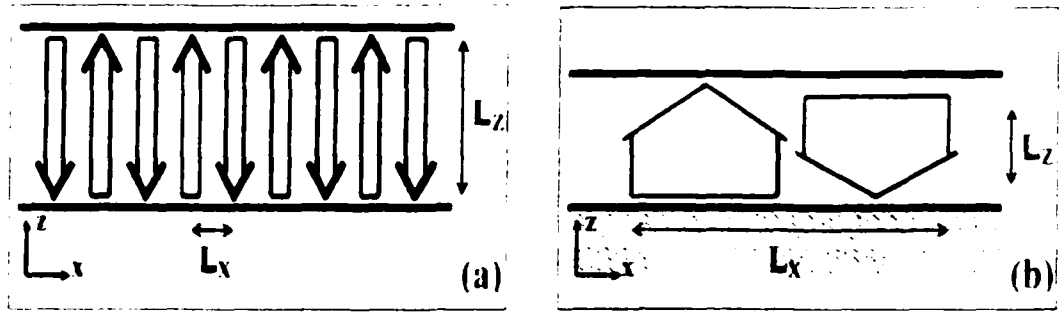


Figure 2.12: Idealized bounded vertical motion (updrafts and downdrafts), with distinct aspect ratios. (a) high aspect ratio; (b) low aspect ratio.

Conversely, if the aspect ratio is low (Fig. 2.12b), then $k^2 \ll m^2$, and the final amplitude for W is reduced as acoustic adjustment occurs. This is equivalent to saying that the vertical wind field responds to the horizontal component of the flow. In this case, the final solution is one that does not restore the original convective circulation since the vertical motion tends to be destroyed/weakened (Fig. 2.11c). This is not a surprise since (2.37) shows that, if $k \ll m$, most of the initial velocity field is projected onto the acoustic mode ($w_{irr}(0)$). High frequency sound waves with large amplitude are generated and the convective mode plays a secondary role in the adjustment process.

Based on the approach above, Fiedler (2002) postulated that, for convective structures with low aspect ratio, it is futile to initialize a storm in a compressible model by specifying only its vertical motion and not initializing a corresponding horizontal velocity field that is consistent with mass conservation¹⁵. This is because vertical velocity will adjust to the horizontal velocity, and not vice-versa. Preliminary sensitivity analysis in the three-dimensional simulation of idealized supercell thunderstorms performed by Weygandt et al. (1999) and Sun and Crook (2001b), and for an idealized bow echo squall line by Nascimento and Droegemeier (2002), appear to agree with

¹⁵Usually, the 3D wind field closely satisfies the anelastic continuity equation when initialized in compressible models (Fiedler 2002).

such reasoning.

2.5 Implications for the present research

As discussed in the previous sections, much has been learned from the linear analysis of dynamic adjustment mechanisms in simplified atmospheric settings. Several of these adjustment processes are relevant for convective scale meteorology, and have implications for stormscale model initialization in the presence of deep convective systems.

The work described herein increases the level of complexity of the modeled atmosphere and examines adjustment mechanisms in a fully non-linear and three-dimensional simulation of an idealized mesoscale convective system. The studies by Wevgandt et al. (1999), Nascimento and Droegemeier (2002) and Fiedler (2002) represent a starting point in that direction, but they do not address some intriguing questions implied by their results.

For example, Fiedler (2002) hypothesizes that for convective flows with *low aspect ratio* the horizontal wind field tends to dominate the process of acoustic adjustment, such that the vertical motion responds to the initial horizontal velocity field. Nevertheless, from hydrostatic adjustment standpoint these results appear contradictory¹⁶, because it is shown that deep convective storms behave as a non-hydrostatic system, for which the convective flow has *high aspect ratio*. This seems to indicate that the aspect ratio of the simulated convective system cannot be determined based on the analysis of a single adjustment process. In addition, actual convective systems do not necessarily represent a “well-behaved” sinusoidal pattern of updrafts and downdrafts as considered in the analytical approach, but a complex distribution of convective

¹⁶ Besides being rather counter-intuitive based on what meteorologists have learned to expect when considering the aspect ratio of the flow in deep convective storms, especially in comparison with the large-scale atmospheric flow

cells that vary from isolated systems (e.g., supercells) to convective lines (squall lines, bow echoes). Some of the dynamical mechanisms that may determine the effective aspect ratio of the flow for acoustic adjustment are discussed in this research.

Chapter 3

The Bow Echo

3.1 Pioneer investigations

Since the early applications of weather radar for operational purposes in the 1950's, several studies focused on the identification of radar signatures associated with the occurrence of severe weather phenomena. Terms such as *weak echo region*, *hook echo* and *bow echo* were coined along the years based on the characteristics of certain "echo" (i.e., returned radar beam) patterns as shown in a radar display, and their relation with storm structures.

Nolen (1959) is considered the first one to identify a configuration in radar reflectivity fields associated with severe weather events. This pattern, called *line echo wave pattern* (LEWP), was defined by Nolen (1959) as a line of radar echoes associated with convective storms organized in a quasi-sinusoidal fashion — as a sequence of adjacent concave and convex shaped echoes. Years later, Hamilton (1970) indicated that LEWPs could also be related to the occurrence of strong straight-line winds at the surface, particularly in the "bulge" or *concave-shaped echo* portion of the line. Nevertheless, it took a series of field and radar investigations on downbursts and

microbursts, led by T. T. Fujita during the 1970's, to provide more detailed information regarding the relation between LEWP in squall lines and strong downdrafts and damaging surface winds.

Fujita (1978) showed that the concave-shaped echo (as mentioned by Hamilton 1970) is often observed embedded in LEWPs, and renamed it as ***bow echo***. Figure 3.1 shows Fujita's depiction of a bow echo, as well as a hook echo — the latter is usually associated with the tornadic phase of supercell thunderstorms.

Fujita (1978) also noted that isolated bow echoes can occur without necessarily accompanying a LEWP. Based on radar data analysis, Fujita (1979, 1981) described a conceptual model for the life cycle of a bow echo which is essentially a revised version of his original model, proposed in Fujita (1978). This conceptual model is shown in Figure 3.2. It depicts the evolution of a mesoscale convective system (MCS) from a deep thunderstorm (or line of thunderstorms), with a well defined gust front, into a bow echo that produces strong surface winds — or *downbursts*. Fujita (1981) indicated that in the mature stage of the bow echo (stage C in Figure 3.2), the bow shaped structure develops a spearheaded sector in the region of strongest surface winds. In Fujita's description, the spearhead is often accompanied by a trailing *weak echo channel* (WEC) in the reflectivity field. In fact, it is recognized that the WEC, also called *rear inflow notch* (Przybylinski 1995), is a distinctive feature often observed with a typical bow echo (Przybylinski and Gery 1983, Burgess and Smull 1990, Funk et al. 1999, among others).

Fujita (1978, 1981) discussed that, as the surface outflow spreads well ahead of the system, the downburst weakens and the bow echo evolves into a *comma-shaped echo* (stages D and E in Figure 3.2) displaying a mid-level cyclonic mesoscale vortex at the northern end (or left end as looking downstream) and a weaker anticyclonic mesoscale circulation at the southern end (or right end). In a more updated nomenclature, the

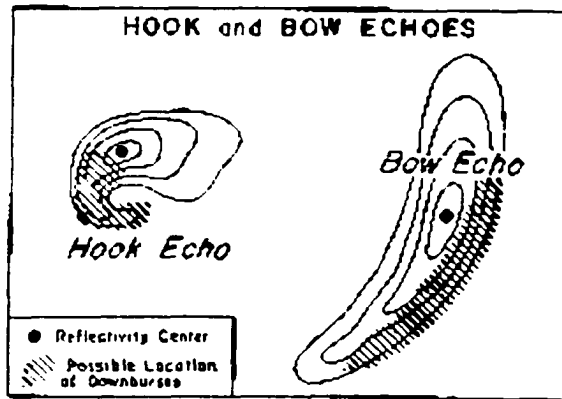


Figure 3.1 Schematic representation of typical hook and bow echoes (solid lines) and regions associated with strong straight-line winds at the surface (hatched areas). (From Fujita 1978)

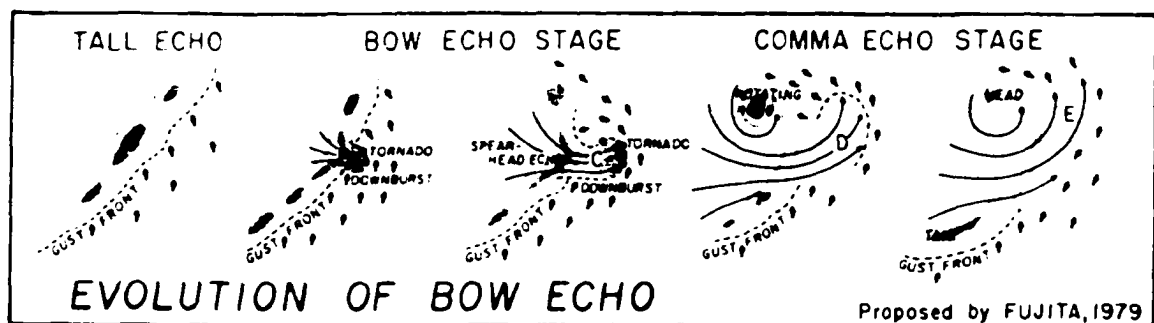


Figure 3.2 Conceptual model for the life cycle of a typical bow echo. Stage A: tall echo, B and C: bow echo, D and E: comma echo. (From Fujita 1979)

comma-shaped echo described by Fujita fits in the *asymmetric-type MCS*, as defined in Houze et al. (1989).

Przybylinski and DeCaire (1985) (hereafter, PD85) analyzed radar data from twenty cases² of warm season bow echo-type MCSs (which were called *derechos*, following Johns and Hirt 1983) associated with widespread areas of damaging winds in north-central and eastern United States. They identified four main patterns of radar echo distribution, as shown in Figure 3.3.

Type I MCS (Fig. 3.3a) consists of a narrow and solid squall line extending for as much as 250 km and with as many as three bowing segments along its leading edge. Each embedded bow echo can reach 100 km in length and may display a mesoscale circulation near its northern end. Several small WECs 10 to 15 km wide are observed along the trailing flank of the convective line. PD85 hypothesized that the WECs are generated by the entrainment of drier environmental air, enhancing evaporative processes. They also suggested a strong relation between the location of the WECs and areas of strongest surface winds, or downbursts. Type II MCS (Fig. 3.3b) represents a shorter system reaching 150 km in length in its mature stage, displaying a solid and dominant bow echo that can be 80 km long, and sometimes showing adjacent smaller bow echoes less than 20 km long. The type II convective system generates more than one WEC, but a predominant (up to 20 km long) WEC is usually evident. Convective elements detached from the main echo line are observed downstream of the main MCS. The isolated cell or cells, developing 50 to 80 km downstream of the major bowing segment, tend to merge with the larger MCS and are intensified as the bow echo approaches.

PD85's type III MCS (Fig. 3.3c) differs from type II in that isolated and scattered convective elements ahead of the system are rarely observed. The type III MCS tends

²Przybylinski (1995) added three more cases to this analysis

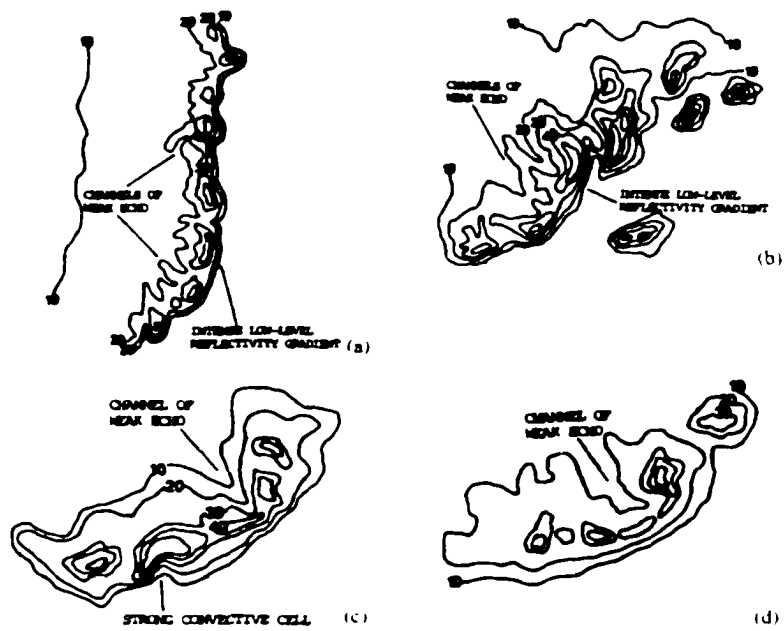


Figure 3.3: Typical radar echo distributions observed in warm season bow echo-type MCSs, as classified by PD85. (a) type I convective system, (b) type II, (c) type III, (d) type IV. Contour lines are low level reflectivity contours in dBZ. The four diagrams shown are not in the same spatial scale (see text for details). (Adapted from PD85).

to be slightly shorter than type II, extending from 40 km to 120 km. Generally, a single and well defined WEC is evident along the trailing flank of the system. The most distinctive feature of a mature type II MCS is the presence of a severe convective cell, occasionally exhibiting supercell characteristics, embedded near the leading edge of the bow echo and usually located south or southwest of the pronounced WEC. From the cases studied by PD85 and Przybylinski (1995), the type III bow echo MCS was the most common one.

The type IV MCS (Fig. 3.3d) was the less common bow echo pattern identified by PD85. The early evolution of this MCS consists of a storm system evolving from a classic to a high-precipitation (HP) supercell. During the HP stage, new convective elements are usually observed developing from 50km to 120 km south and west of the supercell, along the outflow boundary associated with its rear flank downdraft (Przybylinski 1995). The parent supercell gradually undergoes a transition to a bow echo configuration with a solid leading edge (i.e., strong low-level reflectivity gradient), displaying mesocirculation on the northern or northeastern end (comma head), and developing one or more WECs along its trailing sector.

PD85 did not explore in detail the time scales associated with the evolution of bow echoes, nor the typical synoptic forcing associated with them. Some of these topics are briefly reviewed below.

3.2 Bow echoes and derechos

From the investigation of several cases of long-lived and rapidly-propagating warm season MCSs associated with large swaths of damaging winds in the north-central and northeast United States, Johns and Hirt (1987) proposed a refinement in the

definition of the term *derecho*², and their work became an important reference in the study of bow echoes. According to Johns and Hirt (1987) (henceforth referred to as JH87), for a convectively-generated straight-line wind event to be considered a *derecho* it must meet the following criteria:

(i) An area of concentrated reports of convectively induced wind damage and/or convective gusts greater than 26 m s^{-1} must exist, and this area must have a major axis length of at least 400 km.

(ii) Reports within this area must show a pattern of chronological progression, either as a singular swath (*progressive derecho*; see Fig. 3.4a) or as a series of swaths (*serial derecho*; Fig. 3.4b);

(iii) Within the area there must be at least three reports, separated by 64 km or more, of either F1 damage (Fujita 1971) and/or convective convective gusts of 33 m s^{-1} or greater;

(iv) No more than 3-hr can elapse between successive wind damage events³.

It is important to note that the term *derecho*, as defined in JH87, refers to a type of convectively generated damaging wind, and *not to the MCS that generates it*. Moreover, none of the features identified by Fujita (1978, 1981) and PD85 for bow echoes is explicitly mentioned in JH87 when classifying *derecho*-producing MCSs (DPMCSs). However, the radar patterns and schematic depictions for typical DPMCSs described in JH87 shows either a well defined dominating bow echo (as in the case of a progressive *derecho*; Fig. 3.4a), or a long LEWP-type squall line composed by multiple bow echoes (serial *derecho*; Fig. 3.4b). More recently, Johns and Evans (2000) explicitly indicated that the JH87 database consisted *only* of wind and/or wind damage reports

²The term *derecho* was originally coined by Hinrichs (1888) to denote strong straight-line windstorms induced by convective activity.

³Additional criteria to be accepted in JH87's *derecho* database required that the wind event satisfying features (i) to (iv) should display temporal and spatial continuity, as indicated by surface pressure and wind fields (even if the movement of the associated radar echoes are not continuous), and that multiple swaths of wind damage should be a part of the same MCS as indicated by radar summary charts.

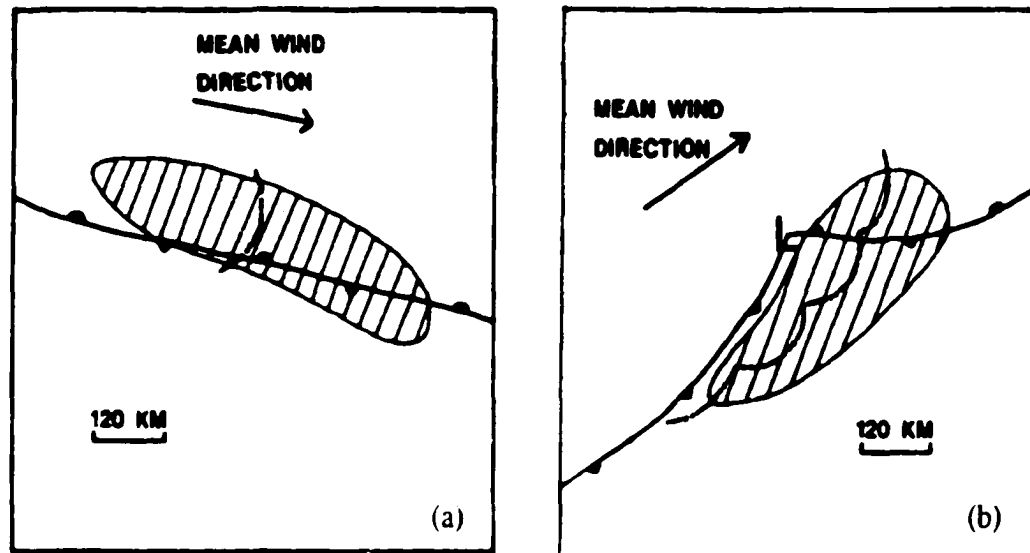


Figure 3.4 Schematic depiction of surface synoptic-scale features associated with the occurrence of (a) progressive derecho (warm season pattern), and (b) serial derecho (dynamic pattern). The hatched areas refer to the sectors affected by strong straight-line winds at the surface (derechos). Front and squall line symbols are conventional. Adapted from JH87.

associated with the bow echo stage of DPMCSs.

On the other hand, while bow echo-type MCSs frequently produce strong surface winds, not all of them generate large swaths of damaging winds that meet the definition of derechos. The results from JH87 showed that MCSs with vigorous long-lived bow echoes — i.e., bow echoes with life span of several hours, and reaching 120 km or more in individual length or combined as a LEWP in a squall line (Johns and Doswell 1992) — are the most likely ones to produce derechos. This characteristic has been confirmed by several case studies, such as Duke and Rogash (1992), Bentley and Cooper (1997), and others.

For the reasons stated above, bow echo should not be considered a synonym for derecho. It should be clear, though, that the 4-year study of derechos carried out by JH87, and extended by Johns et al. (1990) and Johns (1993), indicated an important association between derechos and long-lived bow echoes.

3.3 Mesoscale features in bow echoes

Bow echoes share many of the mesoscale features often observed with linear mid-latitude MCSs, as described in the conceptual model depicted in Figure 3.5, which is a vertical cross section of the kinematic, microphysical and radar-echo structure of a *mature* convective line with trailing stratiform precipitation (Houze et al. 1989). The leading edge of the system consists of deep convective cells associated with high radar reflectivity fields and heavy precipitation; most of the severe weather phenomena accompanying bow echoes occurs in this sector (strong surface winds, derechos, hail, short-lived tornadoes). An active surface cold pool and mesohigh (indicated by H_1 in Fig. 3.5) is formed just behind the gust front and plays an important role in driving strong surface winds (Johnson 2001, Wakimoto 2001).

The schematic in Fig. 3.5 also shows the life cycle of convective activity within the MCS. New convective cells are formed by the lifting provided by the advancing cold pool which behaves as a density current. Because the typical environment conducive to MCSs has high convective available potential energy (CAPE) (e.g., Johns 1993), the new cells develop vertical structure quite efficiently, reaching their mature stage just behind the gust front. As the cells become undercut from the warm and moist boundary layer ahead of the MCS, the mature stage is followed by a decaying stage represented by the “old cell” in Fig. 3.5.

In bow echoes (particularly, derecho-producing bow echoes), low-level convergence along the gust front — i.e., on the downstream side of the storm system — is enhanced compared to backbuilding systems or non-DPMCSs (Evans and Doswell 2001, Cortidi 2002), owing to a stronger surface outflow. The high efficiency in regenerating convective cells ahead of the line combined with stronger mean environmental wind (Evans and Doswell 2001; henceforth referred to as ED01) account for the remarkably

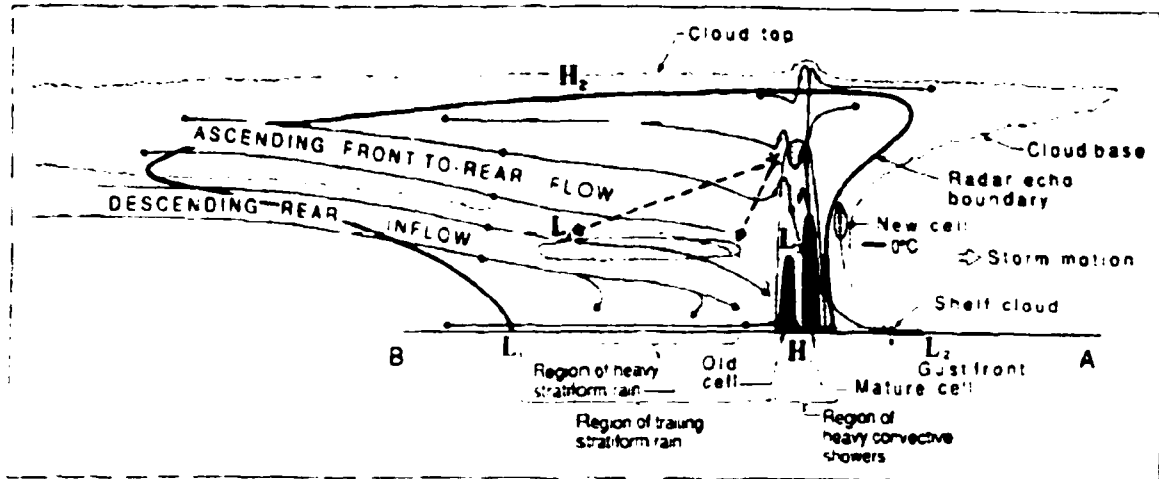


Figure 3.5 Conceptual model of a linear MCS with trailing stratiform precipitation viewed in a vertical cross section oriented perpendicular to the line of convective cells. Medium and dark shadings denote areas associated with intermediate and strong radar reflectivity, respectively. Heavy solid (light scalloped) line represents the boundaries of the storm as indicated from radar reflectivity (direct observation). Storm motion is toward the right of the figure. (Adapted from Houze et al. 1989.)

fast forward motion that characterizes long-lived bow echoes – as fast as 35 m s^{-1} ; Corfidi (2002).

Trailing the convective activity, a region of heavy stratiform precipitation is usually observed (but not always; Yuter and Houze 1995a), and the kinematic structure is dominated by an ascending front-to-rear flow, which results from the mid and upper portions of the leading updrafts leaning upshear, and a descending rear-to-front flow. In strong squall lines, the rear-to-front flow can be locally intense, especially along the axis that coincides with the apex of bow echoes, characterizing a *rear-inflow jet* (RIJ) (Smull and Houze 1987, Burgess and Smull 1990, Weisman 1992, Houze 1993). Ground-relative winds as strong as 50 m s^{-1} are observed with RIJs (e.g., Burgess and Smull 1990). The along-line variation in the rear-to-front momentum field accelerates distinct sectors of the MCS at different rates, leading to the characteristic bow-shaped structures or LEWPs in bow echoes.

The RIJ transports not only momentum but also drier air from mid to lower levels

which favors “cloud erosion” on the upstream flank of the leading convective cells, generating rear-inflow notches or WECs mentioned earlier (Przybylinski 1995). With enhanced evaporation–sublimation in these localized regions, stronger downdrafts and accompanying surface outflow are induced (Wakimoto 2001), being consistent with the fact that WECs are usually good indicators of sectors with intense surface winds (PD85).

One of the mechanisms generating the rear-to-front flow is the formation of a low- to mid-level mesolow (indicated by L_3 in Fig. 3.5) that extends from just underneath the leading updrafts to tens of kilometers behind the gust front. The generation of this mesolow is in agreement with the presence of a mid-level buoyancy source (see section 2.2) — associated with intense latent heating within the main updraft region of the MCS — and induces a rear-to-front pressure gradient force (e.g., Lafore and Moncrieff 1989). The generation of the rear-to-front flow can also be understood from considerations of baroclinic generation of horizontal vorticity (Weisman 1992, 1993) and manifestation of low frequency IGWs (Pandya and Durran 1996). These mechanisms are examined with more detail in chapter 7.

The RIJ is an important mesoscale feature in bow echo dynamics. Based on idealized simulations of bow echoes and applying the theory for long-lived squall lines developed by Rotunno et al. (1988) (known as *Rotunno-Klemp-Weisman* or *RKW theory*), Weisman (1992, 1993) hypothesized that the presence of an *elevated* RIJ plays important role in the maintenance of long-lived bow echoes. He indicates that without the elevated RIJ, MCSs with updrafts that lean upshear, as indicated in Figure 3.6a, undergo a transition from the mature stage (for which the leading updrafts are erect; not shown) to the decaying stage. This is because RIJs that descend well behind the gust front tend to enhance the surface outflow that undercuts the updrafts, weakening the system (Weisman 2001). With the elevated RIJ (Fig.

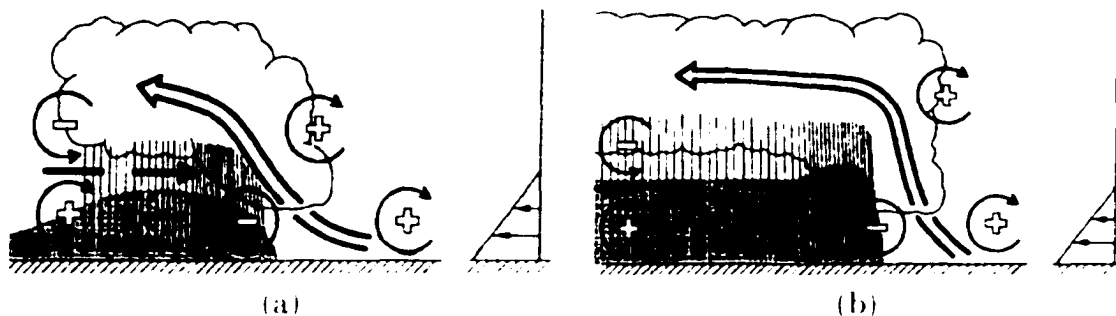


Figure 3.6: Schematic representation of the upshear-tilted convective flow in an idealized bow echo during its mature stage with a (a) developing RII, and (b) well defined elevated RII. Thick, double-lined vector represents the updraft current, thick solid vector denotes the RII, thin, circular arrows indicate convective-scale circulations associated with horizontal vorticity generated either by the ambient vertical wind shear or by the convective system; shading denotes the surface cold pool; regions of lighter or heavier rainfall are indicated by the more sparsely or densely packed vertical lines, respectively; scalloped line denotes the outline of the cloud. (Adapted from Weisman 1993)

3.6b), the circulation induced by the RII in the surface cold pool counteracts the upshear-oriented circulation forced by the gust front (indicated by the circular arrow with a minus sign at low levels in Fig. 3.6b). In this case, the leading updrafts do not tilt in the upshear direction as much as in the descending RII case, and lifting is enhanced in the more erect updrafts which favors long-lived squall lines (Rotunno et al. 1988).

However, it is important to keep in mind that the study by Weisman (1992, 1993) is restricted to MCSs developing in an ambient flow with strong vertical wind shear confined to the low levels, i.e., the environmental conditions for which the RKW theory is developed. Climatological and modeling studies (e.g., ED01, Coniglio and Stensrud 2001) indicate that environments with *deep* shear layers are also conducive to long-lived bow echoes. Further observational studies are necessary to address how often elevated RIJs are present in long-lived bow echoes.

As mentioned in section 3.1, mesoscale convective vortices (MCVs) (sometimes called line-end vortices or bookend vortices) are observed with bow echoes. In fact, RIJs in bow echoes usually are part of the rear-to-front branch of the circulation

induced by MCVs which focuses and strengthens the mid-level rear-to-front flow (e.g., Weisman 1993). Figure 3.7 shows a low-elevation radar reflectivity analysis during the mature stage of a derecho-producing bow echo that affected the north-central United States in 19-20 July 1983 (Przybylinski 1995). The dashed, circular line denotes the position of the accompanying MCV, with a rear-inflow notch in its southern flank. During the developing stage of the bow echo, MCVs are often observed at the right *and* left ends of the bowing segment, but as the storm evolves and becomes long-lived, the cyclonic MCV on the left end (as viewed from the rear of the MCS) tends to dominate.

Two mechanisms are considered responsible for the *generation* of line-end vortices in bow echoes (see Figure 3.8): the tilting of positive ambient horizontal vorticity (i.e., associated with a westerly environmental vertical wind shear) by convectively-generated downdrafts (Fig. 3.8b), and the tilting of negative cold pool-generated horizontal vorticity by the leading updrafts (Fig. 3.8a) (Weisman 1993, Weisman and Davis 1998, Cram et al. 2002). As the bow echo structure evolves, vorticity convergence plays a role in enhancing the vertical vorticity produced by tilting (Cram et al. 2002).

In long-lived bow echoes, for which the influence of the Coriolis force is discernible, the cyclonic vortex (i.e., the northern vortex) becomes the dominant one¹ because of convergence of earth's vorticity on the scale of the bow echo, enhancing the cyclonic mid-level vorticity (Skamarock et al. 1994). Skamarock et al. (1994) point out that the asymmetric distribution of the mid-level positive buoyancy — which is biased toward the north of the MCS owing to a front-to-rear flow that is deflected northward by the influence of the Coriolis force — also plays a role in forming a balanced cyclonic vortex that can persist beyond the cessation of the parent MCS (e.g., Bartels et al.

¹This analysis is conducted for the Northern Hemisphere. In the Southern Hemisphere, the southern vortex becomes the dominant one.

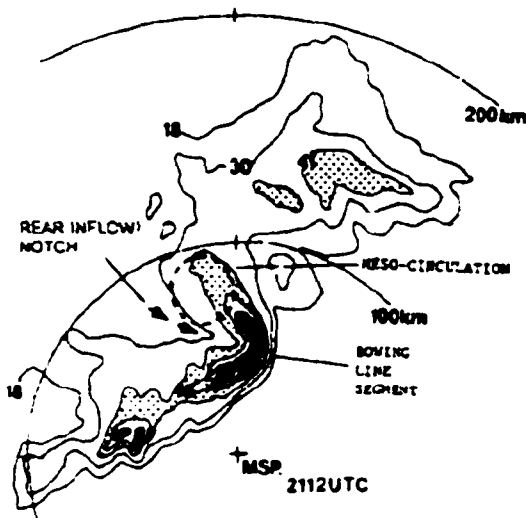


Figure 3.7: Low-elevation, plan-position indicator reflectivity analysis of the 19 July 1983 central Minnesota derecho-producing bow echo at 2112 UTC from Minneapolis-St. Paul, MN (MSP) radar. Reflectivity contours are 18, 30, 41 and 46 dBZ. Shaded region represents reflectivity values greater than 50 dBZ. Vectors denote the rear inflow notch (i.e., the RIJ sector), and dashed, circular line indicates location of the mesoscale circulation. (From Przybylinski 1995)

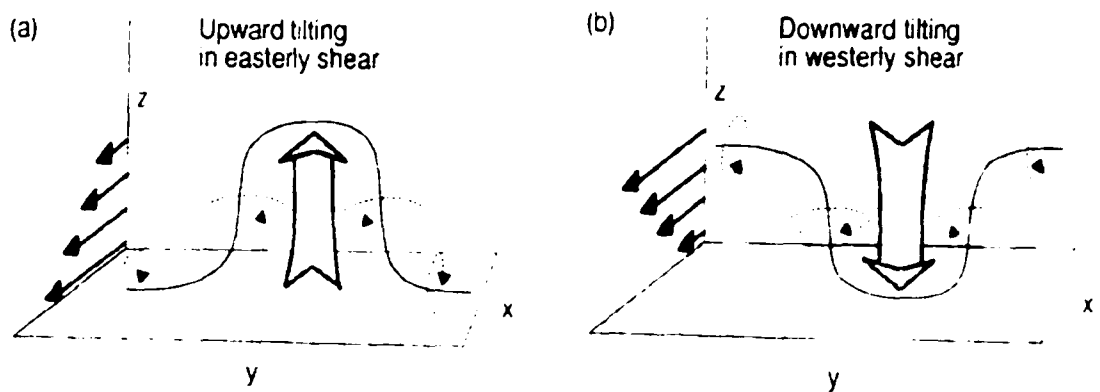


Figure 3.8: Schematic of vertical vorticity generation through vortex tilting within bow echoes. In (a), ascending motion along the leading edge of the bow echo pushes the vortex lines up in the presence of convectively-generated easterly vertical wind shear, resulting in anticlockwise (clockwise) rotation on the north (south) end of the system. In (b), localized descent in an environment with westerly vertical wind shear produces the same line-end vertical vorticity pattern. (From Weisman and Davis 1998).

1997).

3.4 Environmental conditions conducive to long-lived bow echoes and derechos

Synoptic patterns conducive to LEWP-type bow echoes that spawn *serial derechos* are similar to those described in the traditional conceptual model for springtime severe weather outbreaks (e.g., Barnes and Newton 1986), associated with strong, migrating low pressure systems (Johns 1993). In fact, the distinction between synoptic conditions favoring tornado outbreaks and serial derechos can be rather subtle (e.g., Johns and Doswell 1992, Stensrud et al. 1997).

Figure 3.9, adapted from Johns (1993), shows idealized sketches of typical mid-latitude synoptic patterns associated with severe weather outbreaks, contrasting situations favorable for tornadic supercells (Fig. 3.9a) and (serial-) derecho-producing bow echoes (Fig. 3.9b). In the latter, the orientation of the low-level jet (LLJ in Fig. 3.9b) is more parallel to the upper-level flow (polar and subtropical jet streams, PJ and SJ in Fig. 3.9b), indicating a more unidirectional vertical wind shear which tends to favor the squall line bow echo mode of convection, rather than isolated supercells (e.g., Weisman 1993). Johns (1993) refers to the synoptic setting conducive to serial derechos as the *dynamic pattern*.

On the other hand, JH87 and Johns (1993) indicate that the *progressive derecho* is the most common type of derecho during the warm season (May to August), with the parent bow echo usually developing under a relatively quiescent synoptic-scale pattern. This synoptic pattern fits reasonably well within the conditions favorable for northwest flow severe weather outbreaks (Johns 1984), at least qualitatively. Johns (1993) referred to this pattern as *warm season pattern*. In this situation, the DPMCS

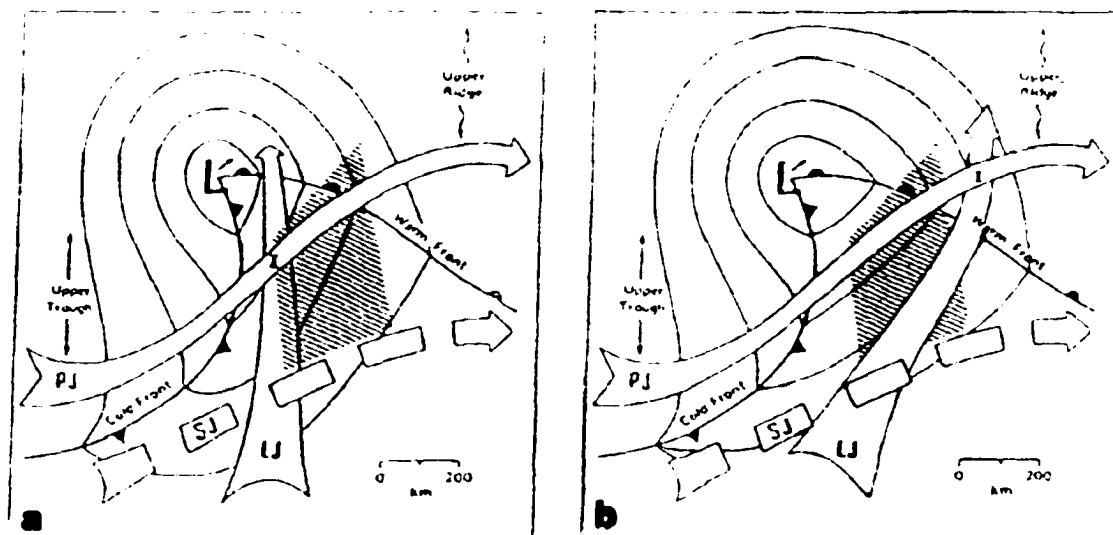


Figure 3.9 Idealized sketches of mid-latitude synoptic-scale situations favorable for development of severe thunderstorms including: (a) tornadic supercells; (b) derecho-producing bow echoes—dynamic pattern. Thin lines denote sea level isobars around a low pressure center with cold and warm fronts. Broad arrows represent low level jet (LLJ), upper level polar jet (PJ), and upper level subtropical jet (SJ). Panel (a) is after Rotunno and Newton 1986; panel (b) is after Johns 1993; both panels are adapted from Johns 1993.

usually has its initiation time between mid-afternoon and late evening along or just north of a quasi-stationary surface thermal boundary—most often, a stationary front or an “old” outflow boundary—with a significant east-west orientation, as schematically shown in Fig. 3.4a. The bow echo, that often (but not exclusively) displays characteristics of PDS’s type II and/or type III MCS, travels just slightly to the right of the mean wind direction, and commonly at a speed greater than the environmental mean wind speed (JH87, ED01). In fact, the impressive translation speed of bow echoes that spawn progressive derechos is one of their distinctive characteristics.

JH87 and Johns et al. (1990) describe the synoptic condition favoring progressive DPMCSs as consisting of a westerly or northwesterly mid-level flow above the surface thermal boundary, with a mid-level ridge (weak short wave trough) over the sector where the DPMCS reaches its mature stage (initiates). A significant pooling of warm and moist air at low levels along and just south of the stationary thermal boundary

acts as a convergence zone. As a result of the intense low-level pooling of warm and moist air, significantly high values of convective instability are generally observed with progressive derechos. CAPE ranging from 2400 J kg^{-1} (at the DPMCS initiation point) to 4500 J kg^{-1} (further downstream along the thermal boundary) are usually observed, with peak values as high as 6300 J kg^{-1} being possible (JH87, Johns et al. 1990). Hence, the average values of convective instability typically associated with progressive derechos exceed the ones observed with any other kind of extratropical severe weather outbreak in the United States. The average CAPE indicated by JH87 agrees fairly well with the values of CAPE for the most unstable air parcel obtained by ED01 for weakly forced derecho events.

Composite charts of wind and temperature fields at low-levels (850 and 700 mb) analyzed by Johns et al. (1990) for several strong progressive derechos shows that considerable low-level warm advection occurs near the initiation point of the DPMCS, often associated with a well defined low-level jet (Bentley and Cooper 1997, Comglio and Stensrud 1998). Further east, following the surface thermal boundary downstream, the warm advection at 850 mb and 700 mb is weaker, with the winds gaining stronger easterly component (see Fig. 3.10). The low-level moisture pooling, however, is stronger downstream, reaching maximum amplitude near the sector where the MCS attains its mature stage – this is the region where convective instability is higher.

JH87 found that the lower mid-troposphere is relatively dry in derecho events, which potentially favors the generation of stronger surface winds by evaporative cooling effects (i.e., by inducing intense downdrafts, and strong cold pool and mesohigh; Johns and Doswell 1992). This agrees with the climatological study by ED01 which shows that weakly forced or warm-season derechos are associated with higher val-

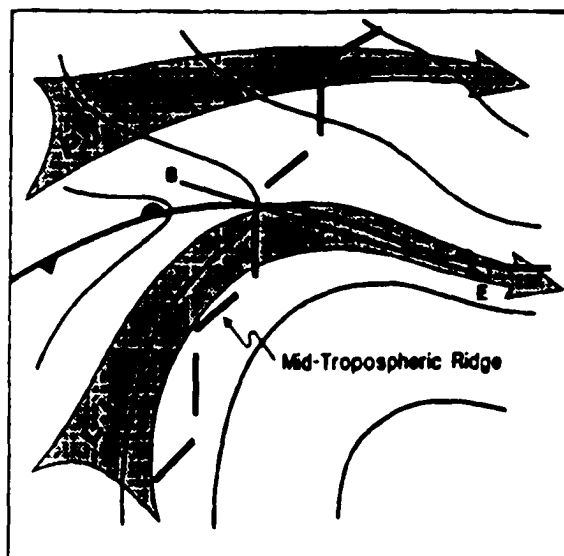


Figure 3.10: Typical mid-latitude synoptic conditions favorable for the development of progressive derecho-producing bow echoes (warm season pattern). The thin arrow, with a WNW-ESE orientation, indicates the main "damage axis" of the progressive derecho associated with the long-lived bow echo convective system (point "B" represents the beginning point of the MCS, "M" represents its mid-point and "E" its end point; the B-M-E path can be as long as 1400km). The broad arrows indicate the positioning of the low-level jet stream (LJ) and the polar jet stream (PJ) aloft. The thin solid lines represent the sea level isobars, with the surface quasi-stationary thermal boundary and the mid level ridge also being indicated. (Adapted from Johns et al. 1990)

ness of downdraft CAPE (DCAPE)⁵. Furthermore, Corfidi (2002) indicates that the presence of dry air at mid levels ahead of the convective system is a common feature observed with derecho-producing bow echoes, in contrast with a nearly saturated low- to mid-troposphere associated with quasi-stationary and back-building MCSs.

The downward transfer of higher horizontal momentum flow from the mid-troposphere to the surface by a descending RIJ (i.e., conservation of horizontal momentum) may also play a role in generating a highly mobile mesohigh in bow echoes (JH87). This hypothesis is based on the finding by JH87 that progressive derecho-producing bow echoes develop in environments with moderate mid-level winds. ED01 also found that *the 0-6 km environmental mean wind in DPMCSs is discernibly stronger than in the non-DPMCSs*. Because the bow echo propagation does not deviate significantly from the mean wind direction (as is the case for supercells), a larger component of the mid-level flow is coincident with the forward motion of the storm system, possibly contributing for the fast translation speed of bow echoes (JH87). Corfidi (2002), however, argued that momentum transfer to the lower levels has a more direct influence in the *direction* of motion of bow echoes than in their speed.

Similar to the dynamic pattern for serial derechos, the composite charts analyzed by Johns et al. (1990) for progressive derechos show that, with exception of the initiation sector of the DPMCS, a nearly unidirectional vertical wind shear vector is present between 850 mb and 500 mb along the surface thermal boundary. The flow is directed almost parallel to the path of the progressive derecho, as schematically shown in Figs. 3.4a and 3.10. The presence of a predominantly straight hodograph (especially above the sub-cloud layer) with moderate mid-level vertical wind shear seems to be a common characteristic with many warm-season derecho events as also indicated by more recent studies (e.g., Bentley et al. 1997, Coniglio and Stensrud

⁵ The magnitude of DCAPE is influenced by low- to mid-level tropospheric dryness: the drier this layer, the higher is DCAPE (e.g., Gilmore and Wicker 1998).

2001), particularly in the region where the parent bow-echo MCS attains its mature stage⁶.

An important aspect discussed in ED01 concerning the development of long-lived warm season bow echoes is that the mid-level *storm-relative* winds (MLSRWs) in such systems tend to be *weaker* than for other modes of severe convection, which seems to agree with the investigation by Brooks et al. (1994). Brooks et al. (1994) developed a conceptual model for the development and maintenance of low-level mesocyclones in severe convective storms in which a balance between the baroclinic generation of low-level horizontal vorticity (in evaporatively cooled air) and the strength of the surface outflow must be attained. Such balance is influenced by the MLSRWs. If the MLSRWs are too strong, precipitating hydrometeors are transported over a longer distance, reducing the baroclinic generation of low-level horizontal vorticity around the main updraft. Weak MLSRWs, on the other hand, tend to favor precipitation very close to the main updraft, increasing the chances of the outflow to undercut the upward motion, leading to short-lived low-level mesocyclones and an outflow-dominated thunderstorm. Stensrud et al. (1997) and ED01 identified this second case as a possible mechanism accounting for the reasonably good relation between weak MLSRWs and derecho-producing bow echoes. ED01 stressed that this relation is more applicable for warm season derechos.

Finally, it is important to stress that outflow-dominated storms can only become long-lived if they display the ability of propagating themselves by the continuous re-development of updrafts along the gust front (Johns and Doswell 1992). In the case of progressive DPMCSs, there is evidence that the enhanced low-level convergence along the surface outflow, combined with a very unstable environment, plays a rele-

⁶ Nevertheless, from an operational perspective, it is recognized that the analysis of the shape of the hodograph not always lead to successful results when trying to discriminate conditions favorable for supercellular tornadoes from those favorable for bow echoes (derechos) (e.g., Stensrud et al. 1997).

vant role in the systematic regeneration of updrafts at the leading edge of the system. ED01 found that low-level storm-relative winds (LLSRWs) in weakly forced derechos are particularly high when compared with their MLSRWs and with the LLSRWs of non-DPMCSs, suggesting a stronger low-level convergence along the leading edge of the cold pool.

Because the environment downstream of a progressive derecho is usually highly unstable with significant moisture pooling at the surface, deep vertical motion is efficiently triggered along the gust front due to a low level of free convection (JH87). Under these conditions, the propagation rate of new cells ahead of the system can exceed cell advection by the mean environmental wind, accounting, at least in part, for the fast translation speed of DPMCSs.

Thus, several processes combined, including the presence of low- to mid-level tropospheric dryness, downward transport of mid-level horizontal momentum, and fast updraft regeneration, appear to favor the development of a highly mobile MCS capable of producing damaging surface winds.

Chapter 4

Methodology and the Control Simulation

4.1 Methodology

The methodology used to examine the mutual adjustment of atmospheric variables in the simulation of a long-lived bow echo follows the same *concept* embodied in the studies addressing dynamic adjustments described in chapter 2.

We follow the approach applied in Weygandt et al. (1999) when addressing the relative importance of specific data fields in the simulation of an idealized supercell thunderstorm. The non-hydrostatic and fully compressible Advanced Regional Prediction System (ARPS), Version 4.5.1, is used as a cloud model to provide a 6-hr stormscale simulation of an idealized bow echo. This simulation is called *control run*, and reproduces most of the features usually observed with bow echoes — to be discussed in section 4.2.

The environment in which the simulated storm evolves is an undisturbed horizontally-homogeneous base state, which remains steady during the entire simulation. Hence,

all perturbation fields in the simulation refer to the mesoscale convective system (MCS) itself, and the full solution satisfies the model governing equations. *Any information missing from the perturbation fields characterizes a deviation from the state governed by the conservation equations.*

With that in mind, a series of numerical experiments is carried out by restarting the control simulation at 4-hr — during the mature stage of the simulated MCS — at which time we artificially remove selected perturbation variables¹ (one at a time). This implies that the “signature” of the MCS is eliminated for the perturbation variable being withdrawn, and all other fields are as in the control case. In addition, the time tendency of the variable being withdrawn is also set to zero at the restart time. (This does not mean that the “memory” of the time evolution of the withdrawn variable is completely eliminated, though. The forcing terms associated with the unperturbed variables in the conservation equations are retained, such that the time tendency of the variable being withdrawn can be restored). These are called *withdrawal experiments* (or *withdrawal runs*), and are integrated for a subsequent 2-hr. Figure 4.1 summarizes the procedure.

The withdrawal runs are compared with the solution of the control run, and the differences are examined. We take into account the mode of convection, magnitude and location of most active updrafts, and presence, strength and location of convectively-generated mesoscale features (namely, mesoscale convective vortices, rear-inflow jet and cold pool surface outflow) that are part of the characterization of a bow echo.

The time evolution of profiles of vertical momentum and heat fluxes, averaged for the simulated MCS, are also analyzed to quantify the deviation of the perturbed solution from CNTRL. Because such flux quantities are useful in characterizing the overall strength of the MCS (e.g., Weisman et al. 1997) we can assess the impact of

¹In other words, we reset the variables back to the unperturbed base state

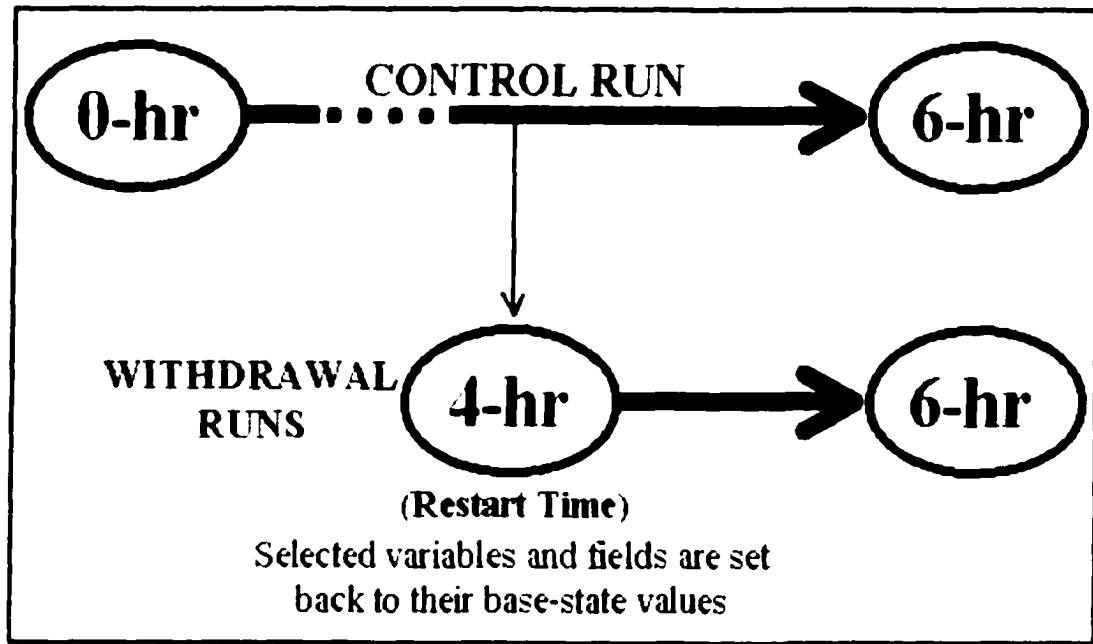


Figure 4.1 Diagram showing the methodology employed to study the dynamic adjustment in an idealized bow echo. A 6-hr simulation of an idealized bow echo (control run) is followed by a series of withdrawal experiments in which selected variables in the control run are reset to their base state values at 4-hr. Each withdrawal experiment produce a 2-hr “forecast”. The evolution of the simulated bow echo from 4 to 6-hr is examined for each case.

the impulsive perturbation on the solution in a more quantitative way.

The processes controlling dynamic adjustment itself are examined by studying the time evolution of different terms of the model governing equations early in the withdrawal simulations. An effort is made to identify the exact sequence of events that describes the behavior of the numerical solution at early stages — from the very first time steps to the first 20-min. in most cases — of the withdrawal runs. By studying this early evolution, a better understanding of the typical time-scale associated with the mutual response is possible, as well as the mechanisms that allow the generation of either a good or poor forecast for the idealized bow echo.

Table 4.1 shows the complete set of withdrawal experiments — the control run will be referred to as CNTRL. As an example, in experiment WVCL, the vertical velocity is set to zero (i.e., the unperturbed base state) everywhere in the domain at

Table 4.1: Summary of the experiments restarting at 4-hr (withdrawal experiments): variables that are set back to the base state values. (The acronym referring to the control run is CNTRL).

<i>Experiment</i>	<i>variable feature being reset to the unperturbed base state</i>
WVEL	vertical velocity
UVVEL	horizontal wind
THETA	potential temperature
VAP	water vapor mixing ratio

4-hr, while in experiment UVVEL, the horizontal winds across the entire domain are set equal to the background vertical profile. Again, no adjustment of the remaining fields is performed at restart time. We intentionally define an IC that describes a physically inconsistent atmospheric structure within the convective system. These experiments are designed to address the impact of the mutual adjustment among kinematic, thermodynamic and microphysical fields upon the simulated bow echo.

Ideally, the lateral boundaries of all withdrawal experiments should be forced, at each time step, by the solution from CNTRL. For computational simplicity this is avoided, under the assumption that the 2-hr prediction time (i.e., from 4 to 6-hr) is sufficiently short, and the region of interest sufficiently removed from the lateral boundaries, to render these effects of secondary importance.

It is evident that the identical twin-experiment approach has its weaknesses. One of them is that we provide the model with *perfect* information about the fields that are *not* withdrawn at 4-hr. In a real situation, perfect data of atmospheric fields are never available. Thus, our results give an optimistic view of the elimination of a given variable. Nevertheless, this approach allows us to *isolate* the information content of the variable (or fields) being withheld, and to assess its relative importance to the simulation.

Another potential weakness is not taking into account model-dependency on the results obtained, assuming that the numerical model is error-free (Atlas 1997). How-

ever, our analysis is restricted to *basic* dynamic processes affecting atmospheric adjustments on the convective scale — including acoustic and hydrostatic adjustments. It is reasonable to expect different stormscale models (i.e., non-hydrostatic fully compressible models) to represent such basic processes in a consistent way, even though the representation of fine details may be distinct.

Based on these points, the identical twin methodology seems appropriate to our purposes. Perturbing the control simulation with errors without completely withdrawing a given field would be an alternative approach, but it would deviate from our primary intention which is to violate the conservation equations at restart time. Another alternative would be to omit the information about an atmospheric field or hold such field constant for a given period of time (say, 5 min) and examine how the remaining fields respond during this period. However, some arbitrariness would be involved when determining the time window for which the field would be omitted or held constant. This latter approach is, therefore, not applied.

4.2 The control simulation

The control simulation (CNTRL) of an idealized bow echo is conducted in a three-dimensional $284 \times 356 \times 18.2 \text{ km}^3$ domain with uniform horizontal and vertical grid spacings of 2 km and 400 m, respectively. The background environment, or base state, is horizontally homogeneous, with vertical temperature and moisture profiles following the Weisman and Klemp (1982) idealized sounding, as shown in Figure 4.2. The sounding has a surface water vapor mixing ratio of 14 g kg^{-1} , surface-based convective available potential energy (CAPE) of 2300 J kg^{-1} and convective inhibition (CIN) of 28 J kg^{-1} . The wind profile, also shown in Figure 4.2, is that used by Weisman (1993) in the moderate shear bow echo case, with a unidirectional

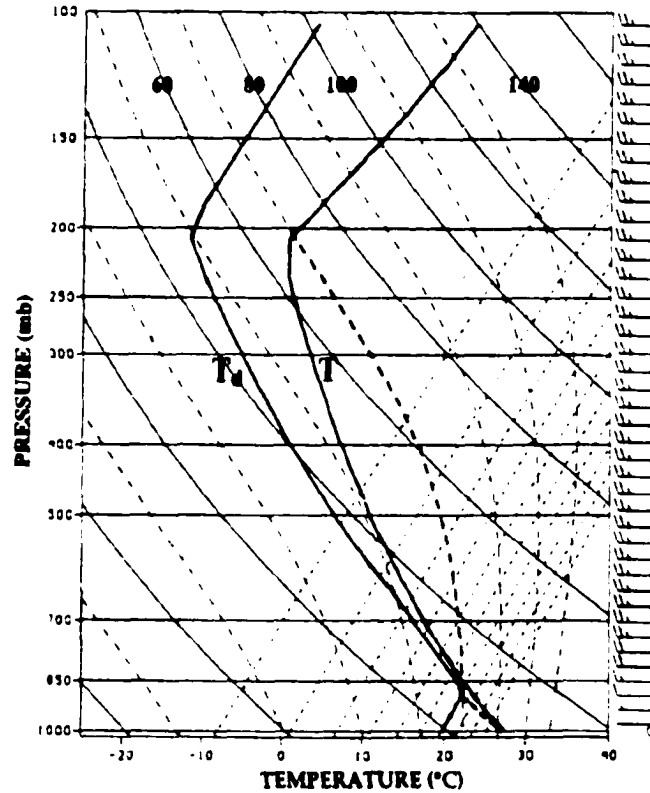


Figure 4.2 Skew-T diagram of the idealized thermodynamic sounding utilized at the initial time for CTRL (environment sounding). Thick solid lines are temperature and dew point temperature profiles. Heavy dashed line depicts the moist adiabat along which a surface-based air parcel ascends. Values shown in the top of the diagram indicate dry adiabats (in Celsius). Wind profile is in m s^{-1} .

westerly vertical wind shear of $1 \times 10^{-2} \text{ s}^{-1}$ confined to the first 2.5 km, and constant winds aloft (equal to 25 m s^{-1}).

Convection is initiated by a single elliptical thermal ($10.0 \times 10.0 \times 1.4 \text{ km}^3$) with maximum $+2 \text{ K}$ perturbation, positioned at $(x, y, z) = (116.0, 178.0, 1.5) \text{ km}$. Note that the bubble is placed in the mid-point of the N-S extent of the model domain.

Because the numerical simulation extends for several hours, the Coriolis force is included. A geostrophically balanced base state is imposed by subtracting the geostrophically balanced pressure gradient from the horizontal momentum equations as indicated below:

$$\left(\frac{Du}{Dt}\right)_{Coriolis} = f(v - \bar{v}) \quad (4.1)$$

$$\left(\frac{Dv}{Dt}\right)_{Coriolis} = -f(u - \bar{u}) \quad (4.2)$$

where f is the Coriolis parameter, and \bar{u} and \bar{v} are the base-state winds.

Note that because $-f\bar{v}$ and $f\bar{u}$ represent the geostrophically balanced pressure gradient force, the Coriolis force acts only on the wind perturbations $[(u - \bar{u}), (v - \bar{v})]$, implying that the base state does not evolve toward thermal wind balance. By doing this we avoid imposing a meridionally-oriented temperature gradient — in thermal balance with the vertical wind profile — in the shear layer that would modify the lower levels of the background sounding (Skamarock et al. 1994). Higher (lower) CAPE would be found in the southern (northern) half of the domain, potentially inducing an unwanted bias in the convective activity towards the south (Richardson 1999).

Due to the presence of acoustically active terms, a mode-splitting technique is used to integrate the governing equations, with a small time step of 1 s for the forward (implicit Crank-Nicolson) numerical scheme in the horizontal momentum (vertical momentum and pressure) equations, and a big time step of 4 s for the leap-frog scheme in the acoustically inactive terms.

Parameterization of surface physics and radiation is *not* included. Ice microphysics (Lin et al. 1983) is switched *on*, including conservation equations for cloud ice (qi), snow (qs) and hail (qh) mixing ratios — in addition to the warm species: water vapor (qv), cloud water (qc) and rainwater (qr) mixing ratios.

Subgrid-scale turbulence is parameterized with a 1.5-order turbulent kinetic energy (TKE) closure scheme. Radiation lateral and top (Durrán and Klemp 1983, Klemp and Durrán 1983, Durrán 1999) boundary conditions are employed, with rigid free-slip

bottom boundary condition being assumed². Note that the top and lateral boundary conditions are “open” for IGWs, not acoustic waves. Therefore, a divergence damping term is included in the momentum conservation equations to *attenuate* acoustic modes (Skamarock and Klemp 1992, Xue et al. 2000)³. A summary of model parameters is shown in Table 4.2.

Figures 4.3 to 4.5 show the solution for CTRL from 4 to 6-hr. At 4-hr (the time at which the withdrawal experiments are initiated), the MCS displays characteristics of a broken squall line with small embedded bow echoes. A well developed surface cold pool (Fig. 4.3a) extends mostly in the N-S direction, and a developing mesohigh is noted near the center of the domain, where the cold pool develops a prominent bow-shaped feature.

Low- to mid-level vortex couplets are evident in the northern end of the MCS, at $y = 256$ km, and also at the southern end, just south of $y = 128$ km (Figs. 4.4a, 4.5a). These line-end vortex couplets are remnants of the initial cell splitting process, with a cyclonic (anticyclonic) updraft and anticyclonic (cyclonic) downdraft in the original right-moving (left-moving) convective cell. Weisman (1993) obtained a similar pattern in the early stages of a simulated bow echo, but in his solution, the line-end vortex couplets no longer were evident at 4-hr. This is because our solution shows a somewhat slower evolution toward a bow echo mode, associated with the effects of ice microphysics – to be discussed in the next subsection.

Figures 4.4a and 4.5a also indicate that a rear-to-front flow is present in the low- to mid-levels of the MCS at 4-hr. The ground-relative winds within this flow exceed 30 m s^{-1} in the most convectively active regions, characterizing a rear inflow jet (RIJ). This feature is better illustrated in Figure 4.6a, where ground-relative zonal (or cross-

²Applying a free-slip bottom boundary condition does not imply that the surface drag coefficient is set equal to zero; rather, it implies that the surface momentum fluxes are set to zero (E. Adlerman, personal communication).

³The use of an implicit scheme for the time integration of the vertical equation of motion and the vertical terms in the pressure equation also attenuates (vertically-propagating) sound waves (Durran and Klemp 1983, Durran 1999).

Table 1.2: Physical and computational parameters used in the numerical simulations.

<i>Parameter</i>	<i>Symbol</i>	<i>Value</i>
Horizontal grid spacing	$\Delta x, \Delta y$	2000 m
Vertical grid spacing	Δz	400 m
Large time step	Δt	1 s
Small time step	$\Delta \tau$	1 s
Coriolis parameter	f	$0.7 \times 10^{-4} \text{ s}^{-1}$
Turbulent Prandtl number	K_m, K_H	0.47
Fourth-order horizontal mixing coefficient	K_4	$1.25 \times 10^{10} \text{ m}^4 \text{ s}^{-1}$
Second-order vertical mixing coefficient	K_2	$120 \text{ m}^2 \text{ s}^{-1}$
Initial thermal perturbation – CNTRL only		
Magnitude	$\Delta \Theta$	2.0 K
Horizontal radius	x_r, y_r	10.0 km
Vertical radius	z_r	1.4 km
Height of center above ground	z_c	1.5 km

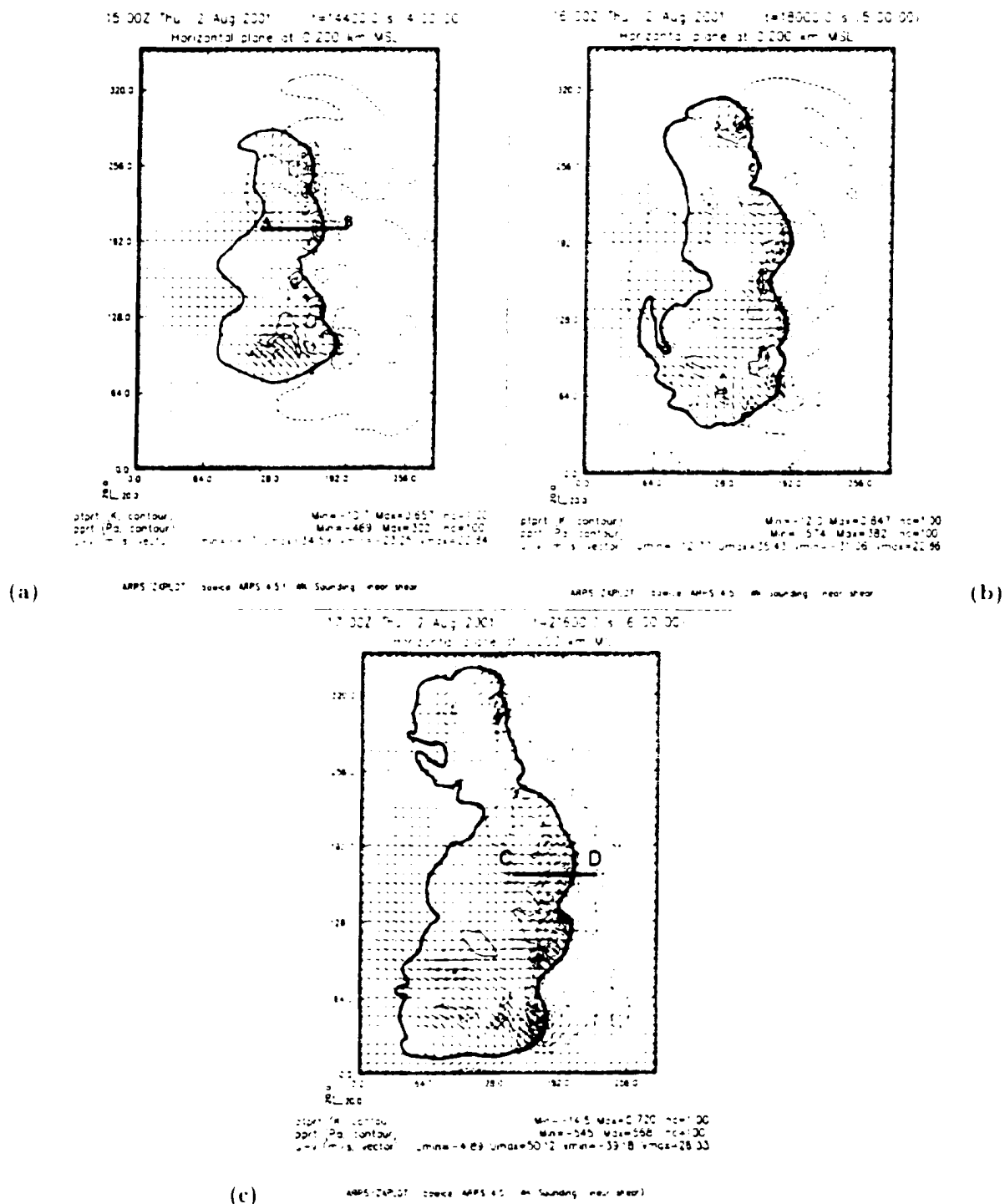


Figure 4.3: Time evolution of CNTRL simulation at the first model level ($z = 200$ m): (a) 4-hr, (b) 5-hr, (c) 6-hr. Thick solid line denotes the -2 K potential temperature perturbation indicating the boundary of the cold pool; pressure perturbation contours at each 100 Pa are indicated by thin solid (positive values) and dashed (negative values) lines. Vectors are ground-relative winds. A domain translation of 22 m s^{-1} in the x-direction is applied from 4 to 5-hr, while an additional domain speed of -1.67 m s^{-1} in the y-direction is applied from 5 to 6-hr.

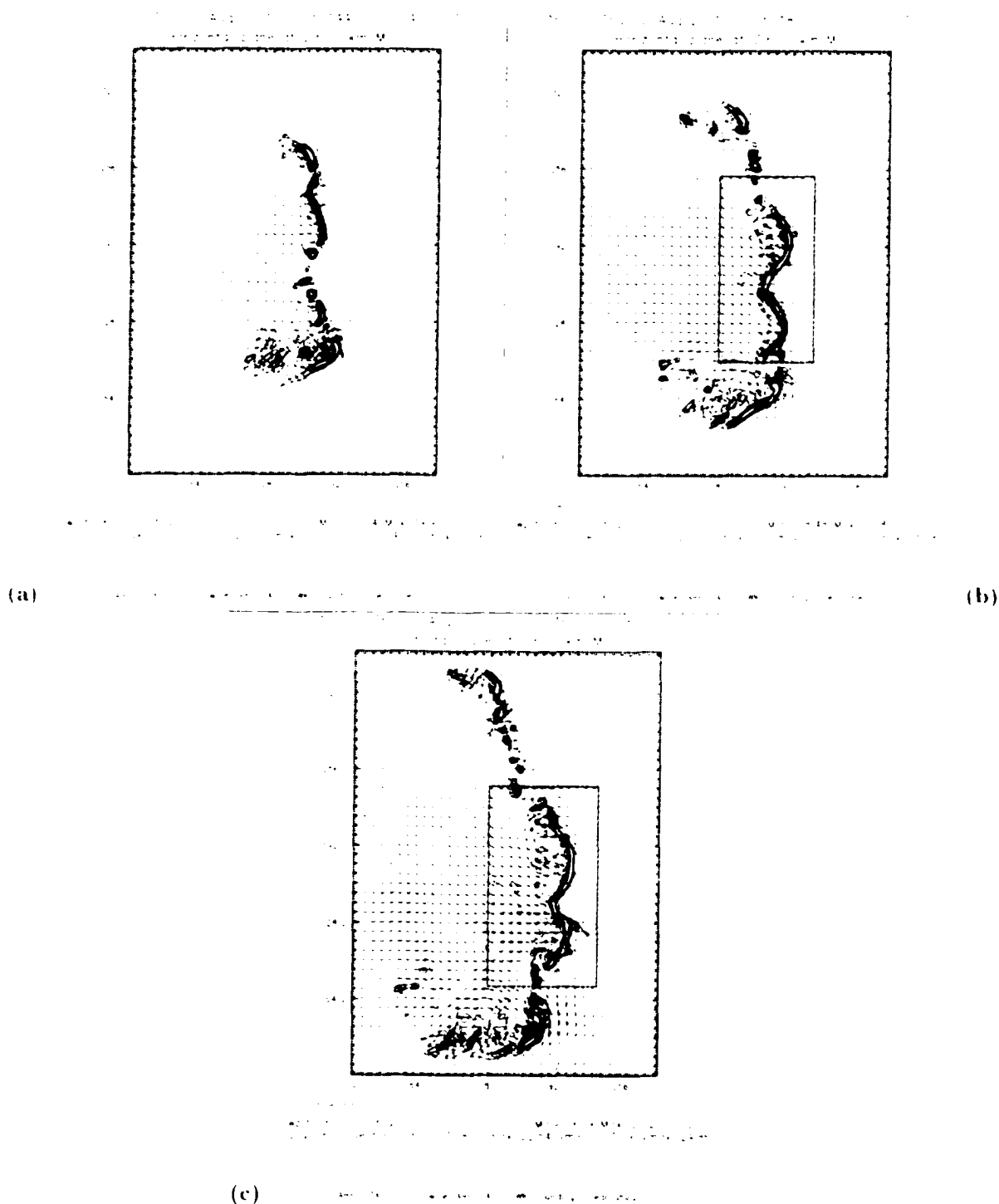


Figure 4.4. Time evolution of CNTRL simulation at $z = 2600$ m: (a) 4-hr, (b) 5-hr, (c) 6-hr. Contours of vertical velocity perturbation indicated at each 2 m s^{-1} . Solid (dashed) lines are updrafts (downdrafts). Vectors are storm-relative winds. A domain translation of 22 m s^{-1} in the x-direction is applied from 4 to 5-hr, while an additional domain speed of -1.67 m s^{-1} in the y-direction is applied from 5 to 6-hr.

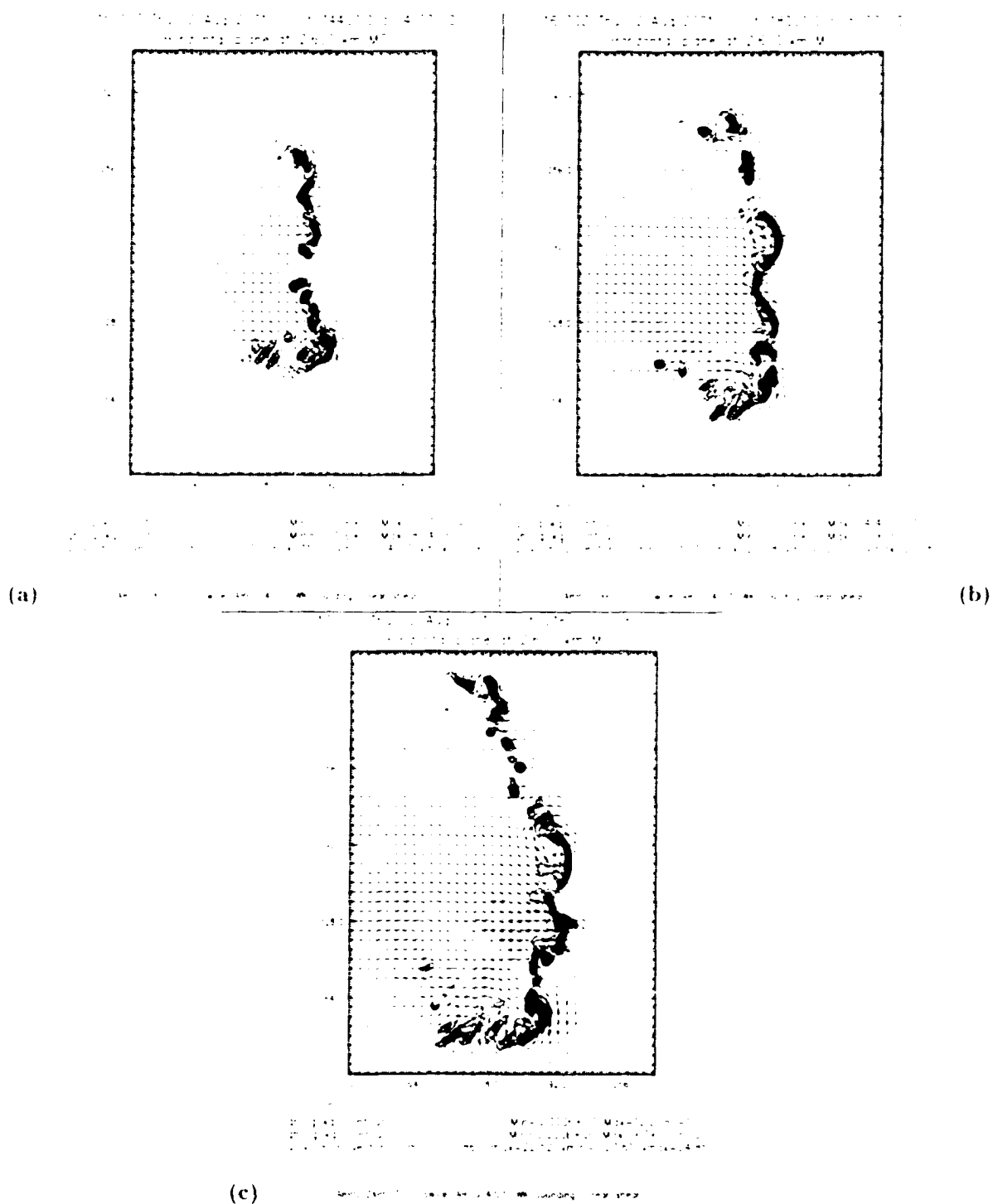


Figure 4.5: As in Fig. 4.4, but for rainwater and hail mixing ratios indicated at 1 g kg^{-1} intervals (contours)

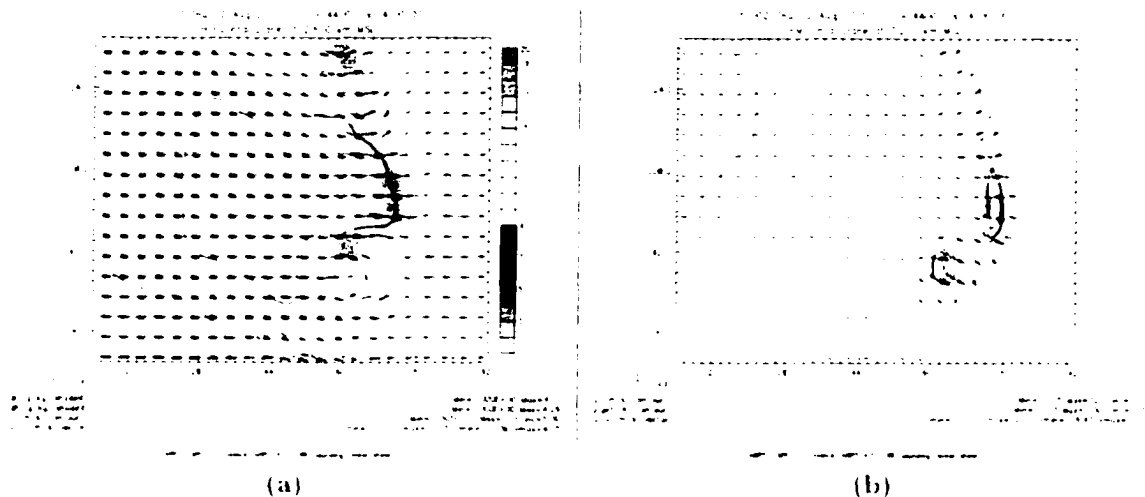


Figure 4.6: Bow echo segment at $t = 4$ hr: (a) $z = 2600$ m: ground-relative wind (vectors), rainwater and hail mixing ratio in g kg^{-1} (shaded), zonal component of the ground-relative wind (contour lines). Solid line encircles region with $u > 30 \text{ m s}^{-1}$; (b) $z = 200$ m: ground-relative wind (vectors), and its zonal component (contour lines). Solid contours indicate values of u greater than 25 m s^{-1} , plotted at each 2 m s^{-1} . Dotted line indicates -2 K potential temperature perturbation representing the boundary of the cold pool. Domain shown is: $104 \text{ km} \leq x \leq 192 \text{ km}$, $170 \text{ km} \leq y \leq 234 \text{ km}$.

line) winds stronger than 30 m s^{-1} are shown superimposed on the rainwater (qr) and hail (qh) mixing ratio contours for a bow echo sector of the MCS. A rear inflow notch is present in the qr and qh fields in a small scale bow echo just north of $y = 192 \text{ km}$, coincident with a local maximum in the rear-to-front flow. This is equivalent to the weak echo channel in radar reflectivity, discussed in chapter 3.

At the surface (Fig. 4.6b), a localized region of cross-line winds greater than 25 m s^{-1} is evident. The areal coverage of this feature is rather limited at this time, which seems to agree with some of the results obtained by Coniglio and Stensrud (2001) in their derecho simulation 3h after convective initiation.

Vertical cross sections along segment \overline{AB} in Figure 4.3a are shown in Figure 4.7. This E-W segment is chosen because it crosses the bow echo shown in Figure 4.6, which becomes the most important convective element during the simulation. Figure 4.7a depicts a relatively strong and (apparently) upright updraft with vertical velocity reaching 22 m s^{-1} just above the leading edge of the advancing cold pool. When

visualizing the vertical motion plotted with the correct aspect ratio (which is not the case in Fig. 4.7), the updrafts show an upshear inclination. Nevertheless, this upshear tilt is not as prominent as the one found by Weisman (1993) at 4-hr of integration, possibly because of the slower evolution of our simulation with ice microphysics.

At mid to upper levels, where the updrafts are strongest, positive thermal perturbations are present, associated with the effects of latent heating. Above the cold pool, a mesolow is well developed, with stronger negative pressure perturbation (-200 Pa) close to the updraft (see Fig. 4.7b), below the region of strongest mid-level warming. The magnitude of the mesolow is slightly stronger than that discussed in Weisman (1993), and its existence is, to a large extent, due to the mid-level buoyancy source, as discussed in section 2.2. This mesolow generates a west-to-east pressure gradient force that plays an important role in developing the rear-to-front flow. Note that the RLJ is confined to the layer where the mesolow is present, and decelerates upon encountering the updraft. Vertical divergence is noticeable at this point, and part of the horizontal momentum from the RLJ is transferred to the cold pool, contributing to the surface outflow shown in Figure 4.6b.

Accompanying the surface cold pool is a mesohigh (Fig. 4.7b). Again, following the discussion in section 2.2, this feature (nearly always observed with organized mid-latitude MCSs; Houze 1993) can be understood as a response of the pressure field to the presence of negatively buoyant air within the cold pool, which is generated mostly by evaporation of raindrops in the sub-cloud layer. This process can be inferred by the relatively large values of q_r at this level (Fig. 4.7c). From mid to upper levels, the hydrometeors are mostly in the solid phase, as seen by the q_h field, and other ice species not shown.

The equivalent potential temperature (θ_e) field (Fig. 4.7d) highlights the transport of mid-level dry air to the surface by downdrafts. Note that the drier air advected by

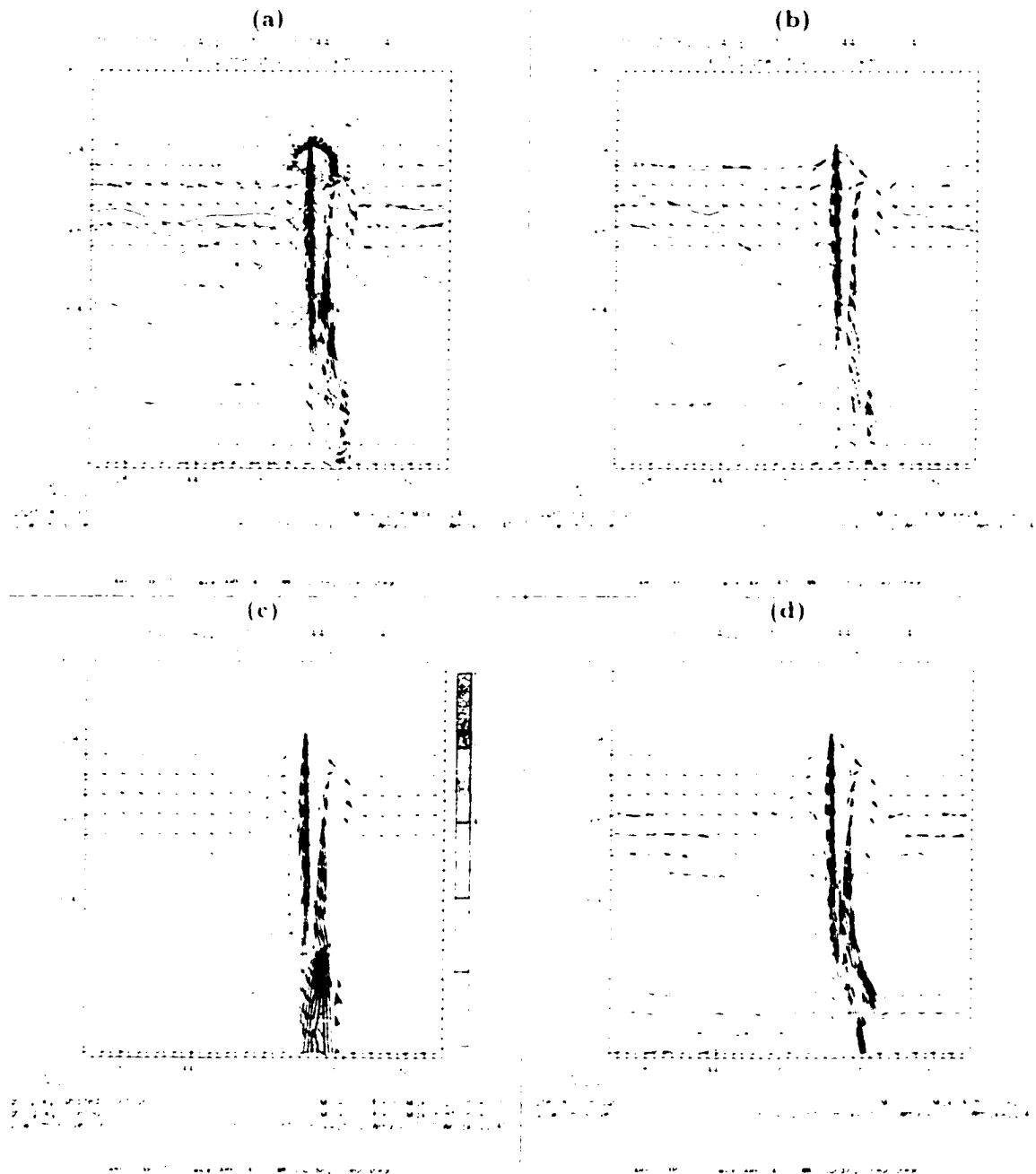


Figure 4.7: Vertical cross section at $t = 4$ -hr across $y = 205$ km (segment \overline{AB} in Figure 4.3a), from surface to $z = 16$ km. All panels contain storm-relative wind vectors presented at every other vertical grid-point. Reference horizontal wind vector of 10 m s^{-1} is indicated on the lower-left corner of each panel. (a) potential temperature perturbation in K; contours plotted at each 1 K; (b) pressure perturbation in Pa; contours plotted at each 50 Pa; (c) rainwater (shaded) and hail (solid contours) mixing ratio plotted at each 1 g kg^{-1} ; (d) equivalent potential temperature presented at each 2 K; only values between $\theta_e = 326$ and 334 K are shown, with $\theta_e = 334$ K being the first contour in the top of the figure. In (a) and (b) positive (negative) perturbations are indicated by solid (dashed) contours.

the RIJ eventually encounters the updraft. This is where “cloud erosion” is expected to occur, generating the rear-inflow notch in the qr and qh fields shown in Figure 4.6a. The updrafts, on the other hand, transport moister air to the mid and upper levels of the convective system, eventually feeding the anvil cloud — well defined in the cloud ice mixing ratio field (not shown). These processes are in agreement with the conservation of θ_e by ascending and descending air parcels in the MCS.

As the integration proceeds, the cold pool (Figs. 4.3b,c) continues to spread, and at 6-hr it covers the entire meridional extent of the domain. The simulated MCS, as a whole, moves mostly eastward at an approximate average speed of 22 m s^{-1} (from 4-hr to 5-hr) and 26 m s^{-1} (from 5-hr to 6-hr). The last hour of integration is the only time period when the bow echo moves faster than the environmental mean wind speed.

Two main regions of strong and widespread surface outflow are noted during the final 2-hr period — one in the center of the domain, associated with a well defined mesohigh, and a second further south, approaching the southern boundary of the domain (Fig. 4.3b,c). A strong southward surge also was obtained by Skamarock et al. (1994) in their squall line simulation that included Coriolis effects. Under the influence of the Coriolis force, the wind field tends to be deflected to the south not only at surface but also at the low to mid levels of the storm (e.g., Fig.3c of Sun et al. 1993), where the rear-to-front flow dominates the kinematic field (Figs. 4.4b,c).

The net effect is the generation of an asymmetric convective system, where most of the convective activity occurs in the southern half of the domain, giving a slight southeast component to the MCS translation. The outflow in the center of the domain, however, still displays a strong eastward component owing to the presence of a widespread mesohigh oriented in the N-S direction. In the present research, our attention is mostly restricted to the center of the domain because the most evident

bow echo is present in that sector (Figs. 4.4b,c and 4.5b,c), and because the south and north ends of the simulated MCS move close to the lateral boundaries and thus may be contaminated by boundary effects.

Two main bow echo segments are clearly evident near the center of the domain at 5 and 6-hr, with updrafts organizing along a bulged line (Figs. 4.4b,c) that resembles a short line echo wave pattern (Nolen 1959). At 6-hr, the mesohighs from both bow echo segments form a single entity, and a much stronger surface outflow is present, as illustrated in Figure 4.8.

Another striking mesoscale feature is a dominant low- to mid-level cyclonic mesoscale convective vortex (MCV) at the north end of the largest bow echo (Figs. 4.4c, 4.5c). This is a feature often observed in asymmetric squall lines (Houze 1993), and has been obtained/studied in several other simulated MCSs influenced by the Coriolis force (Skamarock et al. 1994, Weisman and Davis 1998, Coniglio and Stensrud 2001, and others). Skamarock et al. (1994) and Weisman and Davis (1998) indicated that the bias leading to a dominant cyclonic MCV in the northern end of asymmetric MCSs is due mostly to the system-scale convergence of earth's vorticity associated with the mid-level rear-to-front flow.

Figure 4.9 shows vertical cross sections (at 6-hr) of pressure perturbation and θ_e along segment \overline{CD} in Figure 4.3c. The surface mesohigh has strengthened by this time (Fig. 4.9a), with perturbation pressure reaching 500 Pa. The mesolow aloft has extended rearward in agreement with the upstream spread of the midlevel heating (i.e., buoyancy source, not shown). The mesolow is now deeper than at 4-hr, but with the maximum pressure perturbation still located near the updraft.

Both rainwater and hail mixing ratios, not shown, also broaden slightly rearward with respect to MCS motion. This indicates the continuous development of new updrafts along the gust front, with older updrafts being undercut by the surface

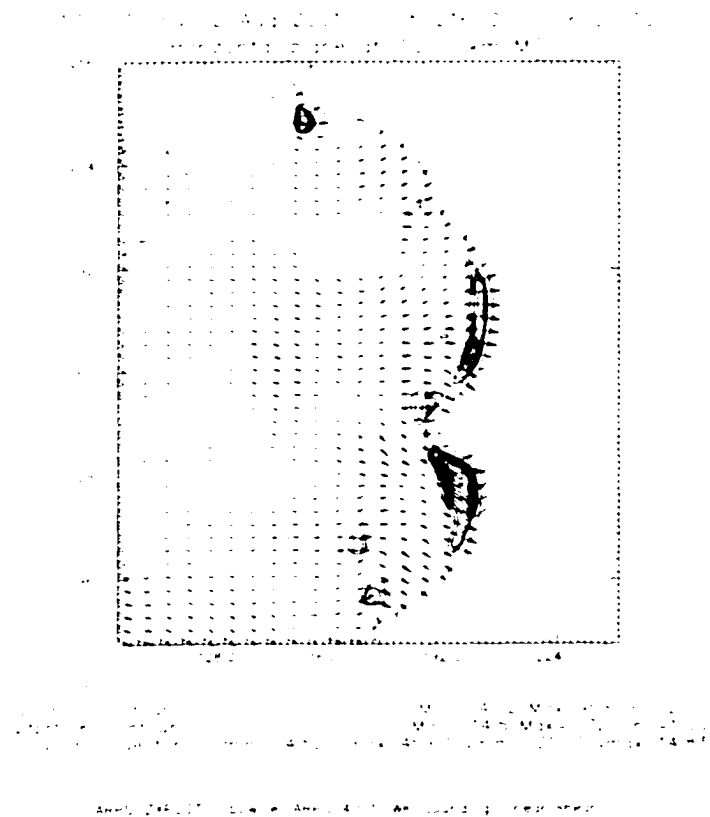


Figure 4.8: As in Figure 4.6b, but at $t = 6$ hr, in a close-up view for the two main bow echo segments shown in Figures 4.4c, 4.5c

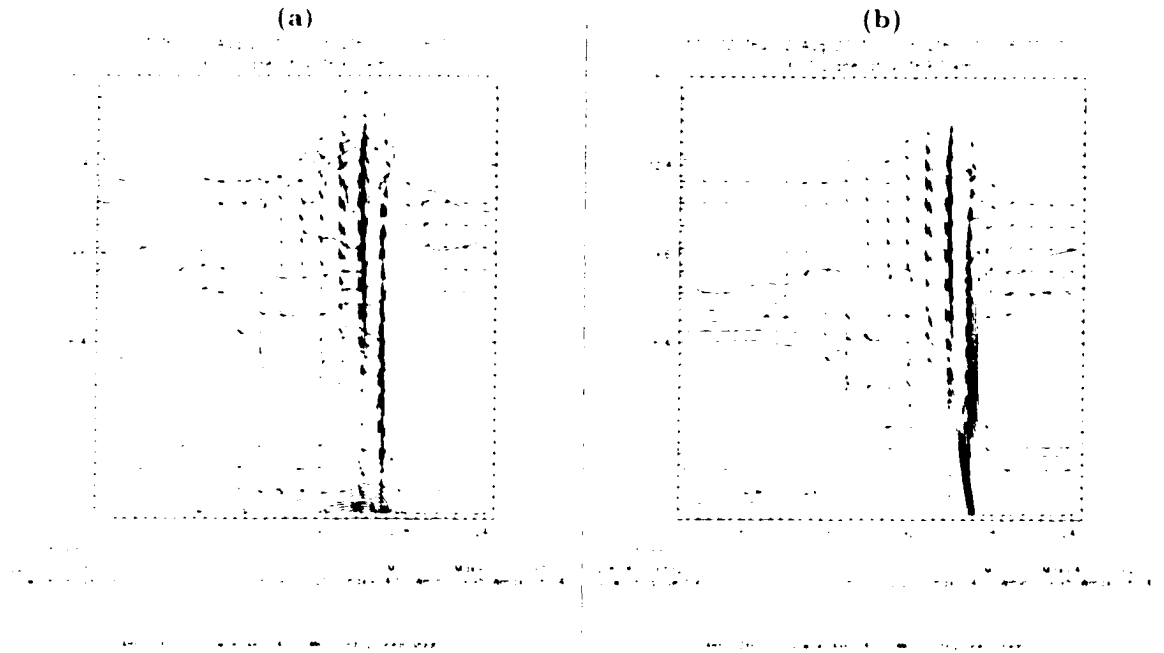


Figure 19. As in Figure 47, but at $t = 6$ -hr, for (a) pressure perturbation and (b) equivalent potential temperature, along segment \overline{CD} ($y = 169$ km) in Figure 43c. Reference horizontal wind vector (bottom of panels) is 20 m s^{-1} .

outflow and lagging behind the leading edge of the MCS. It is possible to identify the remnants of an old updraft at $z = 5$ km, just east of $x = 176$ km in Figure 49b. The θ_e field retains the “signature” of the undercut updraft in that sector, with a localized region of secondary maximum.

The areal coverage of the trailing precipitation sector is relatively narrow because of the inclusion of hail-producing processes in our simulation. Yang and Houze (1995b) showed that, when hail is not taken into account in the ice phase parameterization, the simulated MCS tends to display a longer cross-line extension and generate a broader area of trailing stratiform precipitation because of the weaker precipitation fall-out in the convective region.

In summary, the numerically-simulated MCS obtained in CNTRL from 4 to 6-hr displays several of the main characteristics usually associated with bow echo squall lines: (i) bow shaped convective segments with strong low-level “reflectivity” gradi-

ents; (ii) a well defined mesohigh; (iii) derecho-like surface winds; (iii) low- to mid-level rear-to-front flow, often characterizing a RIJ; (iv) rear inflow notches in the rainwater and hail mixing ratio fields; and (v) well defined cyclonic MCV on the north end of the system.

4.2.1 Sensitivity of the control run to ice microphysics

It is worthwhile to report the sensitivity of experiment CNTRL to the inclusion of ice microphysics. To our knowledge, no study of numerically-simulated bow echoes has investigated this particular sensitivity. The work by Yang and Houze (1995b), for example, did address it for a severe mid-latitude squall line that apparently produced some bowing segments. However, they did not examine how ice microphysics affected the 3-D structure of the system since their numerical experiments were in a 2-D framework. The discussion presented in this subsection is not intended to be a comprehensive analysis and, more importantly, *is not part of the examination of dynamic adjustment in the simulated bow echo*.

Figures 4.10 to 4.12 compare the evolution of two runs with exactly the same parameters (Table 4.2), except for the inclusion of ice microphysics. The simulation without ice microphysics is called NO_ICE, while the simulation with ice microphysics is simply CNTRL.

In general, domain maximum updrafts and downdrafts in CNTRL are stronger than in NO_ICE (Fig. 4.10), in agreement with previous studies of sensitivity to ice microphysics in non bow echo storms (Straka and Anderson 1993, Straka et al. 1993, Johnson et al. 1993). At certain times, the maximum updraft in CNTRL is almost 40% stronger, possibly related to enhanced latent heating at mid levels owing to effects associated with phase change from liquid to ice (Straka et al. 1993, Johnson et al. 1993).

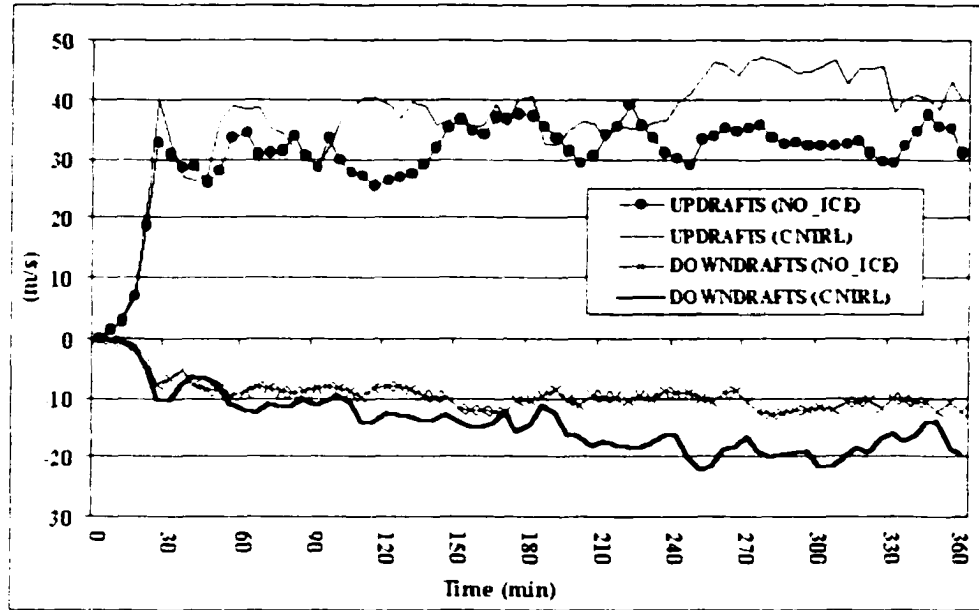


Figure 4.10: Time evolution of domain maximum updrafts and downdrafts for the 6-hr simulation of an idealized bow echo. NO_ICE: no ice microphysics; CNTRL: with ice microphysics.

Stronger downdrafts associated with enhanced cooling are due mostly to the melting of hail. While this mechanism is relevant in accelerating downdrafts in the mid-levels of the storm, its importance is reduced close to surface, where the evaporation of raindrops plays a more significant role in strengthening downward motion (Straka and Anderson 1993). Therefore, the presence of stronger domain maximum downdrafts does not necessarily imply stronger *low-level* downdrafts and surface outflow, as indicated below.

Both runs simulate initial storm splitting in the first hour of integration (Fig. 4.11a,b). NO_ICE generates broader areas of low-level downdrafts in the center of the domain (Fig. 4.11a,c), while in CNTRL, the downdrafts are more localized (Fig. 4.11b,d) because of the presence of heavier hydrometeors which confine the precipitation areas (and related downdrafts) to smaller regions (Jewett et al. 1990). By 2-hr, NO_ICE shows clear signs of transition toward a bow echo convective mode, with a line of cells displaying two bulging segments in the center of the domain.

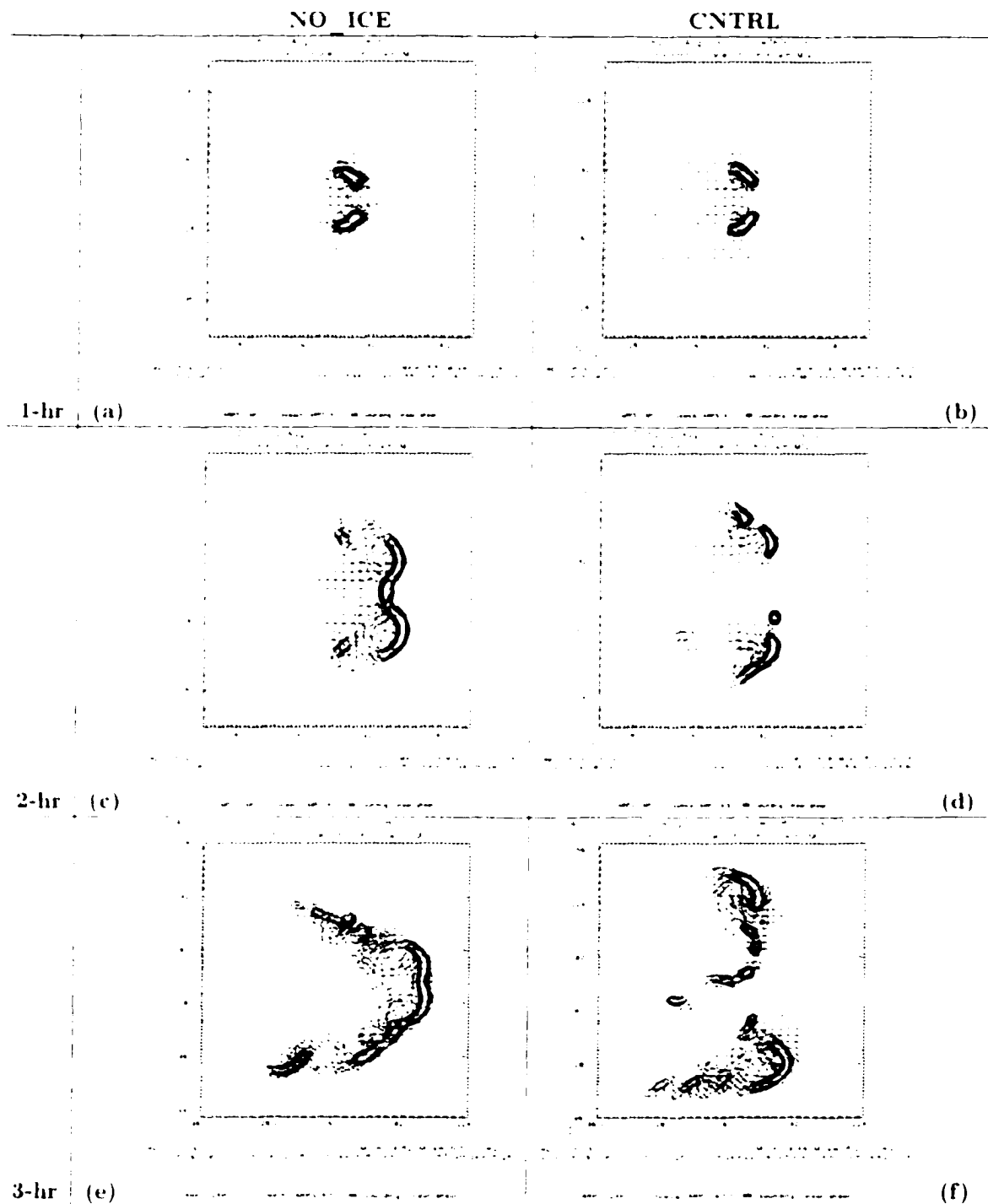


Figure 4.11: Early evolution of the bow echo simulation with and without ice microphysics. Perturbation vertical velocity (w) and storm-relative winds at $z = 2600$ m. w plotted at each 2 m s^{-1} , with solid (dashed) lines representing updrafts (downdrafts). Only contours within $-10 \text{ m s}^{-1} \leq w \leq 10 \text{ m s}^{-1}$ are plotted. (a),(b): 1-hr; (c),(d): 2-hr; (e),(f): 3-hr. First column: NO_ICE; second column: CNTRL. In (a)-(d) the domain size shown is $128 \times 128 \text{ km}^2$; in (e),(f) is $128 \times 164 \text{ km}^2$.

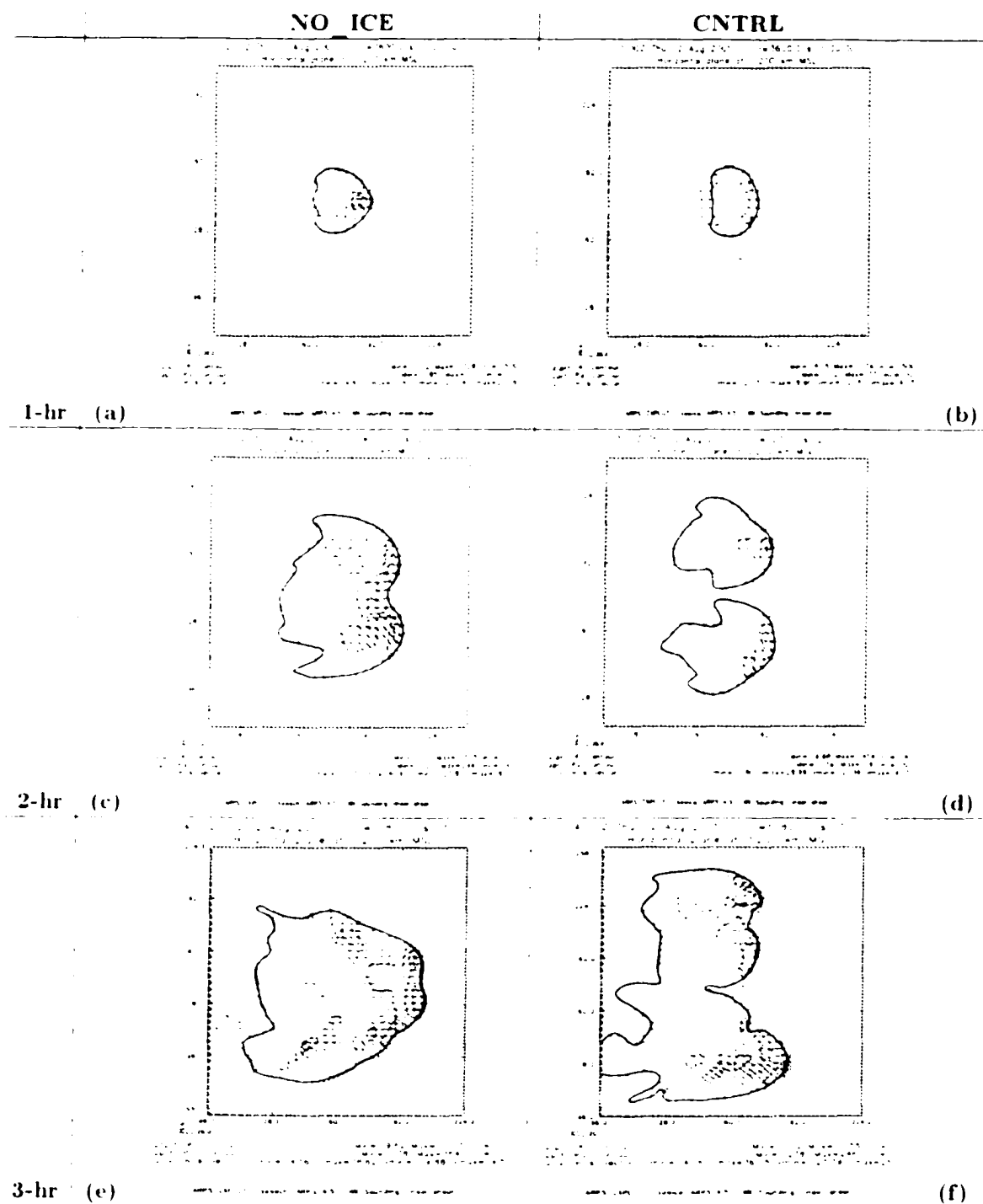


Figure 4.12: Early evolution of the bow echo simulation with and without parameterization of ice microphysics. Surface cold pool, perturbation pressure, and ground-relative winds ($z = 200$ m). Thick solid line denotes the -2 K potential temperature perturbation indicating the boundary of the cold pool; pressure contours at each 100 Pa are indicated by thin solid (positive values) and dashed (negative values) lines. (a),(b): 1-hr; (c),(d): 2-hr; (e),(f): 3-hr. First column: NO_ICE; second column: CNTRL. In (a),(d) the domain size shown is 128×128 km²; in (e),(f) is 128×164 km².

The rear-to-front flow in NO_ICE is better developed, and the solution agrees quite well with that discussed in Weisman (1993). In CNTRL, no convective activity is generated in the center of the domain at this time, and the original right- and left-moving cells trigger new convection locally.

Comparatively larger N-S separation between the two initial storms is evident in CNTRL, indicating that the motion of the convective cells deviates more from the mean wind than in NO_ICE. This agrees with Straka et al. (1993) and Johnson et al. (1993), who found that simulations of supercells with ice microphysics tend to produce storms that deviate more from the mean wind-shear vector than experiments with no ice.

Comparing the early evolution at the surface (Figs. 4.12a-d), a stronger and broader outflow is present in NO_ICE, including a better defined mesohigh. This suggests that more confined areas of precipitation in CNTRL have slowed the expansion of the cold pool and the enhancement of the surface outflow, since the low-level evaporative cooling effects do not cover large areas compared to NO_ICE. The stronger intensity of both the cold pool and mesohigh in NO_ICE is particularly evident in the center of the domain. The greater separation between the initial cells in CNTRL helps retard the merger of the outflows in that part of the domain. Thus, the initiation of new convective cells in that sector is delayed.

As a result, by 3 hours (Figs. 4.11e and 4.12e), the solution obtained in NO_ICE consists of an MCS showing mesoscale features typical of the maturing stage of a (short) bow echo squall line. In contrast, the solution from CNTRL (Figs. 4.11f and 4.12f) displays small-scale bow echoes off the center of the domain. In other words, both simulations show a tendency for the domination of a bow echo mode of convection, but at distinct scales.

The different solutions in the early stages of the simulation have a significant

impact in the resulting bow echo later in the integration, as shown in Figure 4.13 for NO_ICE (compare with Figs. 4.13 and 4.4 for CNTRL). From 4 to 6-hr the storm system simulated in NO_ICE displays a dominating bow echo, resembling a progressive derecho-producing MCS (Johns and Hirt 1987). The MCS has a shorter meridional extent than the one obtained in CNTRL.

Another difference between the runs is that in NO_ICE, the forward storm motion, from 3-hr onward, exceeds slightly the mean environmental wind, varying from 26.5 to 27.5 m s^{-1} , while in CNTRL, the system forward speed only exceeds the mean environmental wind in the last hour of integration (26.0 m s^{-1}). This coincides with the time when the surface cold pool, mesohigh and outflow in CNTRL become broader and stronger in the center of the domain.

At 6-hr the rear-to-front flow in both simulations has comparable magnitude, but in CNTRL the MCV on the north end of the bow echo is more intense. This comes as no surprise since one of the mechanisms behind the formation of this feature is the tilting of near-surface horizontal vorticity by the new updrafts being forced along the gust front (Weisman and Davis 1998, Pandya et al. 2000). With a stronger baroclinic generation of horizontal vorticity along the surface outflow in the late stages of the simulation, the solution in CNTRL should produce a better defined MCV.

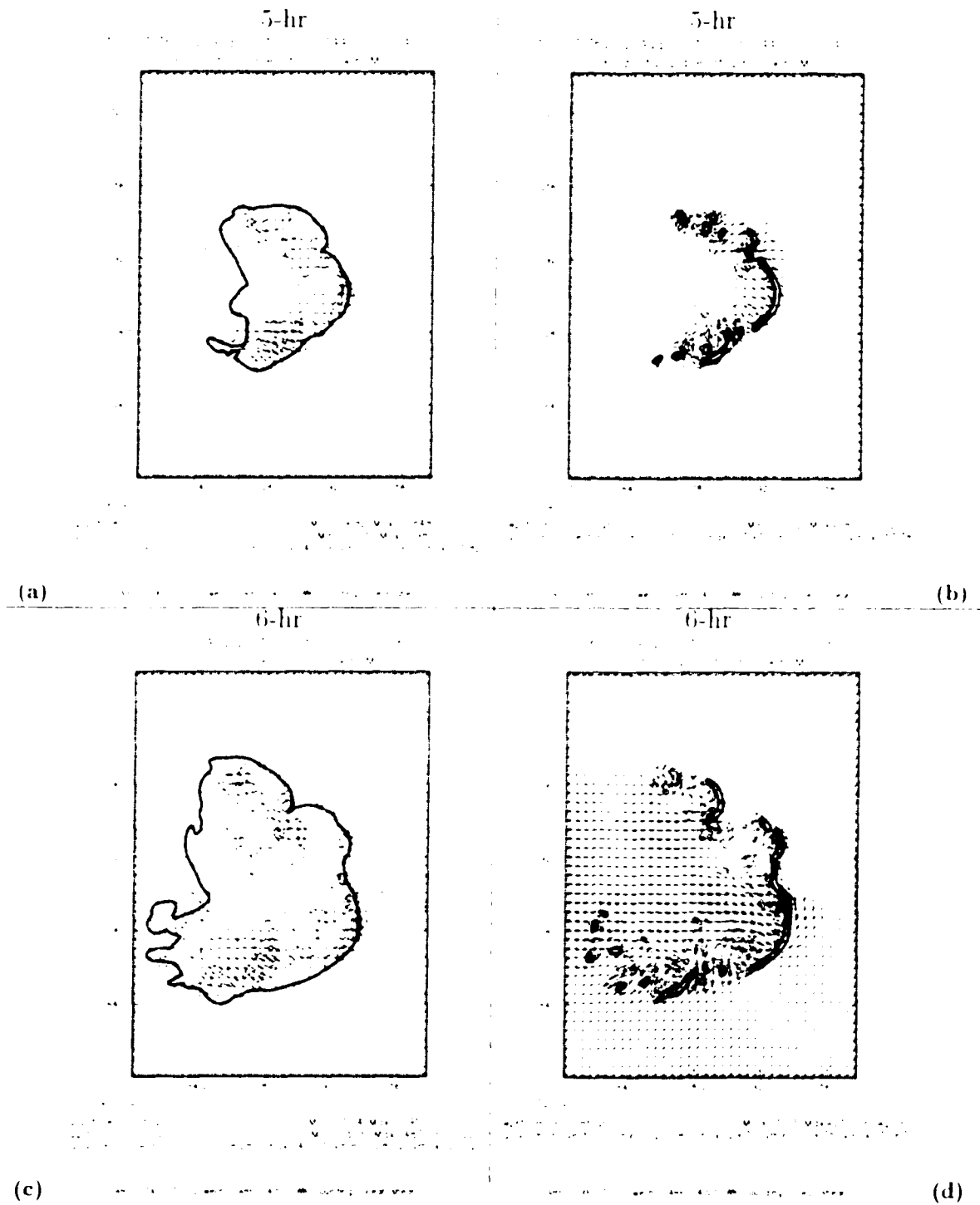


Figure 4.13: NO_ICE simulation at 4-hr (first row) and 6-hr (second row). (a), (c) surface cold pool and outflow – vectors are ground-relative winds, thick solid line represents -2 K potential temperature perturbation indicating the boundary of the cold pool, thin solid (dashed) contours indicate positive (negative) pressure perturbations plotted at each 100 Pa. (b), (d) storm-relative winds (vectors) and vertical velocity contoured at 2 m s^{-1} intervals, at height $z = 2600$ m. Solid (dashed) lines are updrafts (downdrafts).

Chapter 5

Withdrawal of Kinematic Fields

In this chapter we analyze withdrawal experiments in which the kinematic fields are reset to the base state. The specific questions to be addressed are: What happens to the simulation of the idealized bow echo when *incomplete* information of the wind field within the storm system is provided? How important is the vertical motion compared to the horizontal wind field when it comes to the initialization of a mature convective storm in a cloud-scale model? What physical processes drive the response among meteorological variables (particularly, wind and mass fields) in the storm system when the kinematic structure of the MCS is only partially specified?

5.1 General results

In experiment WVEL, the vertical motion is set to zero everywhere at 4-hr, while in experiment UVVEL the horizontal winds are reset to the background shear profile also at 4-hr. The 2-hr simulation (from 4 to 6-hr) in WVEL is shown in Figure 5.1. This run generated a solution that bears a remarkable resemblance to that of CNTRL. Not only did the simulation maintain the proper convective mode, but all key mesoscale

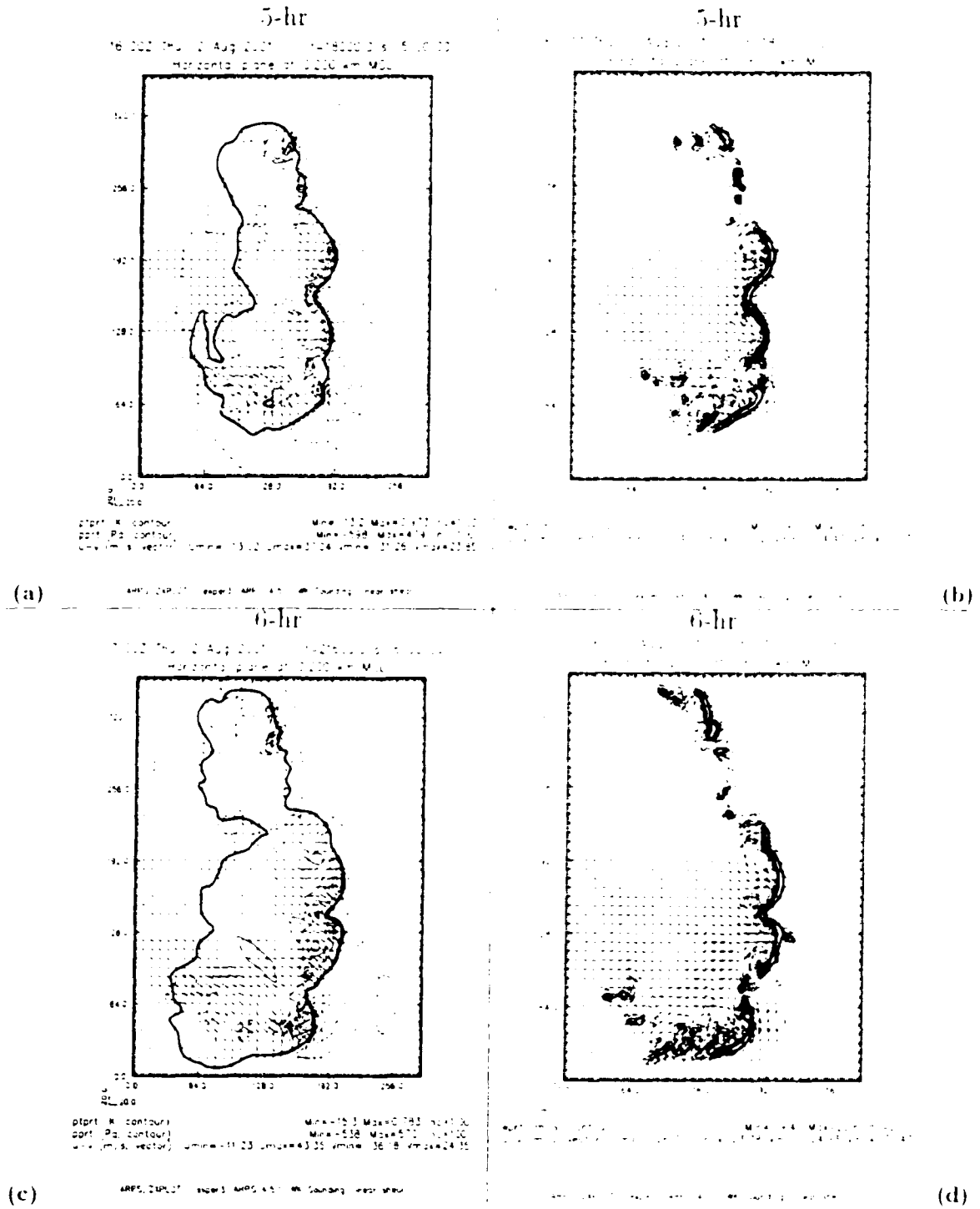


Figure 5.1: Bow echo simulation in WVEL. First row: 5-hr; second row: 6-hr. (a),(c) surface cold pool and outflow: vectors are ground-relative winds, thick solid line represents -2 K potential temperature perturbation indicating the boundary of the cold pool, thin solid (dashed) contours indicate positive (negative) pressure perturbations plotted at each 100 Pa. (b),(d) storm-relative winds (vectors) and magnitude of vertical velocity (contoured at 2 m s⁻¹ intervals) at height z = 2600 m. Solid (dashed) lines are updrafts (downdrafts). Domain translation is as in CNTRL (Figs. 4.3, 4.4).

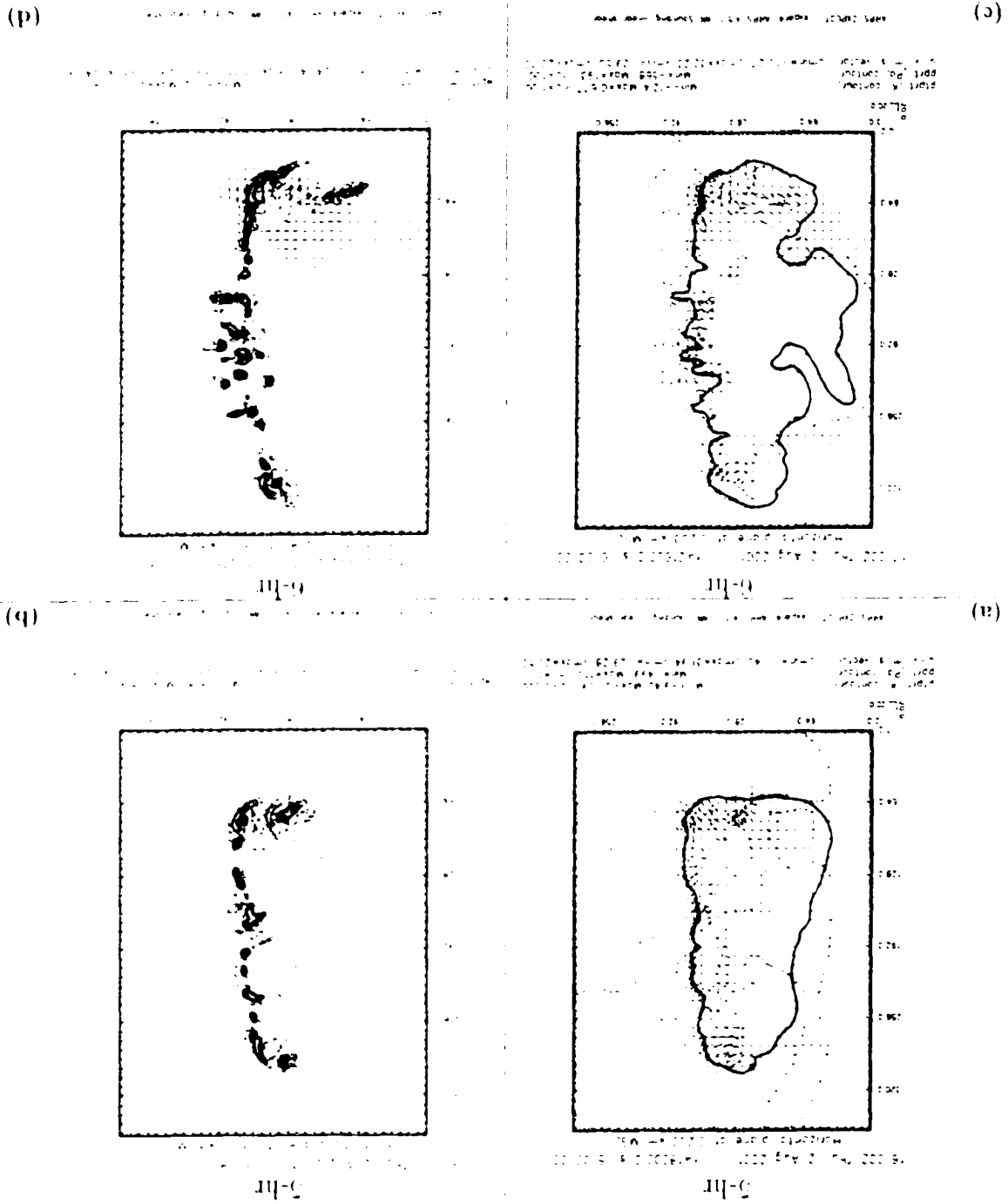
features associated with the MCS are correctly represented: the shape, orientation and strength of the surface cold pool, mesohigh, and outflow (Figs. 5.1a,b) match quite well with CNTRL.

The storm-relative winds aloft do not show significant alteration either (Fig. 5.1b,d), including the positioning and strength of the main MCV in the center of the domain. In terms of the horizontal distribution of the vertical velocity field, the simulation is able to restore the vertical motion effectively. A close inspection of CNTRL and WVEL shows that most of the error in the WVEL “forecast” is due to phase errors, rather than amplitude errors. Aside from that, WVEL reproduced the main characteristics of the bow echo quite well.

The same is not true for UVVEL, as seen in Figure 5.2. The simulated storm in this run was not capable of maintaining the bow echo structure — at least within the 2-hr integration period being considered. Instead, the dominant convective mode is multicellular, particularly in the center of the domain (Figs. 5.2c,d). The change in convective mode also is indicated by the non-generation of the strong mid-level MCV present in CNTRL. The strengths of the surface cold pool and mesohigh were significantly underestimated, and the shape of mesoscale features altered. An important implication is that the surface outflow is not well recovered.

To quantify the impact of the field withdrawals on the overall solution, we analyze Figures 5.3 and 5.4 which show the time evolution of vertical profiles of system-averaged vertical momentum ($\overline{w'u'}$) and heat ($\overline{w'\theta'}$) fluxes at each 10-min for CNTRL, WVEL and UVVEL starting at 4-hr. For all times shown, the system-averaged fields are computed for the area indicated by a rectangle in Fig. 4.4b. Because the averaging is carried out for the most convectively active sector of the simulated bow echo, the vertical fluxes obtained for CNTRL (Figs. 5.3a,5.4a) are stronger than those reported by Weisman et al. (1997), where the profiles $\overline{w'u'}$ and $\overline{w'\theta'}$ were averaged for the *entire*

Figure 5.2. As in Figure 5.1, but for experiment UVEEL.



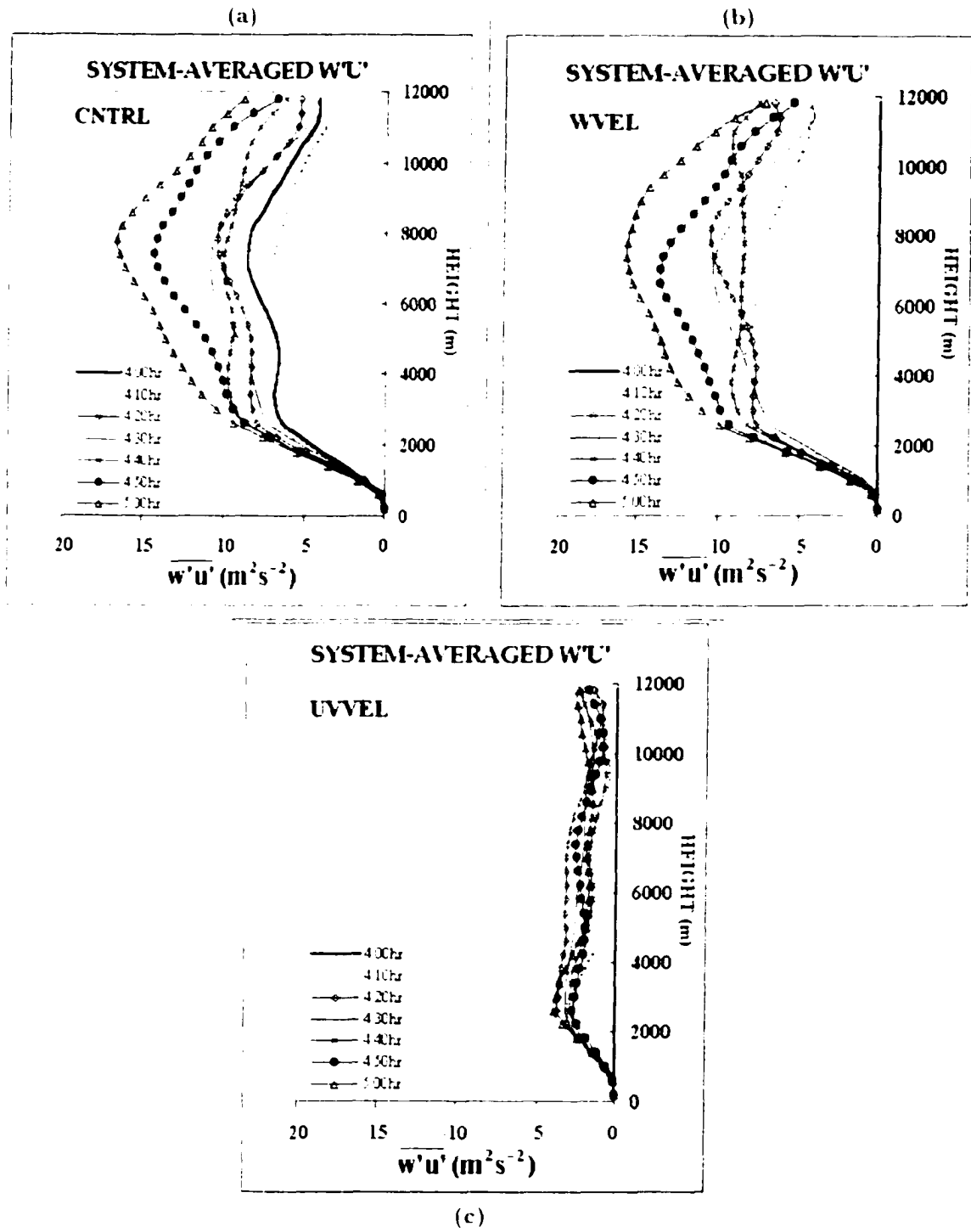


Figure 5.3: Time evolution, from 4-hr to 5-hr (at 10-min increments), of system-averaged profiles of vertical momentum flux ($\overline{w'u'}$) in $m^2 s^{-2}$: (a) CNTRL, (b) WVCL, (c) UVVEL. The averaging is applied for the region enclosed by a rectangle in Fig. 4.4b.

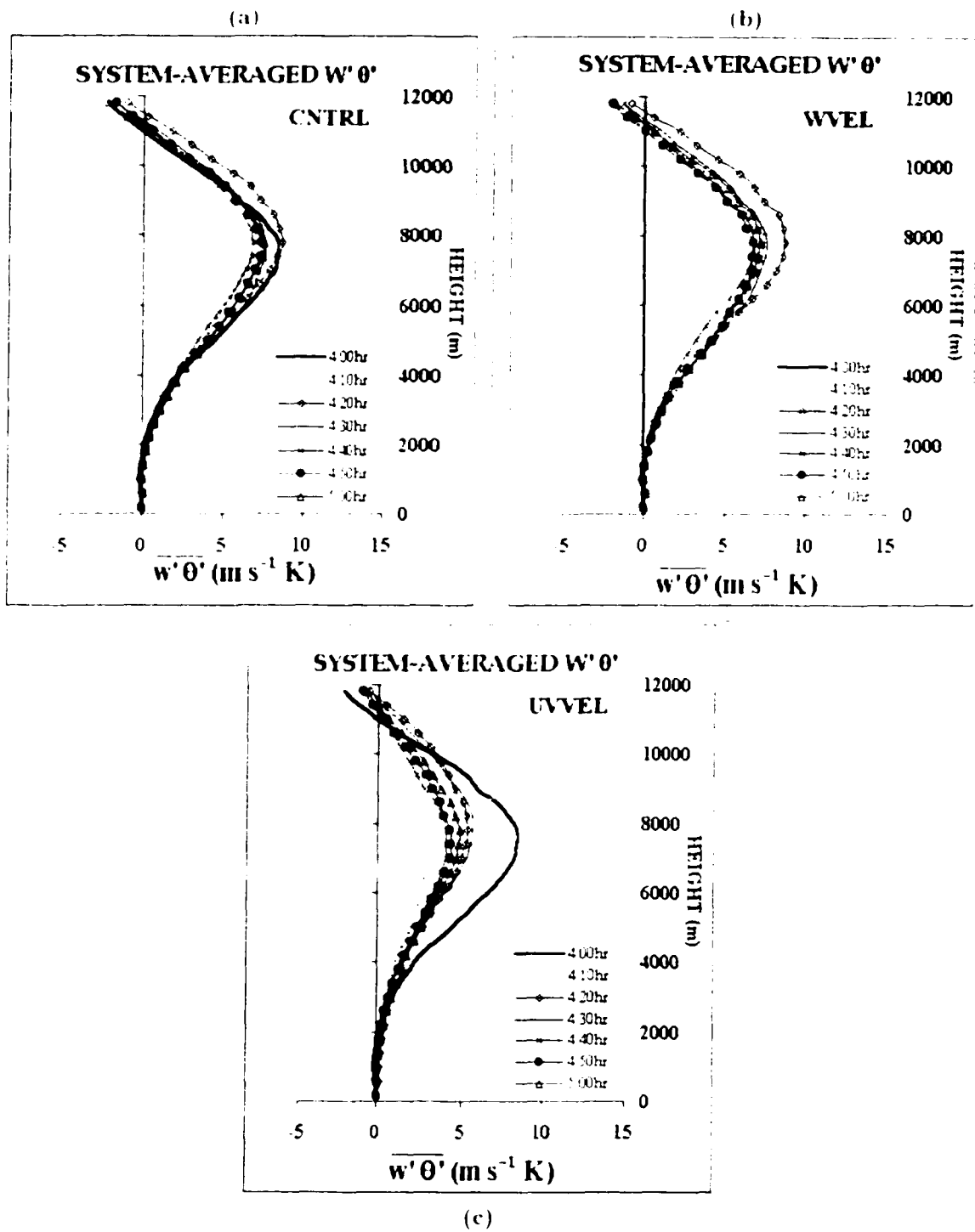


Figure 5.4. As in Figure 5.3, but for vertical heat flux ($\overline{w'\theta'}$) in $\text{m s}^{-1} \text{ K}$.

domain.

A comparison of Figures 5.3a,b and 5.4a,b reveals that the vertical fluxes are efficiently restored in WVFL, despite the total elimination of w field at 4-hr. Ten minutes after restart (dotted lines in Figs. 5.3b, 5.4b), the average vertical momentum and heat fluxes in WVFL already achieve magnitudes comparable to the CNTRL counterparts. In addition, the time evolution follows closely the solution from CNTRL. Conversely, the vertical fluxes in UVFL (Figs. 5.3c, 5.4c) are not consistent with the active MCS present in CNTRL, with the fluxes being substantially weakened. Although the vertical heat flux in UVFL at 4-hr (thick solid line in Fig. 5.4c) is not changed by the elimination of perturbation horizontal winds, it is strongly affected as the solution evolves, being reduced by more than 30% of its maximum value at 5-hr.

Because the $\overline{w'\theta'}$ and $\overline{w'u'}$ fields can be used to characterize the overall intensity of the simulated MCS (e.g., Weisman et al. 1997), it is clear that the elimination of perturbation horizontal winds has a greater impact on the simulation than does the withdrawal of the vertical motion.

One of the main characteristics of long-lived bow echoes is their ability to efficiently generate new updrafts along the gust front, leading to a remarkably fast forward motion (Johns and Hirt 1987, ED01, Corfidi 2002). If vertical velocities undergo significant alteration due to the imposed perturbation in the wind field (as seems to be the case in UVFL), one should expect the distribution of hydrometeors -- and accompanying diabatic effects -- in the MCS also to be modified as the integration proceeds, with possibly devastating effects to the simulated convective storm. Thus, it is important to analyze the early evolution of the wind field around the surface outflow in the withdrawal runs.

Figure 5.5 shows vertical cross sections of the wind field on the gust front sector in a 18 km x 18 km domain, displaying the correct aspect ratio of the simulated

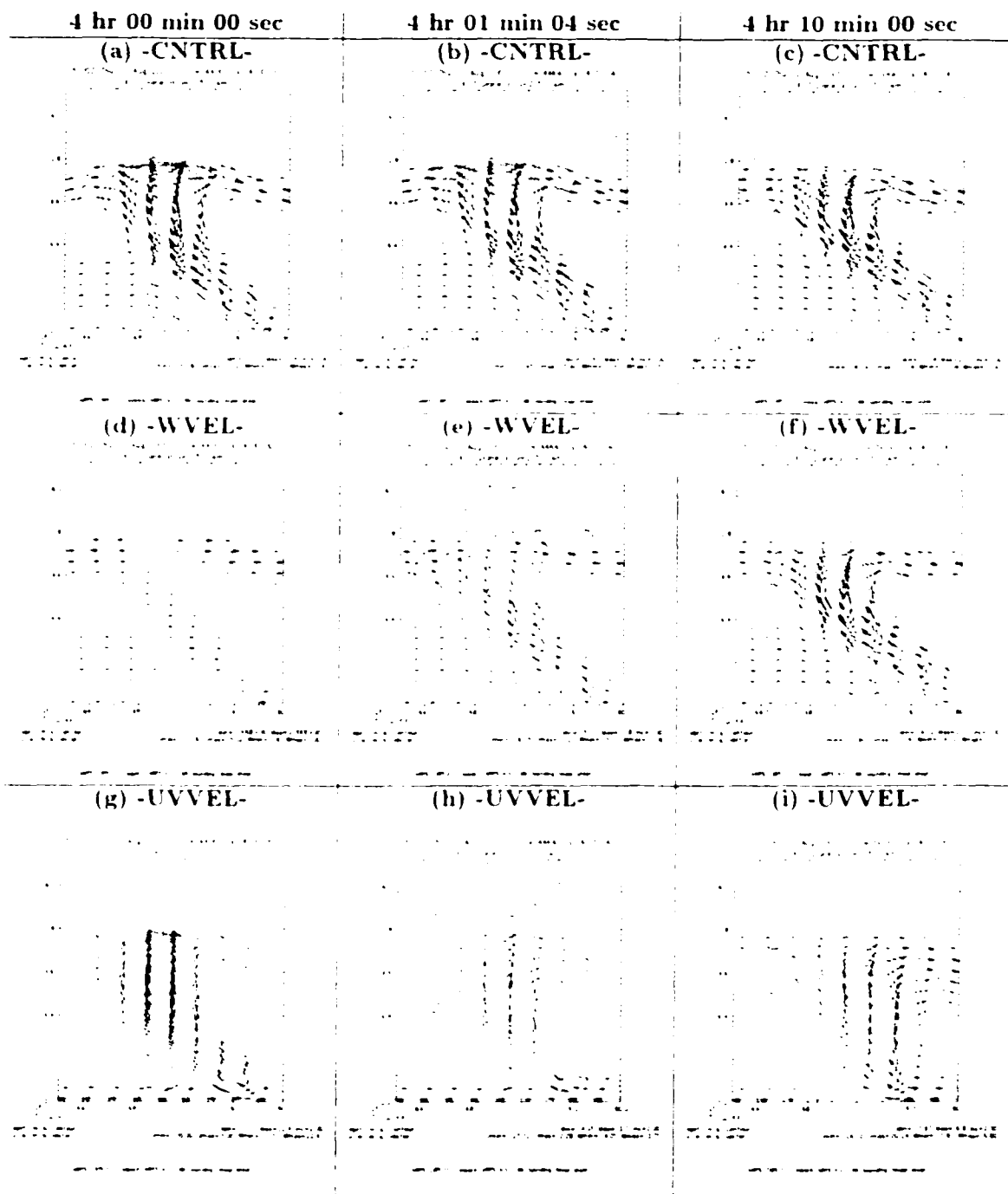


Figure 5.5: Vertical cross-sections in the xz -plane along $y = 205$ km (same y -coordinate of segment \overline{AB} in Fig. 4.3a) for the storm-relative wind field across the gust front. The domain shown is 18 km \times 18 km. First column: $t = 4:00:00$ -hr (restart time for withdrawal experiments); second column: $t = 4:01:04$ -hr; third column: $t = 4:10:00$ -hr. (a)-(c) refer to CNTRL; (d)-(f) to WVEL; and (g)-(i), to UVVEL. Vectors represent the xz -component of the system-relative wind in m s^{-1} , and contours indicate magnitude of the vertical velocity in m s^{-1} (contoured at 2 m s^{-1} increments, with the zero line being suppressed). Solid (dashed) lines indicate updrafts (downdrafts).

flow along $y = 205$ km (apex of the main bow echo segment at 4-hr; Fig. 4.6a) at $t = 4:00:00$ -hr, 4:01:04-hr and 4:10:00-hr, for CNTRL, WVEL and UVVEL. The contours refer to the magnitude of the vertical velocity field. The main features in this active portion of the simulated MCS include a surface-based upshear-tilted updraft, a descending rear-to-front flow, and a (slightly-)descending downshear flow at the anvil-level (see CNTRL solution in Figs. 5.5a-c).

For WVEL, the IC (Fig. 5.5d) shows no vertical motion, but after roughly 1-min (Fig. 5.5e), the solution displays a clear trend toward restoring the main features indicated in CNTRL. After 10-min (Fig. 5.5f), very good agreement is found in amplitude and phase between CNTRL and WVEL. A more detailed examination of this evolution highlights the fast regeneration of the vertical motion field in the very early stages of the simulation, as shown in Fig. 5.6. From a qualitative standpoint, the solution from WVEL already reproduces the main features from CNTRL 8 s after the restart time (Fig. 5.6a). Within the first minute of integration (Figs. 5.6b,c) the magnitude attained by the vertical motion in WVEL is approximately half of that in CNTRL.

The relatively strong downdraft evident in the upper portion of the domain (at and above the model tropopause; $z \approx 12.0$ km) in Figs. 5.6a-c is actually part of the “transient evolution” associated with the adjustment process, and it fades away after an initial oscillatory regime. Around 10-min after restart, this feature is no longer present (Fig. 5.5f). The spurious upper-level downdrafts are forced by the pressure field which is induced by the adjustment process early in the integration to be discussed later in this chapter. Similar behavior of the solution is found along distinct (E-W) cross sections of the simulated MCS (not shown).

In UVVEL, the vertical motion at 4-hr (Fig. 5.5g) is exactly the same as in CNTRL (compare contours with Fig. 5.5a). However the horizontal wind field has been reset

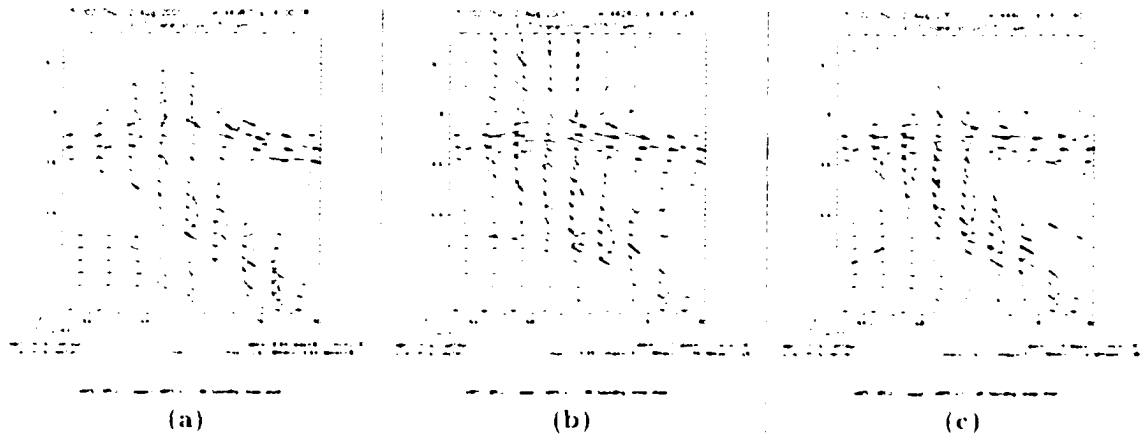


Figure 5.6: As in Fig. 5.5, but only for WVFL, at (a) $t = 400:08$ -hr, (b) $t = 400:24$ -hr, (c) $t = 400:40$ -hr

to its (horizontally) homogeneous environmental state — i.e., there is no horizontal divergence/convergence. As the integration proceeds, the vertical motion is weakened and loses important characteristics, such as its upshear-tilted structure, as revealed by the evolution of the contoured fields in Figs. 5.5g,h,i. Without the strong horizontal surface winds, the leading edge of the gust front — where convergence is maximized — does not advance as fast as in CNTRL. In fact, the horizontal wind field is never correctly restored in UVVEL, and the cold pool is poorly represented (see Fig. 5.7), indicating that the forward motion of the simulated MCS is affected. This evolution is consistent with the very poor “forecast” produced by UVVEL.

The results discussed so far are in agreement with the findings of Weygandt et al. (1999) for a numerically-simulated supercell. Nevertheless, some very important questions need to be addressed: Why does the elimination of the vertical velocity have only a minor impact in the simulation of the bow echo, while the withdrawal of the (perturbation) horizontal velocity leads to a solution that deviates significantly from CNTRL? What is the process controlling such behavior?

As mentioned in chapter 2, Fiedler (2002) indicated that, for convective flows with low aspect ratio, the vertical motion should respond to the initial horizontal wind

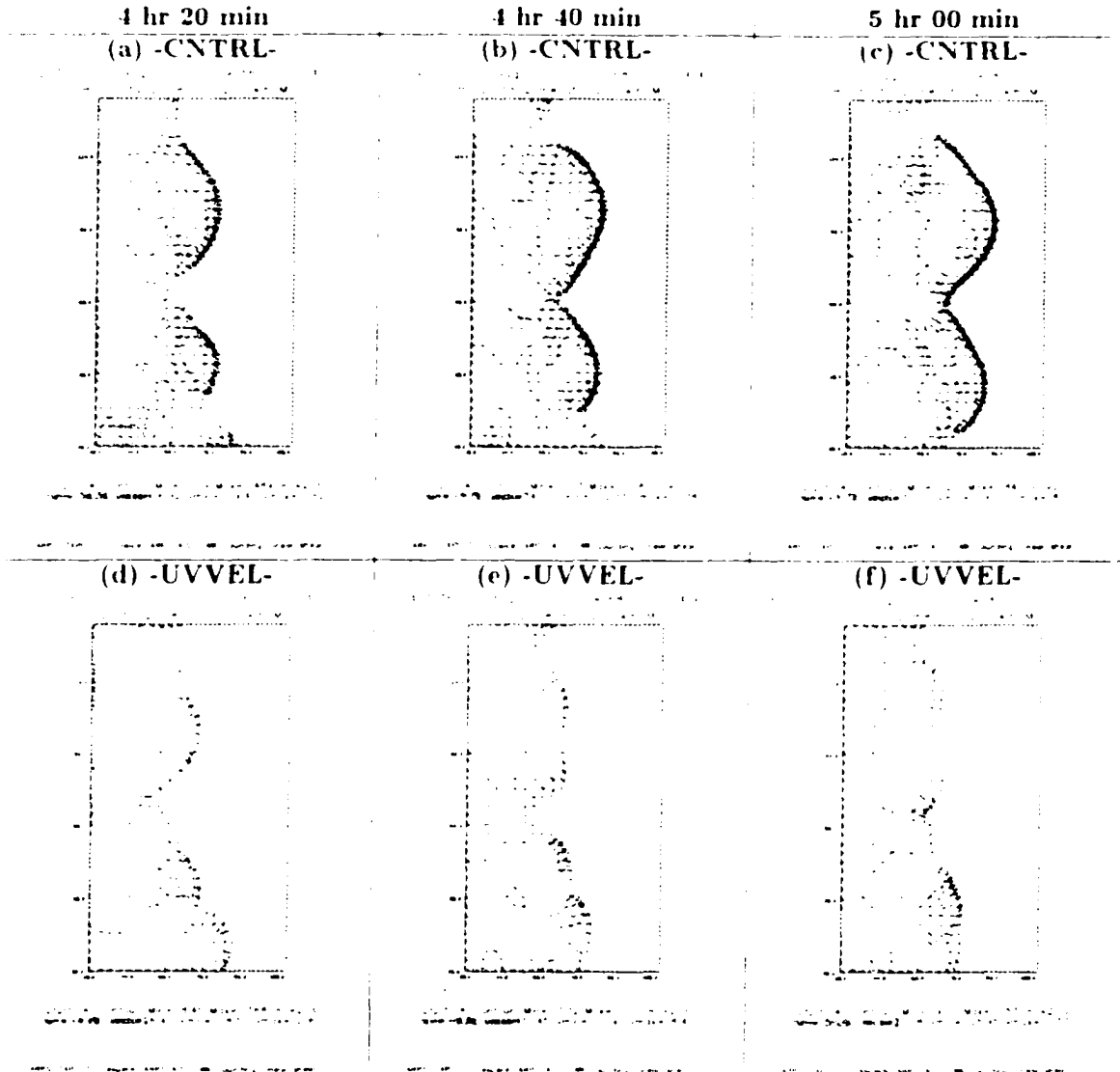


Figure 5.7: Evolution of the simulated gust front for the sector indicated by a rectangle in Fig 1.4b. (a)-(c) CNTRL, and (d)-(f) UVVEL. First column: 4:20:00 hr, second column: 4:40:00 hr, third column: 5:00:00 hr. Dashed lines (referring to negative values) are contours of potential temperature perturbation, plotted at -2 K increments. The first contour from right to left is the -2 K line, indicating the leading edge of the advancing cold pool. Vectors are ground-relative winds in m s^{-1} , with a reference vector of 10 m s^{-1} indicated on the lower left corner of each panel. Note that solution from UVVEL deviates significantly from CNTRL.

field, with the opposite occurring for flows with high aspect ratio. However, just by looking at the cross sections in Figures 5.5 and 5.6, we cannot state that the simulated flow has a low aspect ratio. In fact, it displays an aspect ratio around unity, with the flow changing from updrafts to downdrafts in vertical and horizontal scales of roughly the same order. Hence, a different approach from that of Fiedler (2002) is applied to understand *physically* the processes behind the dynamic adjustment, without explicitly referring to linear wave theory. The propagation of acoustic waves in WVFL and UVFL is studied in chapter 6.

5.2 Analysis of the prognostic pressure equation: divergence forcing

In experiment WVFL, low-level horizontal divergence/convergence along the gust front is maintained at restart time; in UVFL, these structures are removed. Thus, in the very early stages of UVFL, some of the dynamically important adjustment processes occurring in the simulation include: (i) the response of the horizontal winds to the initially unperturbed pressure field, (ii) the response of the pressure field to the strong perturbation imposed in the horizontal wind field, and (iii) the response of the vertical motion to the modified horizontal velocities.

To understand these processes, it is useful to examine the prognostic equation for perturbation pressure. First, consider the equation of state for dry air:

$$p = \rho R_d \theta \left(\frac{p}{p_0} \right)^{\frac{R_d}{c_p}} \quad (5.1)$$

where p is pressure, ρ is density, R_d is the gas constant for dry air, θ is potential temperature, p_0 is a reference pressure (10^5 Pa) and c_p is the specific heat of dry air at constant pressure. ARPS takes into account the effects of water substance in

(5.1), but these effects are neglected for now.

A rearrangement of terms involving pressure in (5.1), followed by taking the Lagrangian (total or material) derivative, yields:

$$\frac{Dp}{Dt} = c_s^2 \frac{D\rho}{Dt} + c_s^2 \frac{\rho}{\theta} \frac{D\theta}{Dt} \quad , \quad (5.2)$$

where c_s^2 is the square of the speed of sound given by (2.14).

The mass conservation equation for a fully compressible flow is:

$$\frac{1}{\rho} \frac{D\rho}{Dt} = -\nabla \cdot \vec{V} \quad , \quad (5.3)$$

where \vec{V} is the 3D wind field. Substituting (5.3) into (5.2) and expanding the Lagrangian derivative of pressure leads to:

$$\frac{Dp}{Dt} = \vec{V} \cdot \nabla p + \rho c_s^2 \nabla \cdot \vec{V} + \rho c_s^2 \frac{1}{\theta} \frac{D\theta}{Dt} \quad (5.4)$$

If we now expand the pressure field into hydrostatic base state and perturbation components, (5.4) becomes:

$$\begin{aligned} \frac{\partial p'}{\partial t} = & \underbrace{\bar{\rho} g w}_{\text{(I)}} + \underbrace{\vec{V} \cdot \nabla p'}_{\text{(II)}} + \underbrace{\rho c_s^2 \nabla \cdot \vec{V}}_{\text{(III)}} + \underbrace{\rho c_s^2 \frac{1}{\theta} \frac{D\theta}{Dt}}_{\text{(IV)}} \quad , \end{aligned} \quad (5.5)$$

where g is the acceleration due to gravity and w is the vertical component of the wind.

Equation (5.5) is, essentially, the pressure equation solved by ARPS. Term (I) is the vertical advection of base-state pressure after applying the hydrostatic relation, and is the only “surviving term” from the base-state pressure advection. Term (II) is the advection of perturbation pressure, while (III) is the divergence term. Term (IV) represents the contribution from diabatic effects, which are usually small (Klemp and Wilhelmson 1978), resulting in this term being neglected in ARPS (Xue et al. 2000).

Terms I and III in (5.5) are typically largest in magnitude, with the divergence term dominating. Figure 5.8 shows contour plots for terms (I), (II) and (III) of (5.5), for experiment CNTRL at 4-hr, in the same vertical cross section of Figure 5.5. The vertical advection of base-state pressure (Fig. 5.8a) and the divergence term (Fig. 5.8c) have comparable magnitude, with the latter displaying larger values (note that different contour intervals are used; see caption of Fig. 5.8). The advection of perturbation pressure is two orders of magnitude smaller.

We first examine the dominant forcing term in the pressure equation, which is the three-dimensional divergence. Consider, first, the upward branch of an idealized convective cell, as depicted in Figure 5.9. Region 1 (2) indicates a sector on the top (bottom) of the updraft, near the upper (lower) boundary. The three-dimensional divergence $\nabla \cdot \vec{V}$ can be written in terms of horizontal and vertical contributions, yielding:

$$\nabla \cdot \vec{V} = \nabla_H \cdot \vec{V} + \frac{\partial w}{\partial z} \quad (5.6)$$

In region 1 (Fig. 5.9) we have: $\nabla_H \cdot \vec{V} > 0$, $\frac{\partial w}{\partial z} < 0$.

In region 2 we have: $\nabla_H \cdot \vec{V} < 0$, $\frac{\partial w}{\partial z} > 0$.

In experiment WVEL (UVVEL), all of the information related to $\partial w / \partial z$ ($\nabla_H \cdot \vec{V}$) is eliminated at restart time while $\nabla_H \cdot \vec{V}$ ($\partial w / \partial z$) remains unchanged. Thus, when experiment WVEL is started, the *three-dimensional* (3D) divergence in region 1 is more positive than it should be, and more negative than it should be in region 2. From (5.5), the pressure field responds to this alteration in the 3D divergence by generating a negative (positive) pressure perturbation in region 1 (2). In other words, an artificial low (high) pressure perturbation is induced at the top (bottom) of the column where the updraft was located before being eliminated, as indicated in Figure 5.10.

Figures 5.11a and 5.11b depict, for experiments CNTRL and WVEL, respectively,

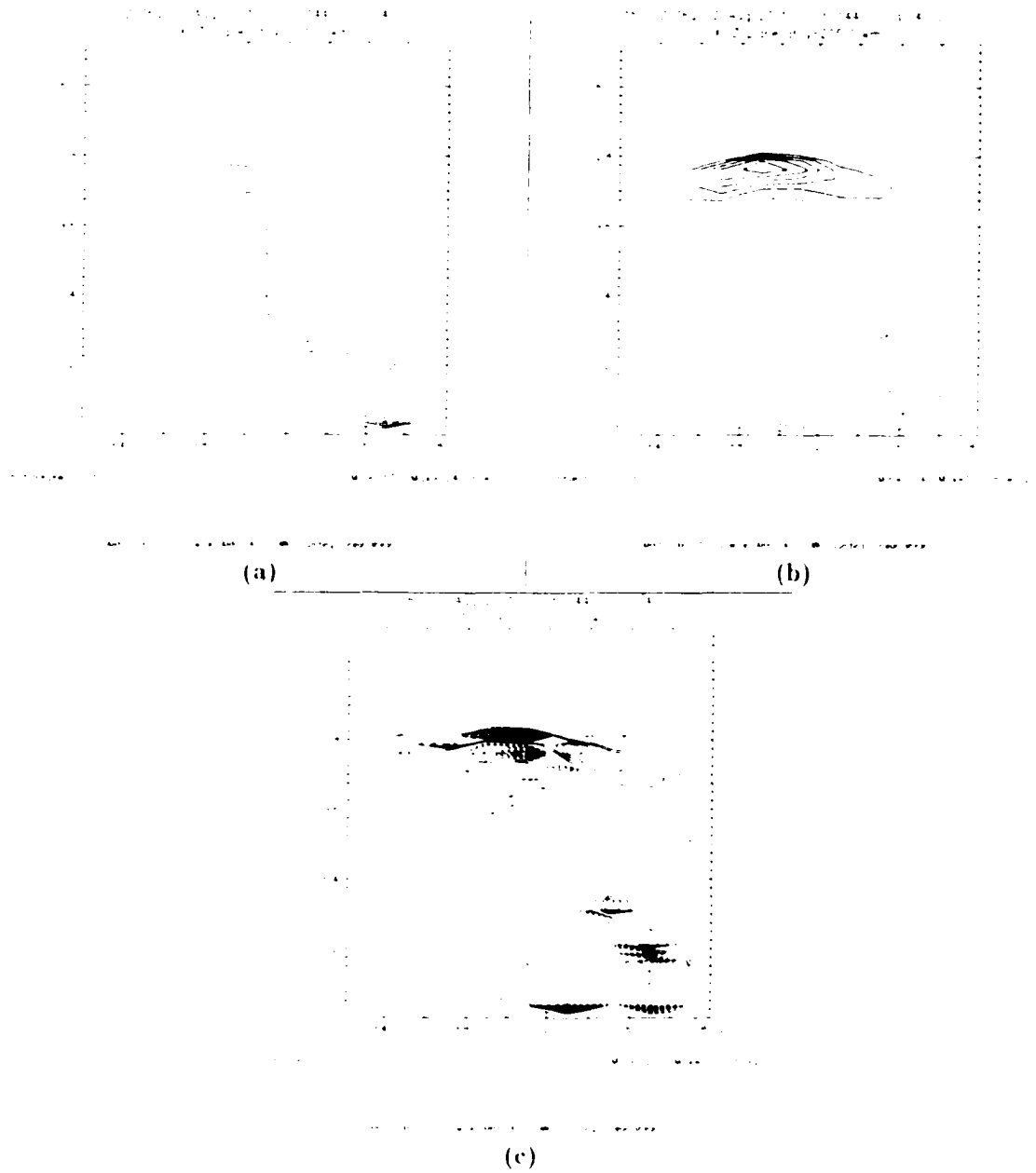


Figure 5.8: Solution at 4-hr for CNTRL along same vertical cross section shown in Fig. 5.5. First three terms on the right-hand-side of the pressure equation (Eq. 5.5.): (a) term I: $\bar{\rho} g w$, contoured at 10.0 Pa s⁻¹ intervals; (b) term II: $-\vec{V} \cdot \nabla p'$, contoured at 0.2 Pa s⁻¹ intervals; (c) term III: $-\rho c_s^2 \nabla \cdot \vec{V}$, contoured at 25.0 Pa s⁻¹ intervals. Zero lines are suppressed.

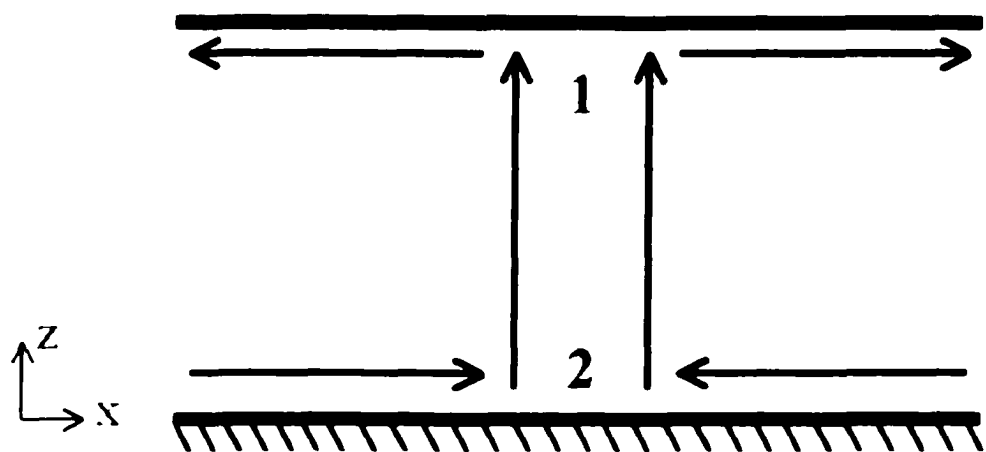


Figure 5.9: Idealized sketch of the upward branch of a convective cell

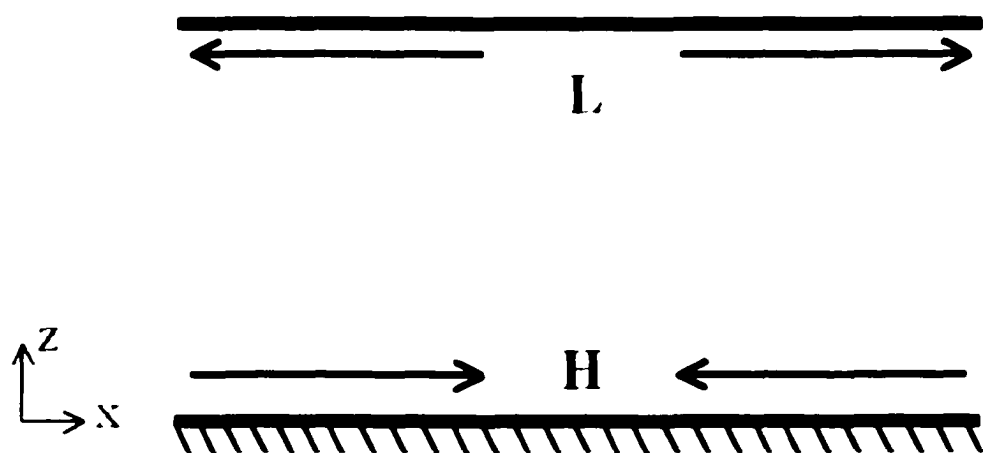


Figure 5.10: Idealized sketch of the pressure perturbation induced shortly after the elimination of the updraft in Figure 5.9 (Proxy for experiment WVEL).

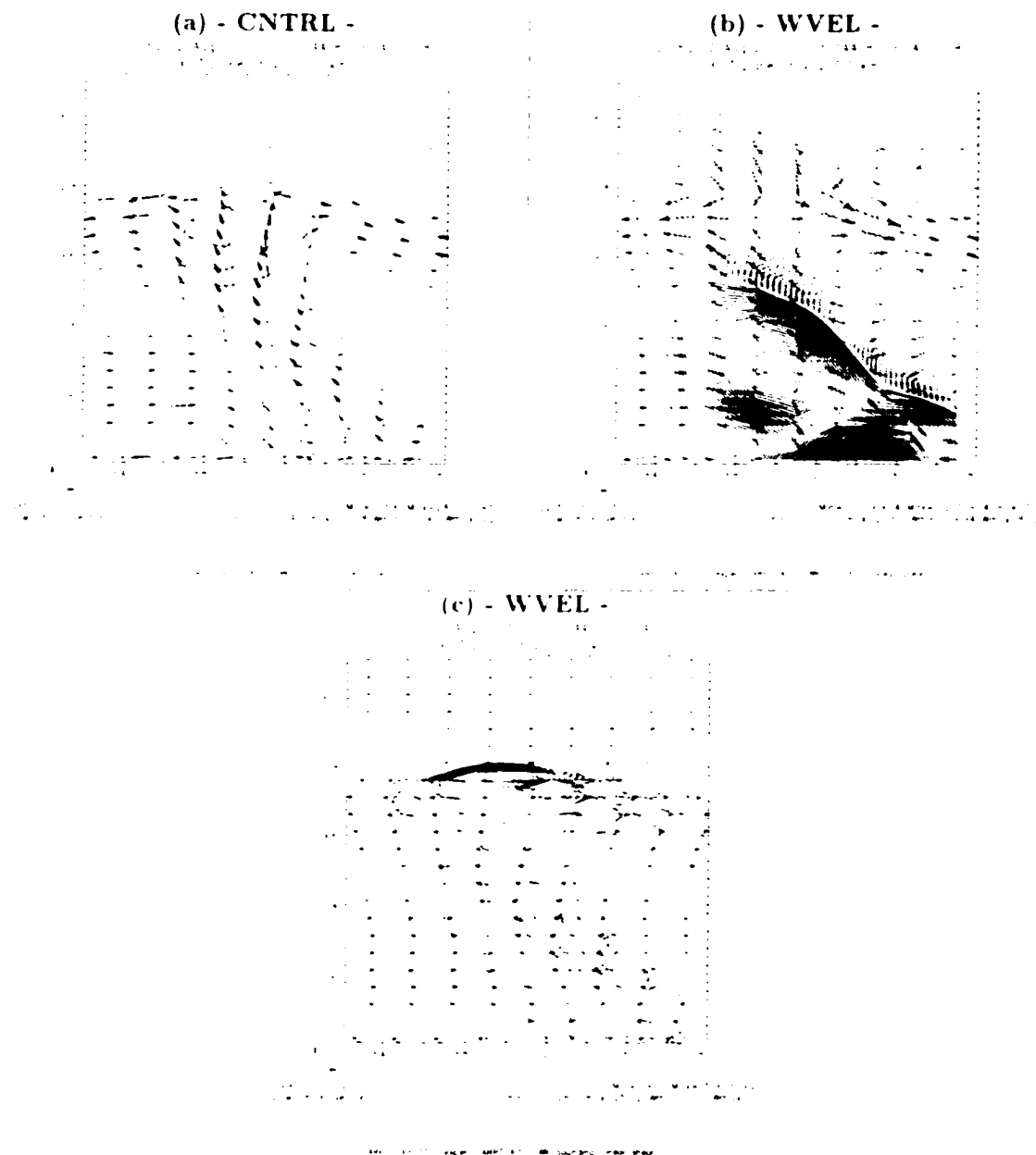


Figure 5.11: Cross-sections in the xz-plane across the gust front (same domain as in Fig. 5.5), for (a) perturbation pressure (Pa): CNTRL; (b) perturbation pressure (Pa): WVEL, both at $t = 4:00:08$ hr; (c) horizontal divergence (10^{-3} s^{-1}): WVEL, at $t = 4:00:00$ hr. In (a) and (b) the fields are contoured at 50 Pa intervals; in (c) the contour interval is $2 \cdot 10^{-3} \text{ s}^{-1}$. In all figures, solid (dashed) lines indicate positive (negative) values, with zero lines being suppressed. All panels show storm-relative winds in m s^{-1} (vectors), with a reference vector of 10 m s^{-1} indicated on the lower left corner of each panel.

the perturbation pressure 8 s after restart ($t = 4:00:08\text{-hr}$)¹, in a xz-cross section across the gust front (same sector analyzed in Fig. 5.5). The solution from CNTRL is the same one shown in Fig. 4.7 b and is repeated here — now zoomed in for the 18 km x 18 km domain — for clarity². It should be emphasized that the perturbation pressure field analyzed here is associated with all terms in the pressure equation, and not decomposed for the divergence forcing alone. However, in the discussion that follows, it is shown that the divergence term dominates the response qualitatively and quantitatively.

In agreement with the discussion for the idealized convective cell, WVEL (Fig. 5.11b) shows a pressure field dominated by a “low-over-high” pattern. The maximum positive (negative) pressure perturbation in Fig. 5.11b agrees quite well with the region where $\nabla_H \cdot \mathbf{V}^*$ is a minimum (maximum) at 4-hr, shown in Fig. 5.11c. Because $\partial u / \partial z$ is zero at this time, $\nabla_H \cdot \mathbf{V}^*$ represents the incomplete 3D divergence and, thus, where $\nabla_H \cdot \mathbf{V}^*$ is positive (negative) a pressure perturbation of negative (positive) sign is induced. Similar structure is also found along distinct cross sections of the simulated MCS, to be discussed below. Note also that the presence of a low pressure center in the upper troposphere in WVEL induces the upper-level downdraft evident in Fig. 5.6. These strong pressure features are transient, and are gradually damped as time evolves. A detailed discussion of the “transient evolution” is presented in chapter 6.

The “low-over-high” pattern in Figures 5.10 and 5.11b suggests that the restoration of the updraft in WVEL is favored by the induced vertical pressure gradient force (PGF). However, in the horizontal, the PGF works against the horizontal wind field, with a positive (negative) pressure perturbation where the winds converge (diverge).

¹There is nothing particularly important about $t = 4:00:08\text{-hr}$. This time is selected for analysis because history files from the withdrawal experiments are saved at each 8 s, which makes the history files referring to $t = 4:00:08\text{-hr}$ the ones closest to the restart time. The results shown for this time are representative of $t = 4:00:04\text{-hr}$ (the first big time step).

²In comparing Fig. 5.11a with Fig. 4.7b we realize how changing the figure’s aspect ratio can dramatically influence the apparent aspect ratio of the simulated flow. In Fig. 4.7b the updrafts look narrow and upright, while in Fig. 5.11a (which shows the solution with the correct aspect ratio) the updrafts are upshear-tilted and broader.

Hence, the question that arises is: Can vertical motion be restored by the vertical PGF more efficiently than the horizontal wind field is destroyed by the horizontal PGF? The evolution of WVFL solution (Figs. 5.5d,e,f) seems to indicate that it can.

An equivalent analysis is conducted for experiment UVVEL, for which $\nabla_H \cdot \vec{V}$ ($\partial u / \partial z$) is eliminated (remains unchanged) at 4-hr. When UVVEL is started, the *3D divergence* in region 1 (Fig. 5.9) is more negative than it should be, and more positive than it should be in region 2. Equation (5.5) indicates that the pressure field will rapidly respond by generating an artificial high (low) pressure field at the top (bottom) of the updraft, as indicated in Figure 5.12.

The corresponding numerical solution is shown in Figure 5.13. The pressure field at early stages of UVVEL (Fig. 5.13b) does show a distinct “high-over-low” feature. Since $\nabla_H \cdot \vec{V}$ is zero at restart, the 3D divergence is due solely to $\partial u / \partial z$ at this time. Hence, the maximum positive (negative) pressure perturbation agrees quite well with the region where $\partial u / \partial z$ is a minimum (maximum), revealed in Figure 5.13c. Again, this result is in close agreement with the discussion for the idealized cell.

In contrast with WVFL, the “high-over-low” pattern in Figures 5.12 and 5.13 suggests that the updraft tends to be weakened by the vertical PGF. However, in the horizontal, the induced PGF tends to favor the restoration of the horizontal winds, with a positive (negative) pressure perturbation where the wind diverges (converges). For this case, the question is: Can the horizontal wind field be restored by the horizontal PGF more efficiently than the vertical motion is destroyed by the vertical PGF? The evolution of UVVEL solution (Figs. 5.5g-i and Figs. 5.7d-f) appears to indicate that it cannot.

Because the induced pressure field plays an important role in dynamic adjustment in WVFL and UVVEL, it is important to examine the acceleration associated with the PGF early in these runs. Figure 5.14 shows vertical cross sections for the pressure

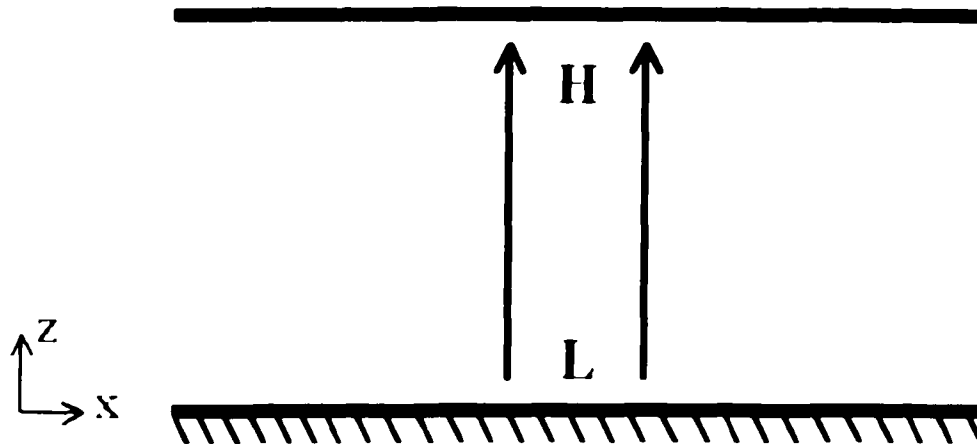


Figure 5.12 Idealized sketch of the pressure perturbation induced shortly after the elimination of the horizontal motion in Figure 5.9. (Proxy for experiment UVVEL.)

gradient acceleration (PGA)¹, 8 s after the restart time, in the zonal, meridional and vertical directions (XPGA, YPGA, and VPGA, respectively) for CTRL (Fig. 5.14a-c), WVEL (Fig. 5.14d-f) and UVVEL (Fig. 5.14g-i). The solution from CTRL is shown for comparison, and in Fig. 5.14a, wind vectors are also plotted to show updrafts and downdrafts. Again, it must be kept in mind that the magnitude of the pressure gradient accelerations shown in Fig. 5.14 are associated with *all terms in the pressure equation*, and not decomposed for distinct forcing mechanisms.

We note first that the accelerations induced by perturbation pressure *early* on experiments WVEL and UVVEL are, at least, one order of magnitude stronger than in the unperturbed solution from experiment CTRL — the contour intervals in Fig. 5.14a-c are different from the ones for WVEL and UVVEL (Figs. 5.14d-i); see caption. This is because of the artificial and extremely high values of perturbation pressure immediately after restart in WVEL and UVVEL, reaching up to 1700 Pa (see Figs. 5.11b and 5.13b).

Second, the XPGA in WVEL (UVVEL) induces horizontal divergence (conver-

¹Note that now we use the expression *acceleration* instead of *force*, since the analysis is made for *force per unit mass*.

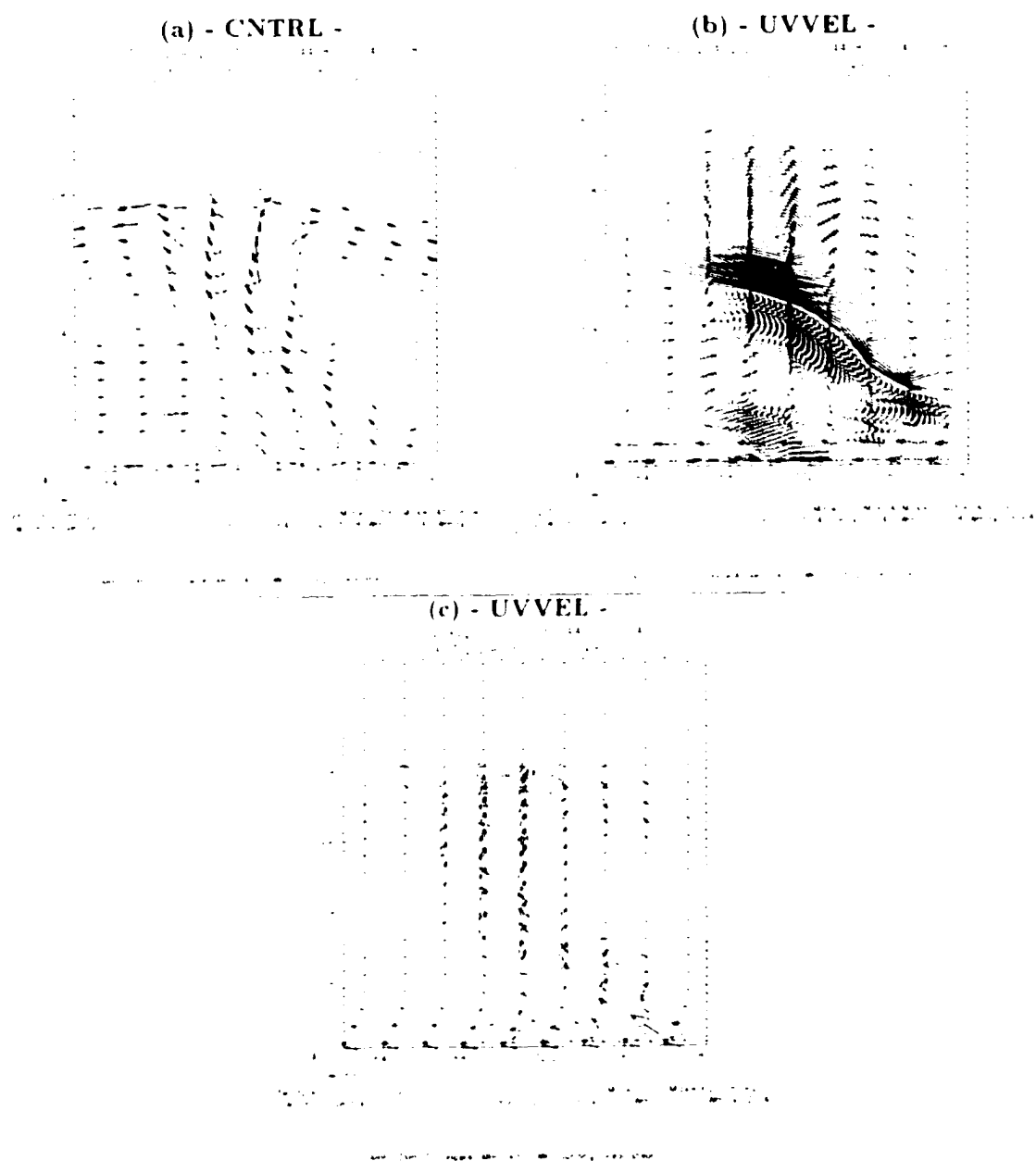


Figure 5.13: As in Figure 5.11, but with (b) referring to UVVEL, and (c) indicating the initial vertical divergence ($(\partial w / \partial z) \cdot 10^4 \text{ s}^{-1}$) for UVVEL.

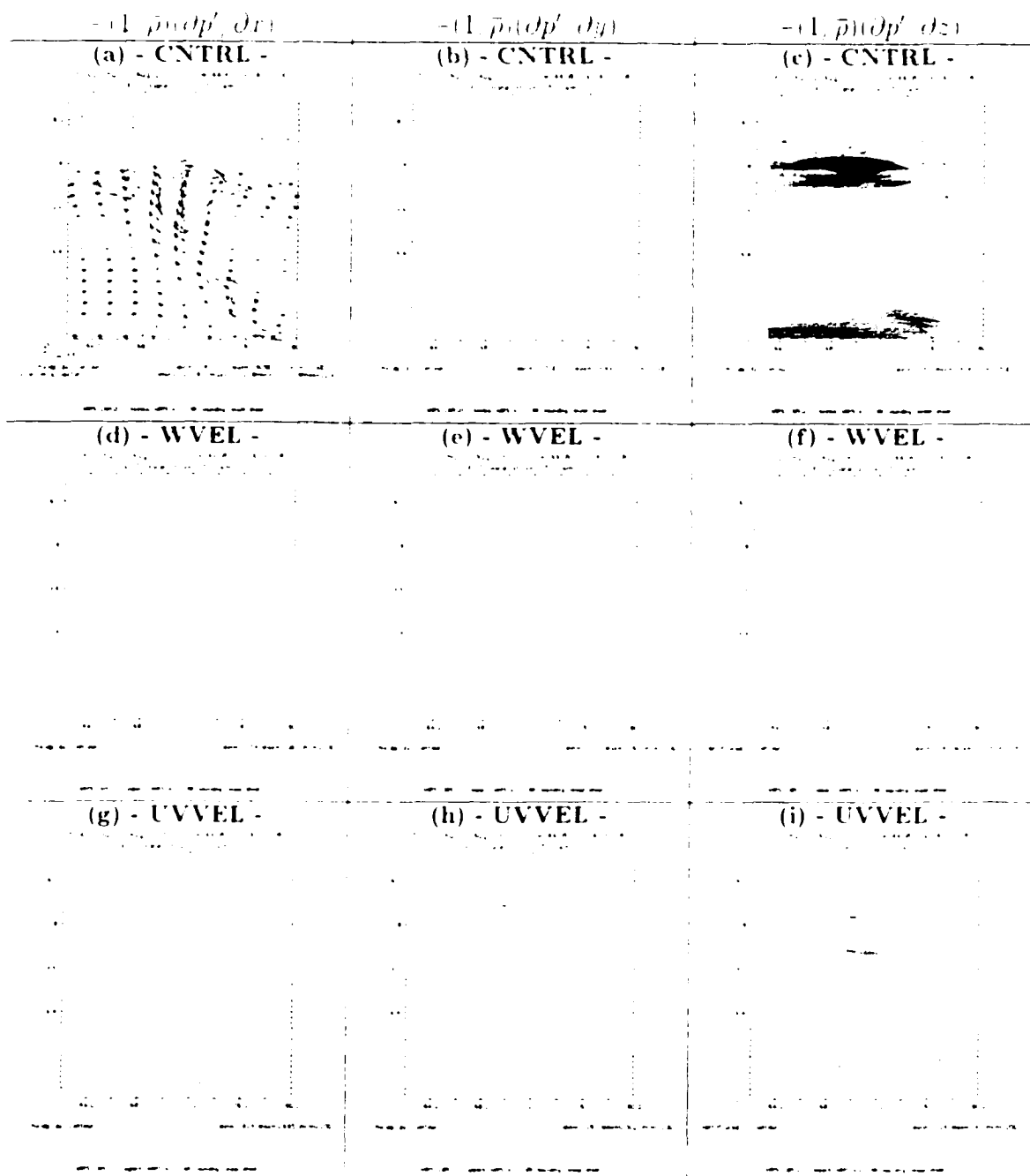


Figure 5.14. Vertical cross sections of pressure gradient acceleration (PGA) in m s^{-2} at $t = 400.08\text{-hr}$: (a)-(c) CNTRL; (d)-(f) WVEL; (g)-(i) UVVEL. First column: zonal PGA (XPGA); second column: meridional PGA (YPGA); third column: vertical PGA (VPGA). For CNTRL the contour interval is 0.025 m s^{-2} , while for WVEL and UVVEL it is 0.2 m s^{-2} . Solid (dashed) lines indicate positive (negative) values, with the zero line being suppressed. Storm-relative wind vectors for CNTRL are also shown in (a), with a reference vector of 10 m s^{-1} indicated in the lower-left corner of the panel. The xz -domain shown is the same as in Figs. 5.11 and 5.13.

gence) in the “midaltitude radial convergence” region¹ and in the gust front region, while inducing convergence (divergence) aloft, at anvil-level, as indicated in Fig. 5.14d (Fig. 5.14g). Thus, the numerical solution indicates that in WVEL (UVVEL), the correct *horizontal* winds in the simulated MCS tend to be destroyed (restored) by the induced PGA. However, both the XPGA and YPGA are *small* compared to the VPGA indicated in Fig. 5.14f for WVEL and Fig. 5.14i for UVVEL. Overall, the difference between the XPGA and VPGA does not reach one order of magnitude, though. Nevertheless, it is important to note that in WVEL, the VPGA tends to restore the main updrafts and downdrafts in their correct position — except for the spurious downdraft in the upper portion of the domain, which is just part of the transient evolution — while in UVVEL the VPGA tends to destroy the correct vertical motion, with downward (upward) acceleration where updrafts (downdrafts) exist in CNTRL, as indicated in Fig. 5.14a. This is also found for different vertical cross sections along the simulated MCS, to be examined later.

Based on the above considerations and on the 2-hr simulations analyzed in the previous section, the overall result suggests that *the VPGA in WVEL restores the correct vertical motion more efficiently than the XPGA destroys the correct horizontal wind field. Conversely, in UVVEL, the VPGA destroys the correct vertical motion more efficiently than XPGA restores the correct horizontal winds.* This analysis provides relevant information on *why the elimination of the vertical motion field is not as disastrous for the simulation of the bow echo as is the withdrawal of the perturbation horizontal wind.* However, because the VPGA is, in average, less than one order of magnitude stronger than the XPGA, no *definite* conclusion can be drawn as yet regarding the role played by the PGA alone in driving the adjustment process

¹The expression midaltitude radial convergence (MARC) is a radar meteorology jargon, and refers to sector where the rear-to-front flow encounters the active region with strong updrafts, enhancing convergence. It is well defined in Fig. 5.11c by the sector dominated by converge within $z = 2.0$ km and $z = 6.5$ km.

between vertical and horizontal wind fields in experiments WVEL and UVVEL. It is necessary to examine how winds respond to the PGA shortly after the restart time in both runs in order to have a more clear view of this process; but before conducting such analysis, it is desirable to study the relative importance of other atmospheric fields on dynamic adjustment in experiments WVEL and UVVEL.

5.3 Buoyancy effects

Because the buoyancy field B is an important forcing term in the vertical equation of motion, one should expect B (which is not perturbed at restart) would contribute to the restoration of vertical motion in WVEL and work against the weakening of updrafts in UVVEL. Figure 5.15 shows, for experiments WVEL and UVVEL, 8 s after restart, the B field alone and the acceleration due to the vertical pressure gradient and B combined (A_{pqB}), i.e:

$$A_{pqB} = -\frac{1}{\bar{\rho}} \frac{\partial \bar{p}'}{\partial z} + B \quad (5.7)$$

where B is given by:

$$B = g \left[\frac{\theta'}{\bar{\theta}} - \frac{\bar{p}'}{\bar{p}} + \frac{q'_k}{\varepsilon + q_v} - \frac{q'_k + q'_{li}}{1 + q_v} \right] \quad (5.8)$$

In (5.8), ε is the ratio of the specific heats at constant pressure and volume, q_k is the water vapor mixing ratio, ε is the ratio of the gas constants for dry air and water vapor ($\varepsilon = 0.622$), and q_{li} is the total mixing ratio for ice and liquid water species (cloud water, rainwater, cloud ice, snow and hail). Primes (overbars) refer to perturbation (base-state) fields.

For both experiments WVEL and UVVEL, the acceleration due to B is not as strong as the VPGA — compare Figs. 5.15a and 5.15c with Figs. 5.14f and 5.14i.

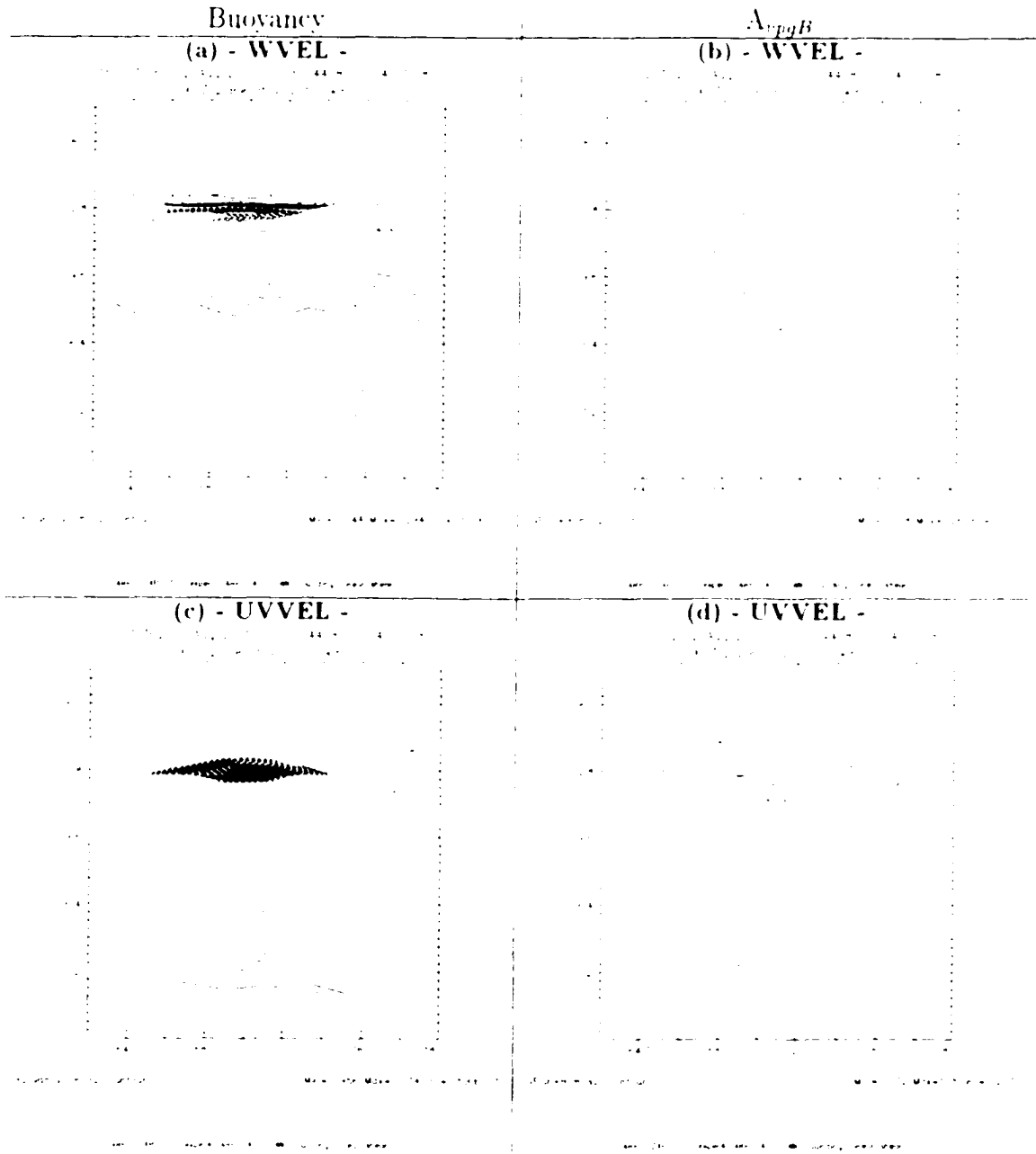


Figure 5.15: Cross sections of vertical acceleration due to buoyancy (first column), and due to vertical pressure gradient *and* buoyancy (second column) in m s^{-2} at $t = 400.08\text{-hr}$: (a),(b) WVEL, and (c),(d) UVVEL. Buoyancy field is contoured at 0.05 m s^{-2} intervals; A_{pgB} field is contoured at 0.2 m s^{-2} intervals. Solid (dashed) lines indicate positive (negative) values, with the zero line being suppressed. The domain shown is the same as in Figs. 5.11 and 5.13.

noting that the contour intervals are different ± 0.01 , and responds to the perturbation pressure field. This response becomes more clear if we compare B from experiments WVLE and UVLE with that of experiment CNTRL, depicted in Fig. 5.16. At 8 s in WVLE (Fig. 5.16a), the broad area of maximum positive B (around $z = 10$ km) is stronger than in CNTRL, and is located slightly higher in altitude than the CNTRL counterpart. The minimum in B close to the ground also is stronger and deeper in WVLE. These results are in agreement with the response in B (through Eq. 5.8) to the perturbation pressure field represented by the “low-over-high” pattern shown in Fig. 5.11b. Strong positive (negative) perturbations in pressure lead to negative (positive) perturbations in B .

An analogous behavior is found in experiment UVLE (Fig. 5.15c), where the maximum positive B (around $z = 5$ km) is stronger and expands further downward than the same feature in CNTRL. In addition, the negative values of B aloft are also stronger, and cover a deeper layer than in CNTRL.

In chapter 2 we studied the response of the pressure field to a buoyancy source (e.g., section 2.2), and in chapter 4 we indicated that the existence of a low- to mid-level mesolow just above the surface cold pool in CNTRL (e.g., Fig. 5.11a) is in good agreement with the presence of the mid-level buoyancy source shown in Fig. 5.16. We now have the situation of B responding to a strong pressure perturbation which is, in turn, induced by the three-dimensional mass divergence. This is physically reasonable because perturbations in pressure *can* lead to perturbations in density as indicated in Eq. (2.8), and, thus, in B (Eq. 5.8).

Although the vertical acceleration associated with B is smaller than VPGA alone early in experiment WVLE, its contribution is discernible. The region of stronger positive B in Fig. 5.15a (around $z = 9.6$ km) coincides with the sector of positive VPGA shown in Fig. 5.14f. When combining both (Fig. 5.15b) the vertical accel-

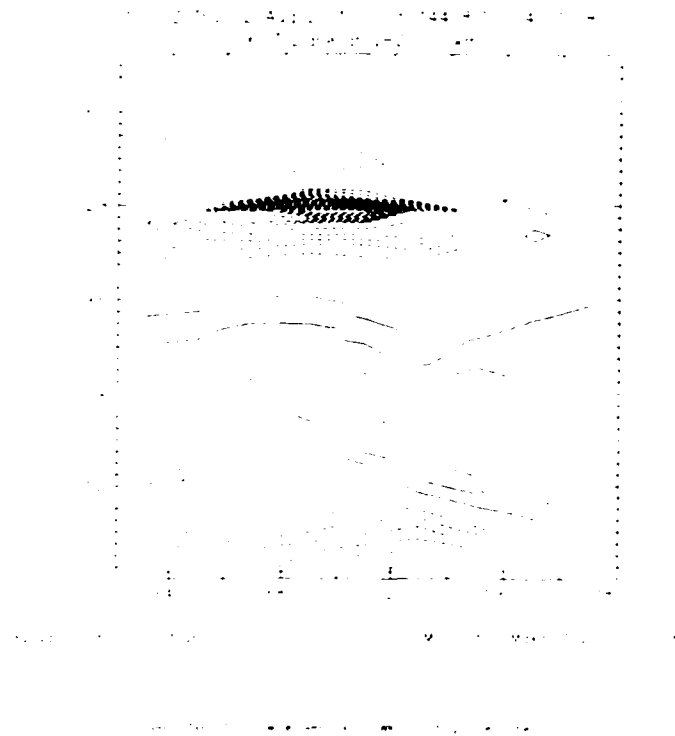


Figure 5.16: As in Figs 5.15a-c, but for CNTRL.

ation A_{pqB} becomes slightly stronger (compare Figs. 5.14f and 5.15b), contributing even more to the restoration of the main updraft. Furthermore, the magnitude of A_{pqB} in the region just below $z = 9.6$ km is *one order of magnitude higher than the corresponding XPGA* (Fig. 5.14d).

It is also important to note that A_{pqB} is positive in a narrow region at the low-levels of the simulated bow echo, just above the gust front ($x = 176.0$ km; lower-right corner of Fig. 5.15b). This favors the restoration of low-level updrafts, which are associated with the mechanism of continuous regeneration of new cells along the gust front. As discussed in chapter 3, this is a relevant mechanism for the maintenance of a long-lived MCS. Despite the fact that the XPGA works *against* the surface convergence in this region ($x = 174$ km in Fig. 5.14d), A_{pqB} tends to dominate, and low-level updrafts are rapidly restored. Similar results also are found for other regions

of the simulated bow echo along the gust front (not shown). Thus, it becomes even more evident that in experiment WVLE, the vertical motion field tends to be restored more rapidly than the horizontal wind field is weakened.

B field also should favor somewhat the maintenance of vertical motion in experiment UVLE. However, the contribution from B to the vertical acceleration early in UVLE is less discernible than in WVLE, especially for mid-level updrafts. By comparing Fig. 5.15d for A_{pqB} and Fig. 5.14h for VPGA, we note that the inclusion of B does not change significantly the magnitude of downward vertical acceleration for the main updraft region, around $z = 9$ km⁵. This is because the level of maximum negative VPGA ($z = 9.6$ km in Fig. 5.14h) coincides with a minimum in magnitude for B (Fig. 5.15c), thus reducing the contribution of B to A_{pqB} at that level. In this case, the phase-offset in the distribution of B with respect to the VPGA does not contribute to a discernible reduction of the downward acceleration found in UVLE.

For low-level updrafts (lower-right corner of Figs. 5.15c,d), B is positive but reduces the downward acceleration only slightly (compare lower-right corners of Figs. 5.15d and 5.14h). Consequently, A_{pqB} remains stronger than the ZPGA — which works toward restoring surface convergence along the gust front: $(x, z = 174.0, 0.0)$ km in Fig. 5.14g — with negative implications for the simulation of the bow echo.

Therefore, early in experiments WVLE and UVLE the inclusion of B in the analysis does not change significantly the acceleration patterns investigated for pressure gradients alone.

5.4 Analysis of advection terms in the pressure equation

The interpretation thus far of the pressure response to the withdrawal of kinematic

⁵Contrast, for example, the number of contour levels in Fig. 5.15d against Fig. 5.14h on the main updraft region around $z = 9$ km; the number of contours is not changed.

fields has been based on an analysis of the divergence term of the prognostic pressure equation. We now examine the remaining terms, namely, the advection of base-state pressure ($\bar{\rho}q\bar{w}$) and advection of perturbation pressure ($-\bar{\mathbf{V}}^T \cdot \nabla p'$).

Based on the solution from CNTRL, it was shown earlier that the advection terms in the pressure equation are smaller than the divergence, especially $-\bar{\mathbf{V}}^T \cdot \nabla p'$ (Fig. 5.8). Do these terms play any significant role on dynamic adjustment in experiments WVFL and UVVFL? Figure 5.17 shows vertical cross sections of the forcing terms for the pressure tendency ($\partial p' / \partial t$) at 4-hr for WVFL and UVVFL in the gust front region analyzed above. The analysis of these fields allows us to examine the relative contribution of each term to the forcing of the pressure field when starting experiments WVFL and UVVFL. As depicted in Figs. 5.17c,f, divergence is clearly the dominating mechanism at restart (note that the contour intervals are distinct for each term; see caption of Fig. 5.17). Because the perturbation pressure field at 4-hr is exactly the same as in CNTRL, again we find that the contribution from $-\bar{\mathbf{V}}^T \cdot \nabla p'$ is practically negligible (Figs. 5.17b,e).

Naturally, the initial forcing from $\bar{\rho}q\bar{w}$ is zero in WVFL, which means that the “low-over-high” pattern found for WVFL immediately after restart (Fig. 5.11b) is almost entirely induced by the divergence forcing (Fig. 5.17c). For UVVFL, however, $\bar{\rho}q\bar{w}$ is not negligible (Fig. 5.17d). In regions where the divergence term contributes most significantly to $\partial p' / \partial t$ — such as the upshear-tilted updraft, with negative values of $\partial p' / \partial t$ in the low- to mid-levels (Fig. 5.17f) — the impact of $\bar{\rho}q\bar{w}$ is less evident, mostly because divergence tends to dominate quite significantly. However, around $z = 9.6$ km, the divergence term has a local minimum in magnitude (Fig. 5.17f). Therefore, the contribution from $\bar{\rho}q\bar{w}$, which is positive at this level (Fig. 5.17d), is more discernible. When we combine the divergence term and $\bar{\rho}q\bar{w}$, the positive pressure tendency from mid- to upper-levels becomes slightly stronger (Fig. 5.17g).

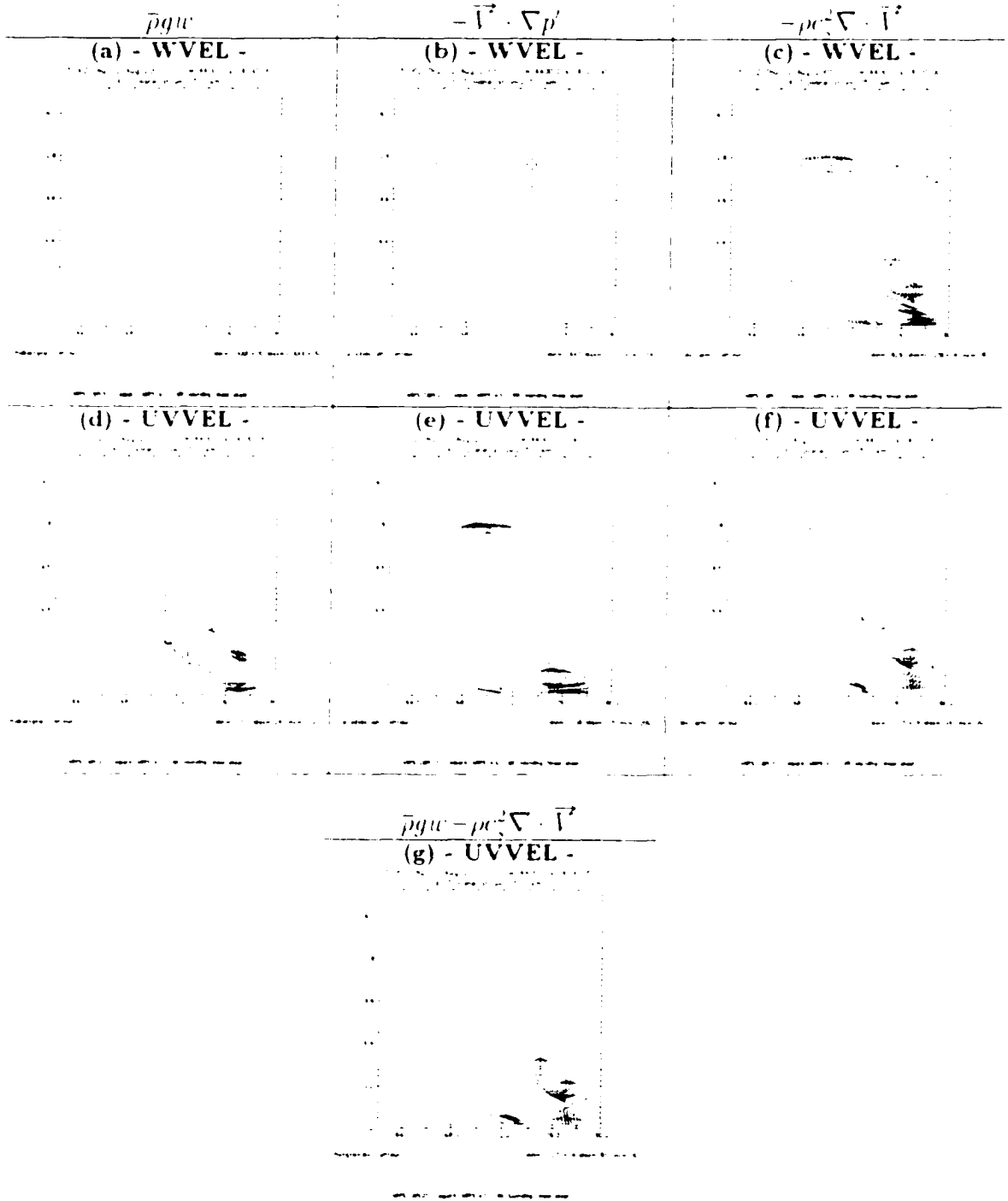


Figure 5.17: Terms of the prognostic pressure equation (Eq. 5.5) at $t = 4:00:00$ -hr (restart time) for: (a)-(c) WVEL; and, (d)-(g) UVVEL. (a),(d): term I (vertical advection of base-state pressure), contoured at 10.0 Pa s^{-1} intervals; (b),(e): term 2 (advection of perturbation pressure), at 0.2 Pa s^{-1} intervals; (c),(f): term III (divergence term), at 100.0 Pa s^{-1} intervals. (g): term I plus term III for UVVEL, at 100.0 Pa s^{-1} intervals. Solid (dashed) lines represent positive (negative) values. Zero lines are suppressed. The xz-domain shown is the same as in Figs. 5.11 and 5.13.

and represents the main forcing for the artificially high pressure perturbation evident in Fig. 5.13b.

As the integration proceeds, divergence remains the most important forcing for the prognostic pressure equation for both experiments WVEL and UVVEL, as depicted in Figure 5.18 which compares the magnitude of the forcing terms 8 s after the restart time. Figs. 5.18c,f show that the divergence forcing has smaller magnitude than at restart (for convenience, the contour interval for the divergence term was changed from 100 Pa s^{-1} in Fig. 5.17, to 25 Pa s^{-1} in Fig. 5.18), but is still the dominant term, with advection (Figs. 5.17a,b,d,e) playing a secondary role. This is particularly true for $-\bar{\mathbf{V}}^2 \cdot \nabla p'$, which remains one order of magnitude smaller than divergence despite the strong pressure perturbations. Therefore, the induced pressure perturbations induced shortly after restart do not change the relative importance of the forcing terms in the prognostic pressure equation.

The reason why the divergence term becomes weaker at $t = 400.08\text{-hr}$ (when compared to its magnitude at 4-hr) is because the 3D divergence at this time contains a contribution from all three components of the wind (i.e., $\nabla_H \cdot \bar{\mathbf{V}}^2$ and $\partial w / \partial z$). When combined, the three components of the wind reduce the magnitude of total divergence compared to the “incomplete” field at 4-hr. Not only does the divergence forcing become *relatively* weak, but also changes sign (for example, contrast Figs. 5.17c and 5.18c). The reason for such behavior becomes more clear in the following section.

5.5 Response of the wind field shortly after restart time

Now that the important fields contributing to dynamic adjustment in experiments WVEL and UVVEL have been identified, it is appropriate to analyze the explicit adjustment of the winds to the withdrawal of kinematic fields in those simulations.

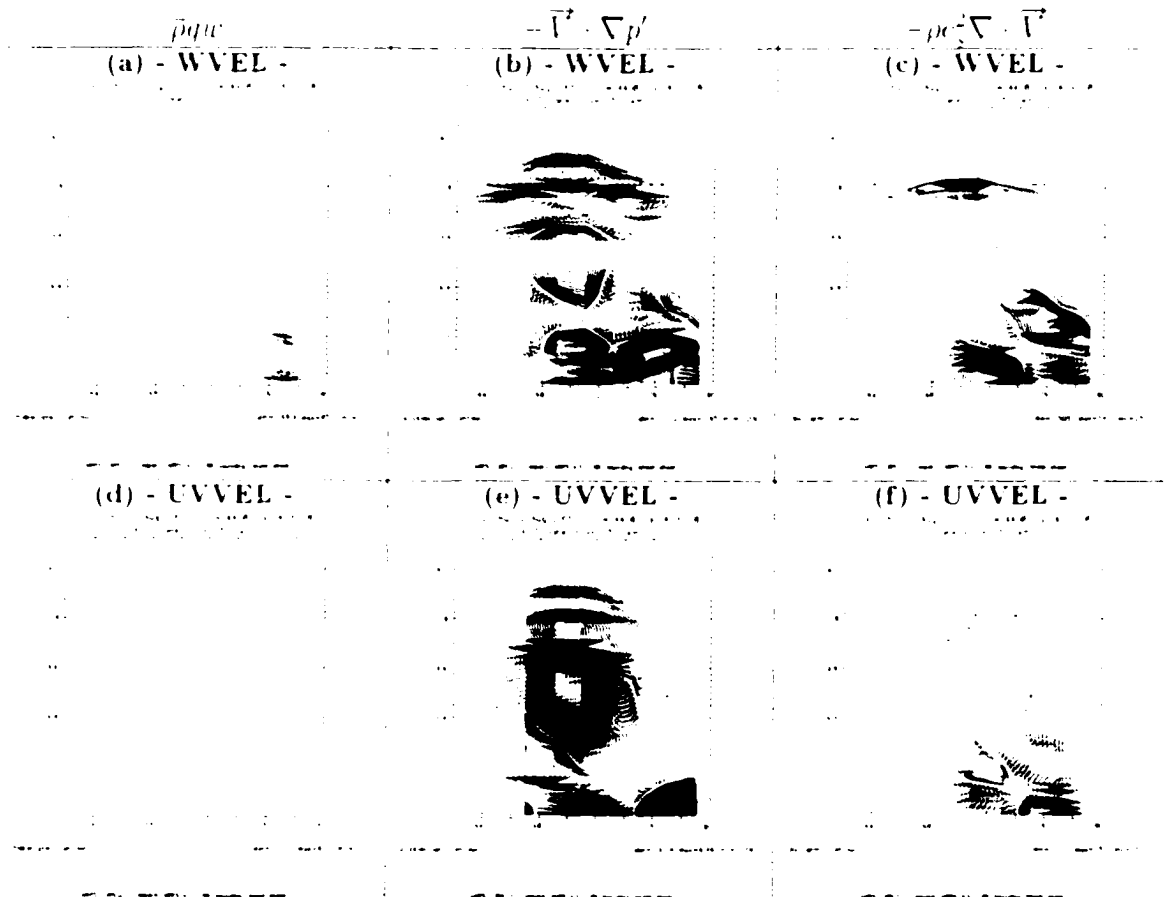


Figure 5.18. Terms of the prognostic pressure equation (Eq. 5.5) at $t = 4.00:08$ -hr for WVEL (first row) UVVEL (second row). First column: term I (vertical advection of base-state pressure), contoured at 10.0 Pa s^{-1} intervals; second column: term 2 (advection of perturbation pressure), at 0.2 Pa s^{-1} intervals; third column: term III (divergence term), at 100.0 Pa s^{-1} intervals. Solid (dashed) lines represent positive (negative) values. Zero lines are suppressed. The xz -domain shown is the same as in Figs. 5.11 and 5.13.

We focus on the response at $t = 4:00:08$ -hr -- again, not because this is a particularly “special” time, but because it refers to the first history file available for the withdrawal runs, which is *representative* of the response immediately after restart time.

Figure 5.19 compares the horizontal ($\nabla_H \cdot \vec{V}$) and vertical ($\partial w / \partial z$) components of velocity divergence at $t = 4:00:08$ hr for experiments CNTRL, WVLE and UVVLE. These fields are used to assess the early response of the horizontal and vertical velocities, respectively.

In WVLE, $\nabla_H \cdot \vec{V}$ (Fig. 5.19c) is associated with the horizontal wind component which is *weakened* by the XPGA (shown in Fig. 5.14d), while $\partial w / \partial z$ (Fig. 5.19d) is associated with the vertical motion field *restored* by the A_{pqB} (shown in Fig. 5.15b). Note that after only 8 s, the $\partial w / \partial z$ field in WVLE already shows a structure that is very similar to that in CNTRL. Below $z = 3.2$ km, the magnitude of $\partial w / \partial z$ is the *same* as in CNTRL, while aloft, above $z = 9.6$ km, this field has been restored to approximately 70% of its CNTRL counterpart, indicating an efficient regeneration of the vertical motion in these sectors. A region where $\partial w / \partial z$ is *not* restored as efficiently, is in the MARC region between $z = 3.2$ km and $z = 6.4$ km, where the RIJ encounters the main updraft and descends. This is a sector where the XPGA is as strong as the A_{pqB} (compare Figs. 5.14d and 5.15b) and, thus, the weakening of the correct horizontal wind field is as evident as the restoration of the correct vertical velocity (Fig. 5.19c). However, overall, the restoration of $\partial w / \partial z$ is more efficient than the destruction of $\nabla_H \cdot \vec{V}$.

In UVVLE, $\nabla_H \cdot \vec{V}$ (Fig. 5.19e) is associated with the horizontal wind component which is *restored* by the XPGA (see Fig. 5.14g), while $\partial w / \partial z$ (Fig. 5.19f) is associated with the vertical motion field *destroyed* by the A_{pqB} (Fig. 5.15d). A different behavior from that found for WVLE is clear. First, the $\partial w / \partial z$ field (Fig. 5.19f) is much weaker than in CNTRL. On the other hand, *nowhere* is the $\nabla_H \cdot \vec{V}$ field

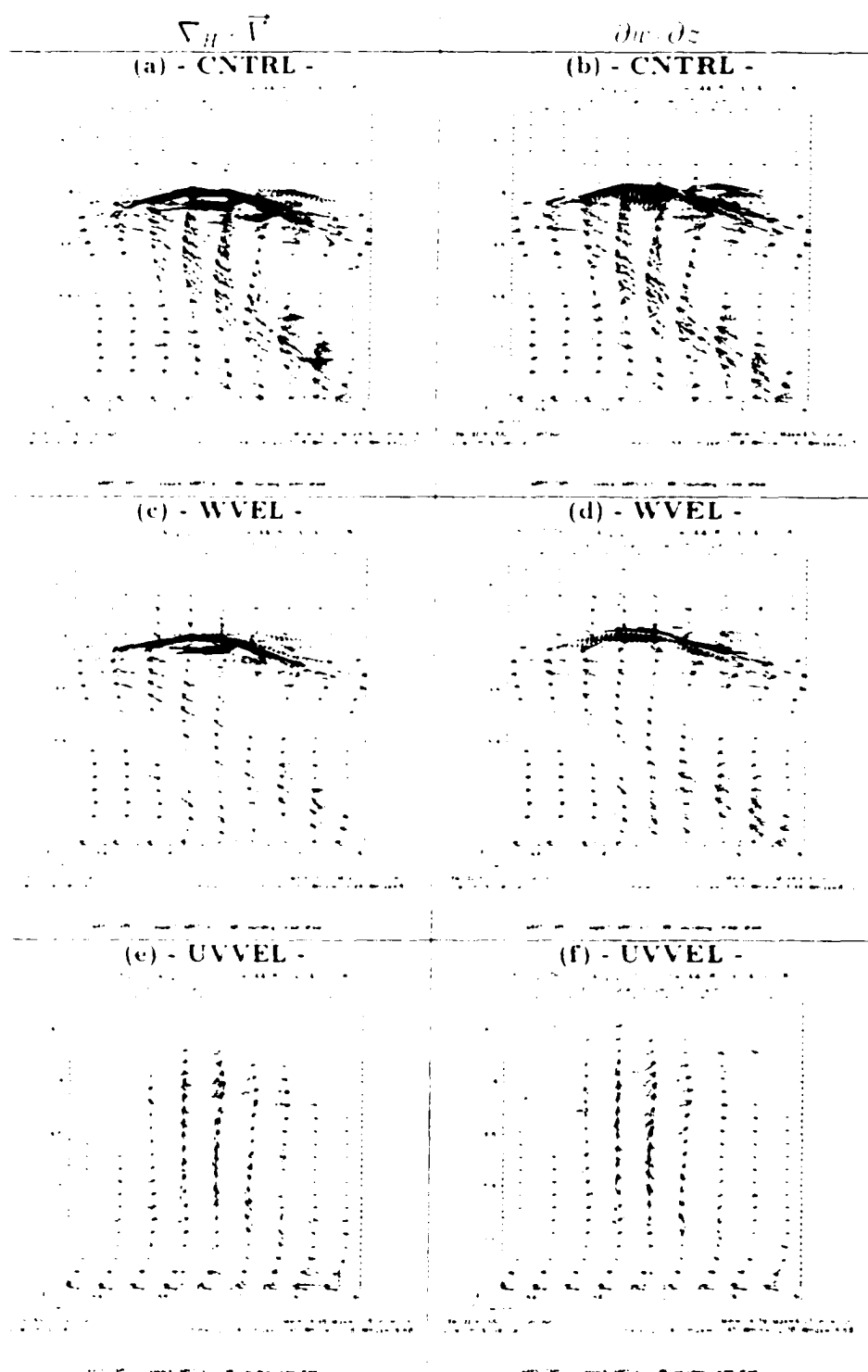


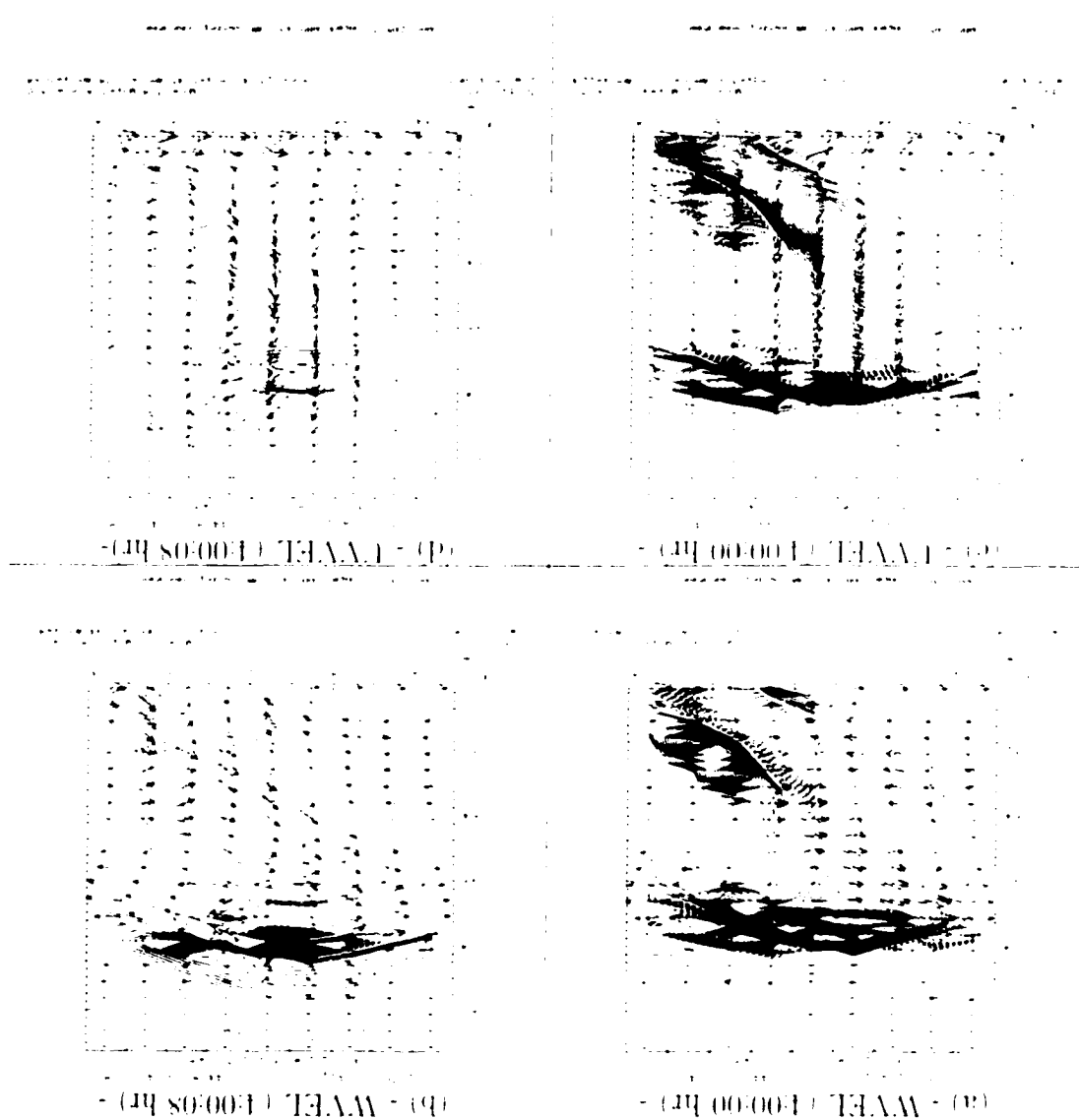
Figure 5.19: Vertical cross sections of horizontal ($\nabla_H \cdot \vec{V}$) and vertical ($\partial w / \partial z$) components of velocity divergence (contours) in 10^{-3} s^{-1} at $t = 100.98\text{-hr}$ for: (a),(b) CTRL; (c),(d) WVCL; (e),(f) UVCL. Contour interval is $1 \cdot 10^{-3} \text{ s}^{-1}$. Solid (dashed) lines indicate positive (negative) values, with zero line being suppressed. Storm-relative wind vectors are in m s^{-1} , with a reference vector of 10 m s^{-1} indicated on the lower-left corner of each panel. The xz-domain shown is the same as in Figs. 5.11 and 5.13.

(Fig. 5.19e) restored to its correct value in CNTRL at 4:00:08-hr. The sector where UVVEL has a better performance in restoring $\nabla_H \cdot \vec{V}$ is in the MARC region. This is where the XPGA is comparable (in magnitude) to the A_{vpqB} , and regeneration of the correct horizontal winds is more evident. Aloft, around and above $z = 9.6$ km the magnitude of the $\partial u / \partial z$ field is *substantially* reduced (Fig. 5.19f), while $\nabla_H \cdot \vec{V}$ (Fig. 5.19e) is restored to less than 40% of the corresponding value in CNTRL. This unsatisfactory response in experiment UVVEL occurs in a region where the A_{vpqB} is effectively one order of magnitude larger than the XPGA, accounting for such behavior. Similar results are found for distinct cross sections along the simulated MCS, not shown.

Figure 5.20 shows the change in the *D divergence* ($\nabla \cdot \vec{V}$) from $t = 4:00:00$ -hr to 4:00:08-hr for experiments WVEL and UVVEL. The $\nabla \cdot \vec{V}$ fields at restart in Figs. 5.20a and 5.20c correspond to the “incomplete” divergence fields in Figs. 5.11c and 5.13c for WVEL and UVVEL, respectively, and are repeated here for convenience (with different contour interval). Figure 5.20 reveals a decrease in magnitude in $\nabla \cdot \vec{V}$ from 4:00:00-hr to 4:00:08-hr which is associated with the recovery of the three components of the wind field, as discussed in the previous section.

Also evident in Fig. 5.20 is the sign change in the $\nabla \cdot \vec{V}$ field in most regions. For example, $\nabla \cdot \vec{V}$ changes from positive (negative) to negative (positive) at surface around $x = 172$ km in WVEL (UVVEL). Referring back to Fig. 5.19, we note that this is consequence of the mutual adjustment among vertical and horizontal wind fields. For instance, Fig. 5.19d reveals that the redevelopment of a descending RIJ in WVEL (around $x = 172$ km) favors the generation of a local $\partial u / \partial z$ field that is more negative than the corresponding $\nabla_H \cdot \vec{V}$ which is positive (Fig 5.19c), while in UVVEL the regeneration of positive $\nabla_H \cdot \vec{V}$ in the same region (Fig. 5.19e) offsets the initially negative divergence field. It is the response of the winds to the induced pressure field

Figure 5.20: Vertical cross sections of three-dimensional velocity divergence (contours) at 1 - 4:00:00 hr (first column) and 1 - 4:00:05 hr (second column) (a) WVEL, (c) (d) TAVEL. Contour interval is $0.5 \times 10^{-3} \text{ s}^{-1}$. Solid (dashed) lines indicate positive (negative) values, with zero lines being suppressed. Storm-relative wind vectors are in m s^{-1} , with a reference vector of 10 m s^{-1} indicated on the lower-left corner of each panel. The xz-domain shown is the same as in Figs. 5.11 and 5.13.



that accounts for the sign changes in $\nabla \cdot \vec{V}$, also evident in the divergence forcing term of the pressure equation mentioned previously.

It should be emphasized that the changes in sign in $\nabla \cdot \vec{V}$ are associated with the redevelopment of the 3D kinematic field as soon as the withdrawal runs are started and are evident in different cross sections along the simulated MCS (not shown), but do *not* represent an oscillatory regime — i.e., the abrupt sign change in the $\nabla \cdot \vec{V}$ field happens only once. This adjustment process is part of a non-linear feedback between pressure and divergence fields early in experiments WVVEL and UVVEL. In section 5.2 we discussed how the divergence field induces pressure perturbations, while now we analyzed how the response of the winds to the induced pressure field affects divergence. It is important to note that the new (and weaker) $\nabla \cdot \vec{V}$ field with inverted sign does affect in turn the pressure field, but is not strong enough to reverse or offset the vertical dipole in pressure induced by the original divergence forcing at restart time. It is the dynamic adjustment associated with the propagation of acoustic waves (and attenuation of their amplitudes) that eventually damps the strong pressure perturbations (chapter 6).

Based on the results presented in this and previous sections we indicate that *the vertical motion in experiment WVVEL is more efficiently restored than the horizontal wind field is weakened, while in experiment UVVEL, the vertical motion field is destroyed more rapidly than the correct horizontal velocities are regenerated. **This is because the induced vertical acceleration forced by pressure and buoyancy perturbations is effectively stronger than the corresponding horizontal acceleration.*** In addition, the strong pressure perturbations generated early in simulations UVVEL and WVVEL are short-lived, such that the HPGA associated with those perturbations is not retained for a sufficiently long time to allow the horizontal winds to fully respond to the pressure field. The strong VPGA also is short-lived,

but since its magnitude is stronger, the response from the vertical wind field is faster.

From acoustic adjustment perspective (Fiedler 2002), the results above are *equivalent* to saying that the vertical motion field responds to the specification of the horizontal wind field. Hence, when perfect information about the horizontal velocities is retained, the vertical motion is rapidly regenerated without major impact on the long-range simulation of the MCS, whereas when the convectively-generated horizontal winds are eliminated, the vertical motion field responds by rapidly weakening. Fiedler (2002) hypothesizes that this is the behavior expected for a low aspect ratio convective flow, suggesting that the convective circulation in our idealized numerically-simulated bow echo has an effective low aspect ratio. What is (are) the mechanism(s) controlling the aspect ratio of the flow? This topic is examined in the following section.

5.6 The aspect ratio of the convective flow and implications for dynamic adjustment

The results presented for the gust front region ($y = 205$ km) are representative of the convective structure along the entire leading edge of the simulated bow echo. On the other hand, to qualitatively examine the aspect ratio issue for the convectively active portion of the MCS, it is desirable to examine the flow configuration at other locations as well.

It was mentioned before that the main updraft along the gust front (e.g., Fig. 5.5) displays an aspect ratio around unity. Nevertheless, it is interesting that the upshear-tilted region of vertical motion, shown in Figure 5.5a, *apparently* displays a horizontal extent larger than it would have if it were completely upright. Does the vertical motion field in other sectors of the storm system show the same structure?

To address this question, two sectors of the MCS highlighted by rectangles in Figure 5.21a are studied at restart time for experiment CNTRL. Close up views of these two sectors are indicated in Figures 5.21b,c , which also show eight line segments across the simulated MCS where vertical cross sections are analyzed. In Figure 5.22, velocity vectors, vertical motion field and the vertical component of divergence ($\partial w / \partial z$) are plotted in vertical cross sections along all segments, in an 18 km x 18 km domain.

Cross sections 1 and 2 are, respectively, on the north and south flanks of the bow echo apex. The updrafts in these regions (Figs. 5.22a-d) are shallower than at the apex of the bow echo, especially in cross section 1 (Fig. 5.22a), and are significantly sheared. $\partial w / \partial z$ displays upshear-tilted orientation, with considerable horizontal extent (Figs. 5.22b and d). Recall that $\partial w / \partial z$ represents the main forcing for the perturbation pressure in experiment UVVEL at restart (i.e., when $\nabla_H \cdot \mathbf{V}^2$ is eliminated), except for the factor $-\rho c_s^2$. In experiment WVVEL, the forcing at restart is similar, but with reversed sign (i.e., $\partial w / \partial z$ is eliminated).

Cross sections 3, 4 and 5 refer to a short bow echo segment located further south (Fig. 5.21c). Cross sections 3 and 4 (Figs. 5.22e-h) reveal a similar structure to that discussed for $y = 205$ km, with low level updrafts being regenerated along the gust front, rapidly becoming sheared, and feeding a stronger vertical motion field at mid to high levels. In cross section 5 (Fig. 5.22i,j), the vertical motion is shallower and displays a more substantial upshear tilt. In all cases, two main vertical divergence patterns are evident (Figs. 5.22f,h,j): a region of positive $\partial w / \partial z$ in the lower portion of the main updraft, and a region of negative $\partial w / \partial z$ just above, extending to higher levels. These tilted patterns in $\partial w / \partial z$ have considerable horizontal extent, and are qualitatively similar to the ones discussed for cross sections 1 and 2, and also for the cross section originally studied (e.g., Fig. 5.19d).

Cross sections 6 and 8 (Figs. 5.22k,o) refer to sectors north and south from the

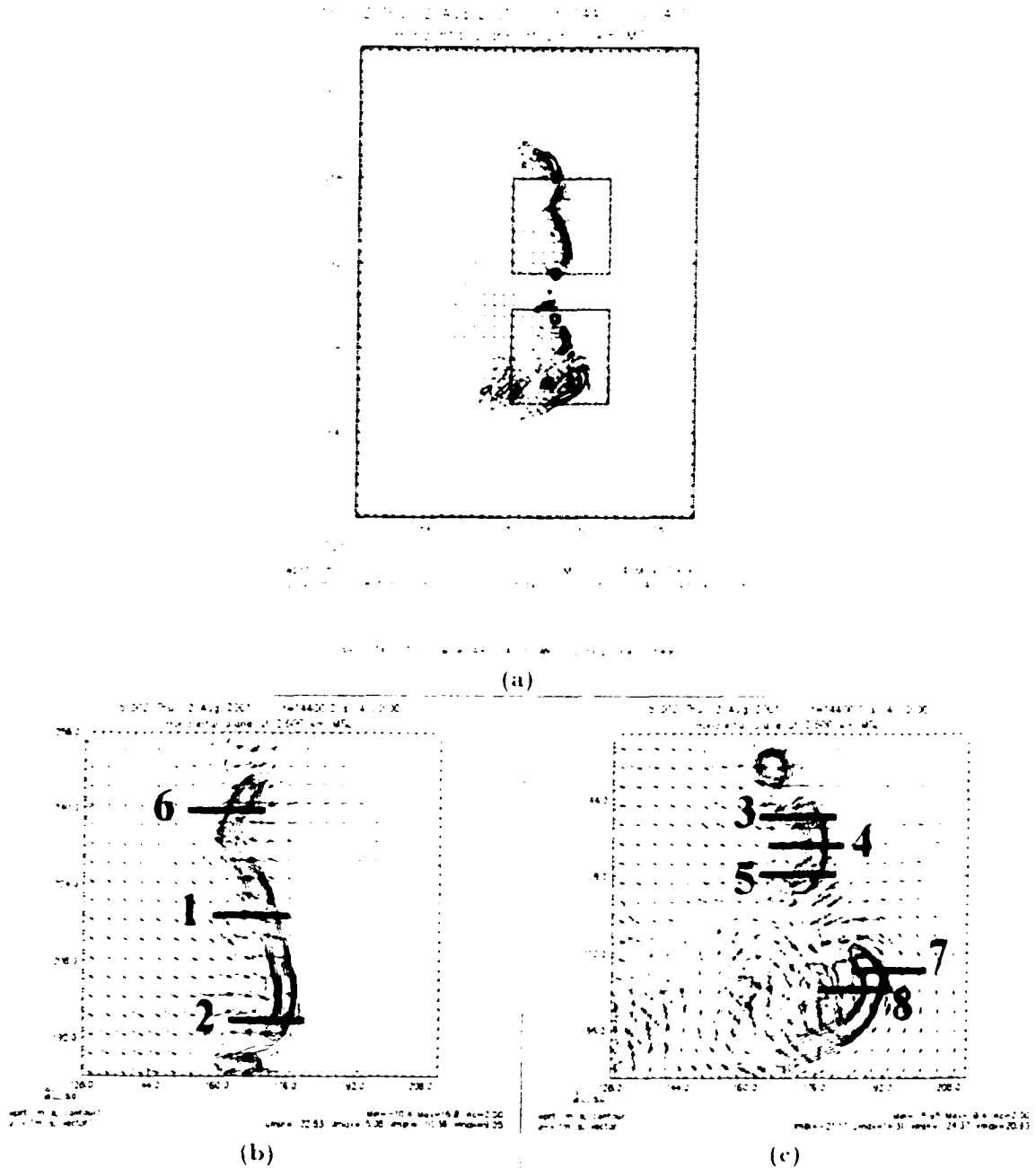


Figure 5.21: Storm-relative winds (vectors) and magnitude of vertical velocity (contours) at $z = 2600$ m and $t = 4:00:00$ hr for CNTRL. Vectors are in m s^{-1} , with a 10 m s^{-1} (5 m s^{-1}) reference vector indicated on the lower-left corner of (a) ((b) and (c)). Vertical motion is contoured at each 2 m s^{-1} , with solid (dashed) lines indicating updrafts (downdrafts). Zero lines are suppressed. (a) is just like Fig. 4.4a, but indicates (with rectangles) sectors where vertical cross sections are taken. (b) and (c) are close-up views for the northern and southern rectangle, respectively. Numbers label cross sections, and line segments indicate their zonal extent (all equal to 18 km): [1]: $y = 219$ km, $x = 158$ to 176 km; [2]: $y = 197$ km, $x = 162$ to 180 km; [3]: $y = 139$ km, $x = 162$ to 180 km; [4]: $y = 135$ km, $x = 164$ to 182 km; [5]: $y = 129$ km, $x = 162$ to 180 km; [6]: $y = 241$ km, $x = 152$ to 170 km; [7]: $y = 108$ km, $x = 184$ to 202 km; [8]: $y = 105$ km, $x = 176$ to 194 km.

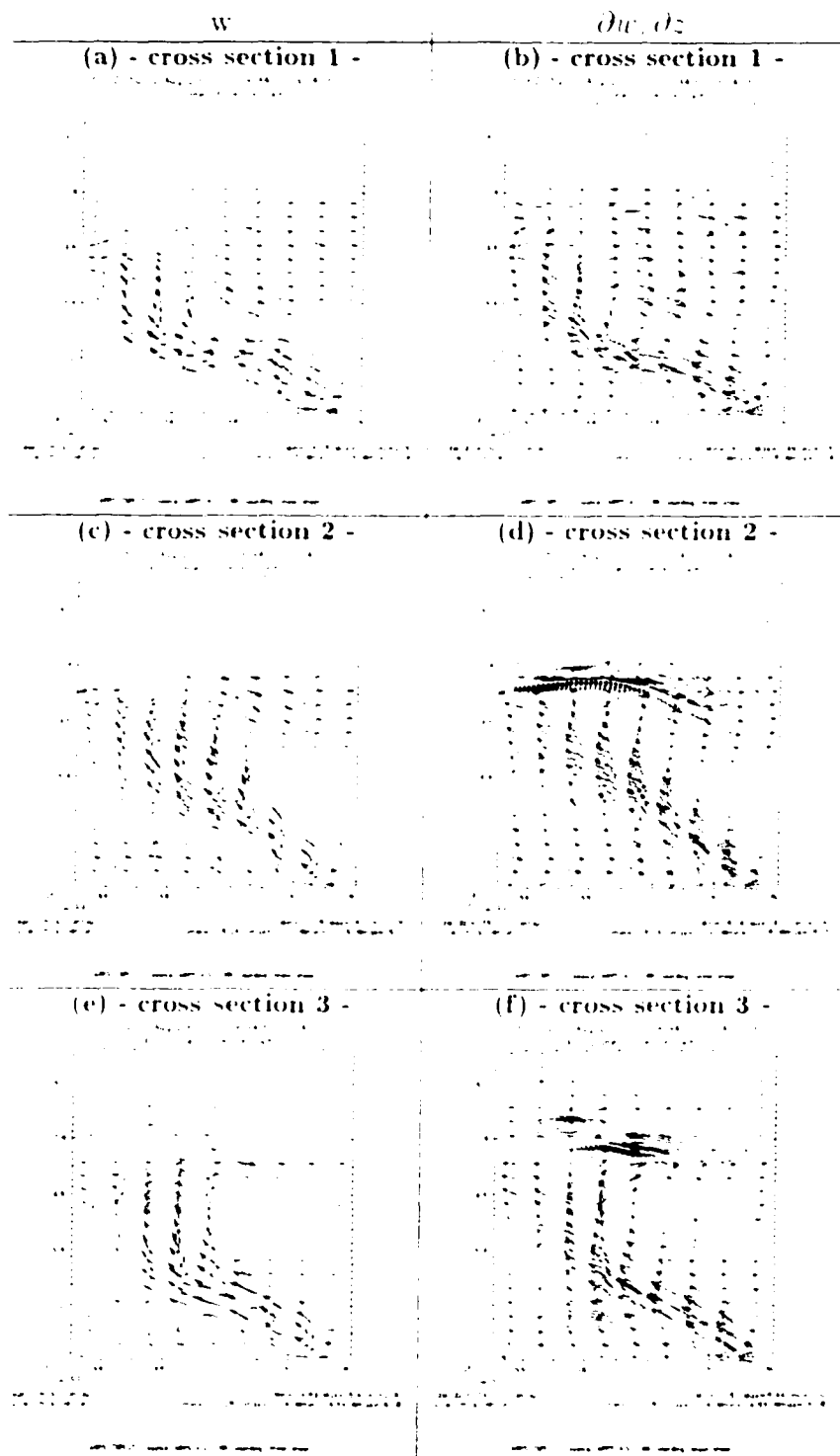


Figure 5.22: Vertical motion field (w) (contours: first column) and vertical component of divergence ($\partial w / \partial z$) (contours: second column) at $t = 4:00:00$ -hr for CNTRL for the vertical cross sections indicated in Figs. 5.21b,c. Solid (dashed) lines indicate positive (negative) values, with zero line being suppressed. Vectors depict the storm-relative wind field in the xz -plane, with a 10 m s^{-1} reference vector indicated on the lower-left corner of each panel. The domain size in all panels is $15 \text{ km} \times 15 \text{ km}$.

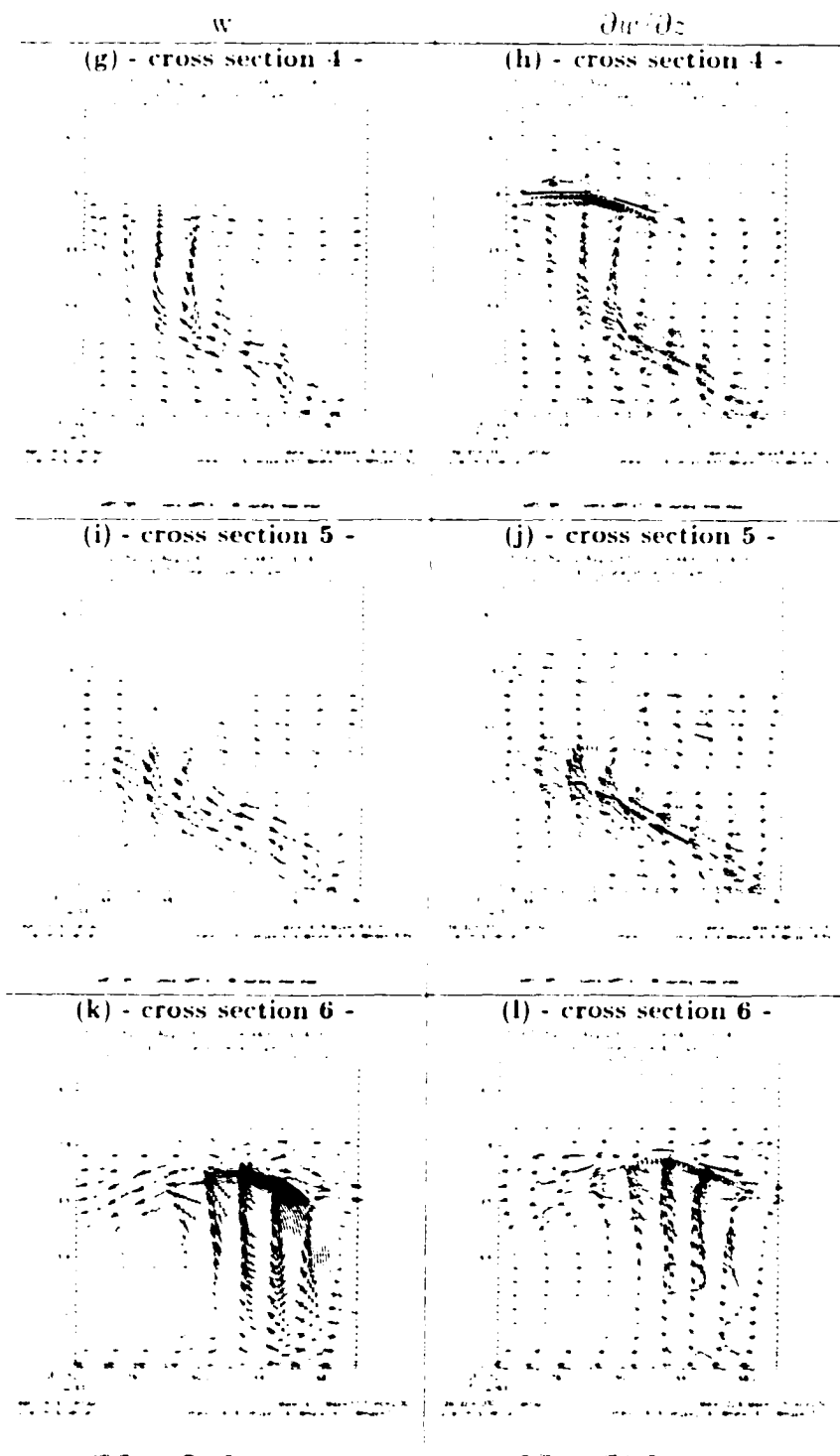


Figure 5.22 (continuation)

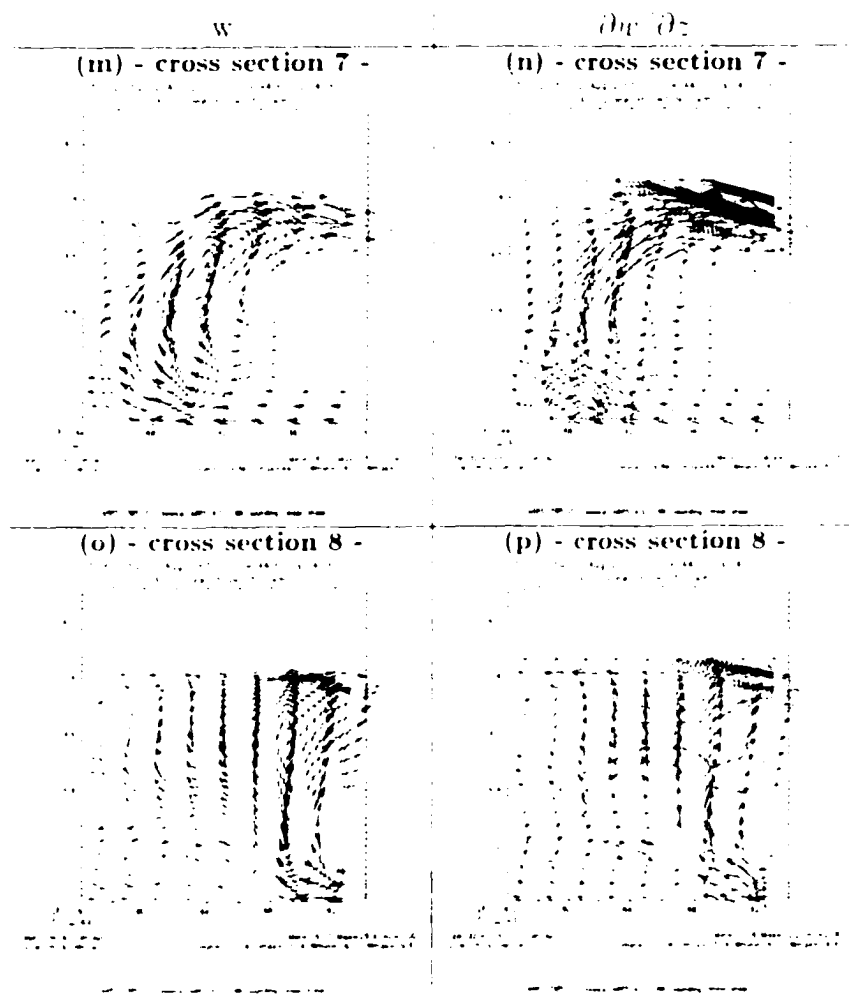


Figure 5.22 (continuation)

center of the domain, respectively, and reveal a more erect updraft. In cross section 6, the region of upward motion is relatively narrow from surface to upper levels (Fig. 5.22k), while in cross section 8 (Fig. 5.22o), the region dominated by updrafts is wider from mid to upper levels, above the relatively narrow surface-based updraft. Without a significant vertical inclination in the flow, the positive $\partial v / \partial z$ patterns in the first 3.2 km are more horizontally confined in cross sections 6 and 8 (Figs. 5.22l,p). However, aloft, where the region of upward motion displays larger horizontal extent, $\partial v / \partial z$ again displays oblate features.

Finally, cross section 7 (Fig. 5.22m) reveals a downshear tilted flow. While $\partial v / \partial z$ patterns at low levels do not show a significant horizontal extent, from mid to upper levels such patterns lean downshear, with increased horizontal orientation (Fig. 5.22n), thus lowering the aspect ratio of the divergence forcing.

Based on the discussion above, most of the convective flow associated with the bow echo segments in the center of the domain at 4-hr displays an upshear-tilted structure, with considerable horizontal extent (cross sections 4 to 5). Off the center of the domain (cross sections 6, 7 and 8), away from the strongest east-west surface outflow, regions where the vertical motion has a more upright orientation or leans downshear become more evident ⁹. In these locations, the horizontal extent of the divergence forcing at low-levels is more confined than in the upshear-tilted flows. However, aloft, such patterns acquire more horizontal orientation, either because of downshear leaning (cross section 8) or because the sector of anvil-level divergence — which efficiently spreads in the horizontal dimension — tends to dominate the structure of the flow (cross sections 6 and 7).

⁹ This specific behavior seems to agree with the RKW theory to explain the orientation of the vertical motion along the leading edge of long-lived MCSs (Rotunno et al. 1988; Weisman 1992, 1993). According to that theory, as the surface cold pool dynamics and outflow become stronger (which, in our case, is more evident at cross sections 4 to 5), the baroclinically-generated upshear-oriented horizontal circulation along the gust front tend to balance and then overwhelm the environmentally-induced downshear-oriented horizontal circulation, favoring upshear-tilted updrafts. Conversely, where the surface cold pool and outflow is not as strong, updrafts tend to be vertically erect or downshear tilted.

Thus, in general, divergence displays a predominantly horizontal orientation in the most active portion of our simulated bow echo. As a result, the divergence forcing ($-\rho c_s^2 \nabla \cdot \vec{V}$) for the pressure equation in experiments WVFL and UVFL at restart time *tends* to have a relatively low aspect ratio, or at least does not display a high aspect ratio. The expected impact on the response of the pressure field is schematically illustrated in Figure 5.23 in a xz-plane. For a divergence forcing with significant vertical extent (Fig. 5.23a), the response from the pressure perturbation field is also vertically oriented and more confined in the horizontal. Hence, isobars are horizontally concentrated and the induced XPGA tends to be stronger than the VPGA.

Conversely, for divergence forcing having a significant horizontal orientation (Fig. 5.23b), the response in the pressure field is more vertically confined and displays a lower aspect ratio, i.e., is “pancake-shaped”. In this case, the isobars are more horizontally separated and vertically concentrated, such that the corresponding VPGA tends to be stronger than the XPGA. This seems to be the predominant — although not exclusive — regime in our simulated bow echo. To illustrate, Figure 5.24 shows vertical cross sections of perturbation pressure, XPGA and VPGA for WVFL, 8 s after restart, for all sectors indicated in Figs. 5.21b,c⁷. In most sectors, the perturbation pressure field (first column in Fig. 5.24) has horizontal extent larger than the vertical, especially where the flow is clearly tilted by vertical wind shear (cross sections 1 to 5, and 7). Overall, the induced XPGA (second column in Fig. 5.24) is discernibly weaker than the VPGA (third column), even though the convective circulation does not display a clear-cut low aspect ratio. When combined with the B field (not shown), the vertical acceleration in WVFL for all cross sections studied becomes slightly stronger. The same analysis is valid based on results from UVFL.

⁷Recall that in WVFL the induced VPGA (XPGA) favors (works against) the restoration of the correct solution.

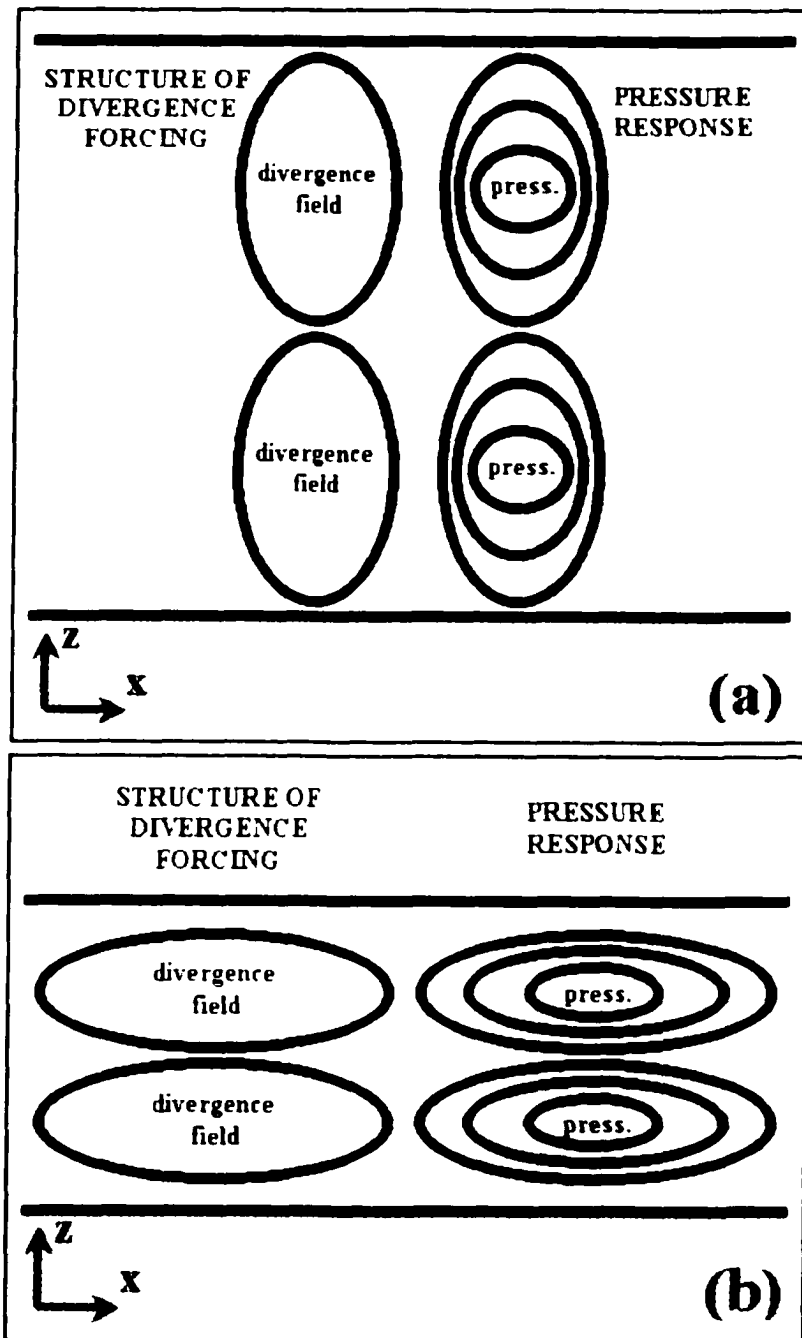


Figure 5.23: Idealized sketch in a xz -plane of the pressure response to an imposed divergence field, as governed by Eq.5.5 (prognostic pressure equation). In (a) the divergence forcing is vertically oriented, displaying a high aspect ratio. Accordingly, the pressure response is also vertically oriented. For this case the induced XPGA is stronger than the corresponding VPGA. In (b) the divergence forcing is oblate, with considerable horizontal orientation and low aspect ratio. The pressure response displays features that are also horizontally oriented, i.e., with considerable horizontal extent. In this case, the induced VPGA is stronger than XPGA.

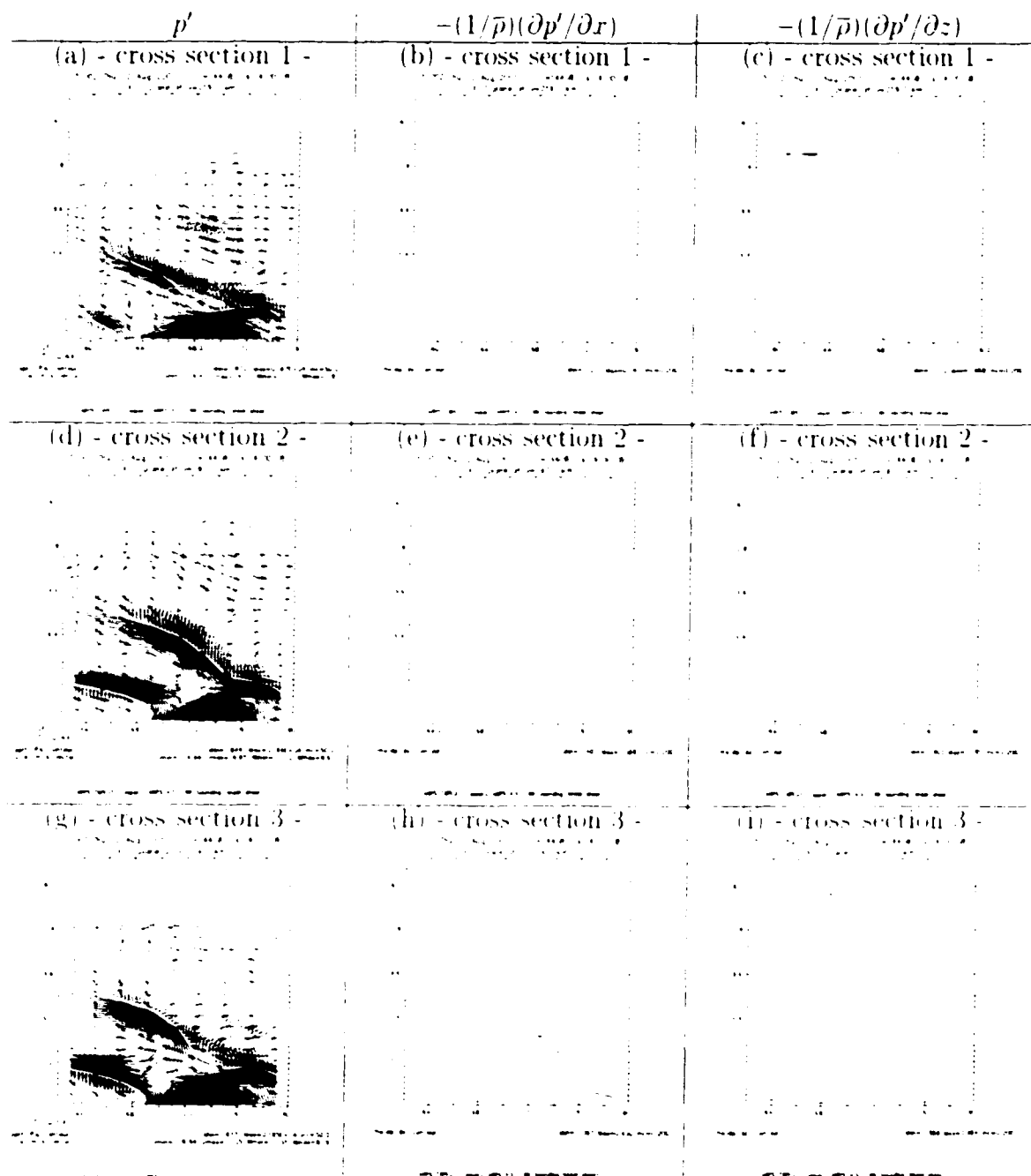


Figure 5.24: Vertical cross sections for storm-relative wind field and pressure perturbation (first column), XPGA (second column) and VPGA (third column) for WVFL at 8 s after restart time. The sectors shown correspond to the same eight vertical cross sections indicated in Fig. 5.22 (Figs. 5.21a,b indicate their position in the simulated MCS). In the first column, storm-relative wind vectors are shown in m s^{-1} , with a reference vector of 10 m s^{-1} indicated on the lower-left corner of the panel; perturbation pressure is contoured in Pa, at 50 Pa increments. Second and third columns display pressure gradient accelerations in 0.2 m s^{-2} contour intervals. In all panels, solid (dashed) lines refer to positive (negative) values, with zero lines being suppressed.

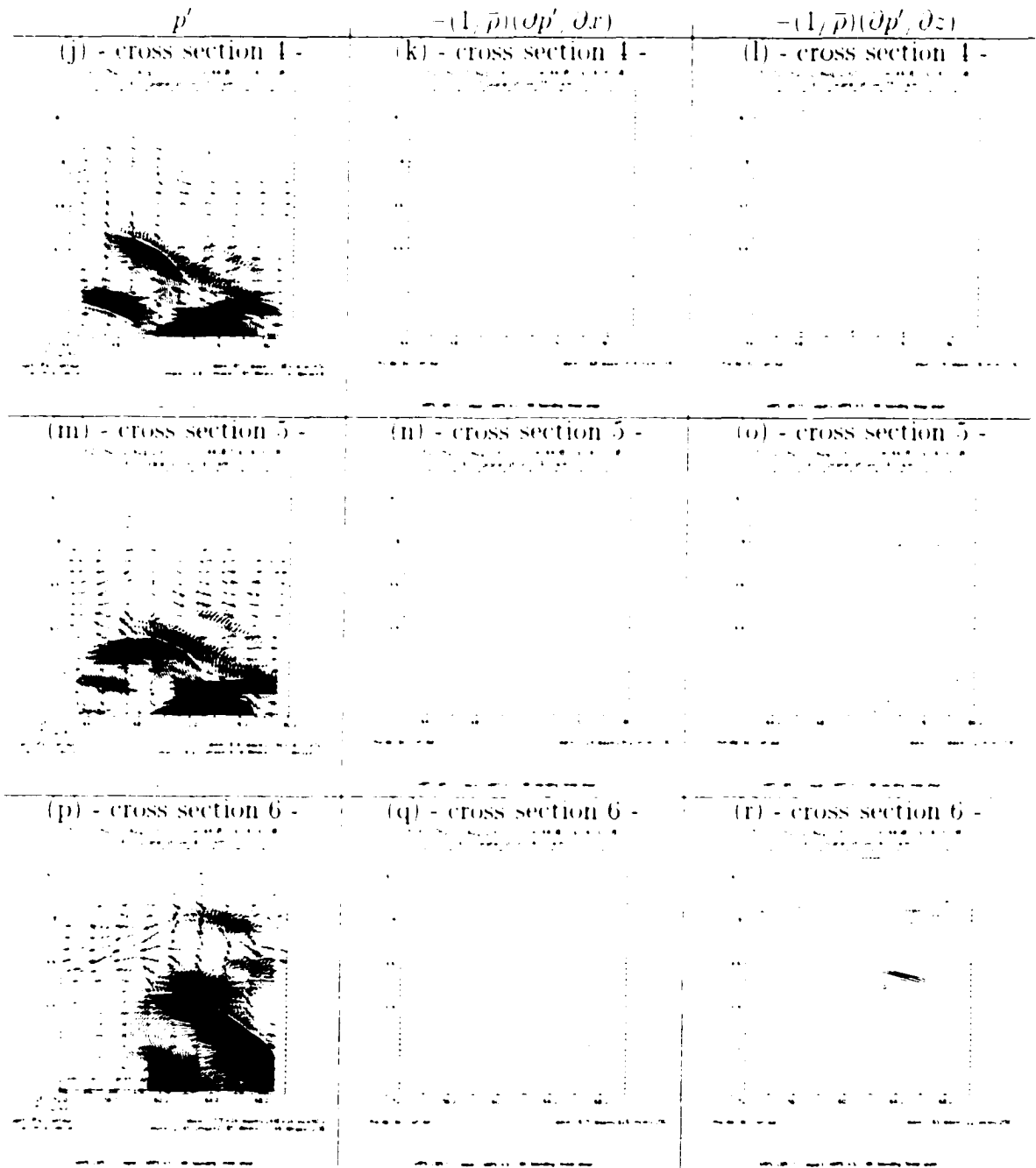


Figure 5.24 (continuation)

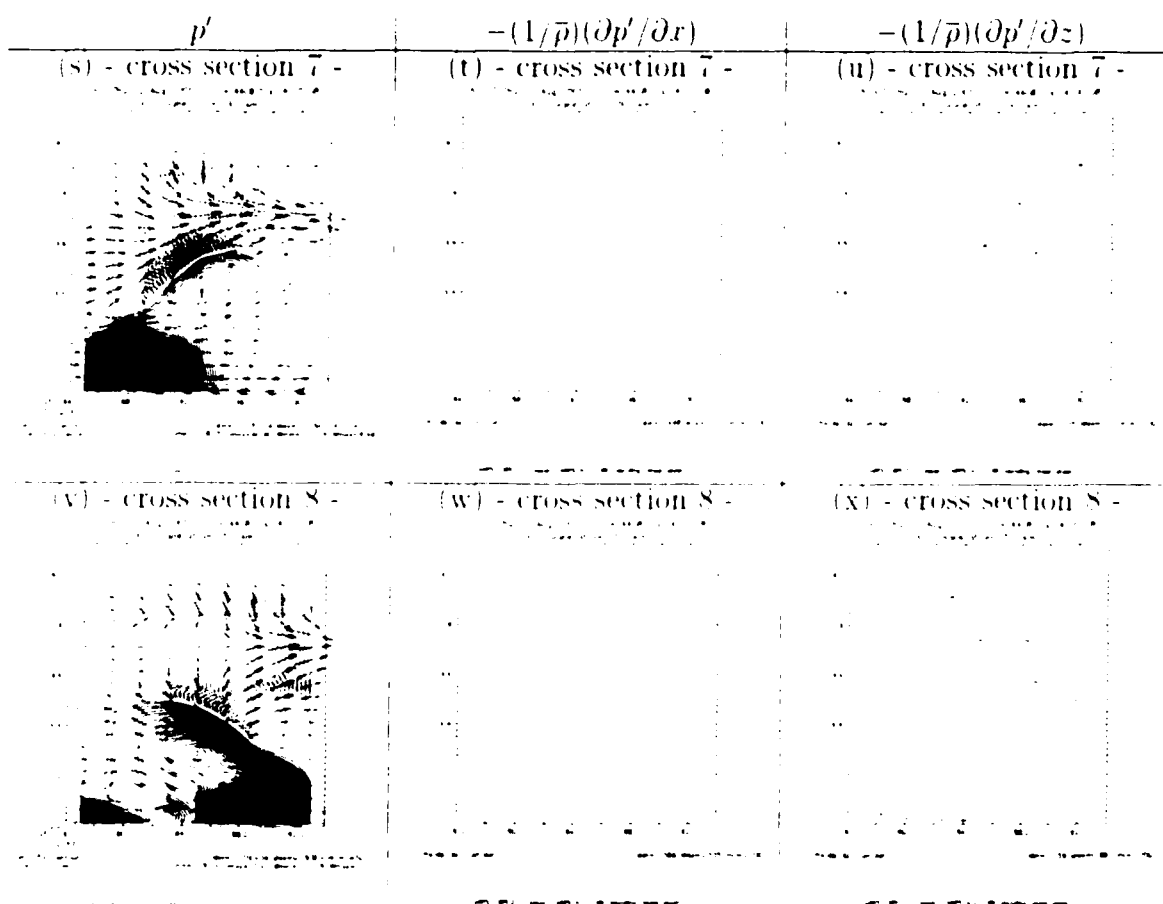


Figure 5.24 (continuation)

(not shown).

5.7 Summary and additional remarks

Based on the results from experiments WVFL and UVVFL, and considerations from acoustic adjustment (Fiedler 2002), *the convective flow in our numerical simulations appears to have an effective low aspect ratio, and the general analysis of the divergence forcing and the corresponding pressure response gives us a better insight of why this is the case.*

The analysis above is a different way of addressing acoustic adjustment. The response of the pressure field to the divergence forcing, and its implication of how the vertical and horizontal wind fields respond to each other, is a crucial physical component of the acoustic adjustment not explicitly explored until now.

It is relevant to note the similarity between the pressure response to divergence forcing in acoustic adjustment, and the response of the pressure field to buoyancy forcing in hydrostatic adjustment (discussed in chapter 2). However, an important difference between these two adjustment mechanisms — in addition to the clear distinction in forcing mechanisms — is that in hydrostatic adjustment, the induced VPGA [horizontal pressure gradient acceleration] always work against [favors] vertical motion. Whether the VPGA hampers or favors vertical motion in acoustic adjustment depends essentially upon the sign of the divergence forcing which, in turn, is dependent upon information contained in the wind field.

It is interesting that hydrostatic adjustment indicates that deep convective storms do behave as high aspect ratio systems in terms of buoyancy (e.g., Houze 1993, B95). Conversely, acoustic adjustment indicates that simulated convective systems can and do display low aspect ratio structure in terms of the divergence field. Thus,

the definition of an effective aspect ratio for a convective storm depends upon the adjustment mechanism being studied.

Our discussion also raised the question of the mechanisms that control the aspect ratio of deep convective storms in the perspective of acoustic adjustment. Our results *suggest* that the orientation of divergence and convergence patterns, influenced by vertical wind shear, plays some role in determining the effective aspect ratio of the flow within a convective system. On the other hand, even in the presence of vertical motion *not tilted* by vertical wind shear (e.g., cross sections 6 and 8), divergence patterns still display several oblate features, especially aloft, within the anvil-level flow. Thus, it is reasonable to expect horizontally-oriented divergence fields even when vertical wind shear does not efficiently tilt updrafts and downdrafts. Further work, spanning several environmental conditions for vertical wind shear, is necessary to address this question from the acoustic adjustment standpoint.

As an additional consideration about the possible influence of vertical wind shear in the results found for experiments WVEL and UVVEL, when the convective circulation is vertically sheared — by either environmental or convectively-generated wind — a larger portion of the momentum field (kinetic energy) is projected into the horizontal. A dramatic example of such structure is depicted in Figures 5.22a and 5.22b. Thus, under vertically-sheared convective environments, it is natural to expect the withdrawal of the perturbation horizontal winds (UVVEL) to remove a larger amount of information from the kinematic field than if the convective system were vertically erect. The withdrawal of vertical motion (WVEL), on the other hand, may have a greater impact for vertically unsheared convective flows, since the momentum field has a more significant vertical component. In this case, a more evident “signature” of the kinematic structure of the MCS is present in the vertical dimension. Future work exploring the mutual adjustment between horizontal and vertical wind fields in

convective storms should address the aspect ratio issue in a more quantitative way by defining aspect ratio in terms of measurable quantities.

In studying acoustic adjustment one *must* also recall that the analytical approach assumes a convective flow behaving as a sinusoidal pattern of vertical motion (e.g., Fig. 2.12), which is *not* necessarily the case in real storm systems. For example, isolated storms (and even squall lines, when observed along their cross-line dimension) represent a “discrete peak” in the vertical motion field. Moreover, the environmental response to thunderstorms often involves the generation of compensating subsidence that travels several tens of kilometers from the localized heating source (e.g., Bretherton and Smolarkiewicz 1989, Mapes 1993, Fovell 2002). Thus, even in the absence of vertical wind shear, other important processes may be present that tend to “lower” the effective aspect ratio of isolated convective systems from an acoustic adjustment standpoint (B. Fiedler, personal communication). These considerations point to some complicating factors when defining the true aspect ratio of the deep convective storms.

For now, the best assessment that we can make about the representativeness of our results is based on the work of Weygandt et al. (1999) and Sun and Crook (2001b) for a simulated supercell. They found similar results regarding the importance of the specification of the horizontal wind field. This indicates that our analysis of acoustic adjustment, via the prognostic pressure equation, should also be valid for other modes of convection.

Fiedler (2002) noted that high aspect ratio flows may be obtained in the simulation of convective storms with high resolution. However, the degree with which the aspect ratio of the flow changes with grid spacing (within the stormscale) is not entirely clear. In recent work, Bryan and Fritsch (2002) examined the sensitivity of a numerically-simulated squall line to different horizontal and vertical resolutions. Among other

important findings, they showed that when very high resolution was used — horizontal and vertical grid spacings of 125 m — the flow became more upshear-tilted. Thus, *an increase in model resolution does not necessarily lead to simulated convective storms with high aspect ratio*. As grid spacing is decreased, a larger spectrum of turbulent eddies becomes explicitly resolved instead of parameterized by the sub-grid turbulence parameterization schemes. This is one important process that effectively changes the behavior of stormscale structures in simulated convective systems (Droegemeier and Wilhelmson 1987, Adlerman and Droegemeier 2002, Bryan and Fritsch 2002).

The vertical and horizontal grid spacings employed in our simulations (see Table 1.2) is sufficiently fine to capture convective-scale processes within a bow echo. We do not imply that the grid spacing used here is ideal (Bryan and Fritsch 2002), but our choice of model resolution turns out to be a *convenient* one for addressing issues associated with model initialization.

Chapter 6

“Transient Evolution” in Experiments WVEL and UVVEL from a Wave Propagation Standpoint

The vertical dipole in perturbation pressure discussed previously in experiments WVEL and UVVEL (Figs. 5.11b and 5.13b) is part of the “transient evolution” in dynamic adjustment induced by withdrawal of kinematic fields. Here the expression *transient evolution* is used within quotes because no final steady-state solution exists in our simulations that allows us to discriminate clearly between the response of a convective storm to the impulsive withdrawal of fields and its natural evolution. Thus, the term *transient evolution* denotes that part of the numerical solution evolution that is dominated by large amplitude spurious *waves*.¹

In chapter 5 we examined the adjustment process in experiments WVEL and UVVEL without making any explicit reference to wave propagation. In describing acoustic adjustment, Fiedler (2002) indicated that high frequency sound waves are

¹Large time tendencies early in the withdrawal runs can also be used to characterize the transient evolution

triggered owing to a perturbation in the wind field that deviates from the relation imposed by mass continuity (section 2.4). Hence, one should expect sound waves to be excited in WVFL and UVVFL, and we examine their evolution here.

Figures 6.1 and 6.2 depict the time evolution at 4-min intervals of the perturbation pressure difference field, with respect to CNTRL, at $z = 200$ m in the first 10-min for experiments WVFL and UVVFL (i.e., WVFL minus CNTRL; UVVFL minus CNTRL). The contour interval is the same in all panels and equal to 20 Pa.

The most striking feature in Figs. 6.1 and 6.2 is the pressure front propagating at the speed of sound (346 m s^{-1} at $z = 200$ m), indicating the “transient evolution” for acoustic adjustment (Fiedler 2002). This pressure front does not characterize a *true* shock wave, though. Shock waves, as in an explosion, are accompanied by significant change in entropy and velocity, and are associated with pressure disturbances propagating at supersonic speeds (Liepman and Roshko 1957, Granger 1995, Kundu and Cohen 2001)². Such is not the case in our simulations.

Figures 6.3 and 6.4 show time series of perturbation pressure, perturbation potential temperature and the zonal wind component at grid-point $(x, y, z) = (140.0, 204.0, 0.2)$ km, just upstream of the main bow echo segment at 4-hr (see Fig. 4.6a). No sharp variation in potential temperature accompanies the pressure perturbations (Fig. 6.3), as would be expected if such disturbances were representative of shock waves propagating through the selected region. The wind field, on the other hand, *does* respond to the pressure perturbations in the first 5-min of integration (Fig. 6.4), but with very weak amplitude — note that velocity ordinates in Figs. 6.4a-b cover a 2 m s^{-1} range only. Although the pressure perturbation reaches extremely high values (up to 5000 Pa in a few locations) *immediately after restart* in both experiments, it

²Here we employ the expression *shock wave* as referring to *strong* shock waves. *Weak* shock waves are also possible, for which the propagation speed is nearly equal to the speed of sound, and variations in entropy and velocity across the wave front are very small (Liepman and Roshko 1957, Kundu and Cohen 2001).

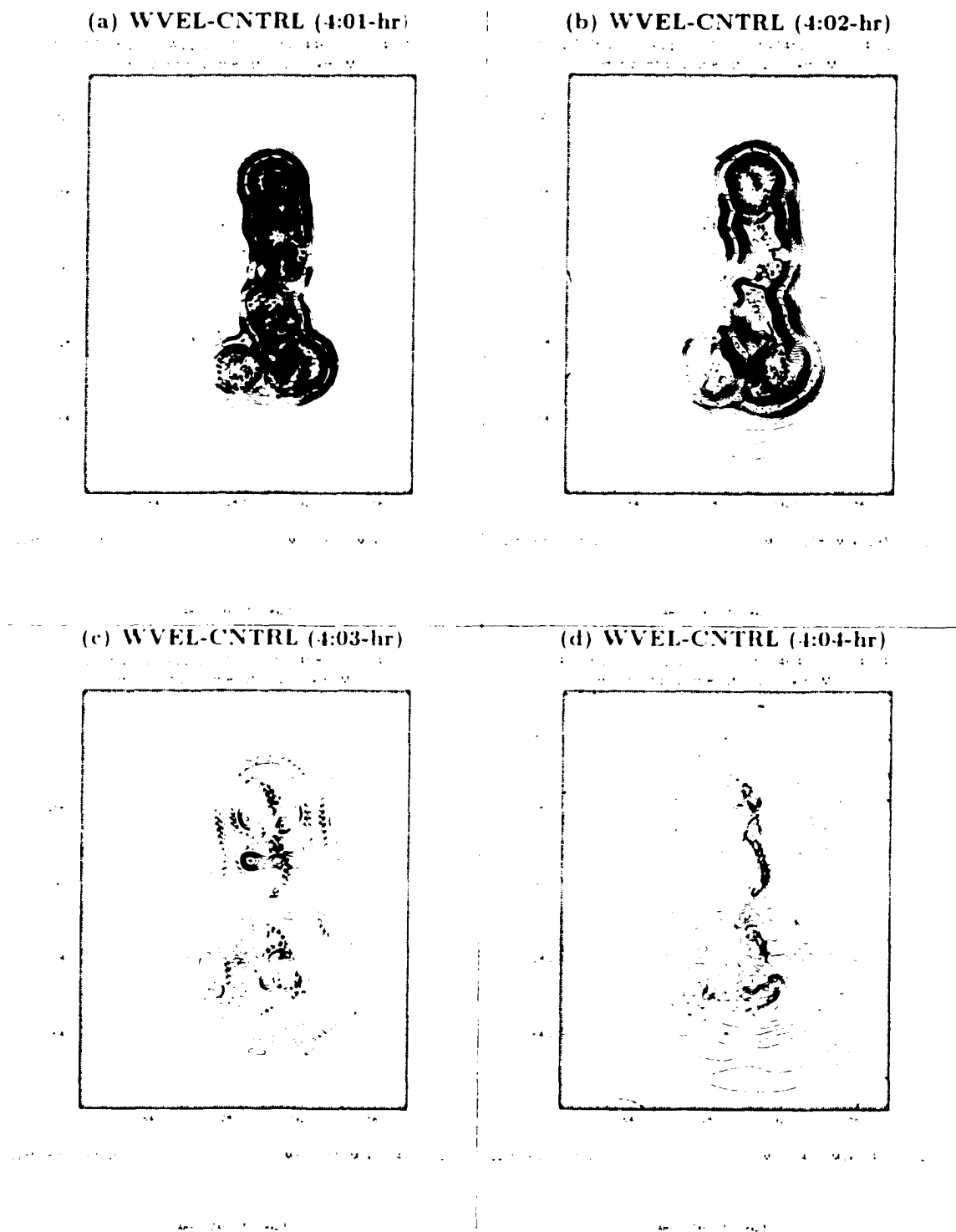
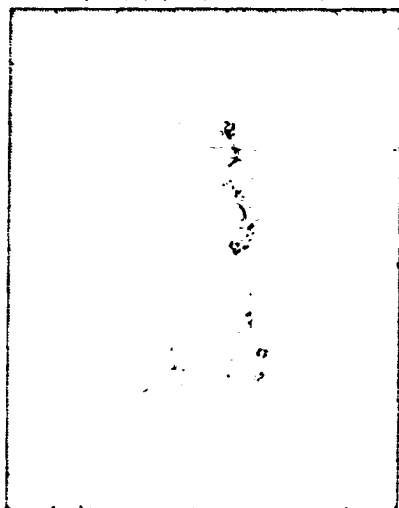
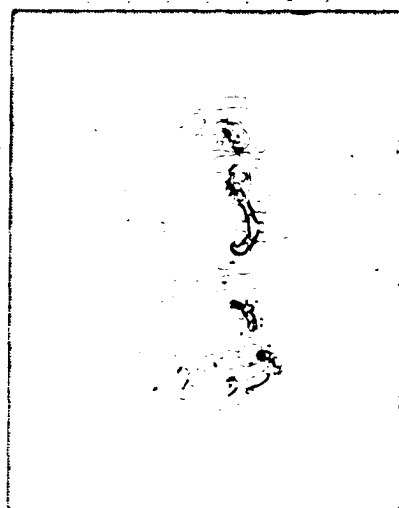


Figure 6.1: Early evolution of the difference field of perturbation pressure in WVEL with respect to CTRL (i.e., WVEL minus CTRL) at $z = 200$ m. The entire horizontal domain is shown. (a) $t = 4:01$ -hr, (b) 4:02-hr, (c) 4:03-hr, (d) 4:04-hr, (e) 4:05-hr, (f) 4:06-hr, (g) 4:07-hr, (h) 4:08-hr, (i) 4:09-hr, (j) 4:10-hr. Contour interval is 20 Pa in all panels. Solid (dashed) lines indicate positive (negative) values.

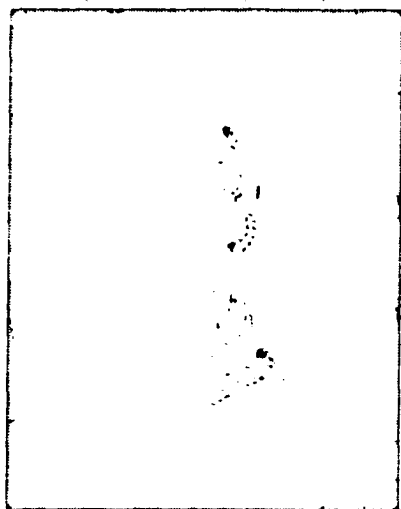
(e) WVEL-CNTRL (4:05-hr)



(f) WVEL-CNTRL (4:06-hr)



(g) WVEL-CNTRL (4:07-hr)



(h) WVEL-CNTRL (4:08-hr)

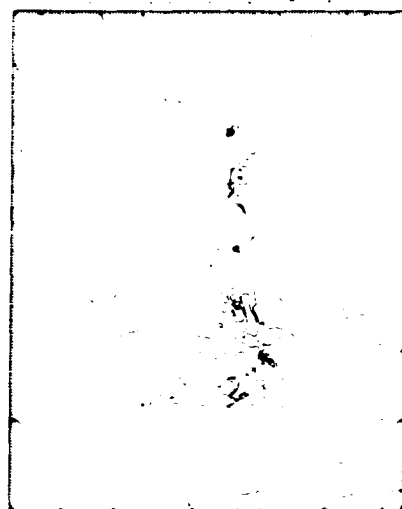


Figure 6.1 (continuation)

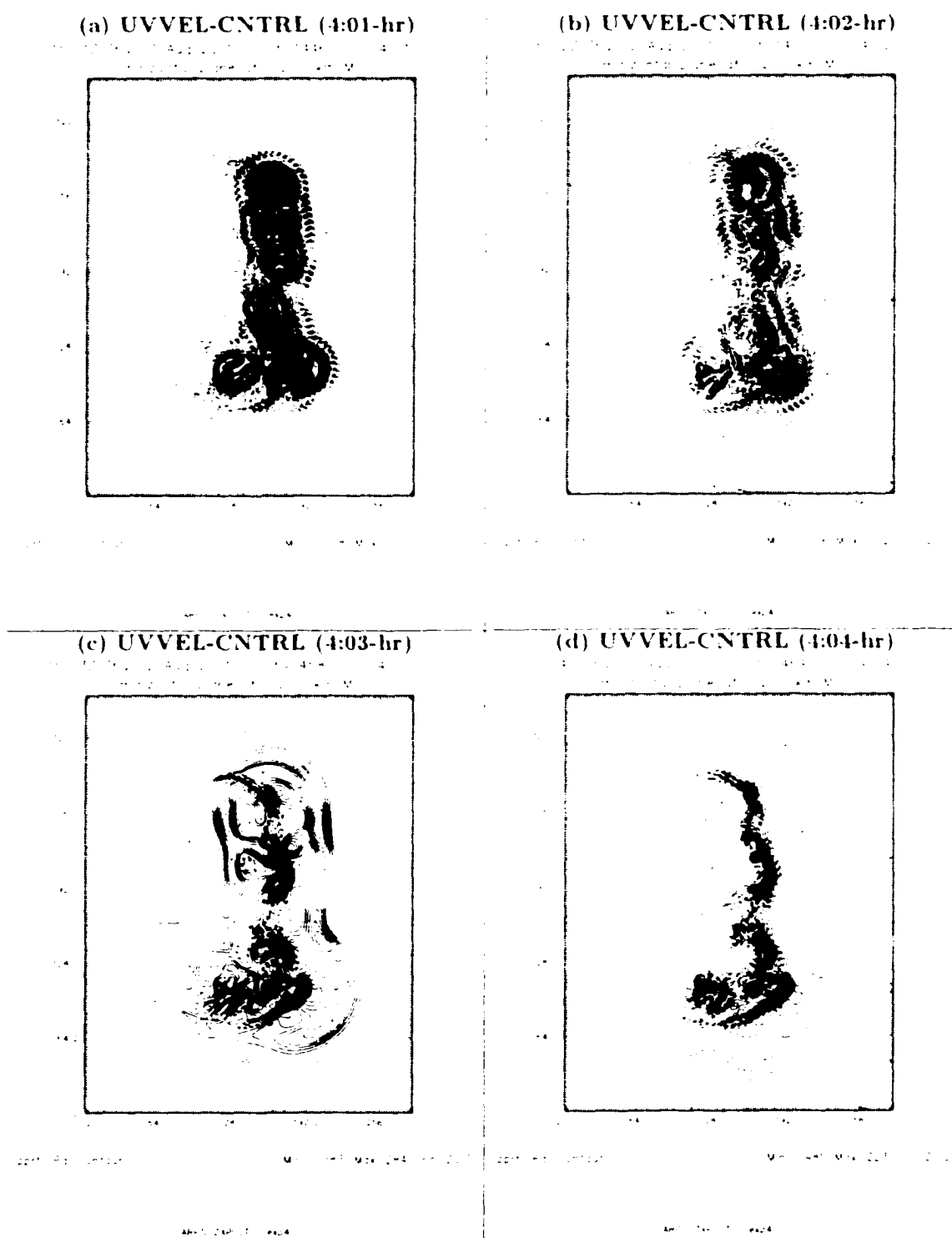


Figure 6.2: As in Fig. 6.1, but for UVVEL minus CNTRL.

(e) UVVEL-CNTRL (4:05-hr)



(f) UVVEL-CNTRL (4:06-hr)



(g) UVVEL-CNTRL (4:07-hr)



(h) UVVEL-CNTRL (4:08-hr)



Figure 6.2 (continuation)



Figure 6.2 (continuation)

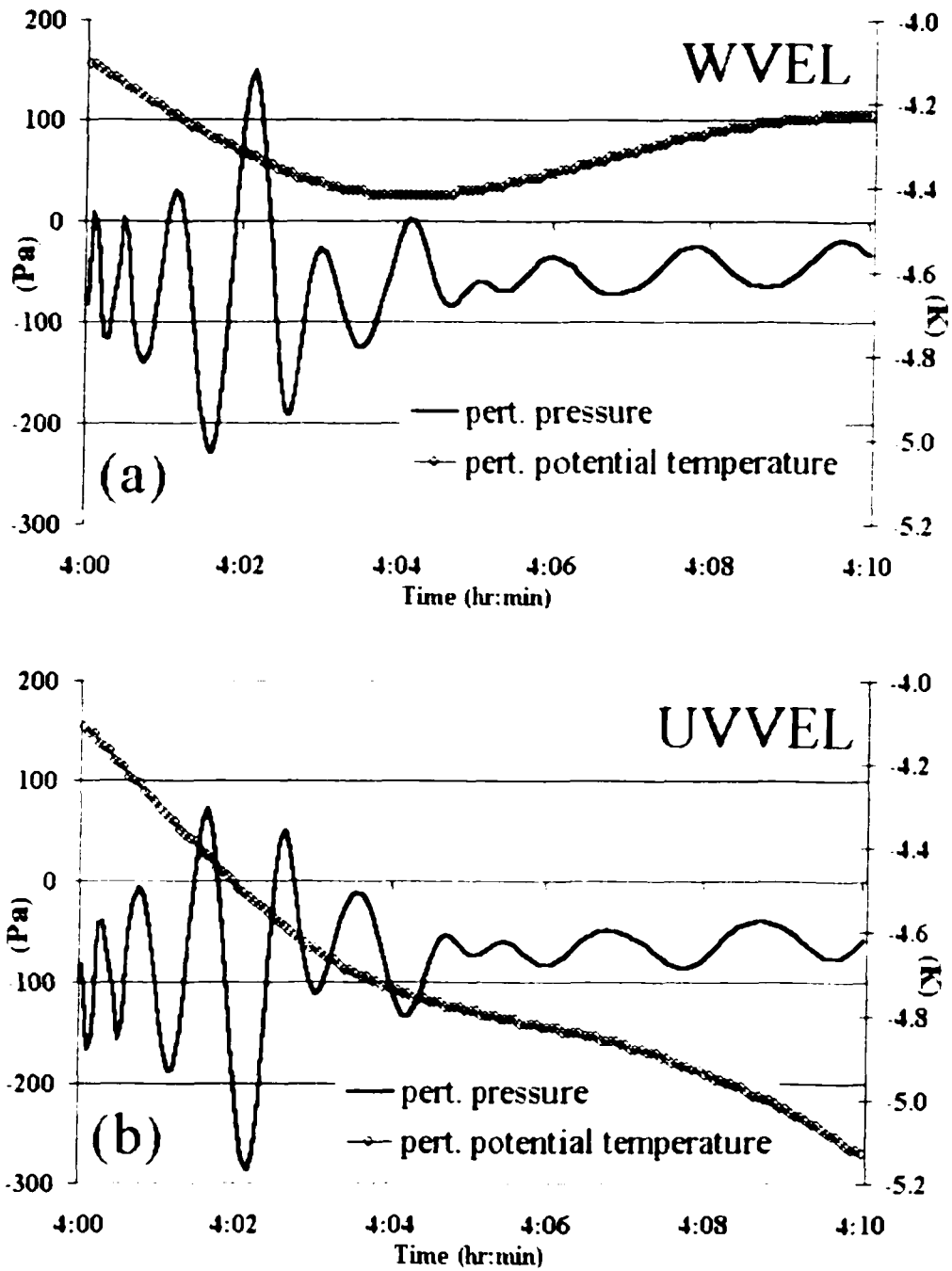


Figure 6.3: First 10-min evolution of perturbation pressure (Pa) and perturbation potential temperature (K) at grid-point $(x, y, z) = (140.0, 204.0, 0.2)$ km. (a) WVEL. (b) UVVEL.

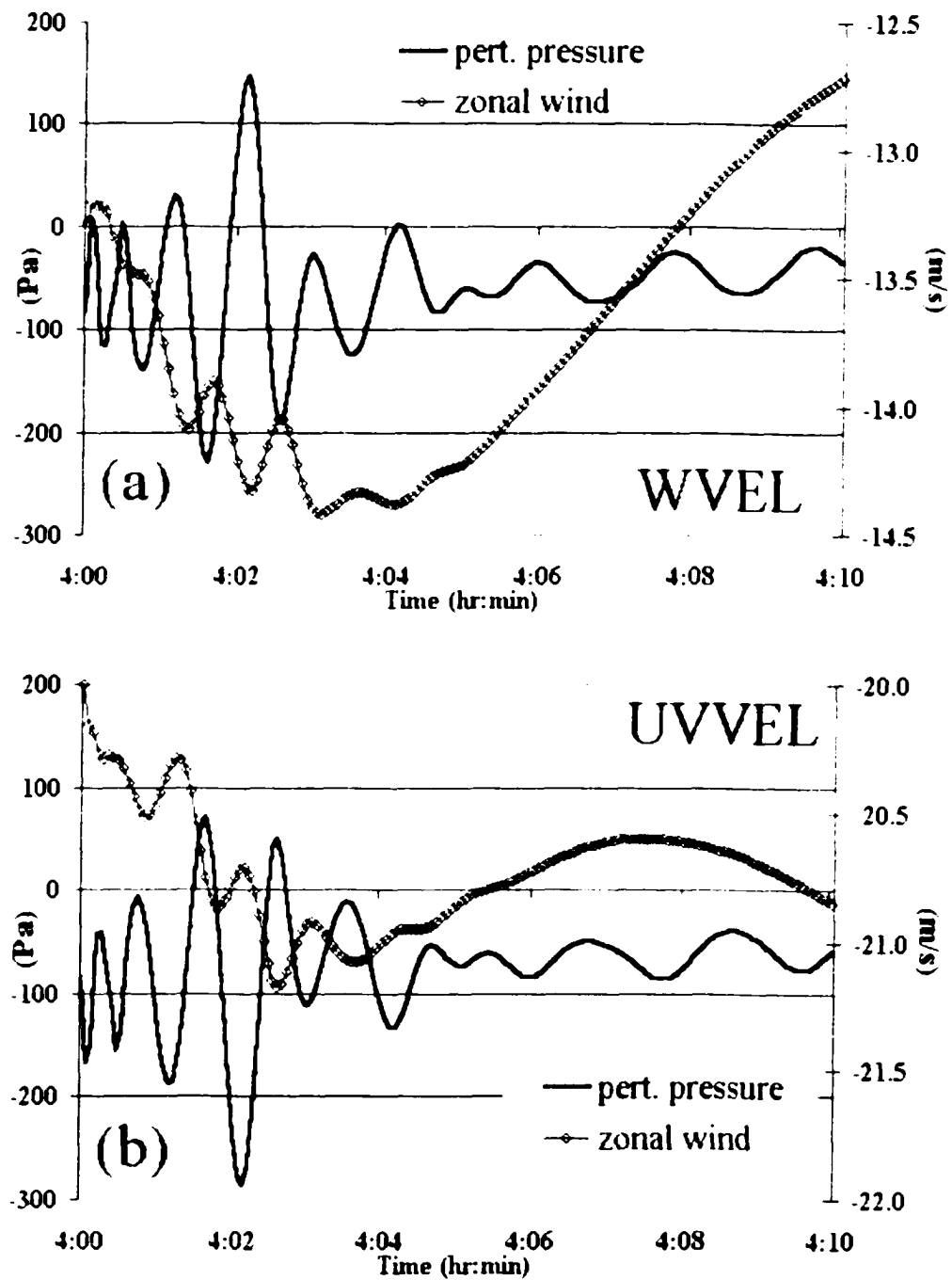


Figure 6.4: As in Fig.6.3, but for perturbation pressure (Pa) and zonal component of the wind (m s^{-1}).

dissipates quickly and a true shock wave is never formed. The attenuation is due, in part, to the divergence damping term in the momentum equations (Xue et al. 2000).

In experiment WVEL (Figs. 6.1a-j), the perturbation pressure difference gradually weakens during the first 10-min, indicating that the solution *converges* to that of CNTRL. In contrast, experiment UVVEL (Figs. 6.2a-j) displays significant pressure deviations at 10-min, as the solution *departs* from the CNTRL counterpart.

Another interesting behavior revealed in Figs. 6.1 and 6.2 is the periodic oscillation of the pressure field. For example, following the sequence from 4:05-hr to 4:08-hr in WVEL (Figs. 6.1e to 6.1h), the pressure difference field changes from mostly negative at 4:05-hr to mostly positive at 4:06-hr, back to mostly negative at 4:07-hr, and then back again to mostly positive at 4:08-hr. Similar behavior is found in UVVEL (Fig. 6.2), except that the perturbation pressure difference field does not decay as in WVEL, as the solution diverges from CNTRL.

To better characterize the oscillatory regime, Figures 6.5 and 6.6 show the first 15-min evolution of perturbation pressure at grid-points $(x, y, z) = (140.0, 204.0, 0.2)$ km and $(x, y, z) = (140.0, 204.0, 5.0)$ km (i.e., at distinct levels) for WVEL and UVVEL. The solution from CNTRL also is indicated for comparison. The first grid-point is the same one analyzed in Figs. 6.3 and 6.4 and is located at the surface, while the second one is located just above the low- to mid-level mesocyclone evident in Fig. 4.7b¹.

The pressure perturbations in experiments WVEL and UVVEL are out of phase by π radians (Figs. 6.5 and 6.6), representing a linear behavior that is consistent with the mirror-image pressure response found immediately after restart time for these runs (e.g., compare Figs. 5.11b and 5.13b). As discussed in chapter 5, this behavior is associated with the divergence forcing in the prognostic pressure equation having

¹There is nothing particularly special about these grid-points, but the oscillatory regime described at these locations is (qualitatively) representative of the behavior found in different grid-points in the 3D domain.

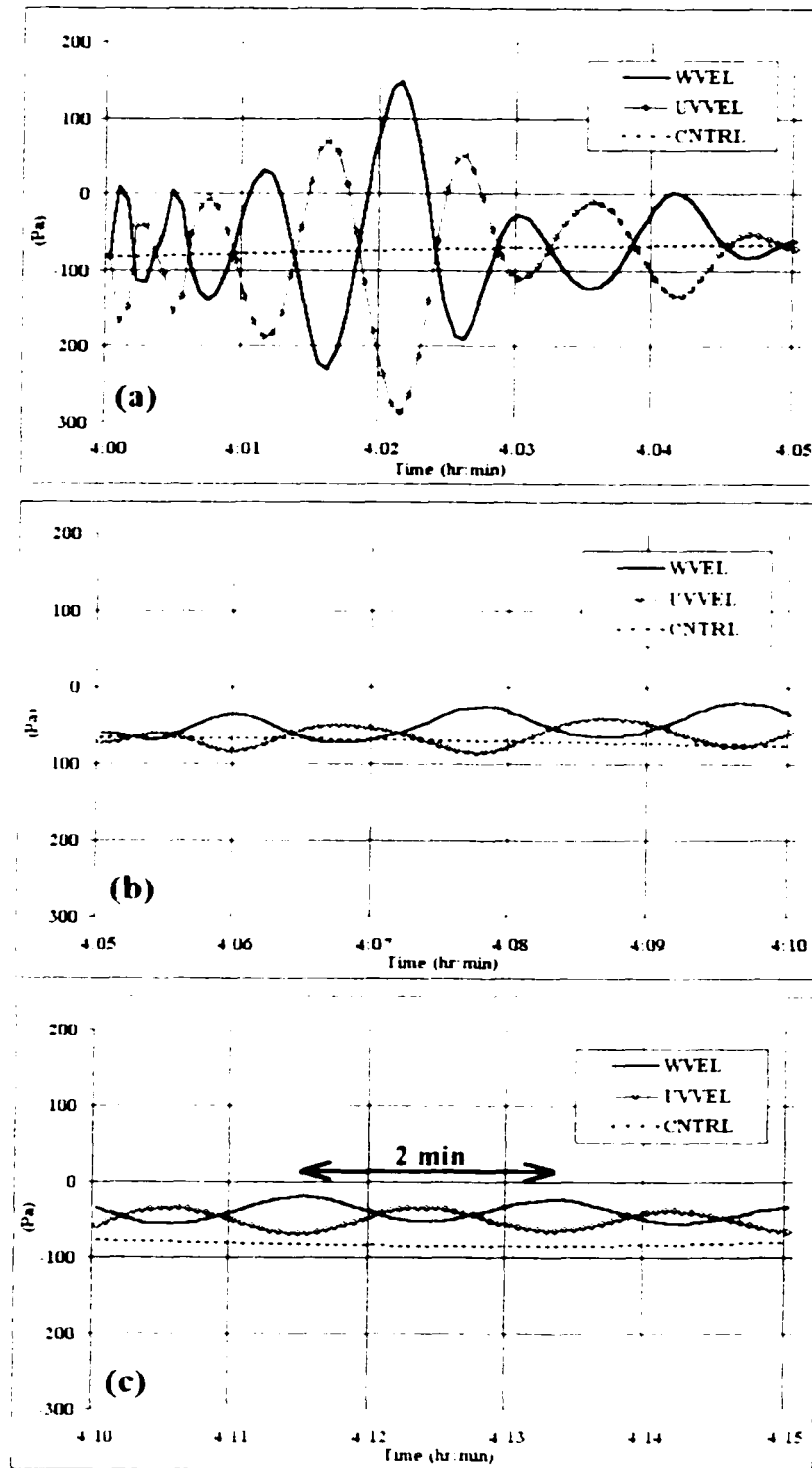


Figure 6.5. Time series for the first 15-min after restart time ($t = 4$ -hr) of perturbation pressure (in Pa) at grid-point $(x, y, z) = (140.0, 204.0, 0.2)$ km for WVEL, UVVEL and CNTRL. (a) 0 to 5-min, (b) 5 to 10-min, (c) 10 to 15-min. The perturbation pressure field is sampled at each big time step (4 s).

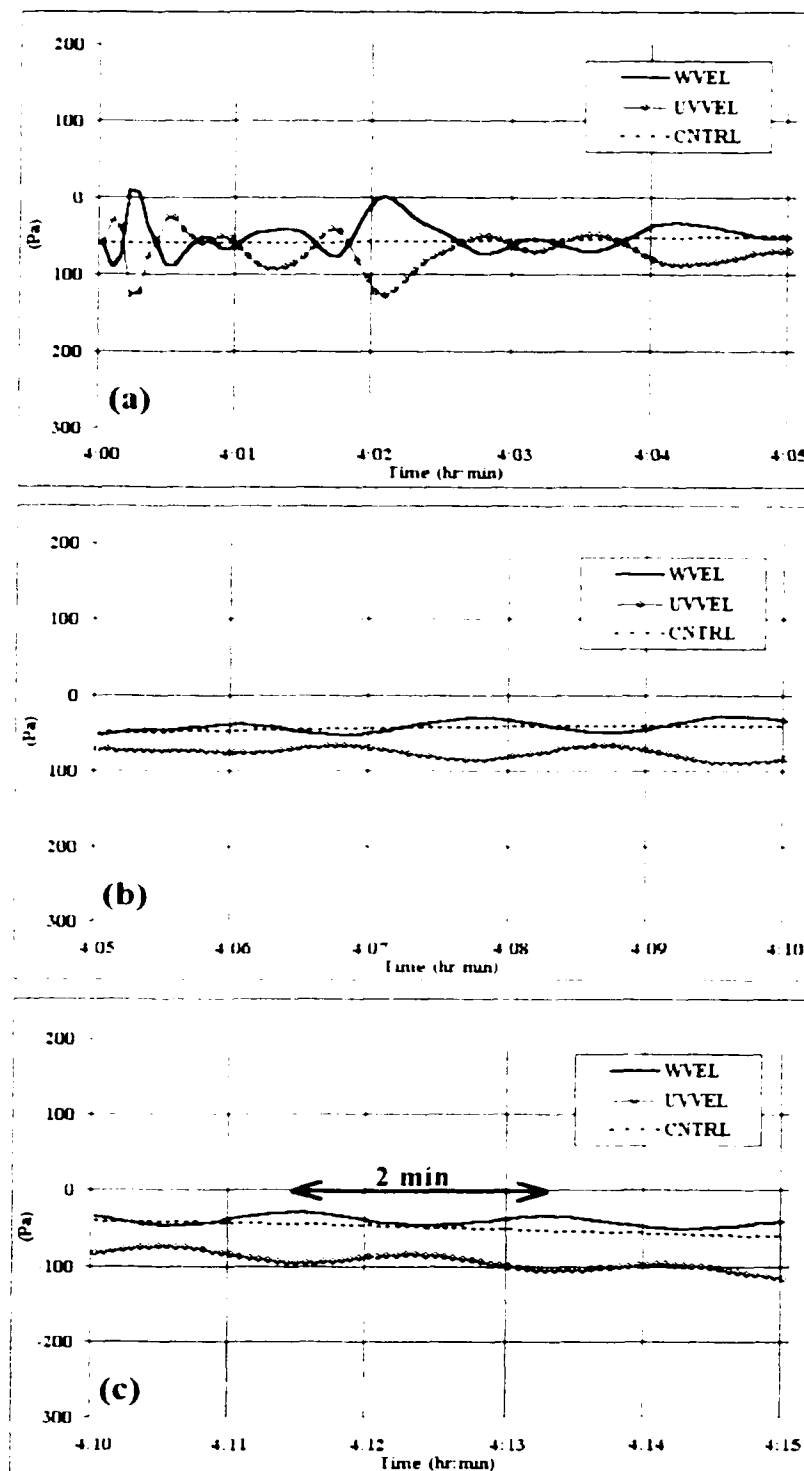


Figure 6.6: As in Figure 6.5, but at grid-point $(x, y, z) = (110.0, 204.0, 5.0)$ km

comparable magnitude but opposite signs for WVFL and UVFL at 4-hr – evident in Figs. 5.11c and 5.13c. Figures 6.5 and 6.6 reveal that, after a higher frequency oscillatory regime in the first 5-min of integration associated with the arrival of pressure fronts at the location being considered, the wave amplitudes in WVFL and UVFL are gradually damped. The period of oscillation in both runs is approximately 2-min at this stage, and the oscillation is in phase vertically for each experiment. In fact, regardless of the location chosen in the 3D domain, the 2-min oscillation is established after approximately 5-min of integration, and the pressure field oscillates in phase (for a given experiment).

Figure 6.7 depicts vertical profiles of the buoyancy frequency (N) and the acoustic-cutoff frequency (N_a), as defined by Eqs. 2.13 and 2.19, respectively. The 2-min oscillation in the pressure field in WVFL and UVFL corresponds to an oscillatory frequency of approximately 0.052 s^{-1} , which is considerably higher than N_a (Fig. 6.7). Recalling that N_a refers to the frequency *above* which vertically-propagating acoustic waves are possible (subsection 2.3.1), this result suggests that the *dominant* wave regime in WVFL and UVFL consists of high-frequency sound waves, in agreement with the description of acoustic adjustment by Fiedler (2002).

However, because the dynamic adjustment is realized in an environment that is statically-stable, it is important to assess the influence of IGWs on the oscillations. To this end, simulations of idealized *dry* convection were performed using a *neutral* sounding (constant potential temperature equal to 303 K), and initialized with a ± 4 K thermal bubble placed at the center of the domain – these will be referred to as *neutral simulations*. All other parameters are the same as in simulation CNTRL and the withdrawal experiments. The initialization triggers acoustic modes that can be examined in the first 15 to 20-min of integration.

Figure 6.8 shows time series of perturbation pressure for the first 15-min of a neu-

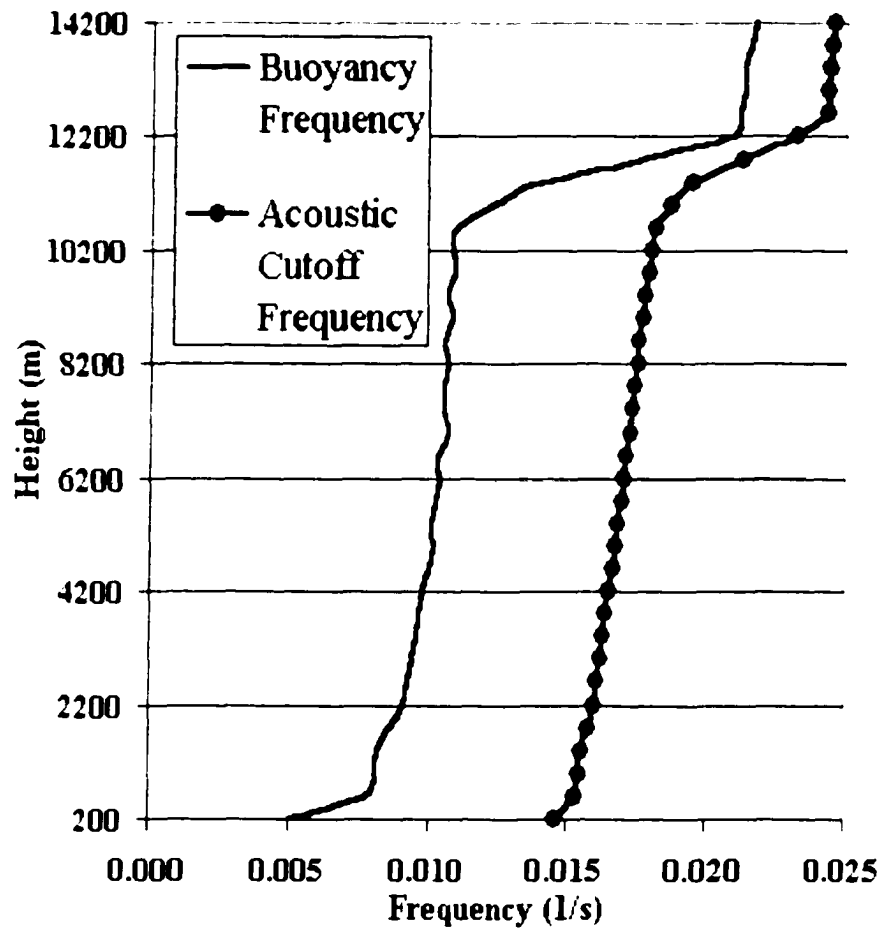


Figure 6.7: Vertical profiles of buoyancy frequency (given by Eq. 2.13) and acoustic cutoff frequency (given by Eq. 2.19) for the base-state environment used in CNTRL and withdrawal runs — associated with the thermodynamic profile depicted in Fig. 4.2.

tral simulation at the same grid-points analyzed in Figs. 6.6 and 6.7. The wave amplitude is not nearly as large as in WVVL and UVVVL but, similar to the withdrawal runs and following a high frequency oscillatory regime early in the simulation (first 5 to 10-min), the pressure perturbations tend to oscillate with an approximately constant period of 1.5-min^{-1} . This is less than the 2-min period found in WVVL and UVVVL. Thus, the environmental stratification appears to impact the frequency of the acoustic modes in the withdrawal runs. Because the waves described in Figs. 6.6 and 6.7 display frequencies well above Na , it is tempting to label them as (pure) high frequency sound waves. The results from the neutral simulation, however, suggest that these waves — particularly after 5 to 10-min of integration — have a small but non-negligible gravitational component, characterizing a high frequency AGW. (Recall from subsection 2.3.1 that AGWs represent acoustic waves that are modified by stability effects, with their two-dimensional DR given by Eq. 2.21 for an isothermal atmosphere.)

It is important to note that the wave-radiating lateral and top boundary conditions used in the numerical experiments are designed to handle impinging IGWs (Durrán and Klemp 1983, Klemp and Durrán 1983, Durrán 1999, Xue et al. 2000), not sound waves. To assess the influence of domain boundaries upon the acoustic modes obtained in our runs, additional neutral simulations were conducted with different domain sizes and lateral boundary conditions.

Figure 6.9 shows time series of perturbation pressure at grid-points (x, y, z) $(70.0, 108.0, 0.2)$ km and $(70.0, 108.0, 5.0)$ km for a neutral simulation in which the horizontal domain is reduced by half in both the zonal and meridional directions — relative to the original domain size, the location of the selected grid-points are equivalent to those in Figs. 6.5, 6.6 and 6.8. Again, after relatively high amplitude

⁴Dry simulations with divergence damping turned *off* were also conducted. As expected, wave amplitudes are larger without divergence damping, but the phase and frequency of oscillation are not changed.

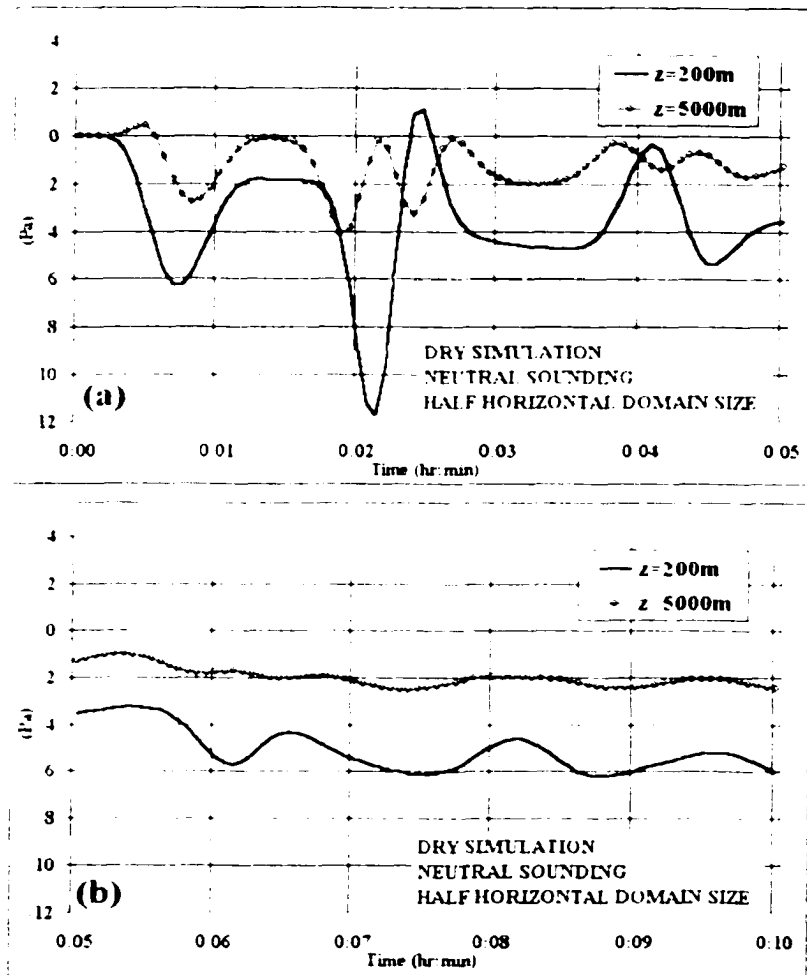


Figure 6.9: As in Fig. 6.8, but for the first 20-min of integration of a neutral simulation with horizontal domain extent that is half of that used in simulations CTRL, WVCL and UVCL. The grid-points from which the time series are extracted are $(x, y, z) = (70.0, 108.0, 0.2-5.0)$ km. In (d) (which refers to the last 5-min of the 20-min window) only the time series for $z = 200$ m is shown, with the vertical scale zoomed in for a 2 Pa range. Time zero refers to the initialization time with a thermal bubble.

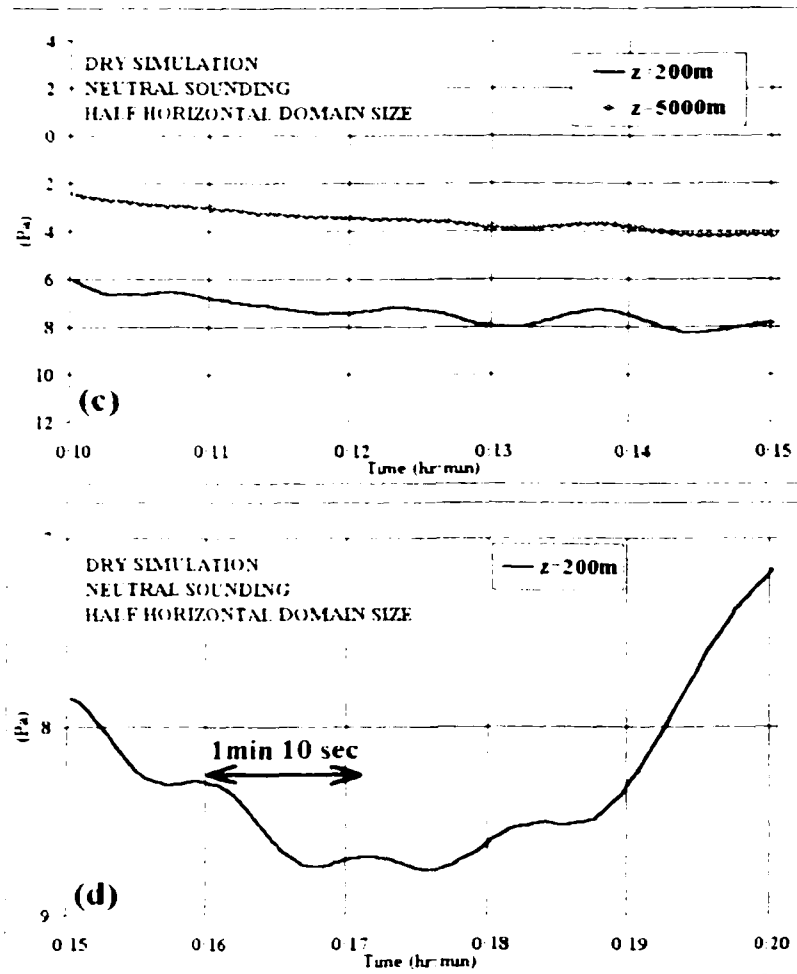


Figure 6.9 (continuation)

waves are damped, the pressure fluctuation oscillates at an approximately regular period of 70 s (Fig. 6.9d; zoomed in for the time series at $z = 200$ m), with very weak amplitudes.

When the domain size is reduced by half in the vertical as well (Fig. 6.10), waves with higher frequency and larger amplitude are evident early in the simulation (Fig. 6.10a). As these waves are damped, a lower frequency regime is established as in the previous runs. The oscillatory period at this stage is approximately constant, around 2-min (Figs. 6.10c,d).

In summary, by comparing the results from the neutral simulations — and noting that the only difference between them is domain size — it seems evident that the frequency of the acoustic modes is influenced by the boundaries. This should not be a surprise because reflection of sound waves is expected to occur along boundaries originally designed to “radiate” slower-moving IGWs (Durrán 1999). The inclusion of divergence damping in the momentum equations, and the numerical integration of the vertical equation of motion and prognostic pressure equation using an implicit Crank-Nicolson scheme, efficiently damp acoustic modes (Xue et al. 2000), thus minimizing the spurious effects of reflecting sound waves.

It is interesting to note that the implicit numerical scheme allows the integration of the compressible equations with a larger time step than that imposed by the Courant-Fredrichs-Lewy (CFL) numerical stability condition for a fully explicit scheme in the presence of sound waves (Durrán 1999). For example, in our simulations a small time step of 1 s is employed (see Table 4.2), when the CFL condition for the leap-frog scheme imposes a 0.36 s time step to stably solve acoustic modes with our grid spacing. Hence, although sound waves are allowed in the compressible model, they are not correctly represented. This is not a major problem for meteorology since acoustic

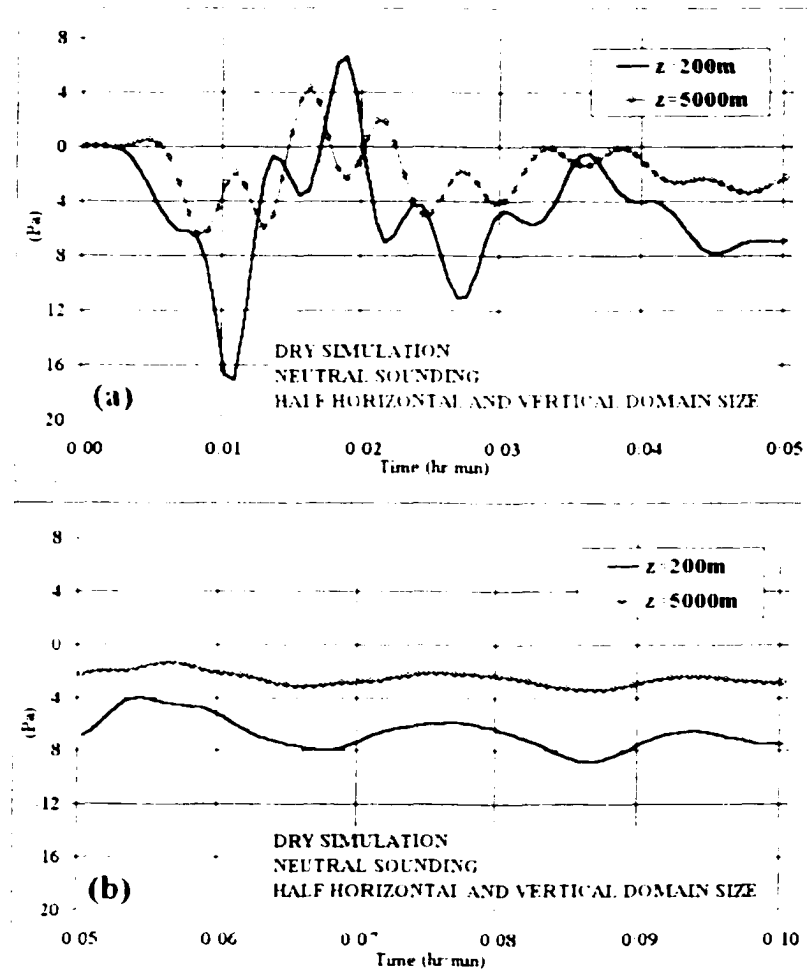


Figure 6.10: As in Fig. 6.8, but for the first 20-min of integration of a neutral simulation with horizontal and vertical domain extents that are half of those used in simulations CNTRL, WVCL and UVCL. The grid-points from which the time series are extracted are the same as in Fig. 6.9. In (d) (which refers to the last 5-min of the 20-min window) only the time series for $z = 200\text{ m}$ is shown, with the vertical scale zoomed in for a 4 Pa range. Time zero refers to the initialization time with a thermal bubble.

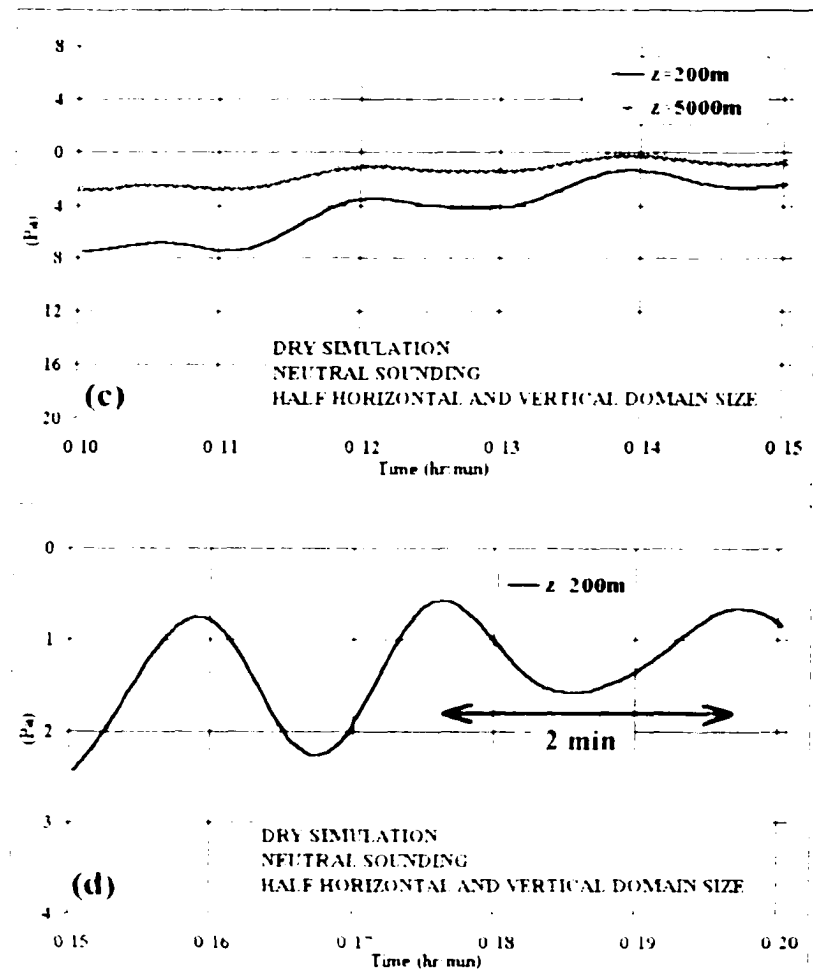


Fig.6.10 (continuation)

waves do not play a significant role on the *dynamics* of atmospheric phenomena⁵. However, the effects of not correctly representing them appear to have some impact on the pressure fluctuations discussed in this chapter. For instance, while the reduction of domain size in the neutral simulations led to the generation of high frequency acoustic waves early in the integration, the frequency of oscillation varied in a rather unpredictable way at later times. The simulation with domain size equal to half the original vertical and horizontal extents produced acoustic waves with lower frequency (Fig. 6.10d) than in the original domain (Fig. 6.8c), while the run with half the original horizontal domain size generated sound waves with the highest frequency after 10-min (Fig. 6.9d). Such behavior is *not* sensitive to the magnitude of the thermal bubble specified at time zero. This suggests that the near-2-min oscillation in the pressure field found in experiments WVEL and UVVEL *after 5-min of simulation* (Figs. 6.5b,c) has no special physical meaning, and is a result of the experimental design (e.g., stratification, domain size, boundary conditions).

To conclude, the examination of pressure fluctuations allowed us to visualize the essence of dynamic adjustment (more specifically, acoustic adjustment) in the context of wave propagation. As the spurious acoustic modes are damped, the solution in WVEL (UVVEL) converges to (departs from) the CNTRL counterpart. This adjustment mechanism is conceptually similar to geostrophic and hydrostatic adjustment with respect to the generation of spurious high frequency waves when specifying ICs that do not satisfy the physical relation governing/constraining the atmospheric motion.

⁵They do play an important role on the energetics of atmospheric flows, though, as discussed in chapter 2.

Chapter 7

Withdrawal of Thermodynamic Fields

Having examined dynamic adjustment in the context of withholding information about the wind field from the simulated bow echo system, we now turn our attention to the response associated with the withdrawal of thermodynamic fields. Numerous questions are addressed, including the following: How important is the specification of the convectively-generated thermal structure and moisture fields in the bow echo simulation? How does the wind field respond to the withdrawal of thermodynamic quantities? And what physical processes govern such responses? What is the role played by latent heating and cooling in dynamic adjustment? What is the importance of specifying the regions of saturation and subsaturation within the MCS? Does wave propagation play any relevant role in dynamic adjustment induced by thermodynamic fields?

7.1 Experiment THETA: General results

In experiment THETA, the *perturbation* potential temperature field (θ') is set to zero at restart time across the entire domain. In other words, the total potential temperature field is reset to the base-state sounding (Figure 4.2) everywhere *except*

where the withdrawal of its perturbation component yields supersaturation. The moisture field is not modified. In this process, deep layers of significant supersaturation (with artificial dewpoint depressions as strong as -13°C) are formed, especially in the middle levels of the convectively active region of the simulated MCS. We choose to avoid creating such a condition because *one* of the objectives of the thermodynamic withdrawal experiments is to assess the influence of the specification of regions of *saturation* and *subsaturation* upon storm evolution. This is motivated by some investigations of Doppler radar data retrieval techniques, in which layers of *saturation* are parameterized in terms of the radar reflectivity field and retrieved vertical motion (e.g., Weygandt et al. 2002b) using rather arbitrary thresholds. In studying the initialization of a cloud-scale model using Doppler radar data of an oceanic MCS, Bielli and Roux (1999) found that realistic simulations were only possible when regions of saturation (subsaturation) were correctly specified in the updraft (trailing) zones of the system. Therefore, one of the issues to be examined in our runs is the extent to which modification of layers of saturation and subsaturation affect storm system evolution.

In experiment THETA, a simple check is performed at each grid-point *after* the θ' field is set to zero: if the resulting air temperature T is less than the dewpoint temperature T_d , then the potential temperature at that point is reset to the corresponding saturation value (i.e., imposing $T = T_d$). Thus, not all of the perturbation thermal field is eliminated. In fact, in some saturated layers in the mid levels of the MCS, the θ' field may not be changed at all. It is important to note that an additional simulation was performed in which supersaturation was allowed to remain after the thermal field was reset to the base state. The results were *not* significantly different, and dynamic adjustment processes to be described for experiment THETA exhibit only a *slight* delay owing to the presence of supersaturation at restart time.

Figure 7.1 depicts the impact on the thermodynamic profile of setting to zero the θ' field at restart. “Soundings” from CNTRL and THETA are shown at 4-hr at (x, y) (160, 200) km, which is just upstream of the bow echo segment shown in Figure 4.6a. Note that in THETA, the environment is warmed at low levels, with the cold pool being eliminated, and cooled at mid levels, where warming due to latent heating is considerably reduced. In other words, mid-level subsaturated layers in CNTRL (Fig. 7.1a) may become saturated in THETA (Fig. 7.1b), implying that regions of mid-level saturation in THETA cover larger areas than in CNTRL at the restart time. In this case, phase changes in the direction of increasing molecular order (e.g., condensation and deposition) are expected to be enhanced at mid levels in association with ice-water saturation adjustment (Lin et al. 1983, Tao et al. 1989). These processes should allow the partial (or perhaps total) restoration of mid-level latent heating as the simulation proceeds.

At low levels, particularly within the surface cold pool, the dewpoint spread is increased when the θ' field is set to zero (see low levels in Fig. 7.1b), thus reducing the relative humidity. Despite withdrawing the thermal structure of the cold pool at restart time, it is reasonable to expect *enhanced* low-level evaporation of rain (and accompanying cooling) in THETA and thus restoration of at least part of the cold pool. The processes described in this brief “thought experiment” are evaluated more fully in the analysis of the numerical results below.

Figure 7.2 shows the solution from experiment THETA at 5 and 6-hr (compare with Figs. 4.3 and 4.4). Despite resetting θ' at restart, the surface cold pool is gradually recovered (Figs. 7.2a,c), and at 6-hr, it is as extensive as in CNTRL. Interestingly, the surface mesohigh and outflow in the center of the domain are stronger in THETA than in CNTRL.

The solution at $z = 2.6$ km (Figs. 7.2b,d) displays a solid squall line with two

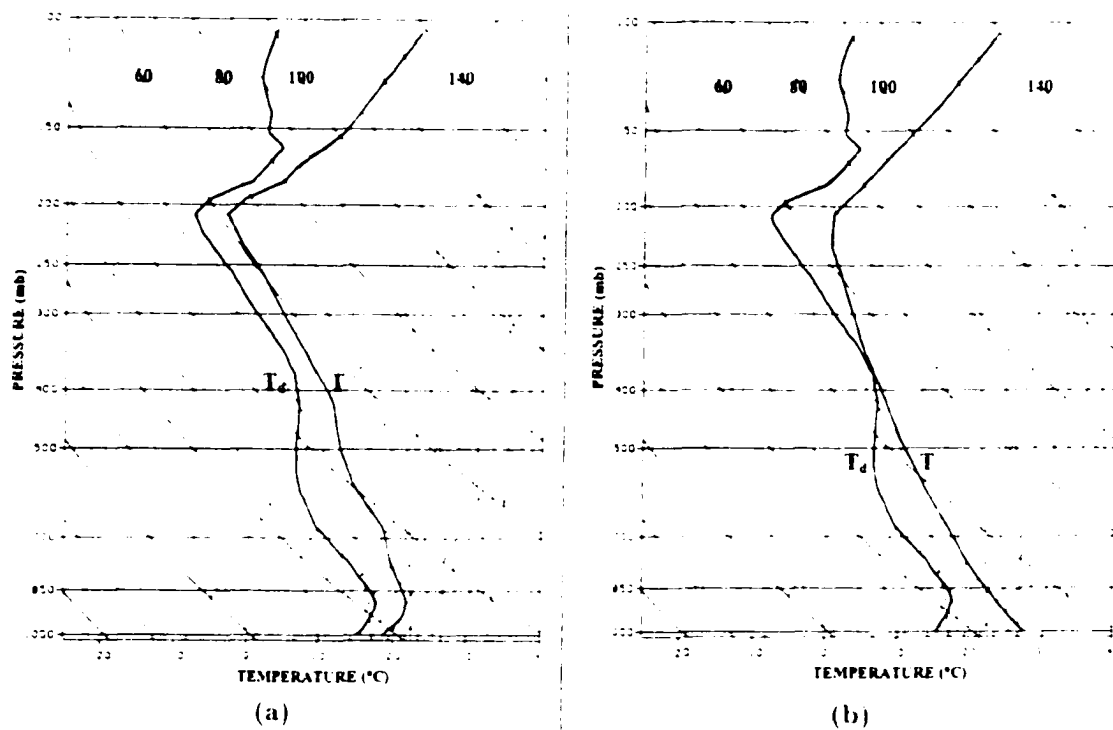


Figure 7.1: Skew-T diagrams for thermodynamic profiles within the simulated bow echo at restart time. Location: (x, y) = (160, 200) km; just upstream of the main bow echo segment at 4-hr (see Fig.4.6a). (a) CNTRL, (b) THETA.

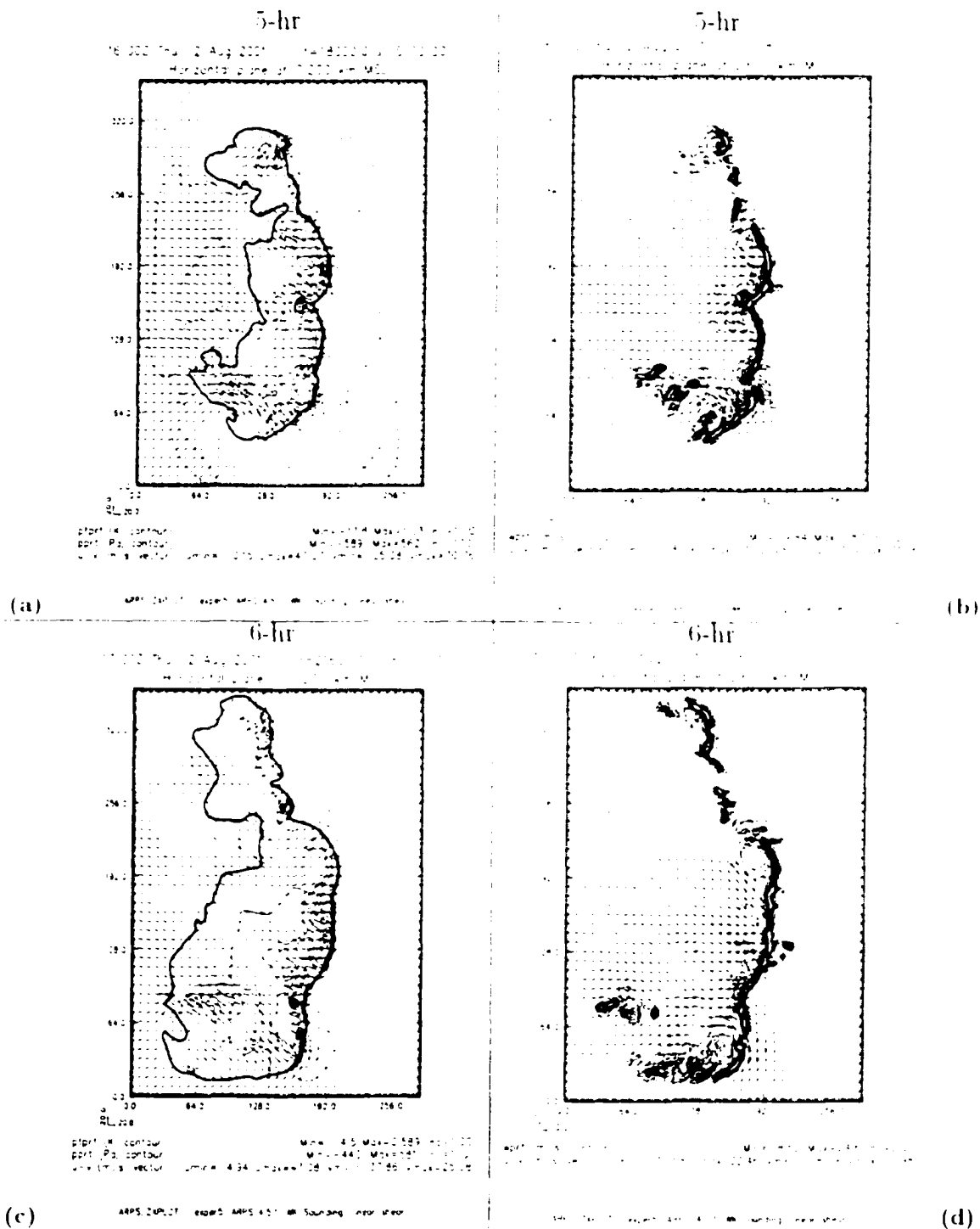


Figure 7.2: Bow echo simulation in experiment THETA. First row: 5-hr; second row: 6-hr. (a),(c) surface cold pool and outflow: vectors are ground-relative winds, thick solid line represents -2 K potential temperature perturbation indicating the boundary of the cold pool, thin solid (dashed) contours indicate positive (negative) pressure perturbations plotted at each 100 Pa. (b),(d) storm-relative winds (vectors) and magnitude of vertical velocity (contoured at each 2 m s^{-1}) at height $z = 2600 \text{ m}$. Solid (dashed) lines are updrafts (downdrafts).

main bow echo segments at 5-hr (resembling the simulated storm in CNTRL; Fig. 4.4b), but evolving into a more linear structure in the last hour (Fig. 7.2d). The magnitude of updrafts at this level is slightly stronger than in CNTRL, indicating that the continuous regeneration of new convective cells along the gust front is not jeopardized. As a result, the forward motion of the MCS in THETA is similar to that in CNTRL.

A strong rear-to-front flow covering most of the central domain is evident in Figure 7.2d. This is illustrated better in Figure 7.3, which compares experiments CNTRL and THETA at $z = 2.6$ km at 6-hr for the box depicted in Fig. 4.4c (showing storm-relative winds, rainwater mixing ratio (indicated by shading) and magnitude of the zonal component of the wind (indicated by contours)). In CNTRL (Fig. 7.3a) two bow echo segments are located where the rear-to-front flow is strongest, characterizing RLJs, whereas in THETA (Fig. 7.3b), the meridional gradient in the zonal momentum field is less pronounced, accounting for a more linear structure of the squall line. Thus, the *fine structure* of the rear-to-front flow is modified somewhat in experiment THETA, especially in the last 1-hr of simulation.

A well defined MCV is generated in experiment THETA (Fig. 7.3b), which displays vertical vorticity comparable to that found in experiment CNTRL (of the order of 10^{-5} s^{-1} ; not shown). The MCV location in THETA is consistent with that in CNTRL, and indicates that the MCS simulated in the withdrawal experiment shares many of the mesoscale features observed in strong squall lines, even though no bow echo segment is evident at 6-hr.

Because the simulations are not extended beyond 6-hr, we cannot state whether bow echoes are formed later in THETA, although the squall line in this experiment does represent a strong MCS. This is also evident when analyzing the vertical profiles of momentum ($\overline{u'u'}$) and heat ($\overline{u'\theta'}$) fluxes for the first hour following restart (Figure

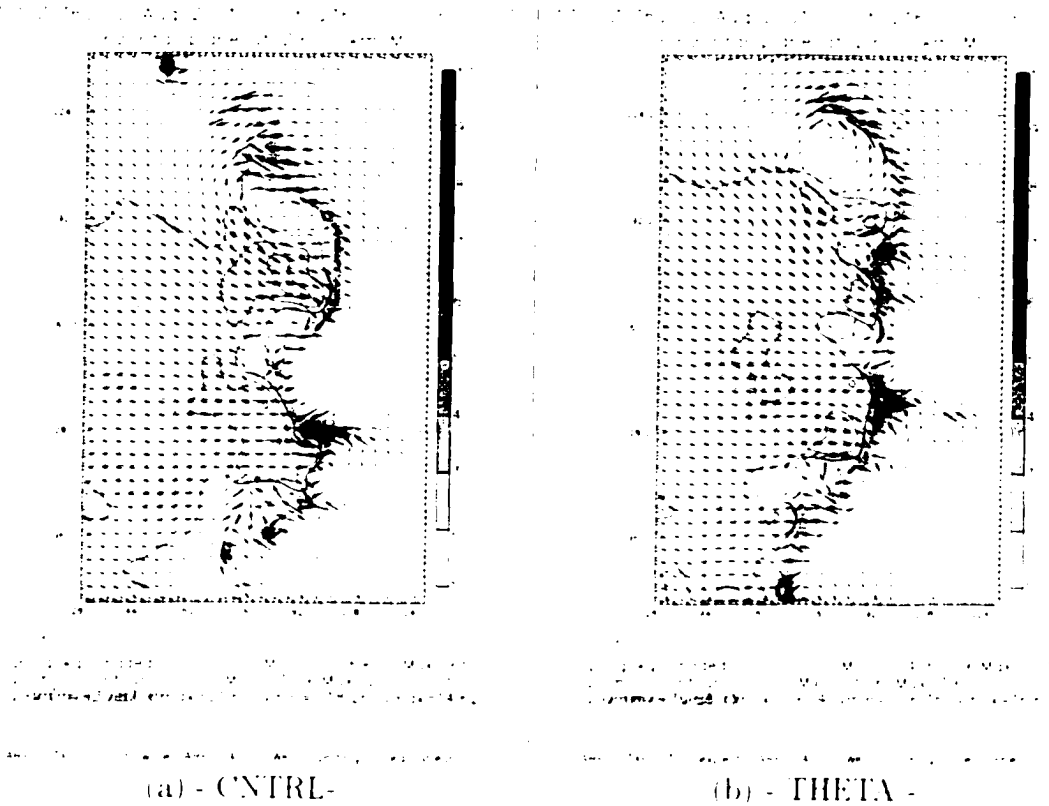


Figure 7.3: Structure of the simulated bow echo at 6-hr at height $z = 2600$ m, zoomed in for the area indicated by a rectangle in Figure 4.4c. (a) CNTRL. (b) THETA. Vectors are storm-relative winds in m s^{-1} , with a 10 m s^{-1} reference vector indicated at the bottom of each panel. Solid lines are magnitude of zonal component of the wind (storm-relative), contoured at each 5 m s^{-1} . Only values equal to or above 10 m s^{-1} are plotted. Storm motion is approximately 26 m s^{-1} in the zonal direction. Shading indicates rainwater mixing ratio in g kg^{-1} .

7.4). (Recall from chapter 4 that quantities $\overline{u'u'}$ and $\overline{u'\theta'}$ provide information about the *overall* strength of the MCS). In THETA, the $\overline{u'u'}$ field displays an evolution similar to that in CNTRL (Figs. 7.4a,b). At times, the mid- to upper-level momentum flux in THETA is visibly stronger than in CNTRL, e.g., at $t = 4:10$ -hr, 4:40-hr and 5:00-hr. Part of this behavior is explained in more detail below. The vertical heat flux in THETA at 4:00-hr (Fig. 7.4d) is weaker, owing to the elimination/weakening of the θ' field at the restart time. However, after 10-min, the heat flux is restored to values comparable to the CNTRL solution, and by 5-hr it is slightly stronger than in CNTRL.

Therefore, although the simulated MCS in experiment THETA does not match exactly the CNTRL solution, it displays the structure of a robust squall line. The overall strength of the convective system, and its ability to regenerate new cells at its leading edge, are not changed to a significant degree in THETA. We emphasize that similar results were found when running a version of THETA in which the θ' field is withdrawn even where it generates supersaturation. Important results regarding the evaporation of rain at low levels and the response among wind, pressure and buoyancy fields are discussed in sections 7.3 and 7.4.

7.2 Experiment VAP: General results

In experiment VAP, perturbations in water vapor mixing ratio (q'_v) are set to zero at restart. As in THETA, supersaturation is not allowed, and for every grid-point where the withdrawal of q'_v yields $T < T_d$, the water vapor mixing ratio field is reset to the corresponding saturation value $(q_v = q_{v,s})^{1/2}$ while the temperature field remains

¹ The determination of saturation water vapor mixing ratio ($q_{v,s}$) in ARPS follows the adjustment scheme developed by Tao et al. (1989), where $q_{v,s}$ is defined as a mass weighted combination of the saturation values over liquid water and ice within the temperature range $-40^\circ\text{C} < T < 0^\circ\text{C}$. For $T > 0^\circ\text{C}$ [$T < -40^\circ\text{C}$] $q_{v,s}$ is defined over liquid water [ice].

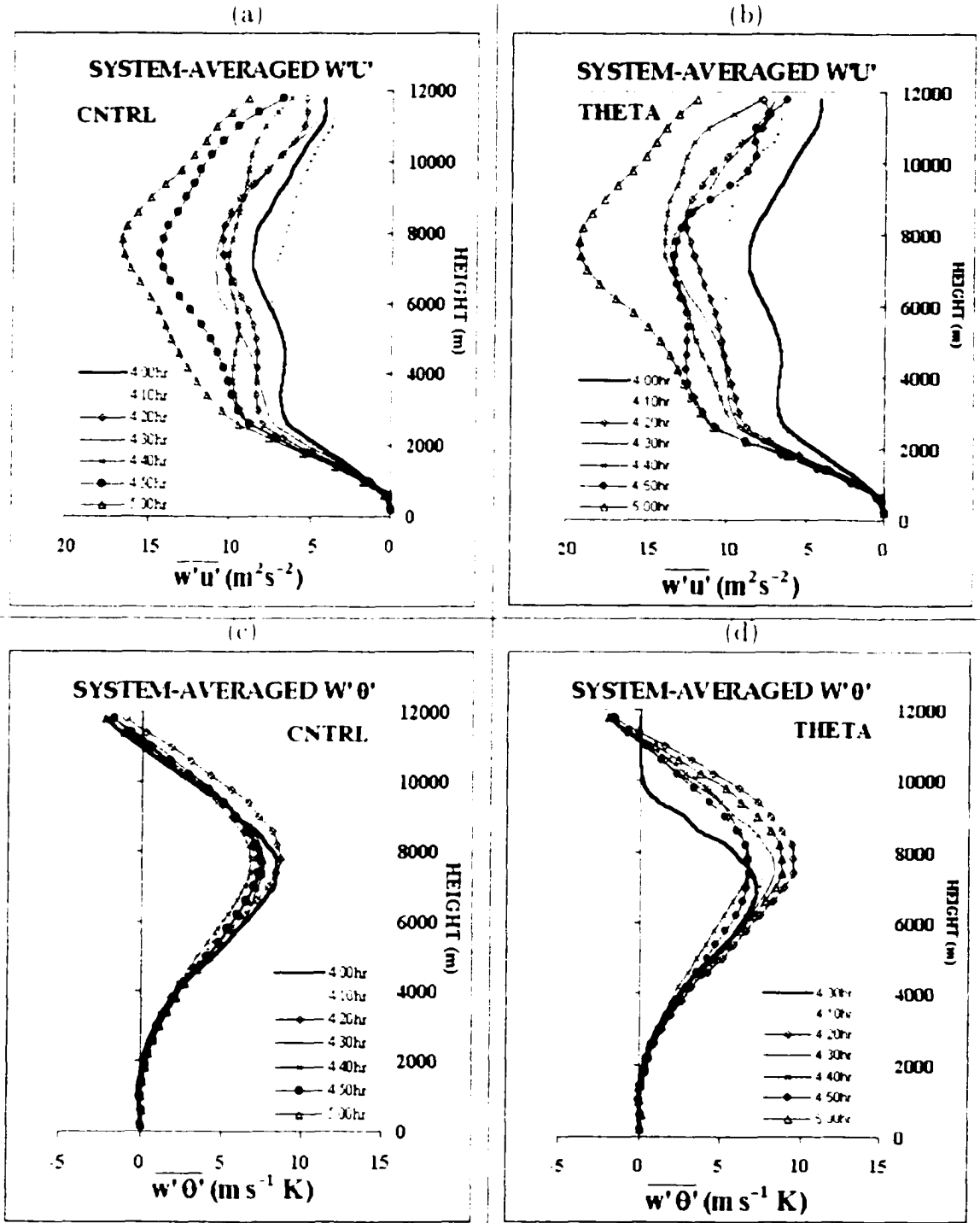


Figure 7.4: Time evolution, from 4-hr to 5-hr (at 10-min increments), of system-averaged profiles of vertical momentum flux ($\overline{w'u'}$) in $m^2 s^{-2}$ (first row), and of vertical heat flux ($\overline{w'\theta'}$) in $m s^{-1} K$ (second row). (a),(c) CNTRL, (b),(d) THETA. The averaging is applied for the region enclosed by a rectangle in Fig. 4.4b.

unchanged. Therefore, not all of the q_c field is reset to the base state, and thus this procedure changes the total amount of water in the domain.

Figure 7.5 shows how the withdrawal of q'_c changes the thermodynamic profile in the MCS at restart time. At low levels, the atmosphere is moistened, with saturation occurring at some locations within the cold pool, as is the case in the grid-point examined in Fig. 7.5b. At mid and upper levels, the atmosphere becomes drier, with an increased dewpoint spread. Thus, mid- and upper-level saturated layers in CNTRL become unsaturated in VAP, and phase changes such as evaporation and sublimation are expected to be enhanced at those levels. (Recall that the mixing ratios of the remaining water species (cloud water, rainwater, cloud ice, snow and hail) are retained as in CNTRL). In addition to the diabatic effects resulting from the withdrawal of q'_c , unsaturated ascent will favor adiabatic cooling. This response may have significant implications for the maintenance of positively buoyant air at mid levels.

The solution from experiment VAP is depicted in Figure 7.6. Although the *thermal* structure of the cold pool is not changed at restart, it is affected subsequently. Specifically, at 5-hr (Fig. 7.6a), the cold pool is weaker and slightly less extensive in horizontal area compared to CNTRL (Fig. 4.3b). Moreover, its eastward propagation is not as rapid as in CNTRL and THETA.

Figure 7.6b shows the corresponding solution at $z = 2.6$ km. In contrast with experiment THETA, the MCS at this time consists mostly of isolated multicells, with a very short linear organization at the center of the domain. The weakening of the surface cold pool and outflow in VAP appears to have influenced the organization of new convective cells along the gust front. Nevertheless, the vertical motion in these cells is as strong as in CNTRL. The rear-to-front flow, on the other hand, is considerably weaker, and there exists no indication of a developing MCV.

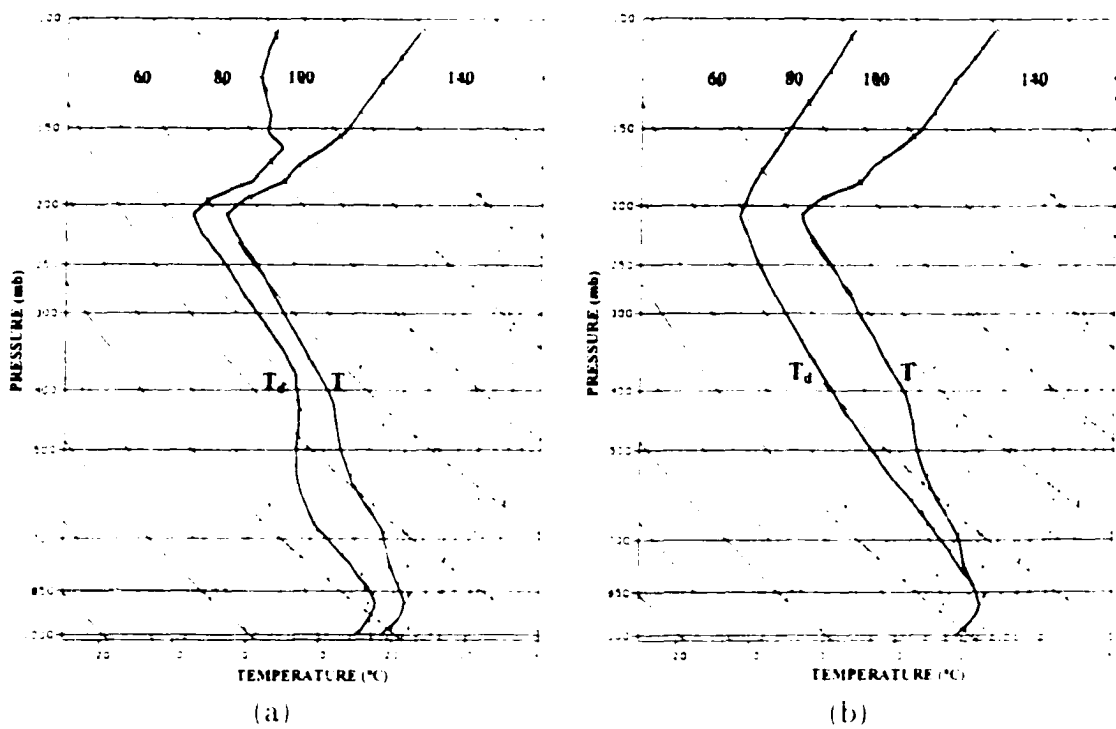
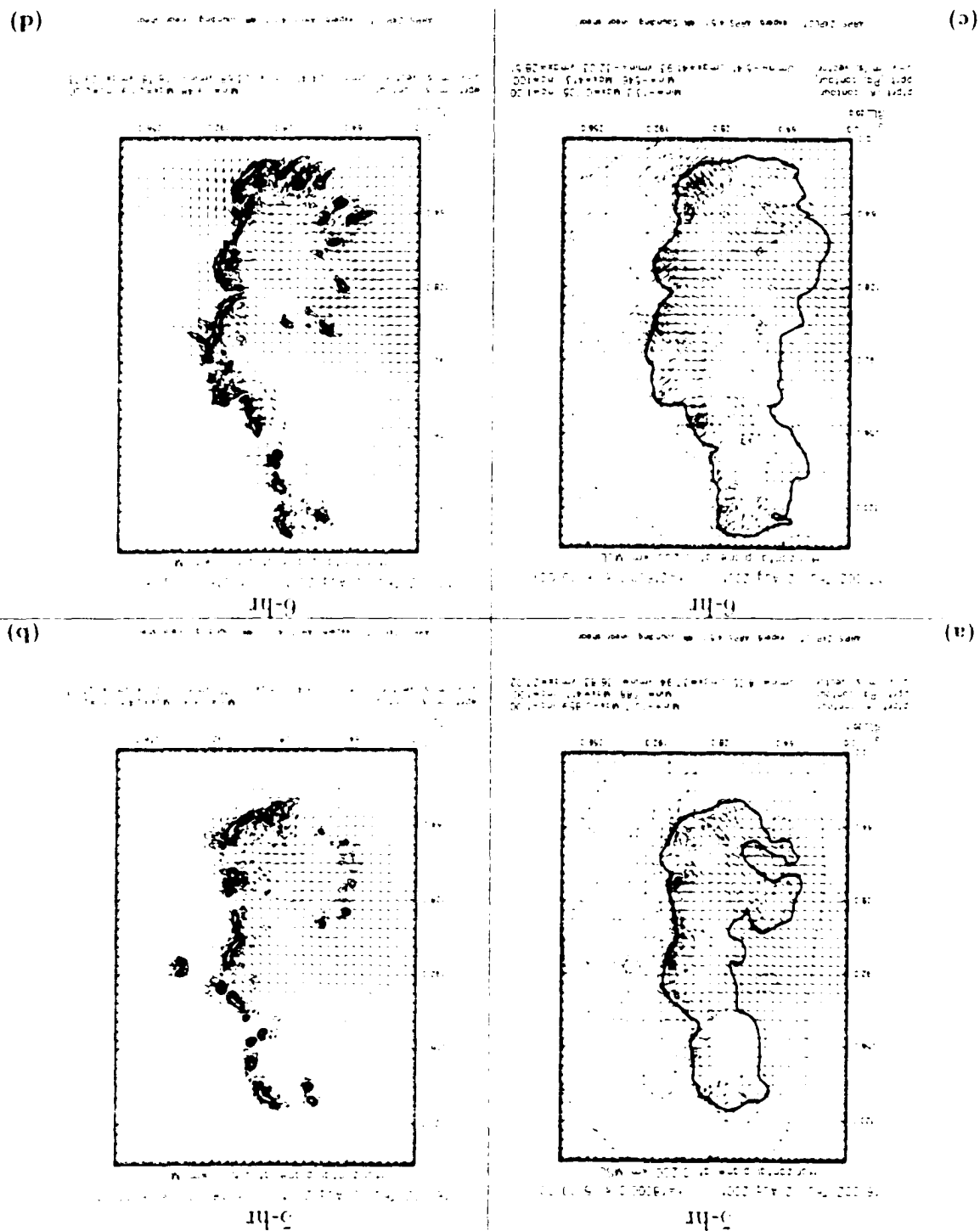


Figure 7.5 As in Fig. 7.1, but comparing thermodynamic profiles from experiments (a) CNTRL and (b) VAP.

Figure 7.6: As in Fig. 7.2, but for VAP



From 5 to 6-hr, the simulated MCS in VAP displays signs of redevelopment. An extensive cold pool is present (Fig. 7.6c), although not as strong as in CNTRL in terms of θ' . The surface mesohigh, which covers large areas in CNTRL and THETA, is relatively confined in VAP. As expected from this structure, the surface outflow is not nearly as widespread and intense in the center of the domain as is in CNTRL and THETA. Aloft (Fig. 7.6d), the dominant mode of convection is more evident, including multicells, short convective lines, and a short bow echo segment. Compared to the solution at 5-hr, the MCS seems to be reorganizing, although the rear-to-front flow is weak and the storm system fails to generate an MCV within the 2-hr simulation.

Figure 7.7 compares the time evolution of vertical profiles of $\overline{u'u'}$ and $\overline{u'\theta'}$ between VAP and CNTRL from 4 to 5-hr. The $\overline{u'u'}$ field remains weaker than the CNTRL counterpart during most of the first hour of simulation (Fig. 7.7b). However, at 5-hr, $\overline{u'u'}$ shows considerable strengthening, in agreement with the previous finding (described for Fig. 7.6) that after a period of weakening, the simulated MCS shows signs of reorganization. Similar behavior is found in the time evolution of $\overline{u'\theta'}$, as revealed by Figure 7.7d. Shortly after restart, the overall $\overline{u'\theta'}$ field in the MCS weakens considerably ($t = 4$ 10-hr in Fig. 7.7d). However, as time evolves, this field is gradually restored to values comparable to those in CNTRL, and by 5-hr $\overline{u'\theta'}$ is actually stronger than in CNTRL, indicating a sign of storm redevelopment.

Figure 7.6 shows that, by the time the simulated MCS in VAP regains strength, the solution has deviated significantly from CNTRL and does not reproduce correctly the important mesoscale features that characterize a bow echo. Again, it is possible that the MCS could regenerate those features if the simulation were continued past 6-hr. However, it is clear from the 2-hr runs studied here that the withdrawal of the moisture field has a greater impact upon the simulation than did the withdrawal of

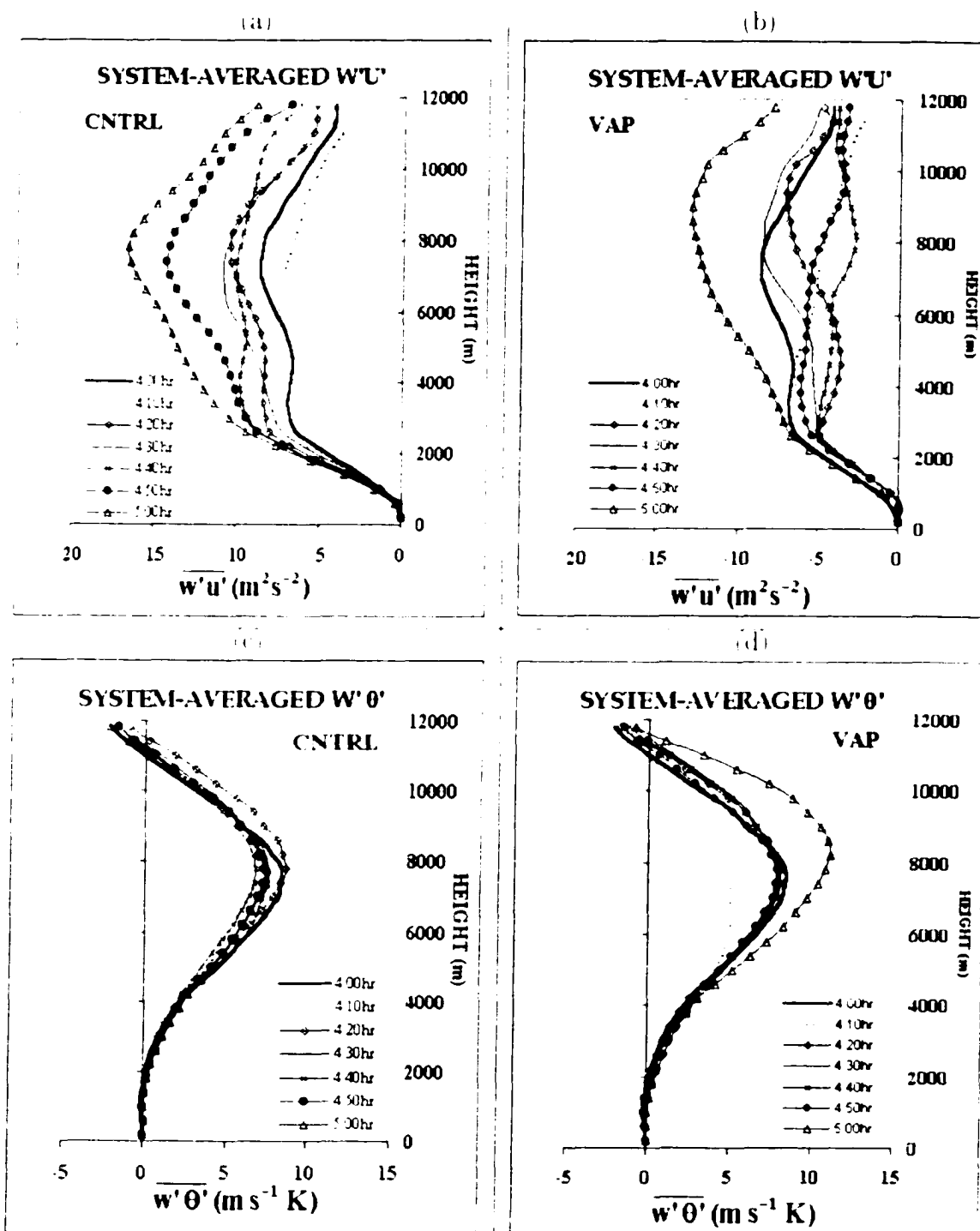


Figure 7.7 As in Fig 7.4, but with (b,d) referring to experiment VAP

θ' . In the following sections we address the dynamic adjustment mechanisms behind this behavior. First we focus on the low-level features of the MCS, followed by an analysis of the response among meteorological fields at middle and upper levels.

7.3 Evolution of the surface cold pool and the role played by evaporation at low levels in experiments THETA and VAP

In this section we focus on the physical processes influencing the behavior of *surface* features in the simulated MCS in experiments THETA and VAP.

Figure 7.8 depicts the evolution — within the first hour after restart — of the surface cold pool for simulations CNTRL, THETA and VAP, zoomed in to the area enclosed by a rectangle in Fig. 4.4b. In experiments CNTRL and THETA (Figs. 7.8a-c and 7.8d-f), the potential temperature shows a sharp gradient along the gust front, highlighting the strength of the advancing cold pool. Again, it is important to emphasize that in THETA, the θ' field within the cold pool is *entirely* withdrawn at restart. Twenty minutes later (Fig. 7.8d), the magnitude of θ' is not only comparable to that in CNTRL, but slightly stronger. As the integration proceeds (Figs. 7.8e-f), the gust front in THETA advances eastward at the same rate as in CNTRL, and the cold pool displays bulging segments associated with bow echo structures in the MCS. The surface outflow in THETA is strong, with derecho-like winds approaching 40 m s^{-1} .

In experiment VAP, (Figs. 7.8g-i) the cold pool is weaker, and the gradient in potential temperature along the gust front is not as sharp when compared to CNTRL and THETA. In addition, the gust front lags behind its CNTRL and THETA counterparts. The surface outflow is comparatively weak during most of the first hour of integration, but gradually regains strength, especially near the center of the domain

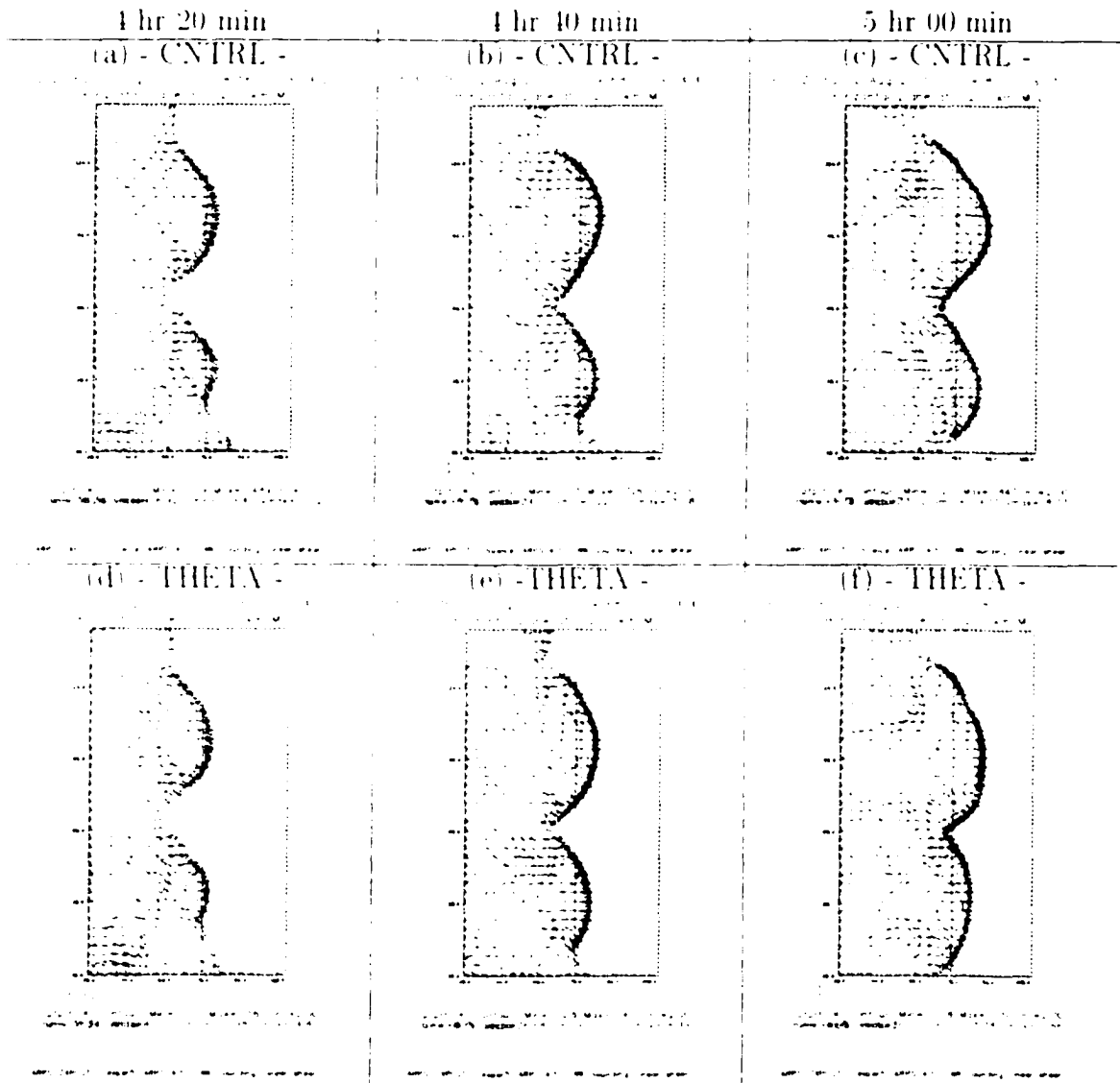


Figure 7.8: Evolution of the simulated gust front ($z = 200$ m) for the sector indicated by a rectangle in Fig. 4.1b: (a)-(c) CNTRL; (d)-(f) THETA; and, (g)-(i) VAP. First column: 4:20-hr; second column: 4:40-hr; third column: 5:00-hr. Dashed lines (referring to negative values) are contours of potential temperature perturbation, plotted at -2 K increments. The first contour from right to left is the -2 K line, indicating the leading edge of the advancing cold pool. Vectors are ground-relative winds in m s^{-1} , with a reference vector of 10 m s^{-1} indicated on the lower left corner of each panel. A line segment along $x = 176.0$ km is indicated in all panels as a reference to compare the eastward progression of the gust front from both experiments.

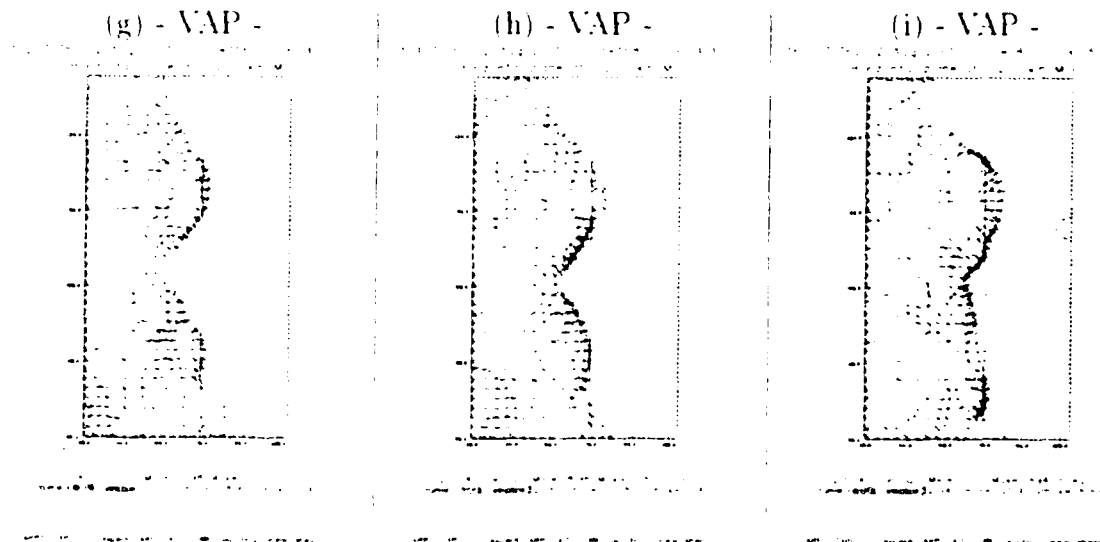


Figure 7.8 (continuation)

(Fig. 7.8i) where convergence supports active convection (Fig. 7.6b) between $x = 128$ km and 192 km.

Because the surface mesohigh owes its existence mostly to the hydrostatic response of the pressure field to negatively buoyant air within the cold pool (e.g., Johnson 2001), similar evolution of the MCS's surface structure is evident in terms of perturbation pressure (Fig. 7.9). Whereas a strong mesohigh is efficiently generated in THETA (Figs. 7.9d-f), supporting the derecho-like winds mentioned earlier, the development of a mesohigh is delayed in VAP (Figs. 7.9g-i). In fact, the magnitude of the pressure perturbations in the first 10-min in VAP actually *decrease* (not shown) before regaining intensity as the integration proceeds. With a weaker mesohigh and outflow, the generation of new convective cells along the gust front is less efficient, thus having an important impact upon the simulation of the bow echo. Not only does the MCS exhibit a decrease in convective activity, but its propagation speed also is reduced.

As recognized by Sawyer (1946) and Fujita (1959) several decades ago, the evap-

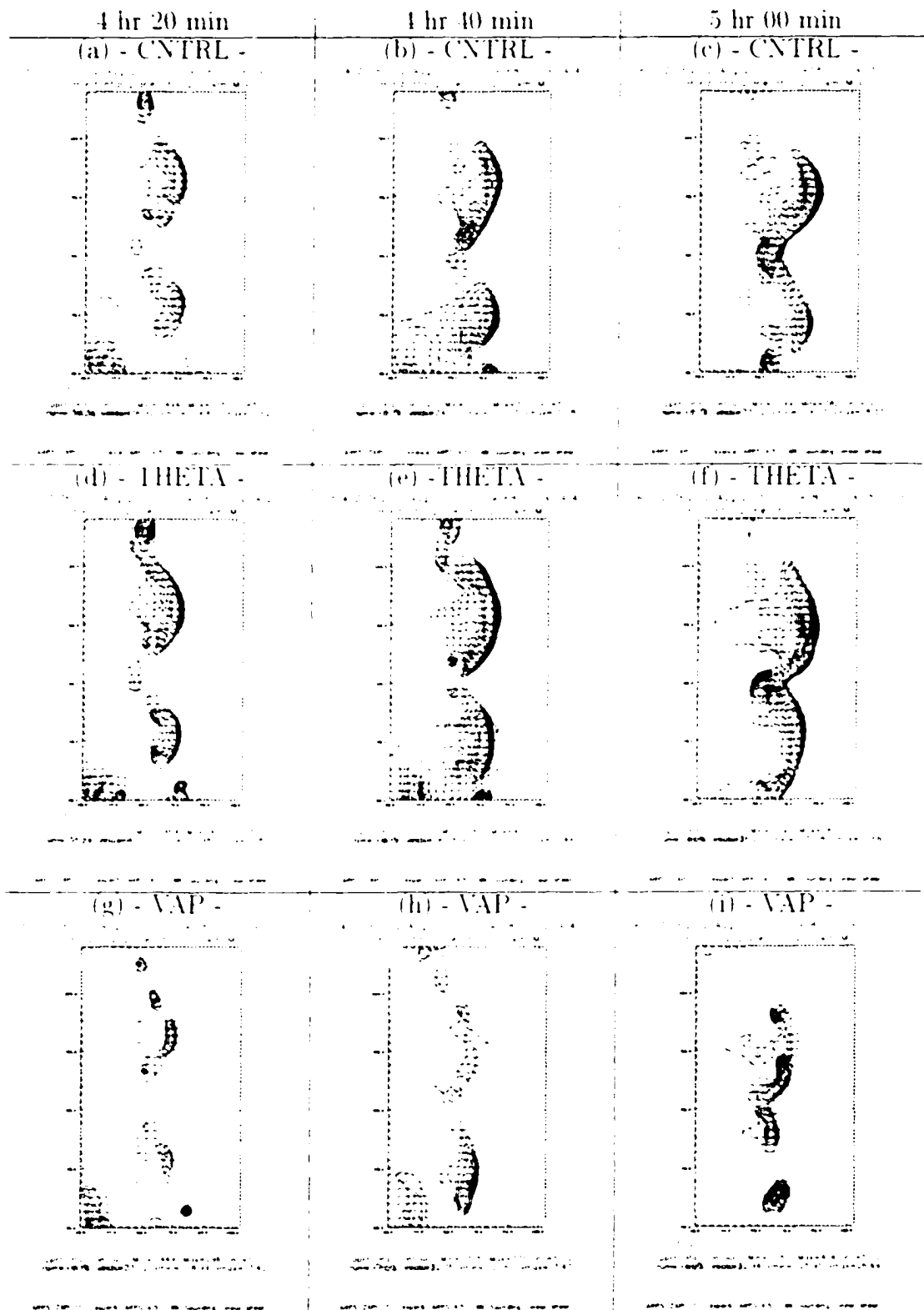


Figure 7.9: As in Fig. 7.8, but for the perturbation pressure field. Contour interval is 50 Pa.

oration of rain at low levels — leading to cooling of environmental air — is the main physical mechanism responsible for creating and maintaining the surface cold pool in MCSs (Johnson 2001). Thus, it is important to quantify the impact upon the low-level evaporation rate in THETA and VAP of setting θ' and q'_e equal to zero.

Figure 7.10 shows time series, from 4 to 5-hr, of rainwater evaporation rate averaged over the first two vertical model levels (i.e., $z = 200$ m and $z = 600$ m) for the area enclosed by a rectangle in Fig. 4.4b. The first 10-min is sampled every 1-min, with the remaining 50-min sampled at 10-min intervals. The evaporation rate (E_r) is computed using the following (Ogura and Takahashi 1971, Klemp and Wilhelmson 1978, Xue et al. 1995):

$$E_r = \frac{1}{\bar{\rho}} C' \left(1 - \frac{q_r}{q_{rs}}\right) (\bar{\rho} q_r)^{0.725} \left(2.030 \times 10^4 + \frac{9.584 \times 10^6}{q_{rs} \bar{p}}\right)^{-1}, \quad (7.1)$$

where C' is the ventilation coefficient, given by:

$$C' = 1.6 + 30.3922 (\bar{\rho} q_r)^{0.2046}. \quad (7.2)$$

In (7.1) and (7.2), the mixing ratios are in kg kg^{-1} , and E_r has units of $\text{kg kg}^{-1} \text{s}^{-1}$.

From Figure 7.10a, it is clear that E_r is significantly enhanced (weakened) starting at 4-hr in experiment THETA (VAP) owing to increased (reduced) dewpoint depression at low-levels, as evident in Fig. 7.1 (Fig. 7.5). In the first 10-min, E_r in THETA is more intense than in CNTRL, indicating that evaporative cooling at low-levels plays an important role in restoring the surface cold pool and maintaining a strong mesohigh.

The rate of change in potential temperature induced by the evaporation of rainwater ($\Delta\theta_{ER}$) can be estimated via (e.g., Tao et al. 1989, Xue et al. 1995):

$$\Delta\theta_{ER} = -L_v (\bar{\pi} c_p)^{-1} E_r, \quad (7.3)$$

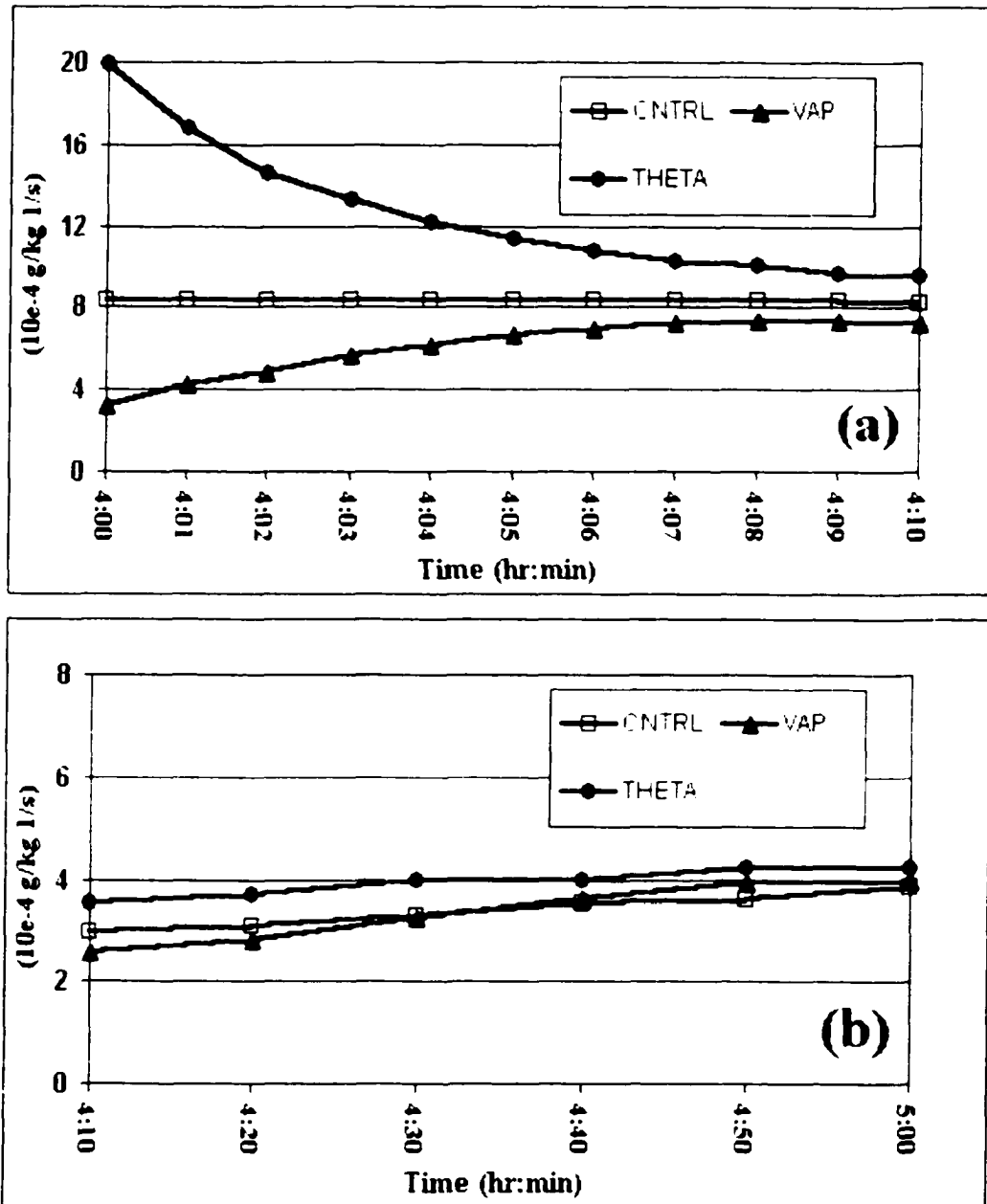


Figure 7.10: Time series of evaporation rate of rainwater (E_r) averaged for the first two model levels within the domain enclosed by a box in Fig. 4.4b for simulations CNTRL, THETA and VAP. Units: $10^{-4} \text{ g kg}^{-1} \text{ s}^{-1}$. (a) time evolution in the first 10-min after restart time, with E_r sampled at every 1-min; in (b) E_r is indicated from 4:10 to 5:00-hr, sampled at every 10-min

where $L_v = 2.5 \times 10^6 \text{ J kg}^{-1}$ is the latent heat of vaporization (or enthalpy of vaporization; Bohren and Albrecht 1998), $c_p = 1004 \text{ J kg}^{-1} \text{ K}^{-1}$ is the specific heat of air at constant pressure, and $\bar{\pi}$ is the Exner function, given by:

$$\bar{\pi} = (\bar{p}/p_0)^{R_d/c_p} \quad (7.4)$$

In (7.4), \bar{p} is the base-state pressure, p_0 is a constant reference pressure (10^5 Pa), and $R_d = 286.04 \text{ J kg}^{-1} \text{ K}^{-1}$ is the gas constant for dry air.

For $E_r = 1.25 \times 10^{-6} \text{ kg kg}^{-1} \text{ s}^{-1}$ — which is approximately the mean domain-averaged value during the first 10-min in experiment THETA (Fig. 7.10a) — and $\bar{\pi} \approx 0.987$, we find that $\Delta\theta_{ER} = -3.15 \times 10^{-3} \text{ K s}^{-1}$, which translates to a θ' of approximately -2.0 K after 10-min². The corresponding value for CNTRL is -1.2 K.

Conversely, in experiment VAP, E_r is *below* the average value found in CNTRL in the first 10-min. This coincides with the period during which the development of the cold pool and mesohigh is delayed. The average $\Delta\theta_{ER}$ in VAP during this time period is around $-1.5 \times 10^{-3} \text{ K s}^{-1}$, leading to a θ' of -0.9 K after 10-min. Thus, as expected, the low-level evaporative cooling in VAP is less efficient.

As the integration proceeds, E_r in experiments THETA and VAP converge to CNTRL values (Fig. 7.10b). By this time (around $t = 4$ 20-hr), the cold pool and mesohigh in THETA are slightly stronger than in CNTRL (Figs. 7.8d and 7.9d), whereas in VAP, such surface features are less intense than the CNTRL counterparts (Figs. 7.8g and 7.9g). Hence, in VAP, the continuously increasing E_r favors the re-strengthening of the surface cold pool and mesohigh (and, consequently, the surface outflow), but only after a significant delay (Figs. 7.8g-i and 7.9g-i), after which the structure of the MCS in VAP differs substantially from that in CNTRL.

²Note that this result underestimates the *maximum* magnitude of (negative) θ' generated in the cold pool after 10-min of integration in THETA, which reaches -9.0 K (not shown). This is because: (i) the -2.0 K found using (7.3) is an *average* value for the domain indicated in Fig 7.8, not the minimum value; (ii) the evaporation of cloud water (q_c) and advection effects also contribute to negative θ' , and are not taken into account in this simple quantitative analysis. The same consideration applies for the values of $\Delta\theta_{ER}$ obtained for CNTRL and VAP, mentioned later.

Figure 7.11 shows the time evolution, from $t = 4$ -hr to 5-hr, of system-averaged profiles of q'_r for simulations CNTRL, THETA and VAP — referring to the area enclosed by a rectangle in Fig. 4.4b. Panel *a* shows that positive (negative) values of q'_r are evident above (below) $z = 5.0$ km, indicating moistening (drying) of the mid and upper levels (lower levels) in the MCS. In THETA, the evolution of the system-averaged q'_r field follows the CNTRL counterpart quite well, and by the end of the first hour the low-level dryness is actually more intense than in CNTRL. In VAP, q'_r is equal to zero everywhere at $t = 4$ -hr, except at low levels (Fig. 7.11b)

because we do not allow supersaturation. With time, the moisture field tends to be restored, but the low-level dryness is considerably underestimated. Because environmental dryness is also an indicator of the cold pool's strength (e.g., ED01), the findings for THETA and VAP are in agreement with the results discussed above. Factors other than near-surface processes are contributing to such behavior in the q'_r field in experiments THETA and VAP, and will be discussed later.

Summarizing, in experiment THETA, enhanced low-level rainwater evaporation — especially during the first 10-min following restart — is one of the mechanisms accounting for the presence of a strong MCS within the first hour of integration, particularly as the thermal structure of the surface cold pool is efficiently regenerated. On the other hand, in experiment VAP, the reduced evaporation influences the intensity of the cold pool and accompanying mesohigh early in the simulation, leading to a delay in their intensification. Such features are gradually regenerated in VAP as the integration proceeds, but with the simulated storm already displaying structures that differ substantially from those in CNTRL.

Using the same idealized sounding as in our study but with a different vertical wind profile (favoring the supercell mode of convection), Weygandt et al. (1999) also found that the surface cold pool was efficiently restored within 20-min in an

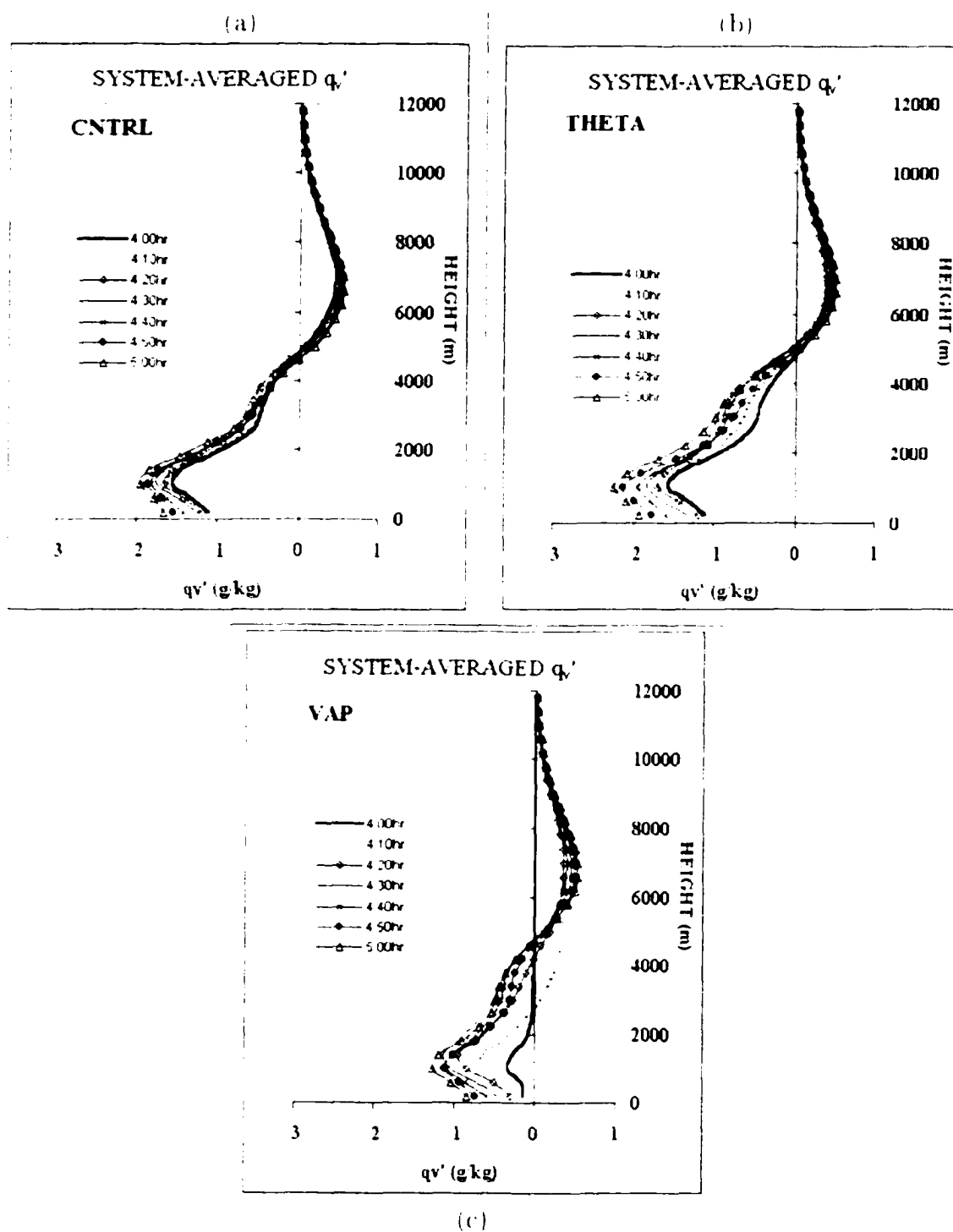


Figure 7.11: Time evolution, from 4-hr to 5-hr (at 10-min increments), of system-averaged profiles of perturbation water vapor mixing ratio (in g kg^{-1}). (a) CNTRL, (b) THETA, (c) VAP. The averaging is applied for the region enclosed by a rectangle in Fig. 4.4b.

experiment in which θ' was set to zero. The recovered cold pool surged further downstream compared to the corresponding control run, suggesting that such surface feature become stronger than in the control simulation, in general agreement with the present results. They did not, however, explore in detail the influence upon the supercell simulation of withdrawing q'_e , but their statistical results suggest that such withdrawal also generated a cold pool that deviated significantly from the control run, especially after 50-min. Figure 7.12 shows their time series of mean *surface* θ' error for each withdrawal experiment. The simulation with q'_e set back to base state (indicated by qv in Fig. 7.12) has relatively large mean error, especially after 60-min.

These results agree with the general notion that a convectively-generated cold pool is important to the dynamics and propagation of squall-lines and bow echoes (e.g., Rotunno et al. 1988, Weisman 1993, Moncrieff and Liu 1999, Fritsch and Forbes 2001, ED01, Corti et al. 2002, and others). Moreover, they highlight the importance of specifying low-level moisture and temperature fields *within* convective systems because the intensity of important surface features can be strongly influenced by evaporation rates at low levels.

On the other hand, there is evidence that the impact upon cold pool evolution of withdrawing q'_e may depend rather significantly upon the environmental thermodynamic profile. In studying the sensitivity of a supercell thunderstorm simulation (initialized with data retrieved from Doppler radar) to the specification of water vapor, Weygandt et al. (2002b) performed a test in which the q_e field was set back to the base state as determined from a proximity sounding. They found that most of the cold pool structure was reasonably recovered after just 30-min of simulation, and that the position of the gust front was not significantly altered during this period in comparison to a control simulation. These results indicate that the weakening of surface features (or the delay in their development) due to the withdrawal of q'_e was

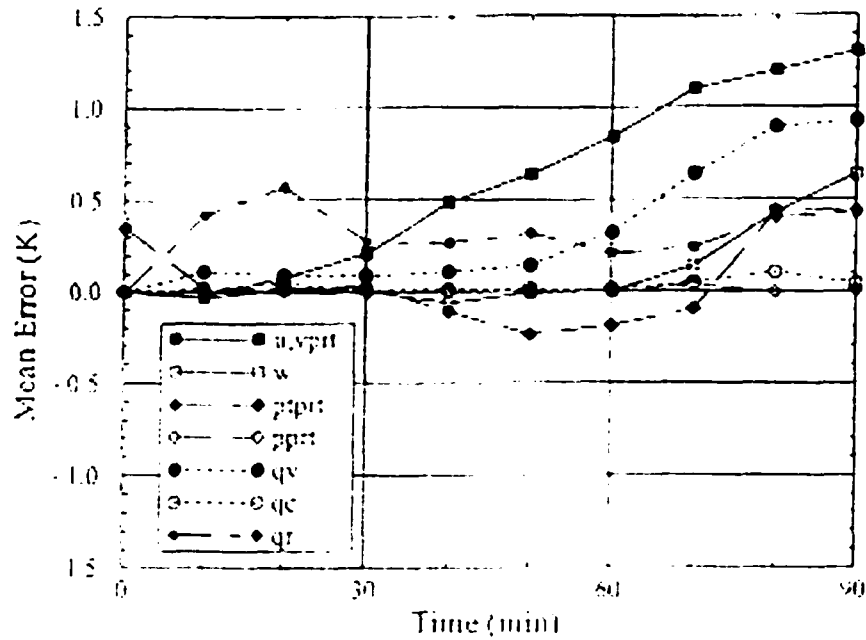


Figure 7.12 Time series of mean surface perturbation potential temperature error for withdrawal experiments in Weygandt et al. (1999). Time zero refers to restart time. (Adapted from Weygandt et al. (1999))

confined to a much shorter period than in our bow echo simulation, such that the storm simulated by Weygandt et al. (2002b) did not deviate from the control run as much as in our case.

In addition to obvious difference in the wind profile, the background environment in Weygandt et al.'s (2002b) study had higher CAPE (around 3100 J kg^{-1}) than the idealized sounding used in the present research. More importantly, the proximity sounding in Weygandt et al. (2002b) was *not* moist throughout the entire troposphere, but displayed a pronounced dry layer between 700 and 500 hPa. This profile should favor the development of stronger downdrafts and transport of low θ_e air into the surface cold pool, thus contributing to a more rapid recovery of the low-level q'_e field and consequently of the low-level E_r — and allowing a good representation of cold pool evolution. Therefore, future studies must address the sensitivity of results upon

the ambient environment, especially with regard to the impact of the moisture field upon cold pool evolution.

Because the surface cold pool (low-level evaporation) is not the only feature (physical process) affected by resetting the thermodynamic fields to the base state, it is necessary to examine the response of meteorological fields in other regions and analyze their impact on the simulation of the bow echo. In the next section, experiments THETA and VAP are analyzed separately, followed by a general discussion.

7.4 Dynamic adjustment aloft: experiment THETA

Figure 7.13 compares vertical cross sections (xz -plane) of θ_e and wind fields for experiments CNTRL and THETA at $t = 4:10, 4:30$ and $4:50$ -hr¹, across the main bow echo segment. The domain shown has an 80 km (12 km) horizontal (vertical) extent. Only the 326 K and 334 K isentropes are indicated (see caption). A detailed analysis of the CNTRL solution was performed in chapter 4 (e.g., Fig. 4.7) and is briefly repeated here for convenience. Figures 7.13a,c,e show the solution from CNTRL, which displays an upshear-tilted updraft that transports boundary-layer moisture (high θ_e air) aloft, with strong horizontal divergence at upper levels. A RIJ also is evident from low to mid levels, embedded in the low θ_e air — the 326 K isentropes upstream from the updrafts basically indicate the vertical extent of the rear-to-front flow. The transport of dry air to the surface cold pool through downdrafts is clear as the RIJ descends near the convectively active region. This is an important process contributing to enhanced E_r at low levels.

In experiment THETA, (Figs. 7.13b,d,f) the updrafts remain strong, which also is revealed by the intense horizontal divergence at upper levels, especially from 4:10-hr

¹These times are chosen because they best summarize the evolution of the simulated MCS in experiment THETA and VAP in the first hour after restart time.

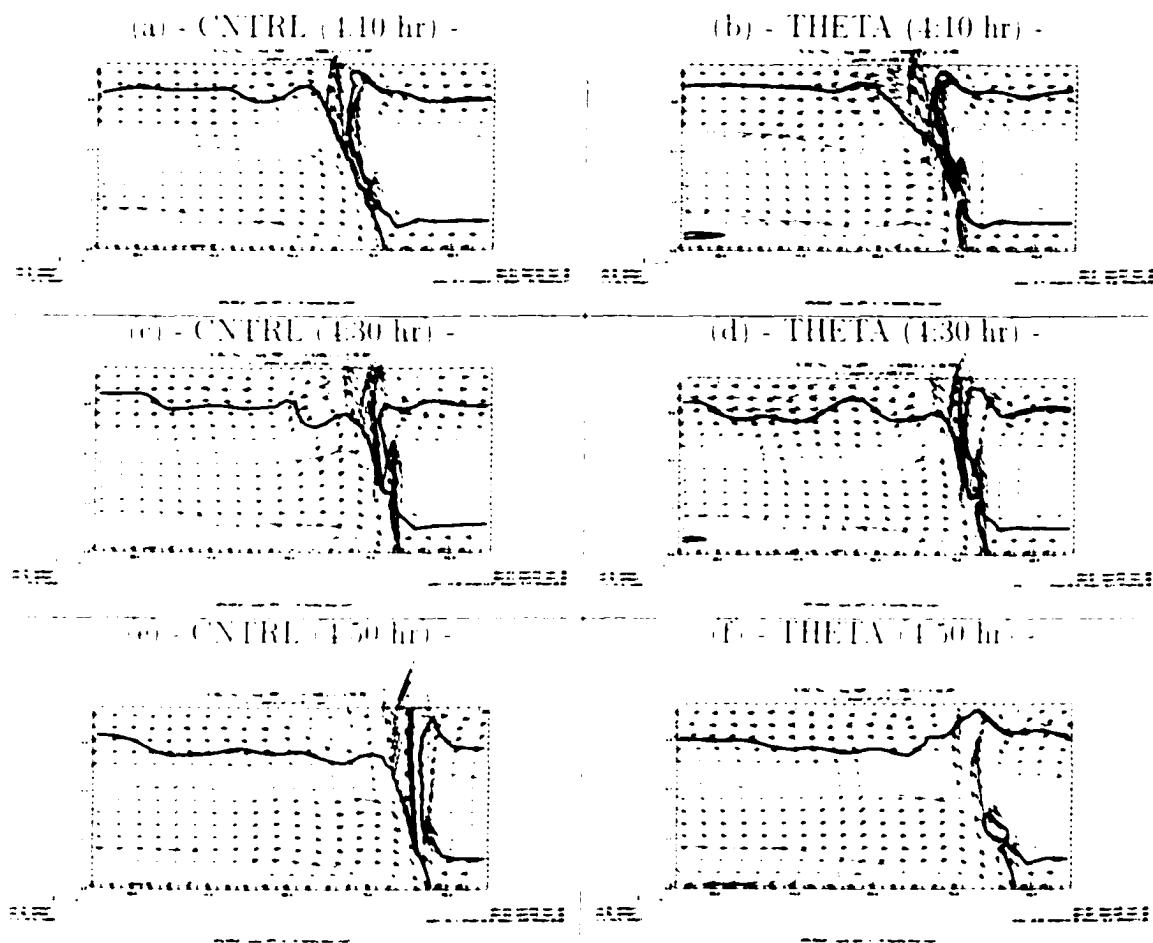


Figure 7.13 Vertical cross sections (xz-plane), from surface to $z = 12$ km, of equivalent potential temperature (θ_e , solid lines) and storm-relative wind field (vectors) at distinct times ($t = 4:10, 4:30$ and $4:50$ -hr) for experiments CNTRL (first column) and THETA (second column). Only the 326 K (thin solid line) and 334 K (thick solid line) isentropes are plotted. At 4:10 and 4:30-hr (a-d) the vertical cross section is along $y = 205$ km, while at 4:50-hr (e-f) it is along $y = 197$ km (following the gradual southward displacement of the apex of the main bow echo segment in CNTRL). The horizontal extent of the domain shown is 80 km long, from $x = 120$ km to $x = 200$ km. Domain translation is eastward at 22.0 m s^{-1} .

to 1:30-hr. At the surface, the horizontal extent of the layer with $\theta_e < 326$ K is narrow at 1:10-hr (Fig. 7.13b) as a consequence of the increased surface potential temperature at restart. However, as the integration proceeds, this layer becomes broader (Figs. 7.13d,f), converging to the CNTRL solution. The RIJ in experiment THETA is well represented in both magnitude and structure in the first hour⁴, and contributes to the recovery of dryness within the surface cold pool due to the downward transport of low θ_e air. This behavior helps explain the presence of relatively intense low-level dryness revealed in Fig. 7.11b, and the efficient regeneration of the surface cold pool in THETA (associated with stronger evaporation at low levels).

Another interesting feature in experiment THETA is the presence of a relatively strong mid-level downdraft trailing the convective region (Figs. 7.13b,d), at times characterizing a mesoscale rotor as it interacts with the RIJ. Downdrafts also are evident just ahead the leading updrafts. With time, the trailing downdraft becomes weaker and propagates rearward. The generation of convective-scale mid-level downdrafts is discussed in several investigations (Knupp and Cotton 1985, Srivastava 1987, Fovell and Ogura 1988, Sun et al. 1993, Igau et al. 1999, Yuter and Houze 1995a,b, Wakimoto 2001, among others), and more than one mechanism can be responsible for them⁵, ranging from melting and evaporation of precipitation (e.g., Srivastava 1987) to dynamically induced downward VPGA (e.g., Rotunno and Klemp 1982). Other studies have addressed processes associated with gravity wave-like propagation of (“compensating”) downdrafts away from heating sources in MCSs (e.g., Bretherton and Smolarkiewicz 1989, Mapes 1993, Fovell 2002). More than one of these processes may be taking place in our simulation concomitantly.

In the discussion that follows, we examine the evolution of buoyancy, pressure and

⁴Recall that during the following 1-hr of integration, the rear-to-front flow in THETA remains strong, but with less meridional variation of the zonal momentum field (compared to the CNTRL solution), as mentioned in section 7.1 (Fig. 7.3).

⁵Wakimoto (2001) contains a comprehensive review on mechanisms driving the generation of mid-level downdrafts.

wind fields early in experiment THETA, and seek to identify the most important mechanisms driving the general behavior of the numerical solution.

7.4.1 Early evolution of buoyancy, pressure and wind fields

Figures 7.14b-g show the time evolution of the buoyancy field, as defined by Eq. 5.8, for experiment THETA at 2-min intervals, from the restart time to 4:10-hr. The solution from CNTRL at 4:05-hr also is shown for comparison (Fig. 7.14a) and, for the purposes of our analysis, is representative of the CNTRL solution in the 10-min period being examined. In CNTRL, the buoyancy field is consistent with an active MCS (Lafore and Moncrieff 1989, Sun et al. 1993, Johnson and Mapes 2001), with negative buoyancy in the surface cold pool and in the anvil-level (above $z = 9.6$ km). Positive values dominate the mid levels, where latent heating plays an important role in maintaining a positively buoyant “plume” (e.g., Pandya and Durran 1996) that extends mostly rearward. In our analysis, this region will be called the *buoyant plume*.

In experiment THETA, the buoyancy field at restart (Fig. 7.14b) is significantly weakened, highlighting the importance of thermal buoyancy to the total buoyancy field. Figure 7.15 illustrates this by comparing the magnitude of each term composing the buoyancy field for the CNTRL simulation at 4:05-hr. These terms are (see Eq. 5.8): thermal buoyancy ($g\theta'/\bar{\theta}$), perturbation pressure buoyancy ($-gp'_x/\bar{p}$), perturbation water vapor mixing ratio term ($gq'_x/(1 + \bar{q}_v)$), and condensate loading term ($-g(q'_v + q_{lc})/(1 + \bar{q}_v)$). The thermal buoyancy clearly is the dominating term (note that distinct contour intervals are used in Fig. 7.15; see caption), followed by water vapor and condensate loading. Therefore, it is no surprise that setting θ' to zero in experiment THETA has a significant impact on the buoyancy field.

With time, the buoyancy field gradually is restored (Figs. 7.14c-g). At low

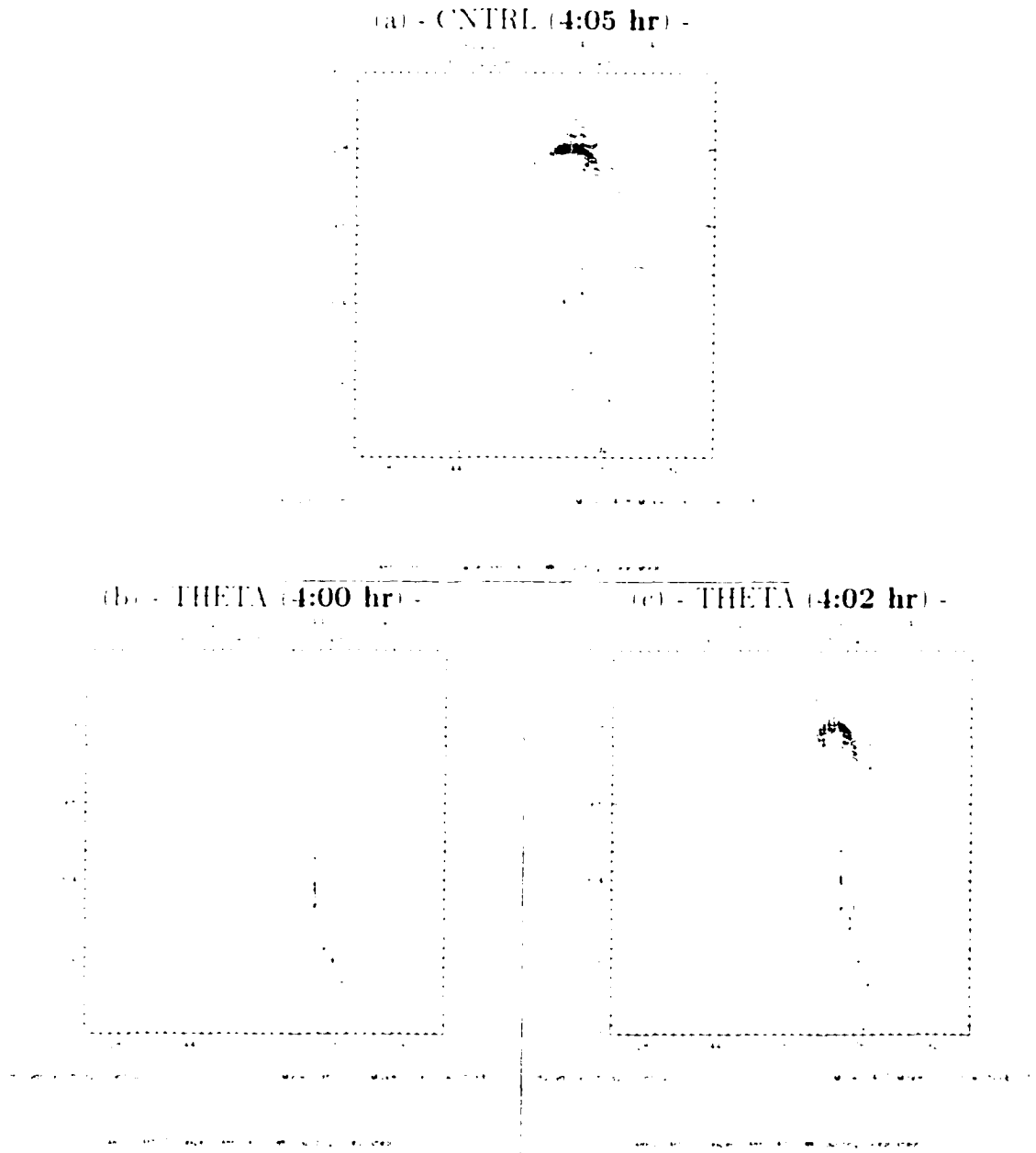


Figure 7.14: Vertical cross sections from surface to $z = 16$ km (along $y = 205$ km) of acceleration due to buoyancy (given by Eq. 5.8), contoured at 0.05 m s^{-2} intervals. (a) solution from CTRL simulation at $t = 4.05$ -hr (reference for comparison); (b)-(g) first 10-min evolution in experiment THETA, with solutions shown at 2-min intervals. Solid (dashed) lines indicate positive (negative) values, with zero lines being suppressed. The horizontal extent of the domain shown is 80 km long, and is the same as in Fig. 7.13. Domain translation is eastward at 22.0 m s^{-1} .

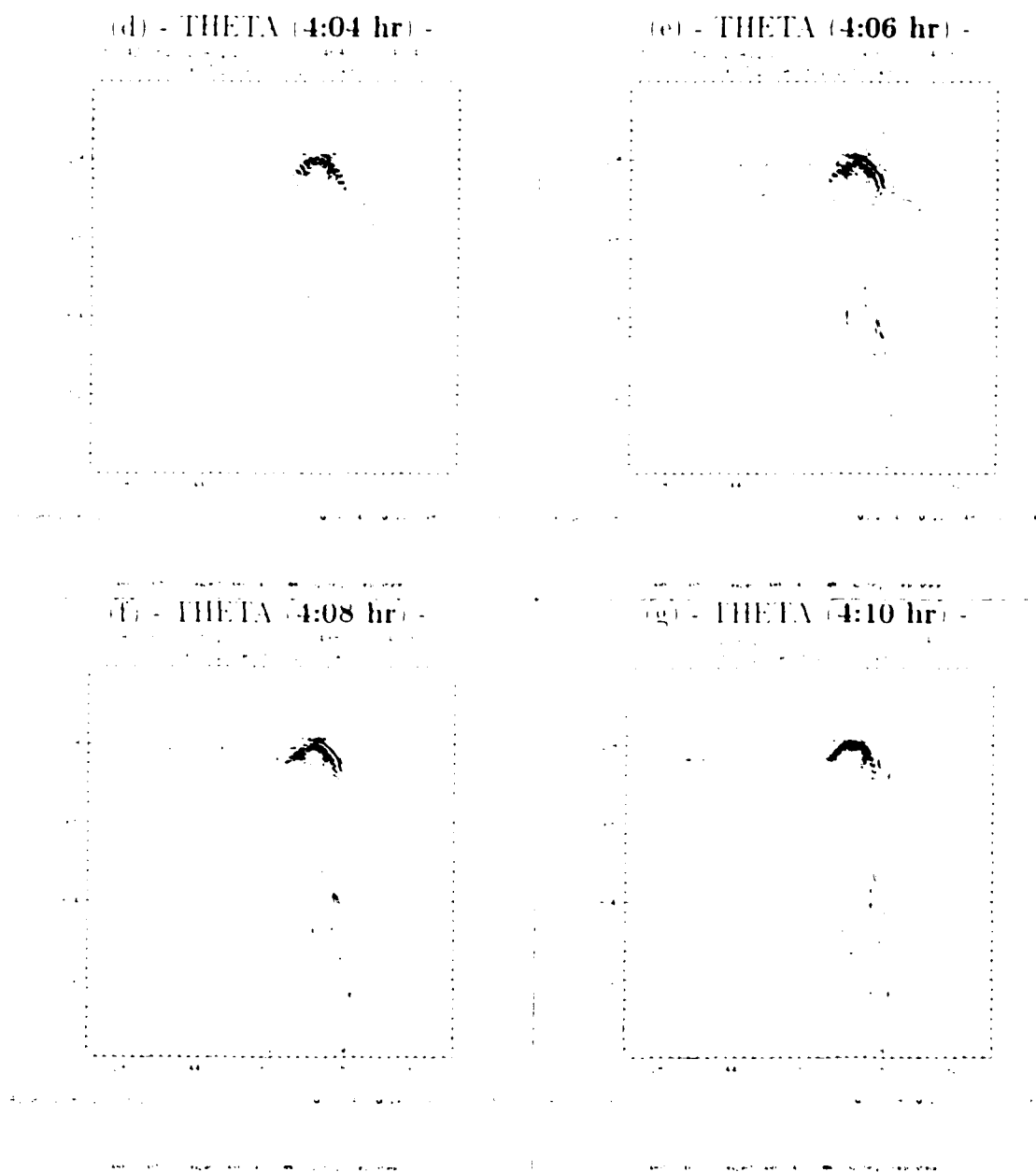


Figure 7.14 (continuation)

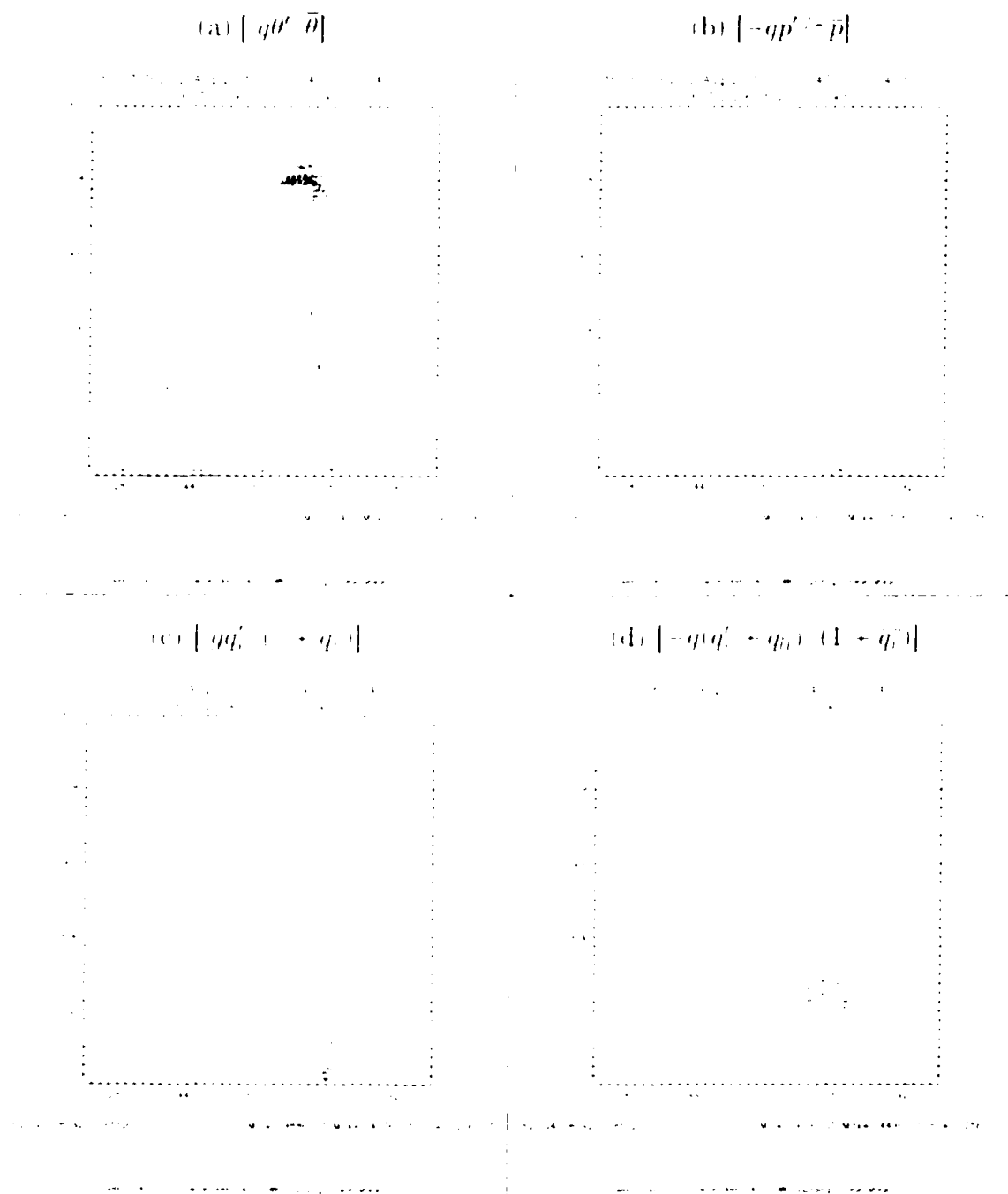


Figure 7.15 As in Fig. 7.14, but for the acceleration induced by distinct terms composing the buoyancy field (given by Eq. 5.8) for CTRL simulation at 4:05-hr: (a) thermal buoyancy; (b) perturbation pressure buoyancy; (c) perturbation water vapor mixing ratio term; (d) condensate loading term. In (a) the contour interval is 0.05 m s^{-2} , while in (b), (c), (d) a 0.0125 m s^{-2} contour interval is used. The domain shown is the same as in Fig. 7.14.

and upper levels, negatively buoyant air is mostly regenerated by enhanced evaporation–sublimation rates which lead to cooling, while the mid level buoyant plume is restored by latent heating associated with enhanced condensation–deposition. The buoyant plume propagates rearward quite efficiently, possibly as a result of both advective effects (e.g., Lafore and Moncrieff 1989, Weisman 1992) and propagation of IGWs forced by an upshear tilted convective line (e.g., Pandya and Durran 1996, Nachamkin and Cotton 2000). A more detailed analysis of such mechanisms is presented below. It is interesting also to note the “signature” of a rapidly developing cold pool in terms of negative buoyancy at low levels.

A very important process regarding dynamic adjustment is the response of pressure to the evolution of the buoyancy field. In section 2.2 we described how a buoyancy source induces perturbations in pressure (Houze 1993, Yuter and Houze 1995b), and discussed that a low (high) pressure perturbation is expected to form just underneath (above) regions of positive buoyancy. This response is clear in our results. Figure 7.16 is similar to Fig. 7.14, but showing the evolution for pressure and wind fields in THETA (Figs. 7.16b–g), as well as the corresponding solution from CNTRL at 4.05-hr (Fig. 7.16a).

At the restart time, the pressure field in THETA is the same as in CNTRL, with a surface mesohigh associated with the cold pool, a low- to mid-level mesolow, and an upper-level high pressure system. This structure is consistent with the *original* distribution of the buoyancy field, as shown in Fig. 7.14a for CNTRL, but *not* with the modified buoyancy field at restart for THETA (Fig. 7.14b). While the pressure perturbations trail rearward for approximately 100 km behind the leading edge of the bow echo, the buoyancy perturbation is confined to a much narrower region. As the simulation starts, the pressure field responds to the modified buoyancy field, as evident in Fig. 7.16c. The surface mesohigh is substantially weakened after 2-min.

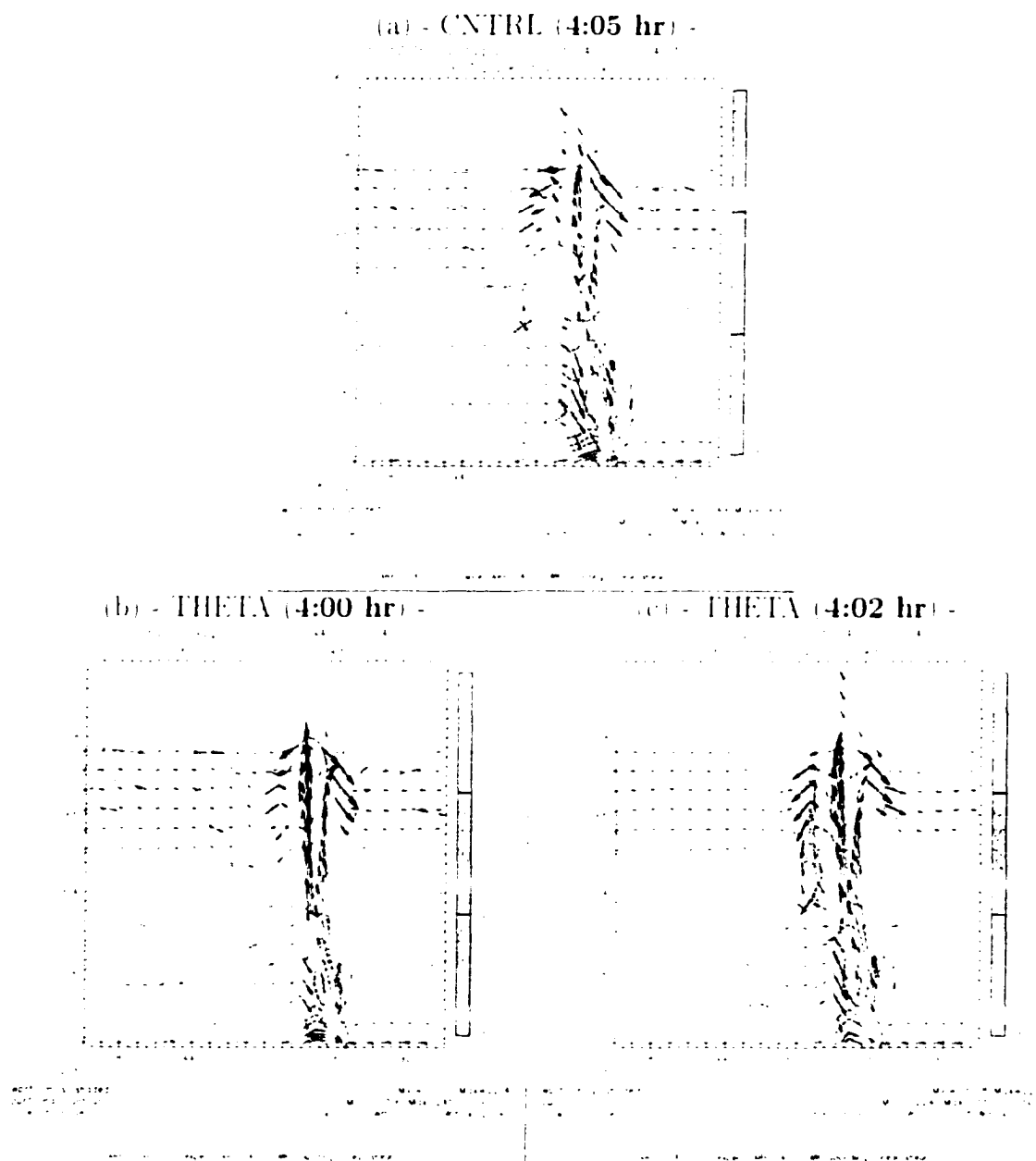


Figure 7.16. As in Fig. 7.14, but for perturbation pressure (contours, Pa) and storm-relative winds (vectors, m s^{-1}). Pressure field is contoured at 50 Pa intervals, with solid (dashed) lines indicating positive (negative) values, and zero lines being suppressed. Areas with downdrafts equal to or stronger than -1 m s^{-1} are shaded (single color shading).

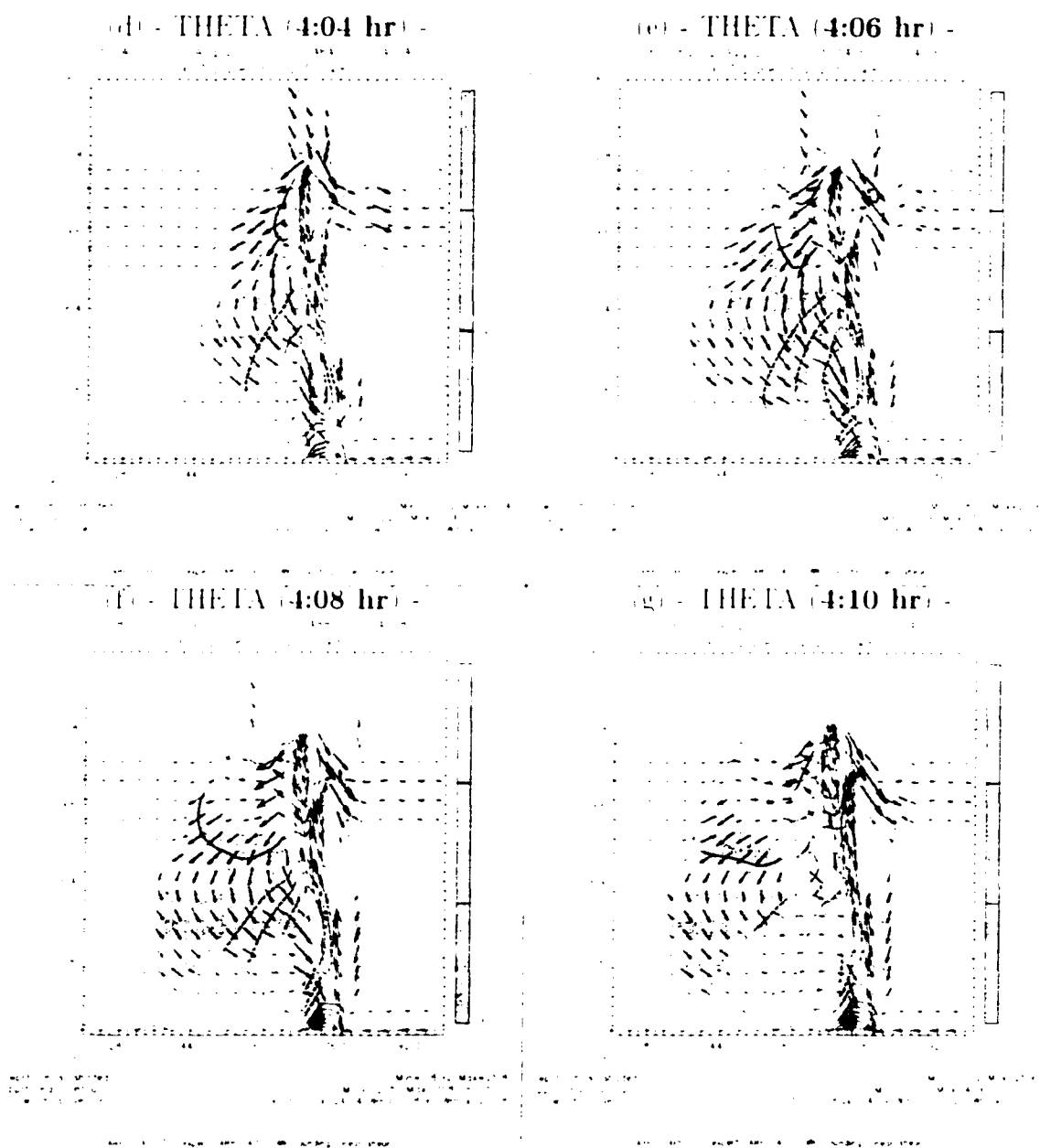


Figure 7.16 (continuation)

and the low- to mid-level mesolow and upper-level mesohigh become more horizontally confined. As the simulation proceeds (Figs. 7.16d-g), the pressure features are restored following the evolution of the buoyancy field. Note, for example, how efficient is the regeneration of the surface mesohigh and how it agrees with the rapid redevelopment of negatively-buoyant air within the cold pool (Figs. 7.14d-g). Strong negative (positive) perturbations in pressure are located just underneath (above) the buoyant plume, agreeing with the adjustment described in an idealized way in section 2.2. Our result also is consistent with the finding from Weisman (1993) that the pressure field structure along the apex of the bow echo is mostly forced by buoyancy effects.

The results above suggest that *correct specification of the pressure field within an MCS is useless if the buoyancy field is not adequately specified*. They also highlight the importance of the specification of regions of saturation and subsaturation in the storm system, given the response of the buoyancy field to latent heating/cooling.

Another important dynamic adjustment evident in Figs. 7.16b-g involves the wind field. While the magnitude of the updrafts on the leading edge of the system is not significantly altered, downdrafts are modified around the buoyant plume. Shortly after restart (Figs. 7.16c,d), a well-defined mid-level downdraft forms just upstream of the leading updrafts, displaying a structure similar to transition-zone downdrafts observed in mature squall lines (e.g., Biggerstaff and Houze 1993, Sun et al. 1993, Braun and Houze 1994). As the integration proceeds (Figs. 7.16e-g), the downdraft gradually propagates rearward — following the same behavior described for buoyancy and pressure fields — and eventually becomes detached from the leading updrafts (Fig. 7.16g). Note that the mid-level downdraft core during this period follows the upstream edge of the buoyant plume described in Fig. 7.14⁶.

⁶Evidently, the use of a low threshold value of -1 m s^{-1} to characterize the downdraft area potentially connects individual downdrafts into a single conglomerate, but the feature which we are interested in is the *general* pattern.

In Figure 7.17, downdraft areas are superimposed on the region with condensate loading acceleration $(-g(q'_c + q'_i)/(1 + \bar{q}_r))$ equal to or less than -0.025 m s^{-2} (dashed contour). Areas with cloud water and cloud ice mixing ratios equal to or greater than 0.1 g kg^{-1} also are shown (solid lines; see caption for details). The time sequence (Figs. 7.17a-f) does *not* display a clear connection between the evolution of the condensate loading term and the rearward amplification of the trailing downdraft area. Furthermore, mid-level latent *heating*, rather than cooling, is enhanced early in experiment THETA due to increased saturation areas, as discussed in section 7.1. Thus, precipitation loading and latent cooling do *not* seem to be important forcing mechanisms behind the *behavior* of the trailing downdraft⁷. In fact, our results do show a trailing mid-level downdraft within a *positively buoyant* layer (compare Figs. 7.14b-g and 7.16b-g).

The presence of positively buoyant mid-level downdrafts is not a new finding. Studying the structure of radar-retrieved fields for a mature mid-latitude squall line, Sun et al. (1993) found mid-level downdrafts within regions of positively buoyant air just upstream of the leading updrafts, indicating that they consist of air being forced downward below its equilibrium level. Although not explicitly reported, positively buoyant trailing downdrafts at mid to upper levels also were generated in a 2-D simulation of a mid-latitude squall line by Fovell and Ogura (1988) (Biggerstaff and Houze 1993). Other studies, such as Trier et al. (1997), Wei et al. (1998) and Igau et al. (1999), focusing on tropical squall lines, reported mid-level buoyant downdrafts as well.

of trailing downward motion spreading rearward. Fovell and Ogura (1988), for example, identified the time-averaged upper-level subsidence on the rear flank of a numerically-simulated 2D squall line as being the net result of convective-scale downdrafts moving rearward relative to the leading convective activity. It is not our objective to study the very fine details of this structure because we mostly aim at identifying the more general dynamic adjustment process.

⁷ This analysis refers to the mid-level *convective-scale* downdraft that **leads** the rearward propagation of the downward motion area, evident in Figs. 7.16b-g, and Fig. 7.13d at later time), not to a *mesoscale* downdraft typical of trailing precipitation areas in MCSs (Zipser 1977) for which *latent cooling* underneath the trailing anvil cloud is important (Ryan and Carstens 1978, Leary and Houze 1979, Stensrud et al. 1991, Yang and Houze 1995b, Wakimoto 2001).

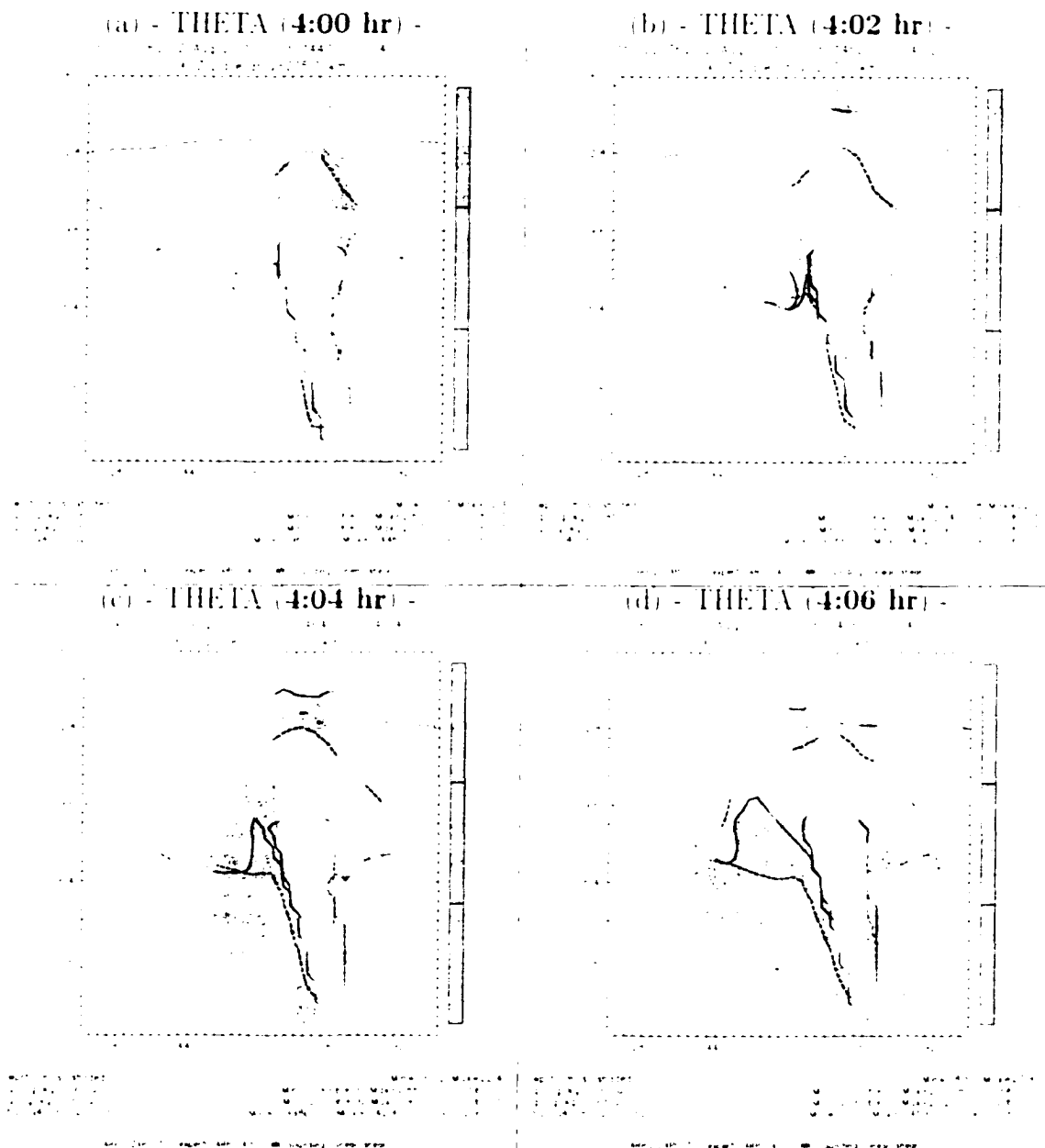


Figure 7.17 As in Fig. 7.14, but for: cloud water (q_c) and cloud ice (q_i) mixing ratios (solid lines); condensate loading term of the acceleration due to buoyancy ($-g(q'_c + q'_i)/(1 + \bar{q}_c)$; dashed line); and downdraft areas (single shading). Only the 0.1 g kg^{-1} mixing ratio line is indicated for q_c and q_i , with the lower (upper) contour referring to q_c (q_i). The dashed line encloses areas with condensate loading term equal to or less than -0.025 m s^{-2} . Areas with downdrafts equal to or stronger than -1 m s^{-1} are shaded (single color shading). (a)-(f) first 10-min evolution in experiment THETA, with solutions shown at 2-min intervals.

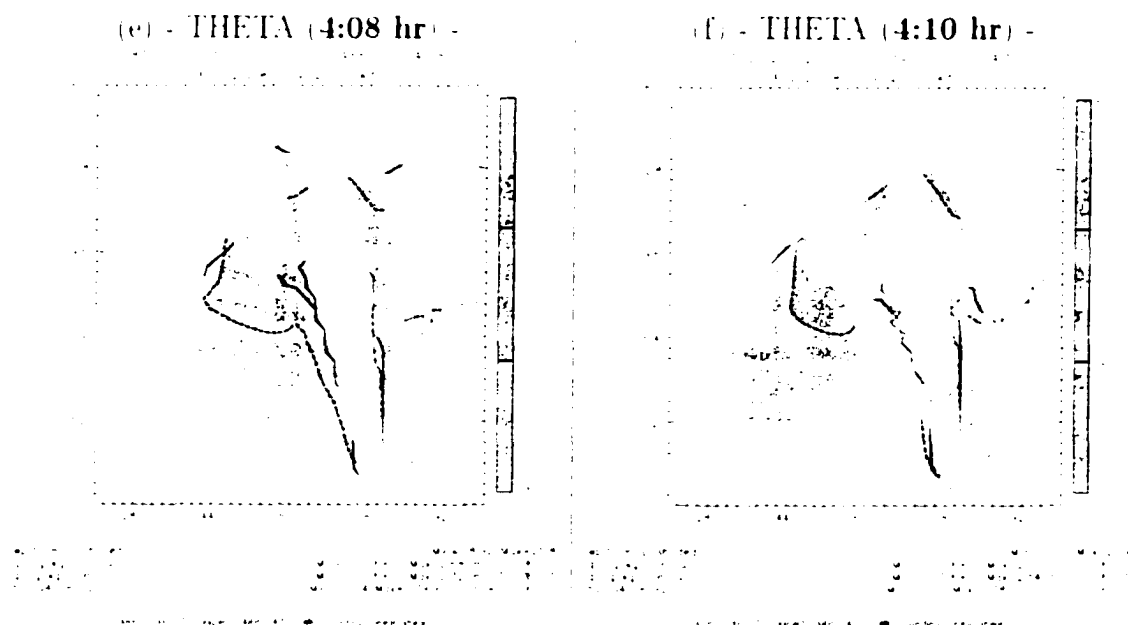


Figure 7.17 (continuation)

Downdrafts can be dynamically related to buoyant plumes through pressure gradient forces required to satisfy mass conservation (Yuter and Houze 1995b, Wakimoto 2001), which is a consequence of the adjustment between buoyancy and pressure fields discussed in section 2.2. Figure 7.18, adapted from Houze (1993) and Wakimoto (2001), illustrates the buoyancy pressure gradient acceleration (BPGA) field induced by an idealized positively buoyant air parcel of finite dimension (i.e., high aspect ratio). The structure shown is obtained analytically from Eq. 2.7 (Houze 1993, Yuter and Houze 1995b). Although the streamlines in Fig. 7.18 do not necessarily represent the actual displacement of individual air parcels, they indicate the direction in which the BPGA forces atmospheric motion. Note that, on the *sides* of the buoyancy perturbation, *downward* acceleration (compensating subsidence) is induced. Interestingly, the numerical solution shown in Fig. 7.14 and 7.16 reveals that *the*

³Yuter and Houze (1995b) identified this physical mechanism as the best “candidate” to explain the observation of mid- and upper-level downdrafts located at the sides of mid- and upper-level buoyant updrafts in a Florida convective line under weak vertical wind shear (Yuter and Houze 1995a).

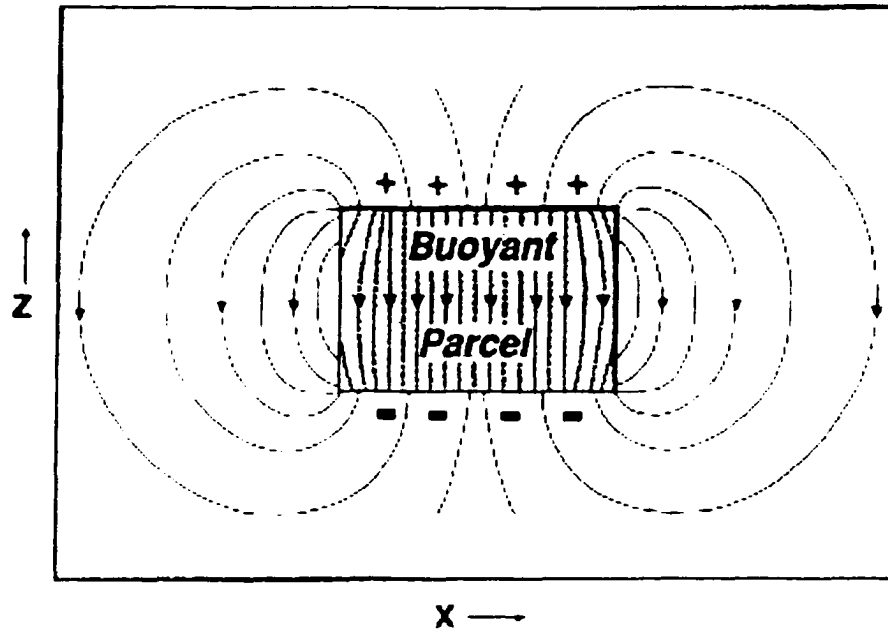


Figure 7.18: Force field in the xz -plane of the buoyancy pressure gradient acceleration (BPGA) induced by a homogeneous and positively buoyant air parcel (or layer) of finite dimensions. Lines of BPGA are shown as streamlines. This field is obtained analytically from Eq. 2.7. Plus and minus signs indicate the sign of the buoyancy forcing (r.h.s. of 2.7). Adapted from Wakimoto (2001) (originally from Houze 1993, Yuter and Houze 1995b). (Note: our Fig. 2.3a is based on the figure above)

*trailing mid-level downdraft forms on the upstream **side** of the buoyant plume*, in a fashion that seems to agree with the discussion above. Moreover, on the downstream flank of the buoyant plume, downdrafts also are formed (Fig. 7.17), although weaker compared to the upstream counterpart.

The physical mechanism involving induced BPGA is valid for situations in which the pressure field is not affected by dynamic forcing, in which case (2.6) can be reduced to (2.7). It is well-known that pressure perturbations can be dynamically induced in deep convective systems under significant vertical wind shear (e.g., Rotunno and Klemp 1982, Klemp 1987, Fovell and Ogura 1988). The simulations described here are conducted in a environment with strong low-level vertical wind shear such that the validity of the mechanism above in explaining the response of the wind field may be

questionable. However, our previous results showed that the evolution of the pressure field is *strongly* associated with buoyancy in the sector being considered (Fig. 7.16). Therefore, it is reasonable to consider the physical mechanism involving the BPGA as one process taking place in dynamic adjustment, especially early in experiment THETA.

As further support for this statement, Figure 7.19 compares the magnitude of vertical acceleration due to buoyancy and vertical pressure gradient (A_{pqB} , as defined in (5.7)) for CNTRL and THETA, 2-min after restart. In THETA, the regions of negative A_{pqB} cover a larger horizontal extent than in CNTRL due to the sharp weakening of the buoyancy field at the restart. More importantly, note the sector of relatively strong (negative) A_{pqB} at mid-levels, just upstream of the developing buoyant plume within $144 \text{ km} \leq x \leq 168 \text{ km}$ (compare with Fig. 7.14c). This feature indicates a sector where the BPGA favors downward motion around a developing buoyant plume, in agreement with the idealized structure shown in Fig. 7.18. This pattern is not evident in CNTRL because the buoyant plume is fully developed at this time, reducing the magnitude of A_{pqB} . On the downstream side of the main updrafts in THETA (Fig. 7.19b), A_{pqB} is also more negative than in CNTRL, although not as evident as on the trailing flank. This is probably because of the preferential upstream development of the buoyant plume.

An alternative way of interpreting the response of the wind field to variations in buoyancy is through the vorticity equation for an inviscid Boussinesq flow (e.g., Houze 1993, Weisman 1993) or, more specifically (and conveniently), its meridional component:

$$\frac{D\xi}{Dt} = \frac{\partial\xi}{\partial t} + \vec{V} \cdot \nabla \xi = -\frac{\partial B}{\partial x} + \xi \frac{\partial v}{\partial y} + (\zeta + f) \frac{\partial v}{\partial z} + \eta \frac{\partial v}{\partial x} \quad (7.5)$$

In (7.5), η is the zonal component ($\partial w/\partial y - \partial v/\partial z$), ξ is the meridional component

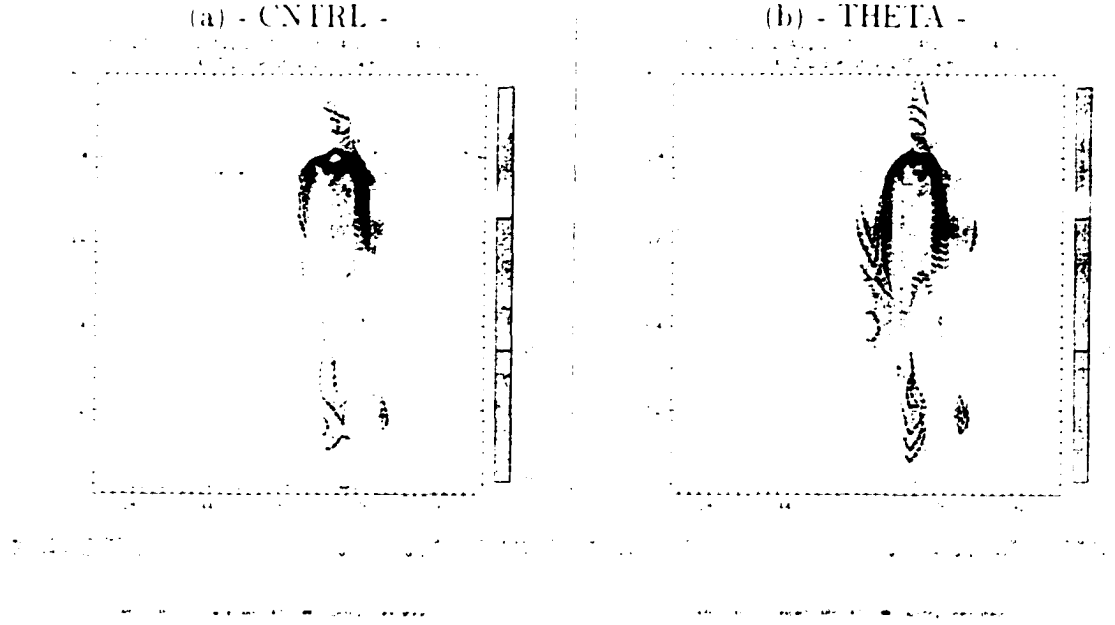


Figure 7.19: Vertical acceleration due to buoyancy and vertical pressure gradient (dashed lines) at 102-min for simulations: (a) CNTRL, and (b) THETA, contoured at 0.01 m s^{-2} intervals. Only negative values are shown. Areas with downdrafts equal to or stronger than -1 m s^{-1} are shaded (single shading). Domain shown is same as in Fig. 7.14.

$(\partial u / \partial z - \partial v / \partial x)$, and ζ is the vertical component $(\partial v / \partial x - \partial u / \partial y)$ of vorticity; f is the vertical component of planetary vorticity; and B represents buoyancy.

From (7.5) is evident that the generation of horizontal vorticity in the meridional direction is, among other things, proportional to minus the variation of buoyancy in the zonal dimension (baroclinic generation of horizontal vorticity). Hence, from Figure 7.18 it is possible to infer that negative (positive) ξ is induced on the west (east) side of the positively buoyant layer, favoring a convective circulation that follows the same sense indicated by the lines of BPGA. Figure 7.20a shows a close-up view in a vertical cross section from the surface to $z = 9.6 \text{ km}$ of the $(-\partial B / \partial x)$ field 10-min after restart in experiment THETA just upstream of the main updraft area (see caption). The region dominated by downdrafts indeed is associated with negative $(-\partial B / \partial x)$ which, from (7.5), favors a counterclockwise horizontal circulation at mid

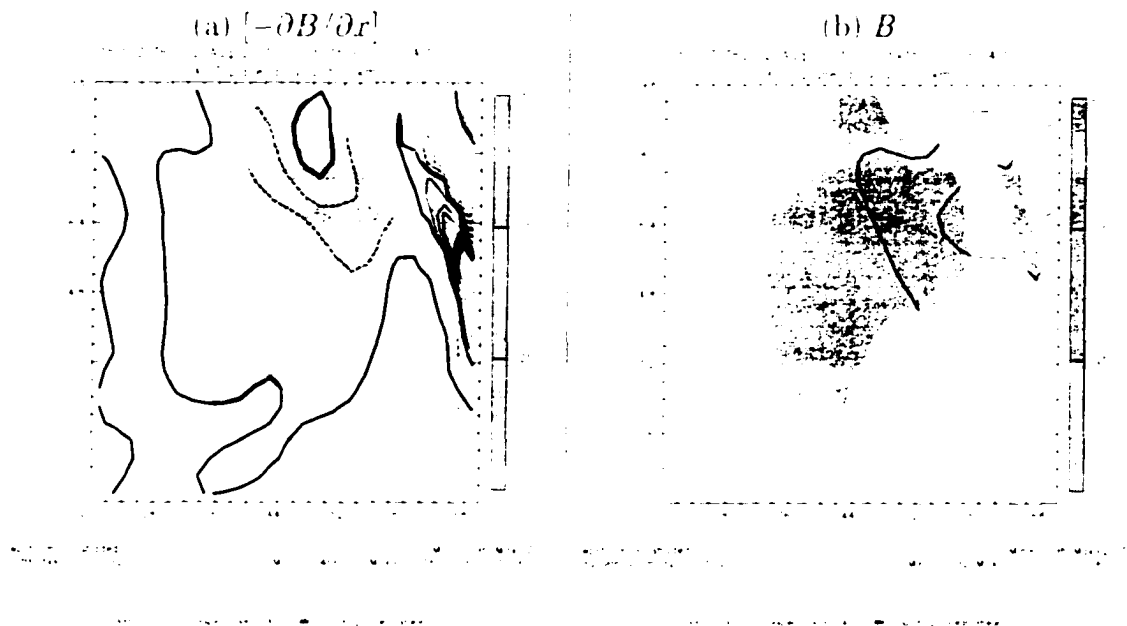


Figure 7.20. Vertical cross sections along $y = 205$ km of (a) $(-\partial B / \partial x)$ ($\times 10^3$ s $^{-2}$) contoured at 0.005 s $^{-2}$ intervals, and (b) acceleration due to buoyancy (given by Eq. 5.8), contoured at 0.05 m s $^{-2}$ intervals, for experiment THETA 10-min after restart time. Dashed (thin solid) lines represent negative (positive) values. In (a), zero lines are plotted as thick solid contours, while in (b) zero lines are suppressed. The cross section shown covers only the lower western portion of the domain in Fig. 7.14 (from the surface to $z = 9.6$ km, and $120 \text{ km} \leq x \leq 170 \text{ km}$). In both panels, areas with downward motion stronger than or equal to -1 m s^{-1} are shaded (single shading).

levels. This region corresponds to the upstream side of the buoyant plume (Fig. 7.20b). It is interesting to note that $(-\partial B / \partial x)$ is positive close to the surface (on the lower right corner of Fig. 7.20a), associated with the western edge of the developing cold pool, i.e., negatively-buoyant air at low levels in Fig. 7.20b. Clockwise horizontal circulation is thus favored in that region. These two horizontal circulations combined play a role in maintaining the “correct” structure of the rear-to-front flow (Weisman 1993).

In fact, an interesting response involving the rear-to-front flow—or more specifically, the RIJ—is present in THETA. The time sequences depicted in Figs. 7.14 and 7.16 seem to indicate that the structure of the RIJ is affected by the evolving buoyant plume and the accompanying mid-level downdraft. Early in the simulation, the wind

field trailing the convective cells has a strong *vertical component* associated with the downdraft area (Fig. 7.16d), due to the downward-oriented BPGA discussed earlier. While the RIJ is still characterized at this stage, its structure is more diffuse than the CNTRL counterpart (Fig. 7.16a). As the downdraft area propagates away from the convective region, the *horizontal component* of the wind gradually dominates the flow in the low to mid levels just upstream of the convective area, and a clear-cut RIJ becomes evident again (Fig. 7.16g).

A better characterization of this response is given in Figure 7.21, which shows vertical cross sections of the evolution of the zonal wind component (storm relative: u_{sr}) from $t = 4.06$ -hr to 4.20-hr in experiment THETA. Solid (Dashed) lines enclose regions with u_{sr} stronger than 8 m s^{-1} ($\pm 12 \text{ m s}^{-1}$)⁹. Focusing first on the RIJ, note how the horizontal extent of the sector with $u_{sr} > 8 \text{ m s}^{-1}$ becomes anchored to the upstream edge of the mid-level downdraft area. Interestingly, the rearward propagation of the trailing *upper-level* outflow also follows the mid-level feature. It is shown below that this important adjustment in the wind field is the result of the propagation of a hydrostatic IGW (Pandya and Durran 1996, henceforth PD96).

7.4.2 Manifestation of IGWs in experiment THETA

The analysis above describes physical processes that are important to understanding the generation of vertical motion around the developing buoyant plume in experiment THETA, but does not explain the rearward propagation of the trailing features. Because our simulated MCS represents a heating source in a stably stratified atmosphere, it is reasonable to expect the triggering of IGWs, especially because of the rapidly evolving thermal structure of the bow echo shortly after restart.

In examining the gravity wave component of dynamic adjustment in THETA, it

⁹These thresholds are chosen because they highlight the evolution of u_{sr} with respect to the trailing downdraft area.

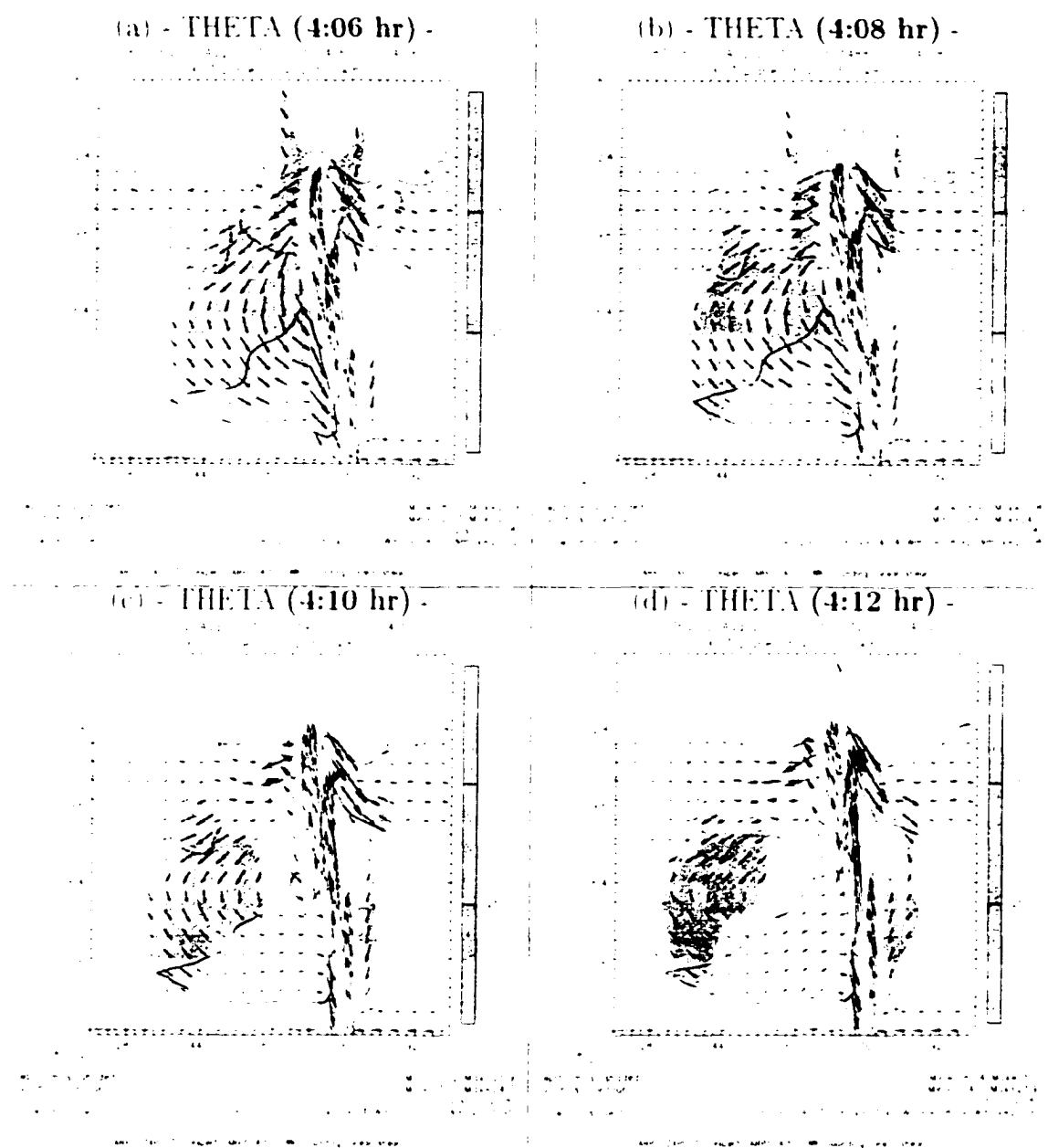
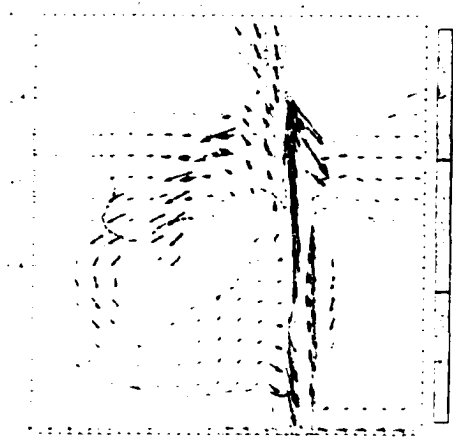


Figure 7.21: As in Fig. 7.14, but for the zonal component of the storm-relative flow in m s^{-1} (contours), from $t = 4:06$ to $4:20$ -hr in experiment THETA. Only contours for $u = -12 \text{ m s}^{-1}$ (dashed line) and 8 m s^{-1} (solid line) are shown. Vectors are storm-relative winds in m s^{-1} , and shading indicates areas with downdrafts stronger than -1 m s^{-1} .

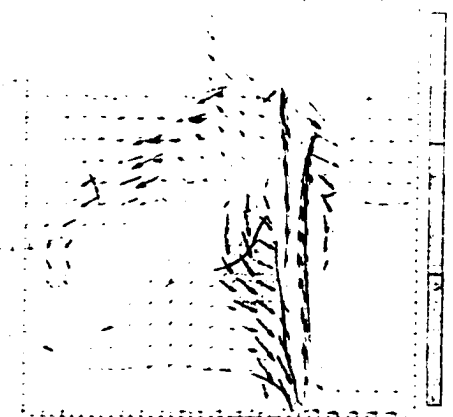
(e) - THETA (4:14 hr) -



(f) - THETA (4:16 hr) -



(g) - THETA (4:18 hr) -



(h) - THETA (4:20 hr) -



Figure 7.21 (continuation)

is important to analyze the evolution of meteorological fields not only in the vertical cross section along the bow echo apex, but also in a horizontal section. Figure 7.22 shows the first 20-min evolution of vertical motion in experiment THETA at $z = 4.8$ km¹⁹, enclosing the main bow echo structure. The line segment plotted near the center of each panel indicates the location of the vertical cross sections examined previously ($x = 205$ km).

Just upstream of the bow echo (i.e., at the center of all panels in Figure 7.22, west of $x = 176$ km), the early time sequence (Figs. 7.22a,b) shows the presence of relatively strong downdrafts. They represent the descending rear-to-front flow and the convective-scale (“transition-zone”) downdrafts induced in THETA. As the simulation proceeds (Figs. 7.22c-e), the downdraft area propagates rearward. Recalling Fig. 7.16, this feature somewhat resembles the deep gravity wave mode described in Nicholls et al. (1991) and Mapes (1993) for the response of a stably stratified atmosphere to idealized heating sources of long duration. They found that the early response consists of a layer of deep compensating subsidence (and positive buoyancy) propagating away from the heating source at the speed of a *hydrostatic* IGW (HIGW). Mapes (1993) called this feature a “buoyancy bore.” We will revisit this topic later in this section.

Shortly after 10-min (Figs. 7.22f,g), an updraft becomes well defined in the central domain and also propagates upstream, trailing the bow echo. By 16-min, a new convective-scale downdraft is formed near the leading cells, characterizing a wave train (Figs. 7.22h-j). Figure 7.23 shows the vertical structure of the wind field 18-min after restart, with a well defined wave train upstream of the leading convection.

The complex patterns illustrated in Fig. 7.22 indicate that the gravity waves display some meridional component as well. The convective cell south of the bow

¹⁹This height was chosen because a good characterization of the wave regime trailing the convective activity is possible at mid levels.

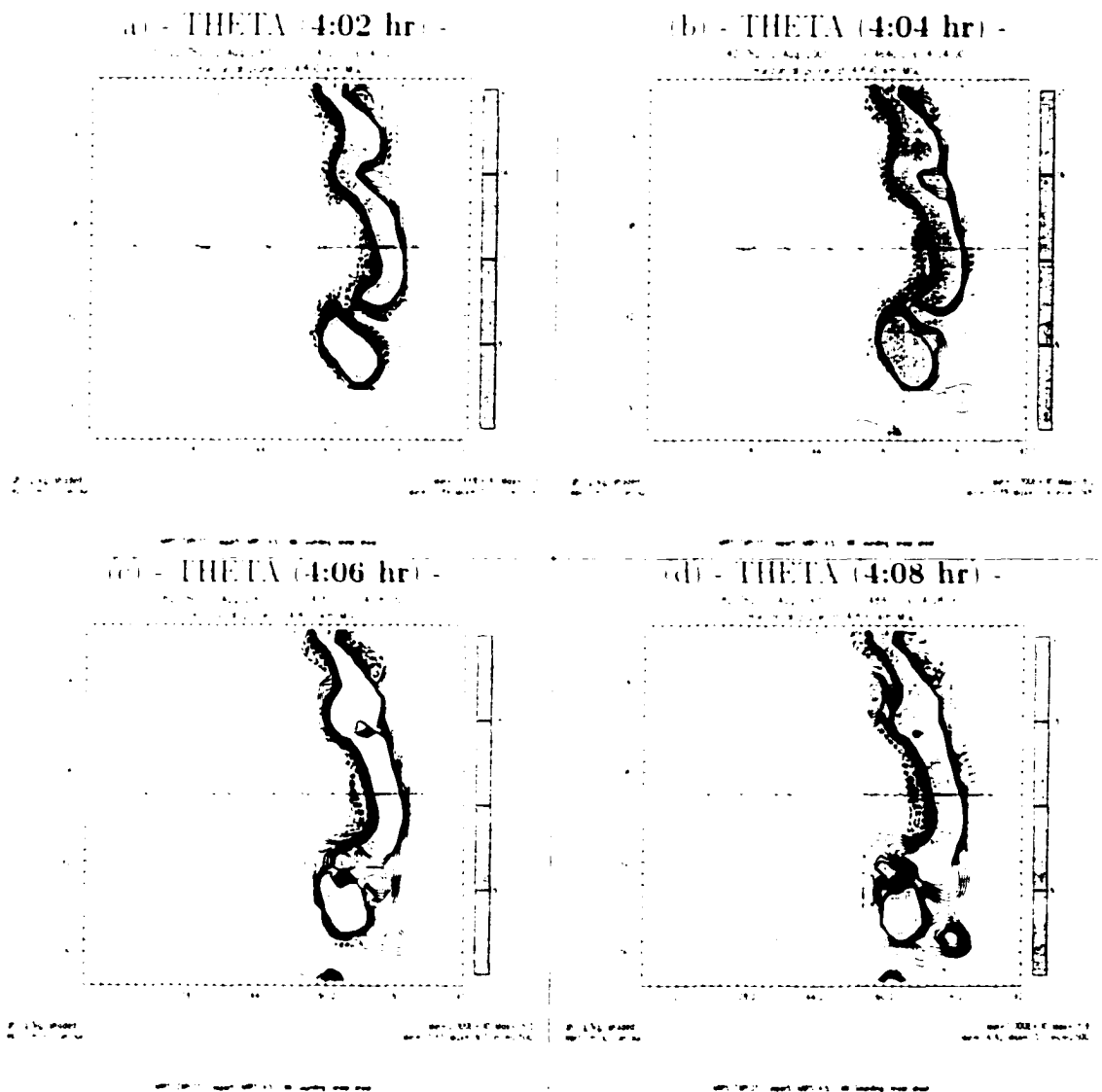


Figure 7.22 First 20-min evolution of vertical motion field at $z = 18$ km in experiment THETA, starting at $t = 4:02$ -hr. Solid (dashed) lines denote updrafts (downdrafts) contoured at 0.5 m s^{-1} intervals, with zero lines being suppressed. Only vertical motions between $\pm 4 \text{ m s}^{-1}$ are plotted. In all panels, light shading indicates areas with hail mixing ratio greater than 1 g kg^{-1} , and an E-W oriented line segment along $y = 205 \text{ km}$ illustrates the location of vertical cross sections studied in previous plots. The horizontal domain shown is the same as in Fig. 4.6, and translates eastward at 22 m s^{-1} .

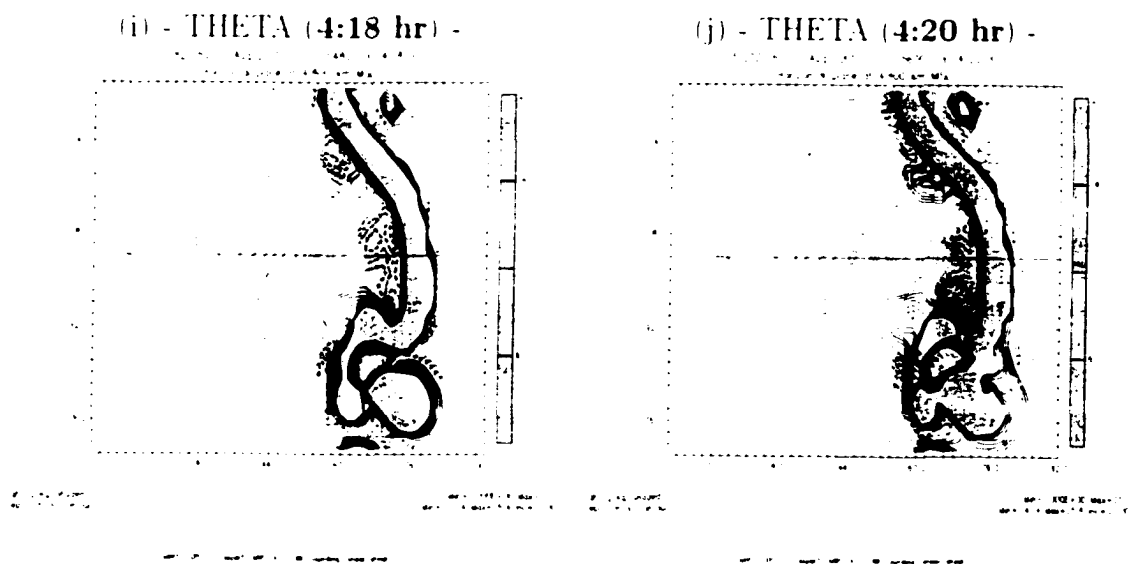


Figure 7.22 (continuation):

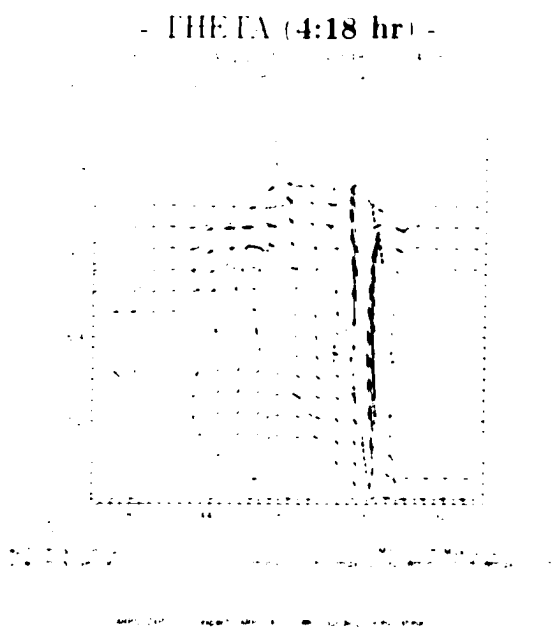


Figure 7.23: As in Fig. 7.14, but for the vertical motion field at $t = 4:18$ -hr. Only contours for $w = -1 \text{ m s}^{-1}$ (dashed lines) and $w = 1 \text{ m s}^{-1}$ (solid lines) are plotted. Vectors are storm-relative winds in m s^{-1} .

echo segment (south of $y = 192$ km and just east of $x = 160$ km) generates its own wave train, with a sequence of downdrafts and updrafts propagating northwestward relative to the MCS, which is particularly evident from 4:08-hr to 4:16-hr (Figs. 7.22d-h). Interestingly, wave fronts emanating from the apex of the bow echo and from the southern storm interact at the center of the domain (see time sequence for updrafts in Figs. 7.22f-j). It is important to mention that the gravity wave response described above is representative of experiment THETA for other sectors of the storm, not shown.

East (i.e., downstream) of the leading edge of the MCS, wave propagation is less active. Figure 7.16, for example, shows downward motion ahead of mid- to upper-level updrafts, but in a much more confined area. Figure 7.24 indicates the solution at $t = 4:20$ -hr for experiment THETA, but showing a larger horizontal domain. Although strong perturbations are evident just ahead of the MCS, they do not display the same complex structure present on the trailing side. Several studies have reported equivalent behavior in observed and idealized MCSs (e.g., Schmidt and Cotton 1990, Fovell et al. 1992, Yang and Houze 1995a, PD96, Nachamkin and Cotton 2000).

In investigating the impact of MCS-like heating sources on the environment, PD96 indicated that only heating sources displaying a vertical tilt are capable of generating realistic “trailing” mesoscale features (such as the rear-to-front flow). They suggest that the vertical leaning of the heating source induce preferential propagation of gravity waves in the direction of the tilt, accounting for the asymmetric response. In agreement with such reasoning, our simulations do show an upshear tilted heating source (Fig. 7.14), i.e., leaning in the same direction of the most intense wave activity.

The storm-relative [ground-relative] zonal propagation speed of the trailing updraft in the center of the domain -- evident from 4:12 to 4:20-hr along the line segment in Figs. 7.22f-j -- is approximately -30 m s^{-1} [-8 m s^{-1}], as indicated in Figure 7.25. In

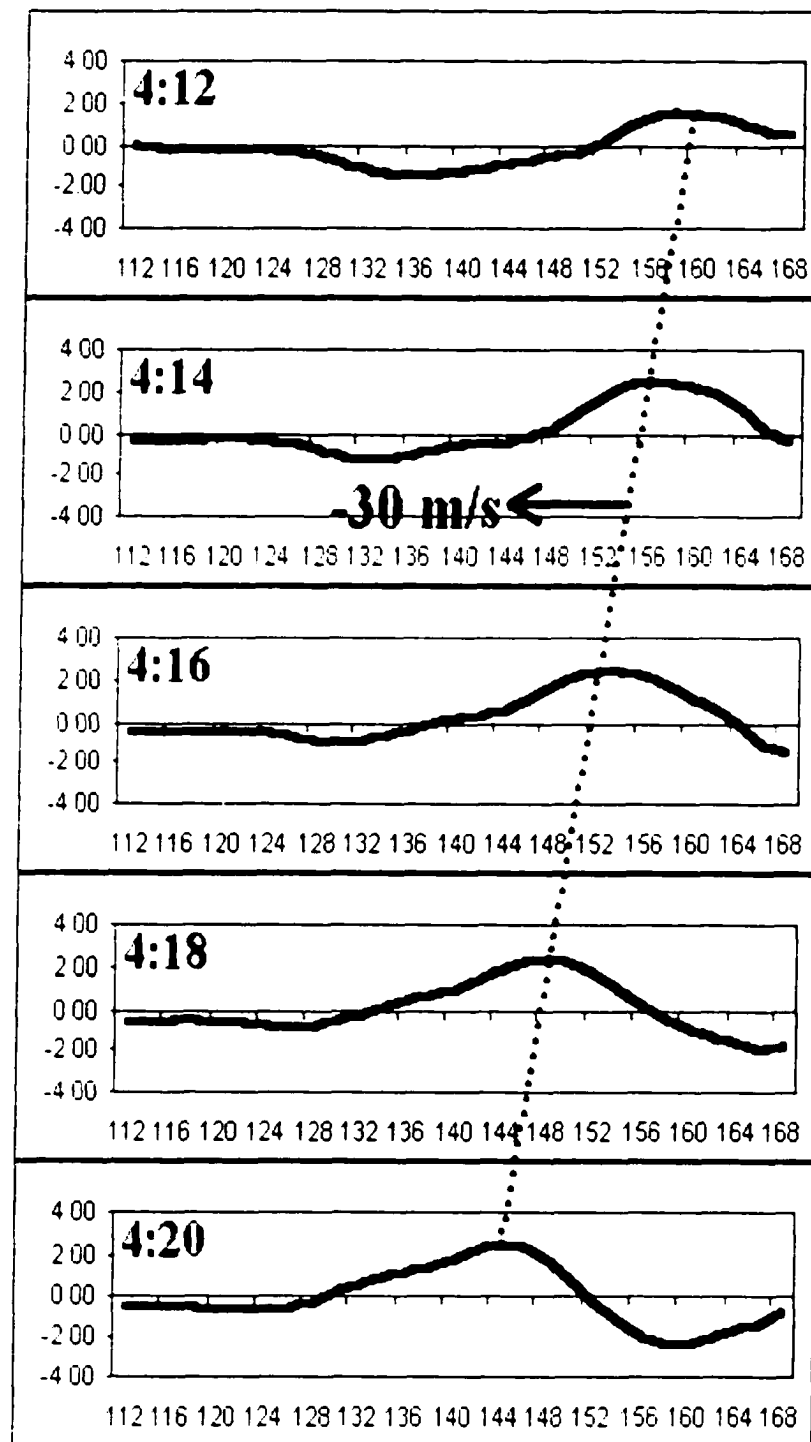


Figure 7.25. Time sequence from $t = 4:12$ to $4:20$ -hr of vertical motion at $z = 1.8$ km along $y = 205$ km (line segment in Fig. 7.22) in experiment THETA for a horizontal domain covering $112 \text{ km} \leq x \leq 168 \text{ km}$ (the abscissa in the panels above). The domain moves eastwards at 22 m s^{-1} which is approximately the propagation speed of the bow echo, such that the phase speed indicated above is storm-relative.

a simulated squall line. Yang and Houze (1995a) found storm-relative phase speeds for IGWs of the order of -30 to -40 m s⁻¹ in the trailing stratiform region, while slower waves dominated the region near the main convective activity. The simulated MCS in the present research is a much narrower system, and the relatively high phase speed of -30 m s⁻¹ is found just upstream of the leading convective updrafts. It is not clear if the different phase speeds found in Yang and Houze (1995a) are sensitive to the extent of the trailing precipitation area.

Based on the theory of hydrostatic adjustment reviewed in chapter 2, one question that arises is whether the gravity wave regime discussed here consists of IGWs in the *non-hydrostatic* limit. The adjustment described in B95, inferred for three-dimensions, “predicts” that an impulsive heating source of high aspect ratio (the situation usually considered for deep convective storms) induces *high frequency* IGWs. If this is case in experiment THETA, then the following expression can be used to estimate their ground-relative zonal phase speed c_x based on linear theory:

$$c_x = \bar{u} - \frac{N}{k}, \quad (7.6)$$

where \bar{u} (ground-relative), N and k are as defined in chapter 2.

Equation (7.6) is obtained from (2.20) by neglecting the term Na^2/c_x^2 , assuming $k^2 \gg m^2$ (i.e., the non-hydrostatic limit), and dividing ϖ by k . The minus sign on the right-hand-side of (7.6) is chosen because we are examining westward-propagating waves. With the aid of Figs. 7.22 and 7.23, the zonal wavelength, λ_x , is estimated to be approximately 40 km, yielding $k (= 2\pi/\lambda_x)$ equal to $1.57 \times 10^{-4} \text{ m}^{-1}$. Figure 7.26 shows profiles of buoyancy frequency squared (N^2) and ground-relative wind speed (\bar{u}), 10-min after restart, averaged for the area enclosed by a rectangle in Fig. 7.22e. At a height of $z = 4.8 \text{ km}$, $N \approx 0.011 \text{ s}^{-1}$ and $\bar{u} \approx 25 \text{ m s}^{-1}$. Substituting these values into (7.6) yields $c_x \approx -45 \text{ m s}^{-1}$ relative to the ground, which is a substantial

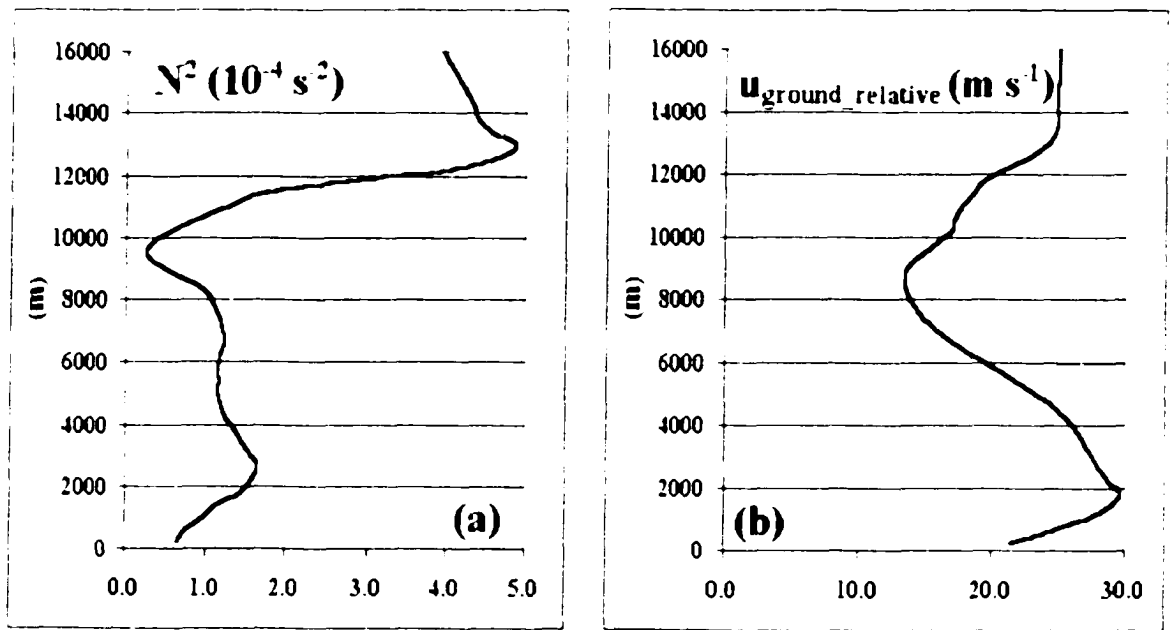


Figure 7.26: Vertical profiles of (a) buoyancy frequency squared, N^2 ($\times 10^{-4} \text{ s}^{-2}$), and (b) zonal component of ground-relative winds (m s^{-1}), in experiment THETA at 4.10-min averaged for the area enclosed by a rectangle in Fig. 7.22c.

overestimation when compared with the corresponding value found for a gravity wave propagating just upstream of the bow echo ($\sim 8 \text{ m s}^{-1}$). This discrepancy may have multiple origins, ranging from the inadequacy of linear theory in explaining wave propagation in regions where turbulence mixing and non-linear effects are important, to an inaccurate estimate of the zonal wavenumber (Figs. 7.22 and 7.23) and phase speed (Fig. 7.25) based on a single “pulse”¹¹. However, the most likely source of the large discrepancy comes from the assumption that $k^2 \gg m^2$, as shown below.

Figure 7.27 shows time series of vertical motion at $(x, y) = (160, 205) \text{ km}$ (just upstream of the bow echo in Fig. 7.22) at 3 different levels, for the first 20-min of simulation in THETA. Note that high and low frequency oscillations are superimposed in the waves, with the former being associated with acoustic modes to be examined

¹¹ Another important limitation in the use of (7.5) is the fact that it is derived for an atmosphere with constant \bar{u} and N , while the numerical simulations are conducted for a vertically sheared environment, with non-constant N . This problem is minimized when taking values for c_T , \bar{u} , N and k at the same level, assuming that \bar{u} and N does not vary significantly in a shallow layer.

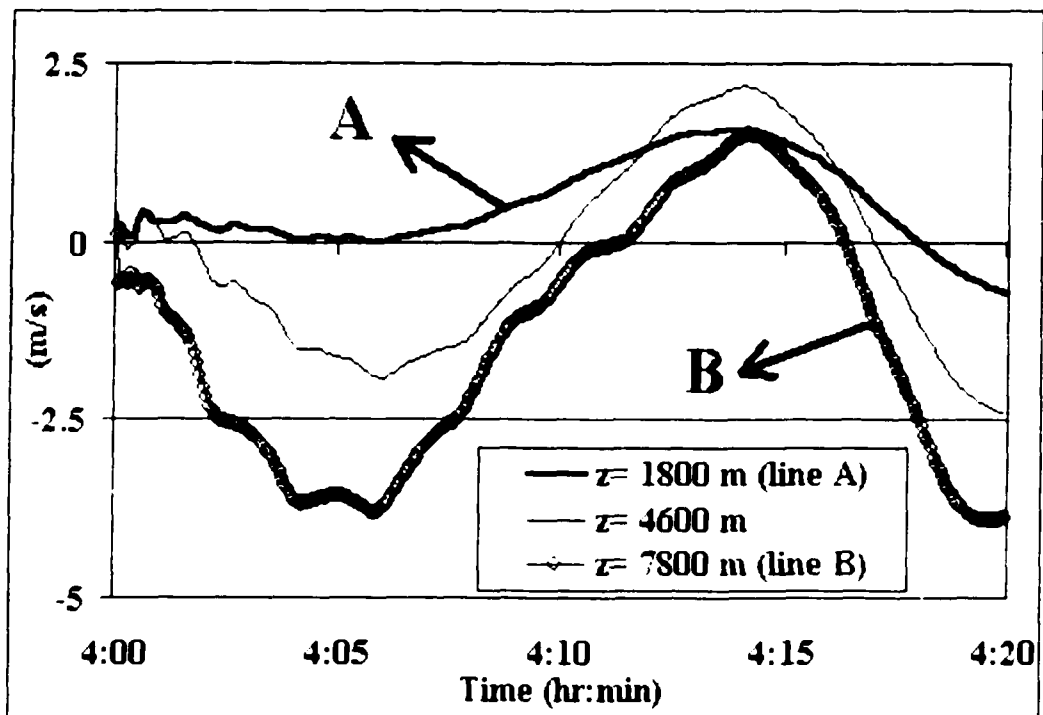


Figure 7.27: Time series of vertical velocity in m s^{-1} at $(x, y) = (160, 205)$ km and $z = 1.8$ km, 4.6 km, 7.8 km, for the first 20-min of experiment THETA. The vertical velocity field is sampled at each 4s.

later. For now, it is important to note that the period of oscillation of the gravity wave component in Fig. 7.27 is around 15-min, which is longer than the buoyancy period of 9.5-min associated with $N = 0.011 \text{ s}^{-1}$ at mid levels. Therefore, the oscillatory regime *does not* consist of the *highest* frequency IGWs that are supported in the environment modified by the bow echo¹². In other words, the waves do not reach the upper limit of “non-hydrostaticity” implied by the assumption $k^2 \gg m^2$. Hence, m^2 cannot be neglected in Eq. (7.6), suggesting that vertical structure is present.

It is interesting, however, that the wave train shown in Fig. 7.23 displays very little vertical structure or tilt in almost the entire *troposphere*, just west of the main updrafts. The lack of vertical structure also is evident in Fig. 7.27, where the oscillations are vertically in phase. This behavior is possible in the case of vertically trapped IGWs (e.g., Durran 1986). In an idealized setting, Nicholls et al. (1991) found significant trapping of wave energy in the vertical as a response of the atmosphere to thermally forced gravity waves. In the numerical simulation of a squall line, Yang and Houze (1995a) indicate that vertically trapped IGWs are possible on the trailing portion of MCSs when a decrease in N^2 *and* increase in wind speed are observed concomitantly in the upper troposphere on the upstream side of the system¹³. Physically speaking, a sharp decrease in static stability at upper levels means that higher frequency mid-tropospheric IGWs cannot travel through the upper layers (where N is reduced) and therefore become evanescent, or vertically trapped. Combined with an increase of wind speed with height, the *Scorer parameter* (Scorer 1949, Durran 1986, Yang and Houze 1995a) is reduced, increasing the likelihood of trapped IGWs.

¹²One may argue that the buoyancy frequency estimated from Fig. 7.26a is not necessarily representative of the region where the IGWs are initiated (i.e., near the sector of active convection). However, the vertical profile of N^2 (determined for a narrower region just upstream of the bow echo) does not show significant changes compared to Fig. 7.26a (not shown), except at upper levels where a sharper decrease with height is evident for N^2 below the tropopause.

¹³These are the same atmospheric conditions that favor vertically trapped IGWs downstream of mountains (Scorer 1949, Durran 1986).

The decrease in N^2 shown in Fig. 7.26a from 7.0 to 10.0 km gives a hint that the atmospheric profile is favorable for trapped IGWs, at least in terms of static stability. On the other hand, \bar{n} (Fig. 7.25b) does increase above 8.0 km, although the layer of decreasing N^2 and increasing \bar{n} is shallow. The structure of the tropospheric wave train shown in Fig. 7.22 — especially close to the leading edge of the bow echo — is very similar to the one found in Yang and Houze (1995a) for trapped gravity waves. Therefore, conditions seem favorable for this specific wave regime.

7.4.2.1 Interpretation of the results

Based on the discussion above, we note that the solution in THETA is *not* dominated by IGWs in the non-hydrostatic limit ($k^2 \gg m^2$). Recalling the analysis of hydrostatic adjustment (B95), Figure 2.7 indicates that the gravity wave response to an *impulsive* heating source with *large horizontal* wavenumber and *small vertical* wavenumber is dominated by non-hydrostatic IGWs — i.e., the regime close to (far from) the abscissa (ordinate) in Fig. 2.7. While the horizontal extent of the heating source in experiment THETA is limited in the zonal direction (cross-line dimension), it is considerably elongated in the meridional direction (along-line dimension). Thus, the effective horizontal wavenumber in THETA is lowered. In addition, latent heating/cooling in our simulation does have vertical structure, consisting of low and upper-level cooling and mid-level warming (Fig. 7.14). These factors, combined, define a regime that does *not* reside very close to (far from) the abscissa (ordinate) of Fig. 2.7. In this case, IGWs with periods close to the buoyancy period are not the dominant mode¹⁴.

Another very important point is *strong evidence that points to very low frequency IGWs (i.e., IGWs on the hydrostatic limit, with $k^2 \ll m^2$) also being present in dynamic adjustment described in THETA*. This evidence comes from the examination of

¹⁴Note, however, that the gravity waves obtained in THETA are still of relatively high frequency and therefore are not hydrostatic.

Fig. 7.21, which shows that the structure of the trailing mesoscale features (RIJ and front-to-rear upper level outflow) is linked to the propagation of the buoyant plume. Results from PD96 suggest that these trailing features result from the propagation of a HIGW induced by the *low-frequency component* of the convective thermal forcing of a MCS. By “low frequency component” we mean the *aggregate structure* of the heating source in the MCS, for which the impulsive behavior of the discrete convective elements is not relevant. This latter component is more closely associated with hydrostatic adjustment in the presence of truly impulsive heating sources of high-aspect ratio, which trigger the higher-frequency IGWs (PD96). The “long duration” component of the thermal forcing, on the other hand, excites hydrostatic pulses that play an important role in determining the response of the environment to the MCS, including deep layers of compensating subsidence (Bretherton and Smolarkiewicz 1989, Nicholls et al. 1991, Mapes 1993, Fovell 2002), and the formation of trailing rear-to-front and front-to-rear flows (PD96).

PD96 indicated that the early response of the environment to a tilted steady-state heating source — representing a mature MCS — consists first of a fast-moving pair of pulses propagating laterally away from the source at the speed of a HIGW with vertical wavelength *twice the depth* of the thermal forcing. These are followed by another pulse moving at the speed of a HIGW with vertical wavelength *comparable to* the depth of the heating source. This second wave travels only in the direction of the heating source’s tilt. All these pulses are evident when analyzing the horizontal wind field. As the second pulse propagates away, it leaves behind the structure usually found in the trailing side of MCSs: a front-to-rear and a rear-to-front flow.

In experiment THETA, we did not manage to capture the first pair of pulses, probably because of the design of our simulation. The wind field at restart time already is consistent with a well developed MCS in THETA, and the signal of the first pair

of pulses may be masked by strong convective circulations in the bow echo. However, the second pulse seems to be the one associated with the propagating buoyant plume and mid-level downdraft analyzed in the previous section, and associated with the adjustment described in Fig. 7.21. To check this possibility in a quantitative way, we first estimate the storm-relative propagation speed of the upstream edge of the sector having winds stronger than 8 m s^{-1} in the RIJ shown in Fig. 7.21. With the aid of the time sequence in Fig. 7.21, we find a value of $\sim 22 \text{ m s}^{-1}$. On the other hand, the system-relative group velocity, or phase speed, c_{HIGW} , for a westward-propagating HIGW is given by ¹⁷:

$$c_{HIGW} = -N/m, \quad (7.7)$$

where N and m are as defined before.

The vertical wavenumber can be estimated from the structure of the buoyancy field in Fig. 7.14. A full vertical wavelength λ_z (i.e., low level cooling - mid level warming - upper level cooling) is spanned in an approximately 13.2 km deep layer, yielding $m \approx 4.76 \times 10^{-4} \text{ m}^{-1}$. From Fig. 7.26a, the buoyancy frequency at mid levels is approximately 0.011 s^{-1} . Substituting these into (7.7) yields $c_{HIGW} \approx -23 \text{ m s}^{-1}$, which is in very good agreement with the propagation speed estimated from Fig. 7.21. Hence, the rearward evolution of the buoyant plume, and the response involving the RIJ and the trailing upper-level outflow in experiment THETA, are consistent with the manifestation of a HIGW, in agreement with PD96. Note that the expression “gravity wave” is rather misleading in this case because the response refers to a single pulse, rather than an oscillatory regime (evidently that the oscillations described earlier are *not* HIGWs).

Therefore, the adjustment process in THETA involves a complex response in-

¹⁷Note that, in the hydrostatic limit, both the phase speed and group velocity of an IGW reduce to the same expression

cluding low *and* high frequency IGWs. The former are associated with the slowly evolving aggregate structure of the bow echo's thermal forcing (i.e., heating source of long duration) that implicitly is present in the perfect specification of the moisture and condensate fields at restart. The latter are related to the transient behavior of cell regeneration along the leading edge of the bow echo (i.e., impulsive heat sources).

As expected, high frequency IGWs are present in CNTRL as well, as indicated in Figure 7.28 for the same grid-points and time period analyzed in Fig. 7.27 for THETA. This means that the "transient evolution" in THETA cannot easily be separated from the regular behavior of the solution in terms of high frequency IGWs, which are ubiquitous in MCSs. The low frequency regime, however, does provide a signature of the "transient evolution" because it is associated with irreversible processes (Mapes 1993). For example, once the hydrostatic pulse moves out the domain of interest, the overall kinematic structure trailing the bow echo cannot significantly be altered without a change in the heating source in the convective sector of the system (PD96).

Because the thermal field in THETA is restored with its correct phase, the overall structure of the MCS is not modified by "hydrostatic waves", and a strong squall line results. The differences from CNTRL are mostly in the fine structure. This important finding indicates that *a reasonably accurate specification of the **relevant** thermal field of an MCS is not necessarily obtained from the temperature field alone, but from the quantities that control the correct phase of latent heating and cooling within the system.* This result is in conceptual agreement with studies addressing diabatic initialization of numerical models in the large- and stormscale (e.g., Krishnamurti et al. 1991, Zhang 1999), in which latent heating-cooling rates are used to estimate vertical motion that is consistent with the precipitation distributions.

The discussion above raises the crucial question of *the importance of observed/retrieved temperature field within convective systems (more specifically, squall lines and bow*

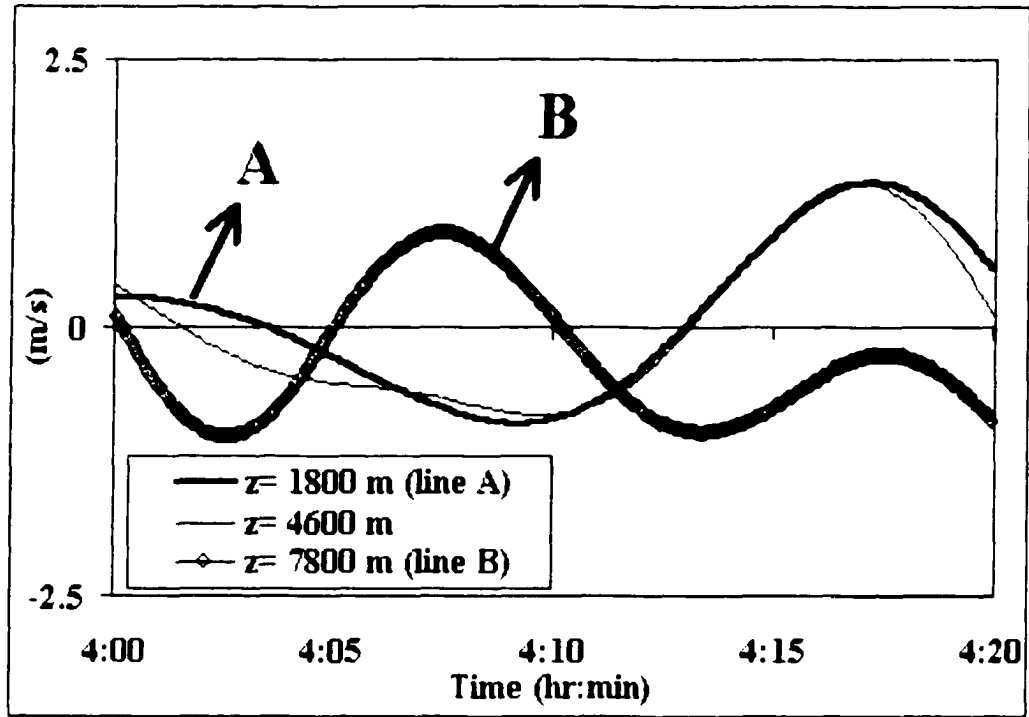


Figure 7.28: As in Fig. 7.27, but for simulation CNTRL.

echoes) of condensate and water vapor fields are not adequately specified. Our results suggest that temperature contains redundant information regarding the effective thermal field of a MCS.

7.4.3 Manifestation of acoustic modes in experiment THETA

Given that the ARPS is a fully compressible model, acoustic modes also are expected as a response in experiment THETA (B95, NP94a,b). Figure 7.27 shows high frequency oscillations superimposed on gravity waves. This very high frequency regime is not present in the CNTRL solution and represents the manifestation of acoustic modes¹⁶ as part of the dynamic adjustment process in experiment THETA.

Figure 7.29 depicts time series of perturbation pressure, highlighting the acoustic

¹⁶Actually, acoustic waves are present in simulation CNTRL as well, but with very small amplitudes that are efficiently attenuated by divergence damping. In THETA, the strong (and artificial) thermal perturbation at restart time triggers sound waves of larger amplitude.

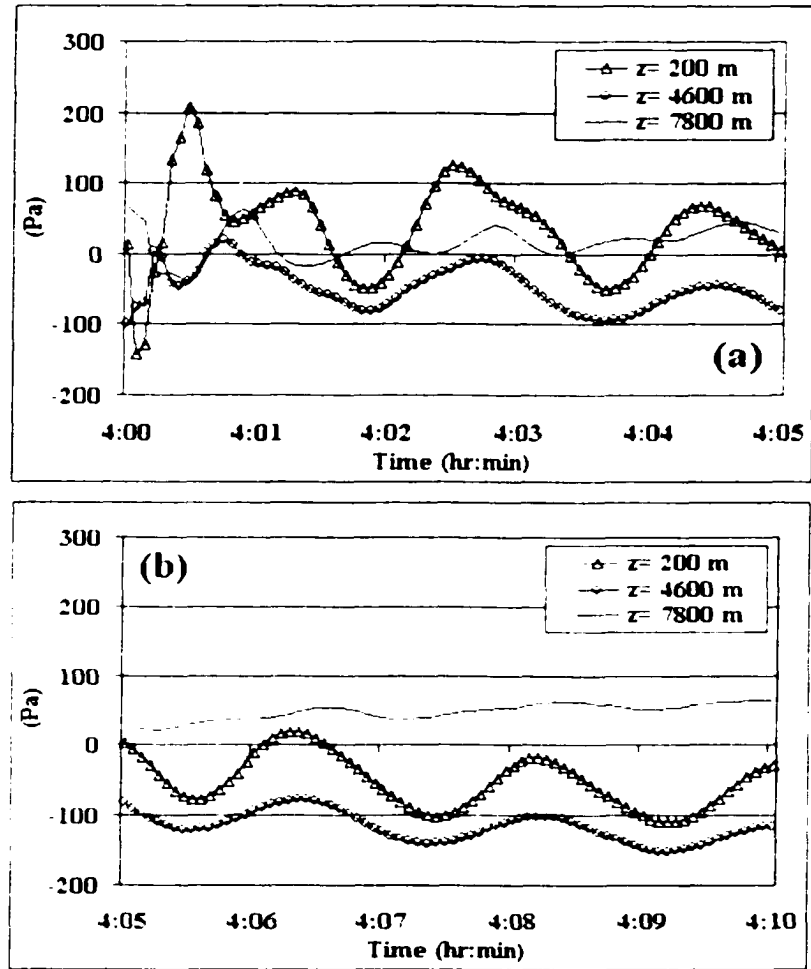


Figure 7.29: Time series for the first 20-min after the restart time ($t = 4$ -hr) of perturbation pressure (in Pa) at $(x, y) = (160, 205)$ km and $z = 1.8$ km, 4.6 km, 7.8 km (just upstream of the bow echo in Fig. 7.22) for experiment THETA. (a) 0 to 5-min, (b) 5 to 10-min, (c) 10 to 15-min, (d) 10 to 15-min. The perturbation pressure is sampled at each big time step (4 s).

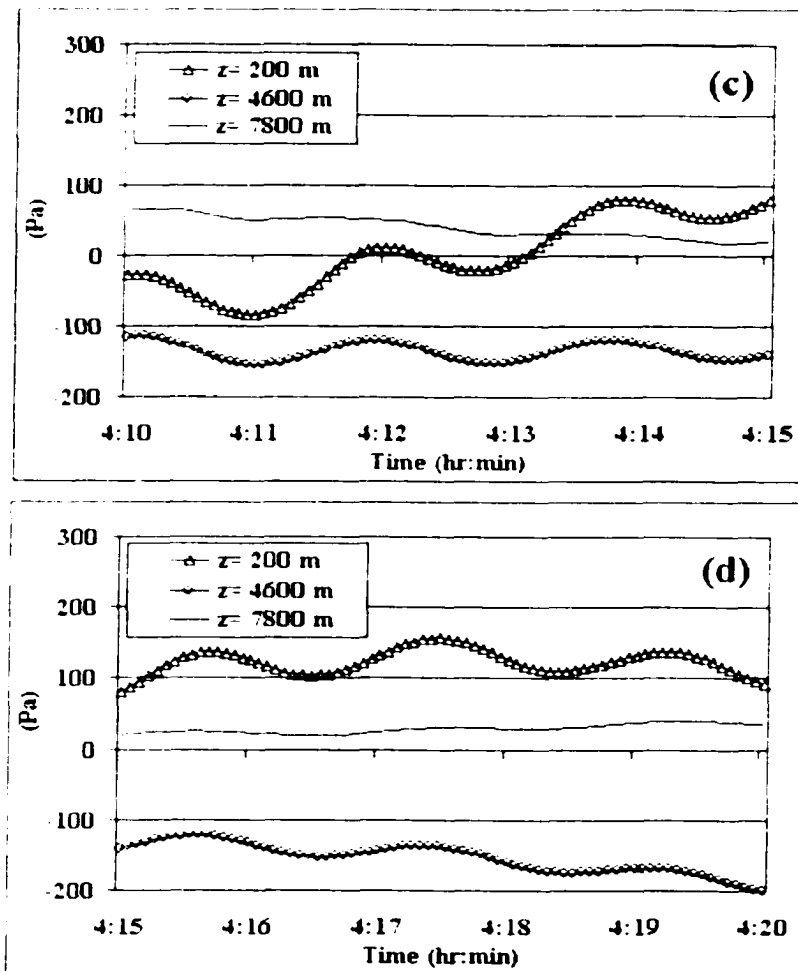


Figure 7-29 (continuation)

modes for the first 20-min at three different levels for the same grid-point studied in Fig. 7.27. In the first 5-min (Fig. 7.29a), high frequency sound waves are evident, with amplitudes comparable to the WVLE and UVLE counterparts (e.g., Fig. 6.5). Their amplitudes decrease with height, which is a pattern qualitatively similar to Lamb waves (Lindzen and Blake 1972) and TCWs (NP94a,b; section 2.3.3). However, they are not quite vertically in phase in the first few minutes and their frequency is considerably above the acoustic cutoff frequency (Fig. 6.7). Thus, vertical propagation seems evident, which is inconsistent with Lamb waves. Again, based on linear theory, the heating source in THETA displays some vertical structure and therefore displaces the expected wave regime away from the abscissa in Fig. 2.7, being sufficient to allow for the vertical propagation of sound waves.

With time, the wave amplitudes decay in response to divergence damping, and after 5-min the waves acquire a stable oscillatory regime, with a period of around 2-min. This is the same stable period of oscillation found for the acoustic modes in experiments WVLE and UVLE. Thus, the behavior of the sound waves in WVLE, UVLE and THETA is very similar, despite the different forcing mechanisms. In analyzing the acoustic modes in chapter 6, we suggested that static stability influences their frequency of oscillation, i.e., that these waves are in the AGW regime (Table 2.1). On the other hand, because the Crank-Nicolson implicit numerical scheme allows the use of a timestep larger than required to solve for the sound waves correctly, and because the boundary conditions also affect their behavior (see chapter 6), it is possible that the similar regime found in the different experiments may be an artifact of the numerical schemes.

The physically important point is that the acoustic modes are clearly part of the “transient evolution” in experiment THETA, as expected from theory (chapter 2). However, in contrast with experiments WVLE and UVLE, the sound wave compo-

ment of the adjustment does not control the time scale with which the adjustment is performed, this being controlled by the IGWs. Therefore, dynamic adjustment in experiment THETA has a characteristic time scale that is longer than in experiments WVCL and UVCL.

7.5 Dynamic adjustment aloft: experiment VAP

Having studied dynamic adjustment at mid and upper levels in experiment THETA, we now conduct a similar analysis for experiment VAP. Figure 7.30 compares vertical cross sections (xz -plane) of θ_e and the wind field for experiments CNTRL and VAP at $t = 410$, 430 and 450-hr, across the main bow echo segment. The low-level moistening induced at restart in VAP is evident by the increased θ_e at low levels and by the presence of a shallower mid-level dry layer trailing the convective activity (Fig. 7.30b,d,f).

Updrafts at mid and upper levels are substantially weaker compared to CNTRL, and do not display an “overshooting top”, while the surface-based updrafts are still somewhat active at 410-hr (Fig. 7.30b). This is because the boundary layer *ahead* of the bow echo is not modified by resetting q'_h to the base state, and thus surface air parcels traveling up and over the gust front reach their level of free convection just as in CNTRL. Conversely, the impact is significant aloft owing to the drying of the originally saturated layers in the updraft sector, which promotes unsaturated ascent (leading to adiabatic cooling) and enhanced evaporation and sublimation (leading to latent cooling). Combined, these processes favor the generation of mid-level negatively buoyant air, which weakens the updrafts.

A strong convective-scale downdraft is present just upstream from the shallower updrafts at 410-hr (Fig. 7.30b), while a weaker downdraft also is evident in the

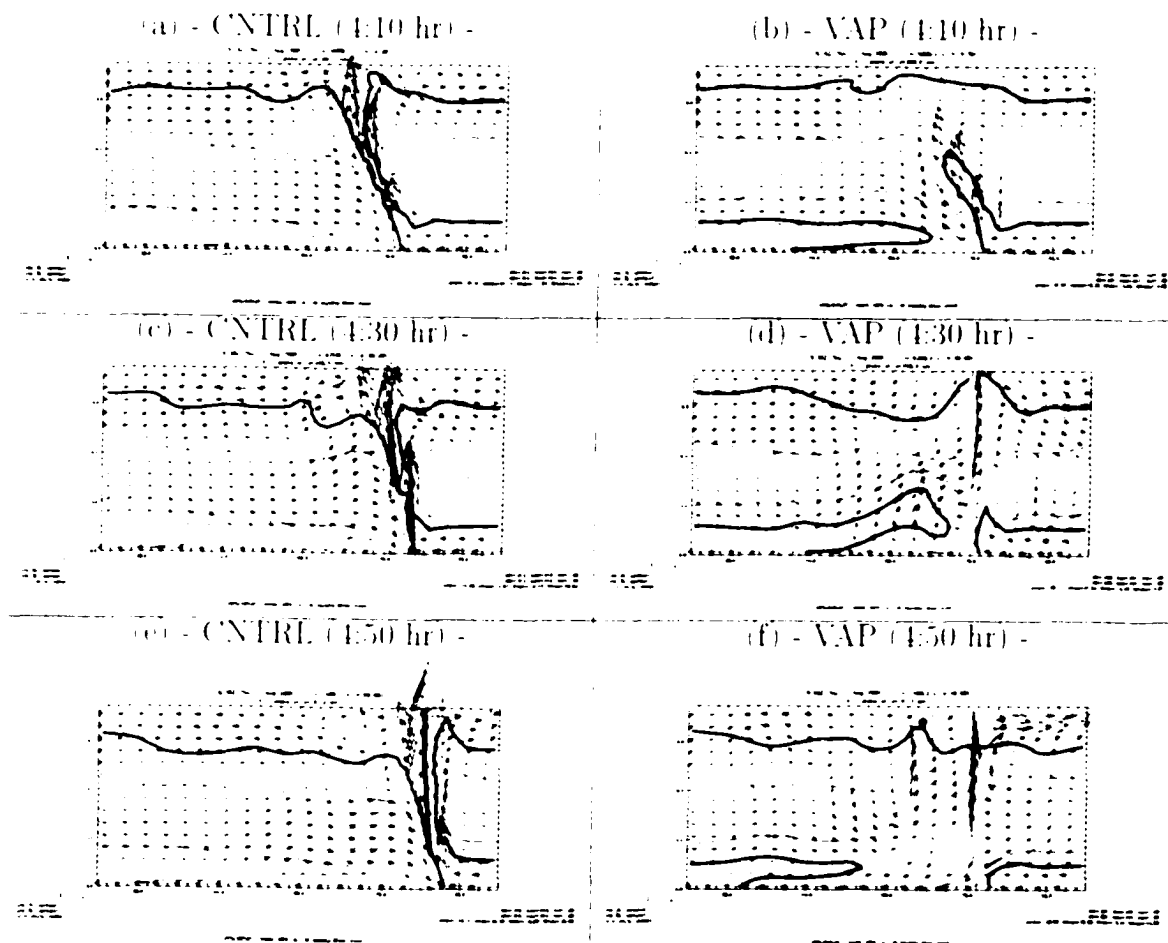


Figure 7.30: As in Fig. 7.13, but comparing experiments CNTRL and VAP.

downstream side. In contrast with the trailing mid-level downdraft discussed in experiment THETA, the VAP counterpart is located close to the leading edge of the bow echo at 410-hr. The RIJ also is weaker in VAP than in CNTRL.

As the simulation progresses, substantial modification of the MCS structure occurs (Fig. 7.30d). The upshear side of the mid-level dry layer becomes shallower instead of being restored because a low- to mid-level updraft forms *behind* the weaker gust front and advects moister air aloft. The shallow surface-based updrafts evident 20-min before are no longer present. Curiously, the upper-level updrafts in the leading edge show signs of re-strengthening, even though they are undercut from the surface. A complex wave pattern (possibly dominated by IGWs) follows and the flow structure indicates a dissipating system 50-min after restart time (Fig. 7.30f). These features are investigated with more detail in the next section.

It is important to mention that, in contrast with THETA, the behavior described in the given vertical cross section is *not* a good representation of what happens in other sectors of the MCS. As indicated in Fig. 7.6, some convective cells redevelop in localized regions of stronger convergence along the gust front (particularly where the cold pool acquires a structure similar to colliding outflow boundaries; see Figs. 7.8g-i). However, we choose to focus on the sector where the MCS weakens because it will indicate adjustment processes that lead to an evolution that deviates from that in CNTRL, especially when compared to experiment THETA.

7.5.1 Evolution of buoyancy, pressure and wind fields in the first 10-min

Figures 7.31b-g depict the first 10-min of evolution of total buoyancy in VAP. The initial field (Fig. 7.31b) is very similar to that in CNTRL (Fig. 7.31a). Because thermal buoyancy ($g\theta'/\bar{\theta}$) is the largest contributor to the total buoyancy field (Fig. 7.15), the withdrawal of q'_e has only a secondary impact *at* restart. However, as

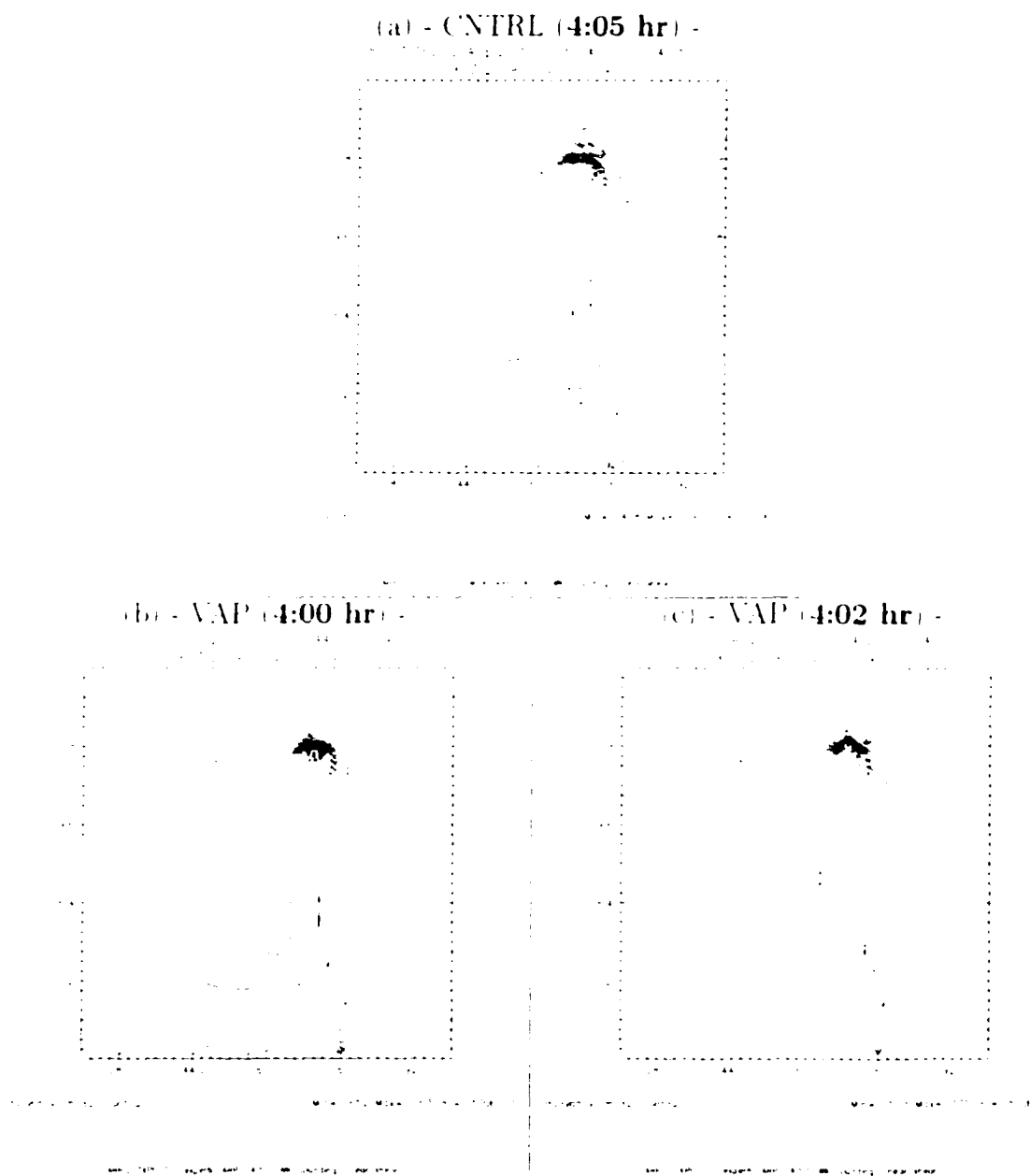


Figure 7.31 As in Fig. 7.14, but for experiment VAP.

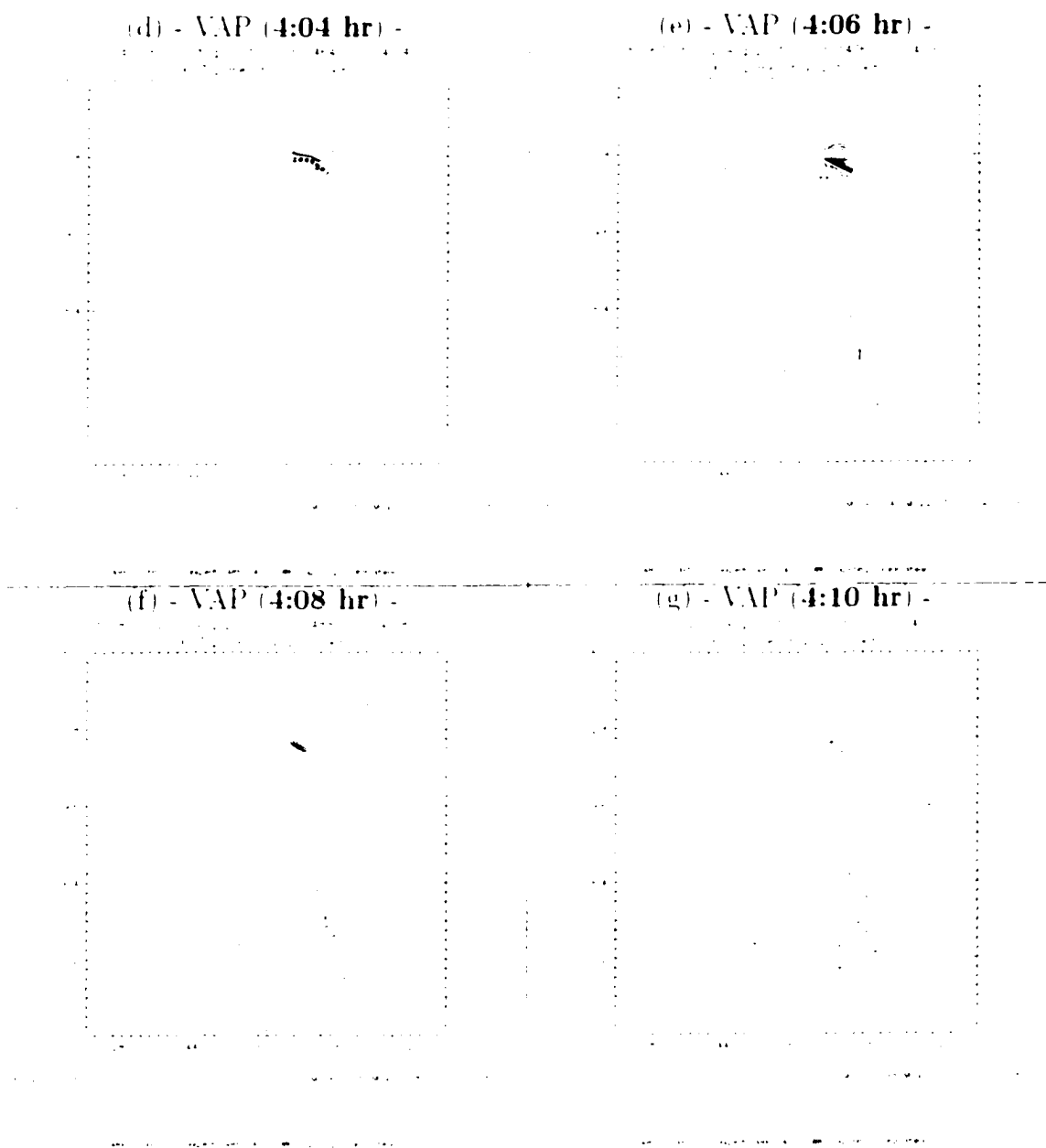


Figure 7.31 (continuation)

the simulation proceeds, negatively buoyant air is generated in the updraft due to unsaturated lifting and enhanced diabatic cooling. Thus, the mid-level buoyant plume leading the MCS is rapidly eroded (Fig. 7.31c). This process is well characterized in Figure 7.32, which shows the change in $g\theta' - \bar{\theta}$ and $-q(q'_i + q_{ci}) - (1 + \bar{q}_i)$ (condensate loading) of the total buoyancy field from $t = 400$ -hr to 402-hr (note that different contour intervals are used). There is a discernible *decrease in magnitude* in $-q(q'_i + q_{ci}) - (1 + \bar{q}_i)$ (Figs. 7.32b,d) in the first 2-min of integration, in agreement with the decrease in $g\theta' - \bar{\theta}$ (Figs. 7.32a,c). This behavior highlights the role played by enhanced diabatic cooling, which is driven by evaporation and sublimation, in the weakening of the buoyant plume in the convective sector.

With time (Figs. 7.31d-g), the low level updrafts forced along the gust front restore a shallow layer of saturation, where latent heating recovers the buoyancy field locally. In contrast, a layer of negatively buoyant air aloft — confined above $z = 9.6$ km in CTRL — descends, characterizing the presence of shallower updrafts evident in Fig. 7.30b. At low levels, where evaporative cooling is weakened (section 7.3), the pool of negatively buoyant air gradually loses depth and strength (compare with Fig. 7.31a).

It is clear that the early response in VAP describes a structure in the buoyancy field that is unfavorable for the maintenance of deep leading-edge updrafts and strong surface outflow, and is inconsistent with an active MCS (e.g., Sun et al. 1993). This is in contrast with the corresponding evolution in THETA, where buoyancy is gradually restored to its approximately correct distribution in the first 10-min.

The response of the pressure field follows closely the evolution of the buoyancy field, as evident in Figure 7.33. At restart (Fig. 7.33b), the pressure field describes the normal structure of the bow echo. Shortly thereafter, the relatively strong low- to mid-level mesolow and upper-level mesohigh weaken near the leading updrafts (Fig. 7.33c), in response to the erosion of the mid-level buoyant plume. Note, however, that

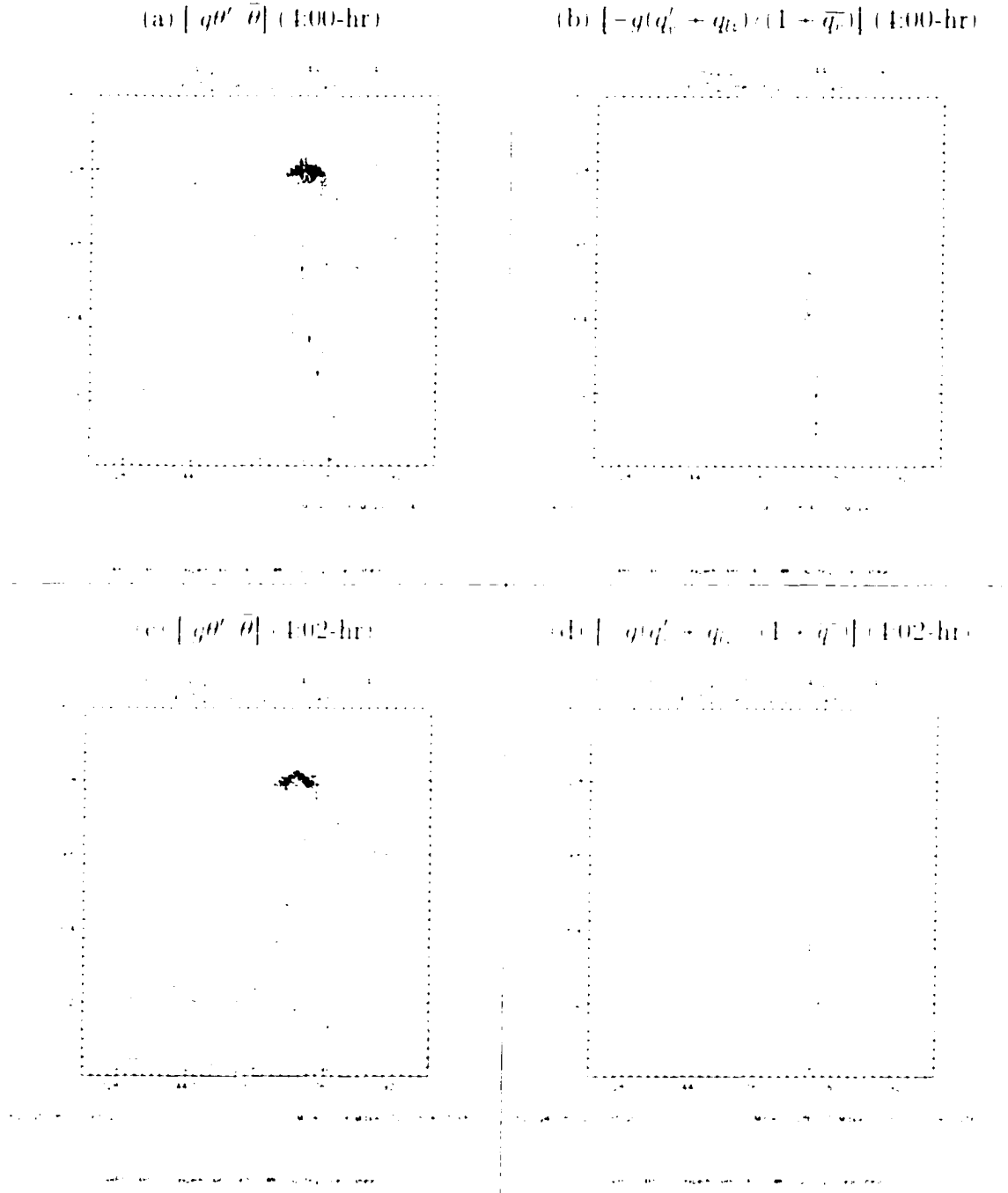


Figure 7.32: Vertical acceleration induced by thermal buoyancy (first column) and condensate loading (second column) terms of the total buoyancy field at $t = 4.00\text{-hr}$ (first row) and 4.02-hr (second row) for experiment VAP. In (a),(c) the contour interval is 0.05 m s^{-2} , while in (b),(d) a 0.0125 m s^{-2} contour interval is used. The domain shown is the same as in Fig. 7.31

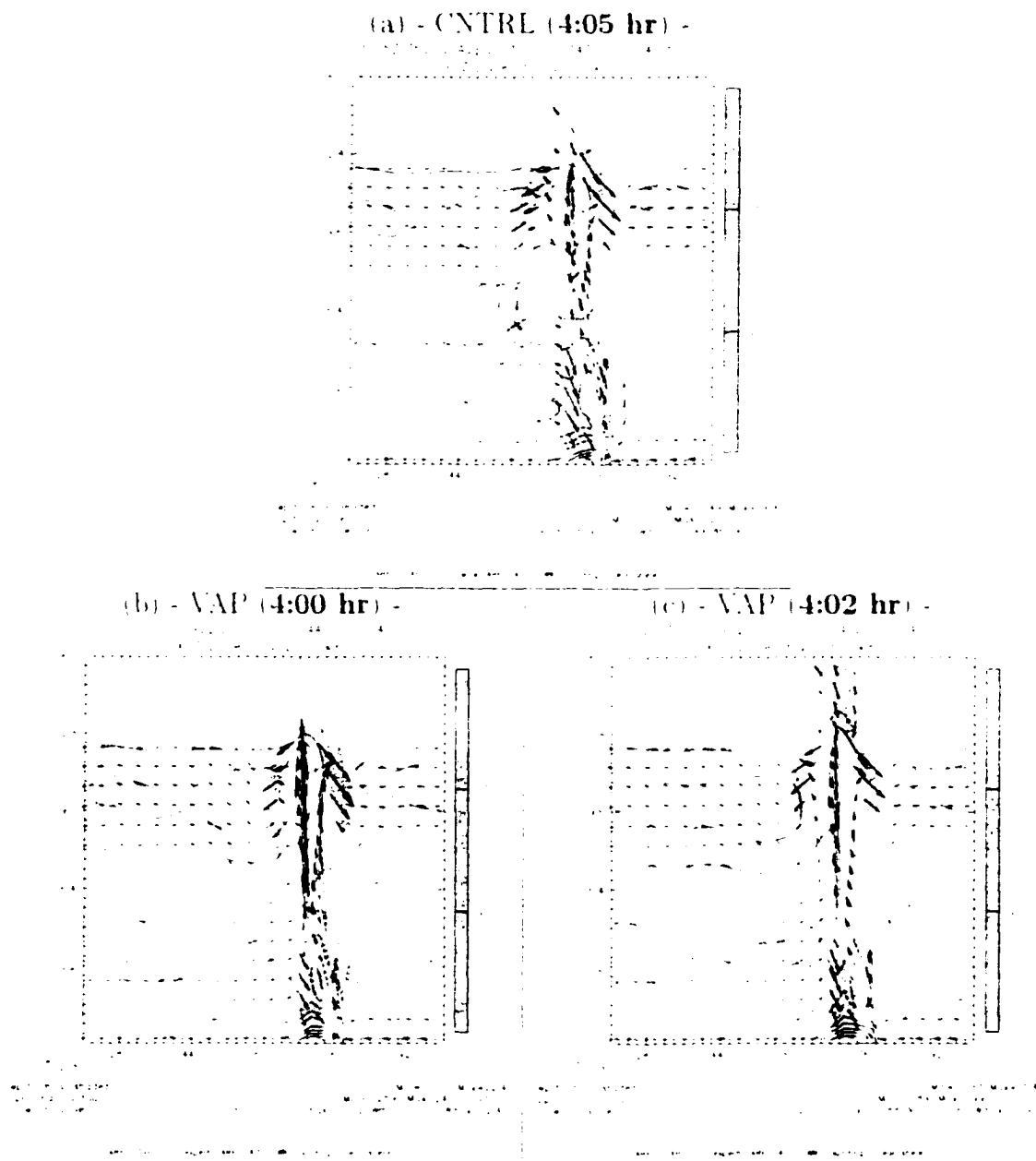


Figure 7.33: As in Fig. 7.16, but for experiment VAP.

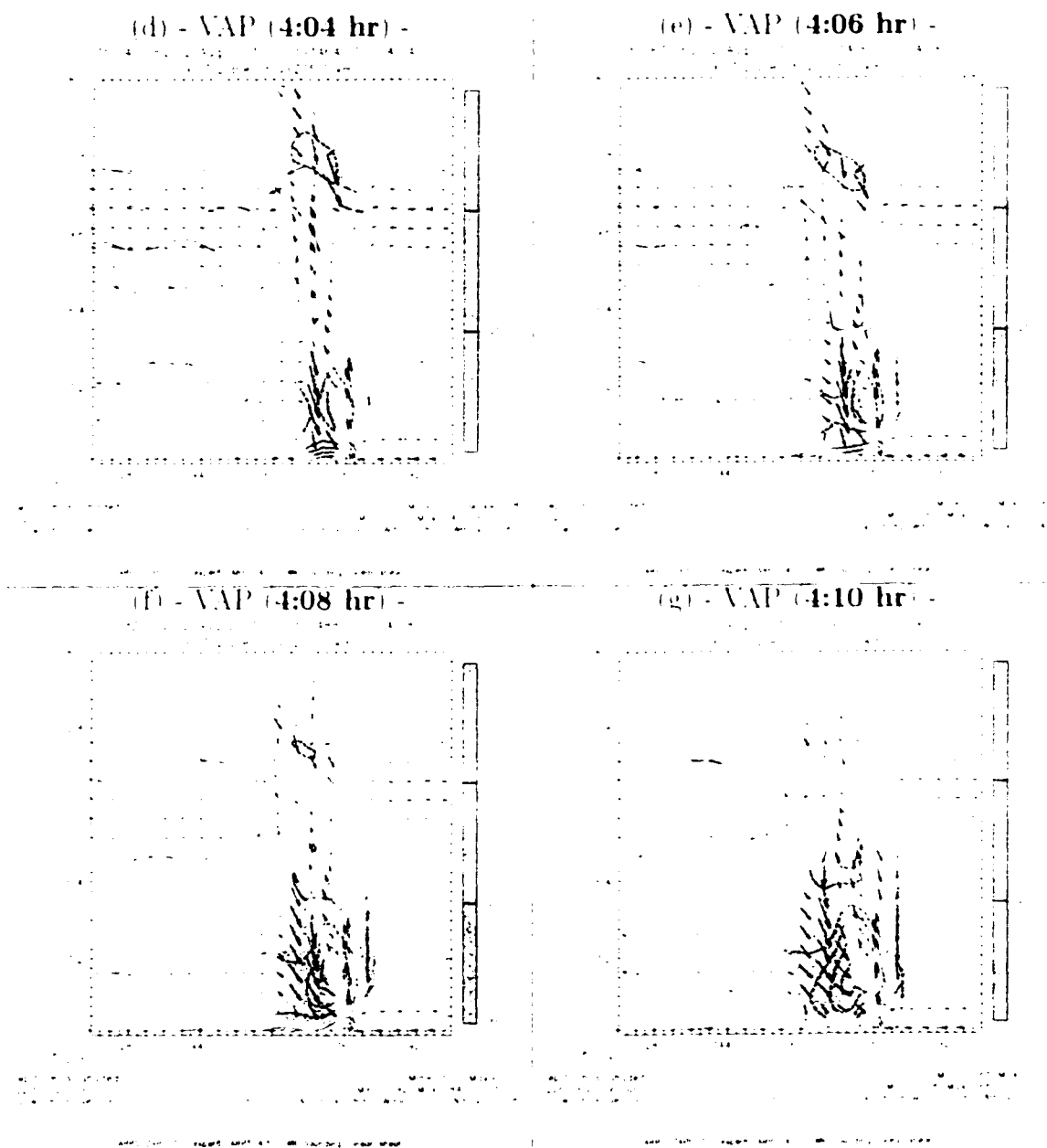


Figure 7.33 (continuation)

these pressure features retain part of their structure *away* from the leading edge of the bow echo. This is where the buoyant plume undergoes a more gradual weakening, in contrast to its “impulsive” disruption in the updraft sector (Figs. 7.31b-c).

The surface mesohigh also loses intensity with time, but at a slower rate, as a hydrostatic response to the weaker cold pool or, equivalently, weaker E_r at low levels (Fig. 7.10a). The mid- and upper-level pressure features, on the other hand, become active again as the buoyant plume redevelops from lower levels (Figs. 7.33d-g). The developing “high-over-low” pattern in the updraft is shallower than the CTRL counterpart (indicated in Fig. 7.33a), and is consistent with an equally shallow buoyant plume at this time (compare Figs. 7.31d-g with 7.33d-g). These results ratify our previous analysis that the pressure field in the bow echo responds strongly to buoyancy. It is possible that at later times, when a strong MCV is formed (e.g., Figs. 4.4b-c), dynamic pressure perturbations may have a more discernible contribution to the low- to mid-level mesolow (Weisman 1993), especially in the northern portion of the bow echo where the MCV is centered. Nevertheless, even in that case, *buoyancy remains an important driving mechanism for the pressure field that must be adequately specified in the storm system.*

Because pressure and buoyancy are significantly altered in VAP, the wind field responds as well. The evolution shown in Figs. 7.33b-g highlights the generation of a strong downdraft on the upstream side of the leading convective activity. In contrast with the mid-level downdraft in THETA, the counterpart in VAP forms at low levels, with gradual development upward as the simulation progresses. This is the same behavior displayed by the buoyant plume (Figs. 7.31c-g), suggesting that the downdraft is associated with the buoyancy source, possibly through a downward BPGA as discussed for experiment THETA (Fig. 7.18). We return to this topic in the next section.

The downdraft on the upstream side of the MCS, however, does not show a clear rearward propagation in the first 10-min in VAP. Thus, it is necessary to examine the response of the meteorological fields as the simulation proceeds. In fact, it is shown below that the most crucial processes affecting dynamic adjustment in experiment VAP occur more than 10-min following restart.

7.5.2 Evolution of buoyancy, pressure and wind fields in the first 20-min

Figure 7.34 shows the evolution of the total buoyancy field from $t = 4:12$ -hr to 4:20-hr in experiment VAP. The solution for CTRL at 4:15-hr is shown for comparison (Fig. 7.34a). By 4:12-hr, the magnitude of positive buoyancy *in the updraft* is actually stronger than in CTRL, and is located at mid-levels (Fig. 7.34b). Hence, updrafts regain strength locally and latent heating becomes quite strong. With time, part of the buoyant plume trails the leading edge of the MCS, with a westward propagation with respect to the storm system (Figs. 7.34b-f). This result indicates a delay in the regeneration of the mid-level heating source in VAP when compared to experiment THETA. In fact, the behavior of the buoyant plume in VAP is similar to that found in the first 10-min in THETA, except that: (i) the magnitude of the trailing mid-level positive buoyancy is considerably stronger in VAP; (ii) a well-defined layer of *minimum* in buoyancy develops just upstream of the leading convective line, as the strong buoyant plume moves rearward, characterizing two maxima in buoyancy (Figs. 7.34d-f). These points will be specifically addressed later in this section.

The corresponding evolution in the pressure and wind fields is shown in Figure 7.35. From panels b-f, we note that deep updrafts and downdrafts are present in VAP after 4:10-hr, following the development of the buoyant plume. Again, the strongest pressure perturbations in the low- to mid-level mesolow and upper-level mesohigh remain confined to the region where the buoyant plume evolves (Figs. 7.35b-f). A

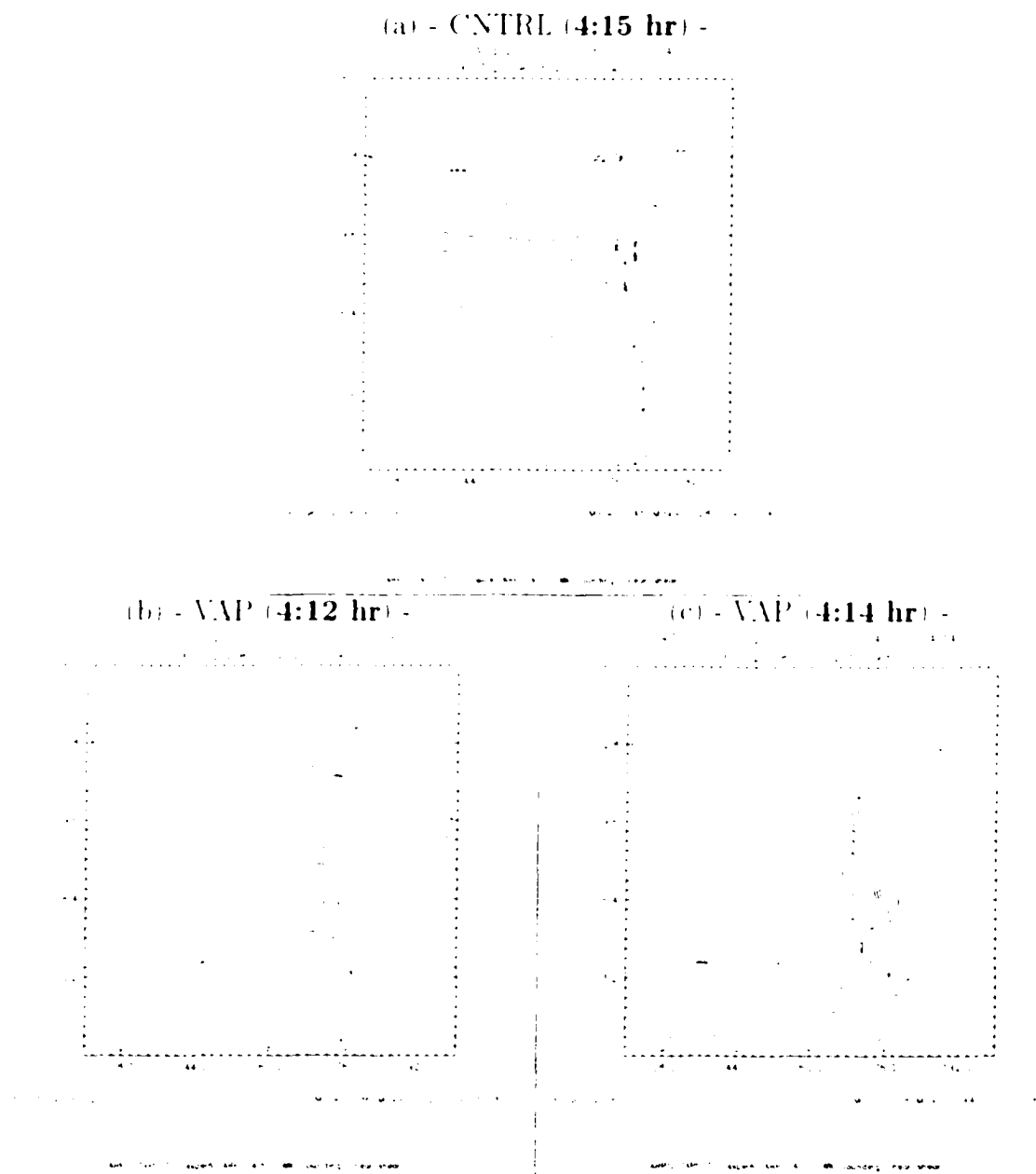


Figure 7.34: As in Fig. 7.14, but for experiment VAP, from $t = 4:12$ -hr to 4:20-hr.

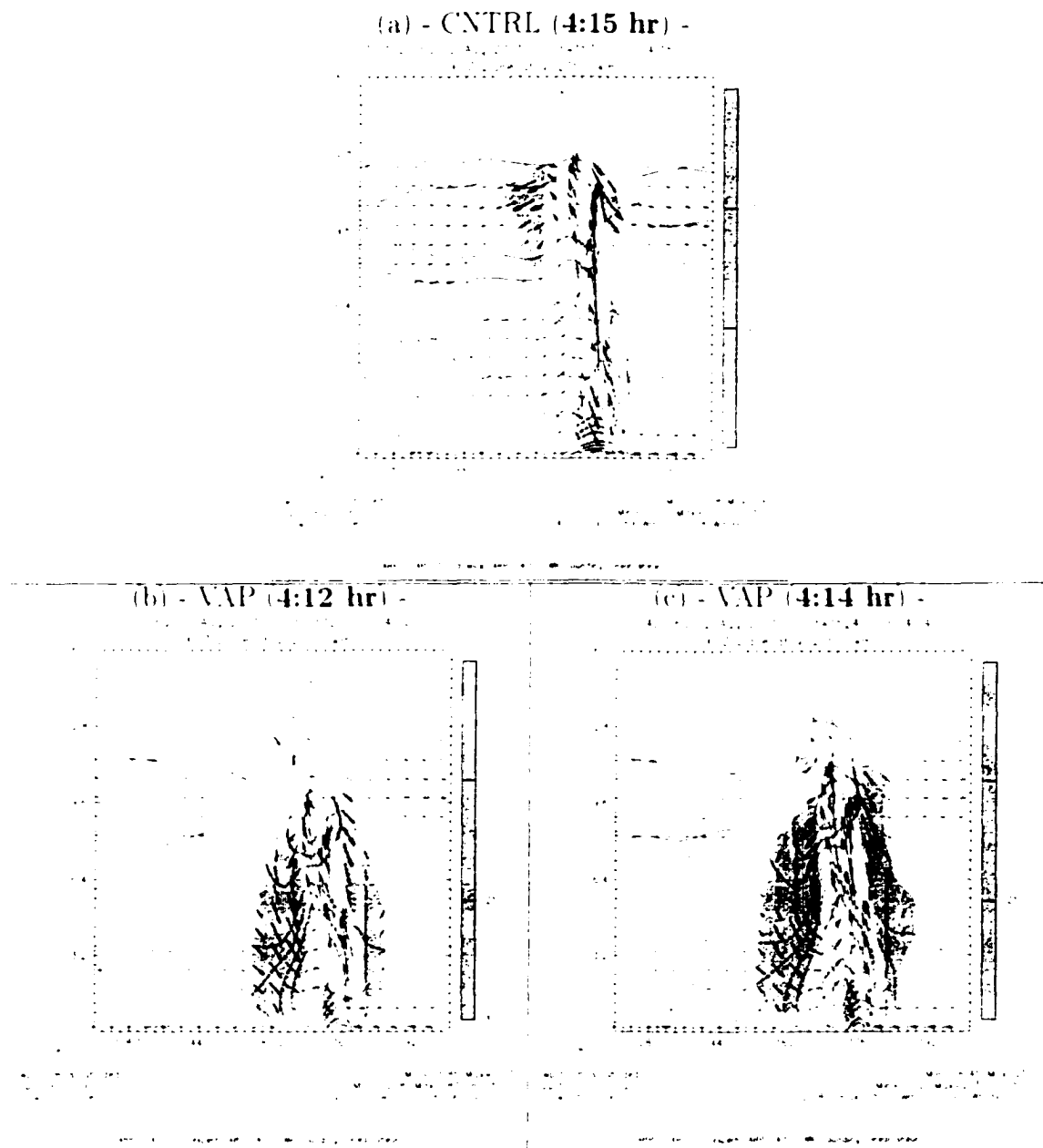
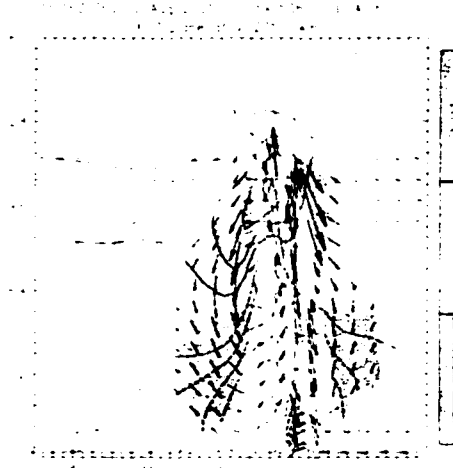
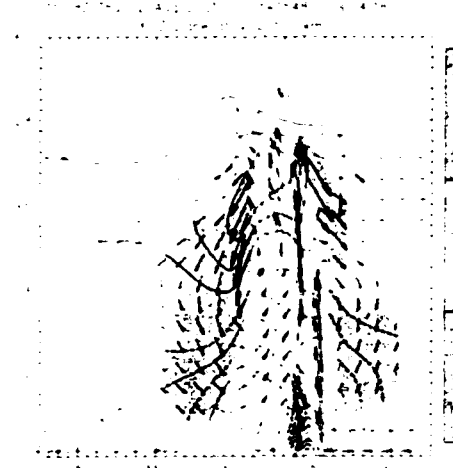


Figure 7.35: As in Fig. 7.16, but for experiment VAP, from $t = 4:12$ -hr to 4:20-hr.

(d) - VAP (4:16 hr) -



(e) - VAP (4:18 hr) -



(f) - VAP (4:20 hr) -

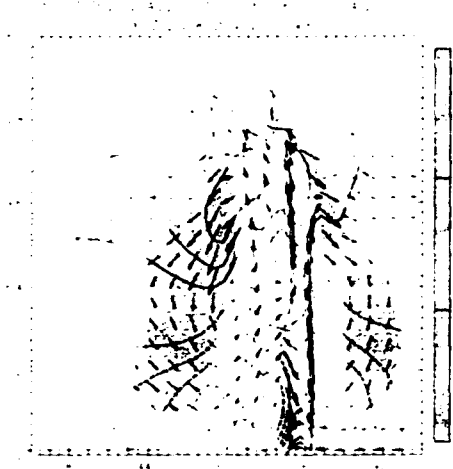


Figure 7.35 (continuation)

more intense pre-squall low forms in VAP, especially after 4:16-hr (low levels, within $176 \text{ km} \leq x \leq 192 \text{ km}$ in Figs. 7.35d-f), in agreement with stronger and deeper downdrafts ahead of the MCS. Compensating subsidence downstream of convective systems, associated with unsaturated descent that leads to warming, is recognized as the principal mechanism in the generation of pre-squall lows through hydrostatic considerations (e.g., Hoxit et al. 1976, Johnson and Hamilton 1988, Johnson 2001). Stronger downdrafts form in VAP (in comparison to CNTRL and THETA) on the leading flank of the convective system in response to a more upright orientation of the buoyancy source, as discussed below.

Figures 7.35b-f indicate a region of strong downdraft, *trailing* the convective updrafts, that propagates rearward at approximately -25 m s^{-1} relative to the storm from 4:12-hr to 4:20-hr. In experiment THETA, we found that the trailing mid-level downdraft propagated at the phase speed (or group velocity) of a HIGW with vertical wavenumber comparable to that of the heating source in the convective area. If this is case in VAP, then we may use equation (7.7) to estimate the vertical wavelength associated with the heating source.

Figure 7.36a shows the vertical profile of N^2 at $t = 4:15\text{-hr}$ for VAP — averaged for the same area enclosed by a rectangle in Fig. 7.22c — from which the buoyancy frequency at mid levels can be estimated to be approximately 0.010 s^{-1} . Substituting $c_{HIGW} = -25 \text{ m s}^{-1}$ and $N = 0.010 \text{ s}^{-1}$ into (7.7) yields $m \approx 4.0 \times 10^{-4} \text{ m}^{-1}$, which leads to $\lambda_z \approx 15.7 \text{ km}$. This result is an overestimate of the vertical wavelength of the heating source at the leading edge of the MCS at 4:12-hr (Fig. 7.34b), but is consistent with a deeper heating source minutes later (Figs. 7.34d-f).

To gain more insight into the behavior of the propagating downdraft, it is useful to investigate the response from the zonal component of the wind in the upstream flank of the bow echo. If the trailing downdraft and buoyant plume are in fact a

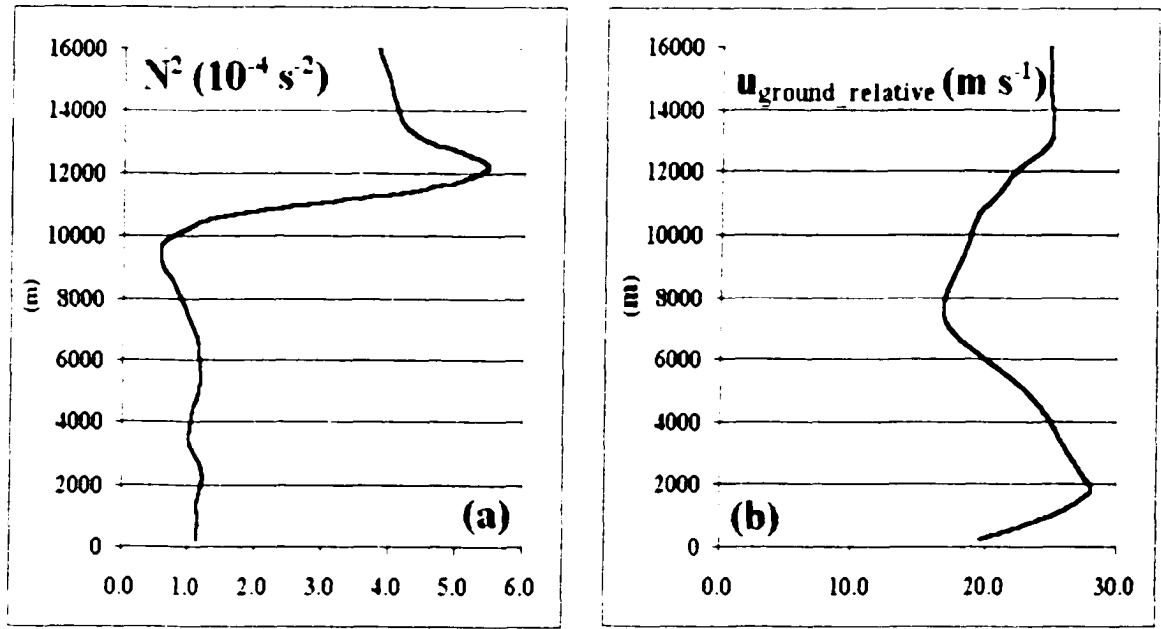


Figure 7.36 As in Fig. 7.26, but for experiment VAP at $t = 4:15$ -min.

manifestation of a HIGW induced by the developing heating source, then we should detect a connection between the structure of the RIJ and upper-level outflow and the propagating downdraft area (PD96), as found for experiment THETA (Fig. 7.21).

Figure 7.37 shows the evolution, from $t = 4:10$ -hr to $4:20$ -hr, of the zonal component of the wind in experiment VAP. Note that from $4:10$ -hr to $4:14$ -hr (Figs. 7.37a-c) the region with storm-relative winds stronger than 8 m s^{-1} (solid line) within the RIJ is rather limited compared to its counterpart in THETA (Fig. 7.21). In addition, the *trailing* outflow at upper levels is considerably weaker, such that the region with winds stronger than $\sim 12 \text{ m s}^{-1}$ (dashed line) is not clearly evident. In fact, the profile shown in Figure 7.36b shows that the average zonal component of the wind in the region of interest does not reach the same peak values as in THETA (Fig. 7.26b). At this stage, there is no clear indication of a link between the zonal wind structure and the mid-level downdraft.

However, from $t = 4:14$ -hr onward (Figs. 7.37e-f), when the westward propagation

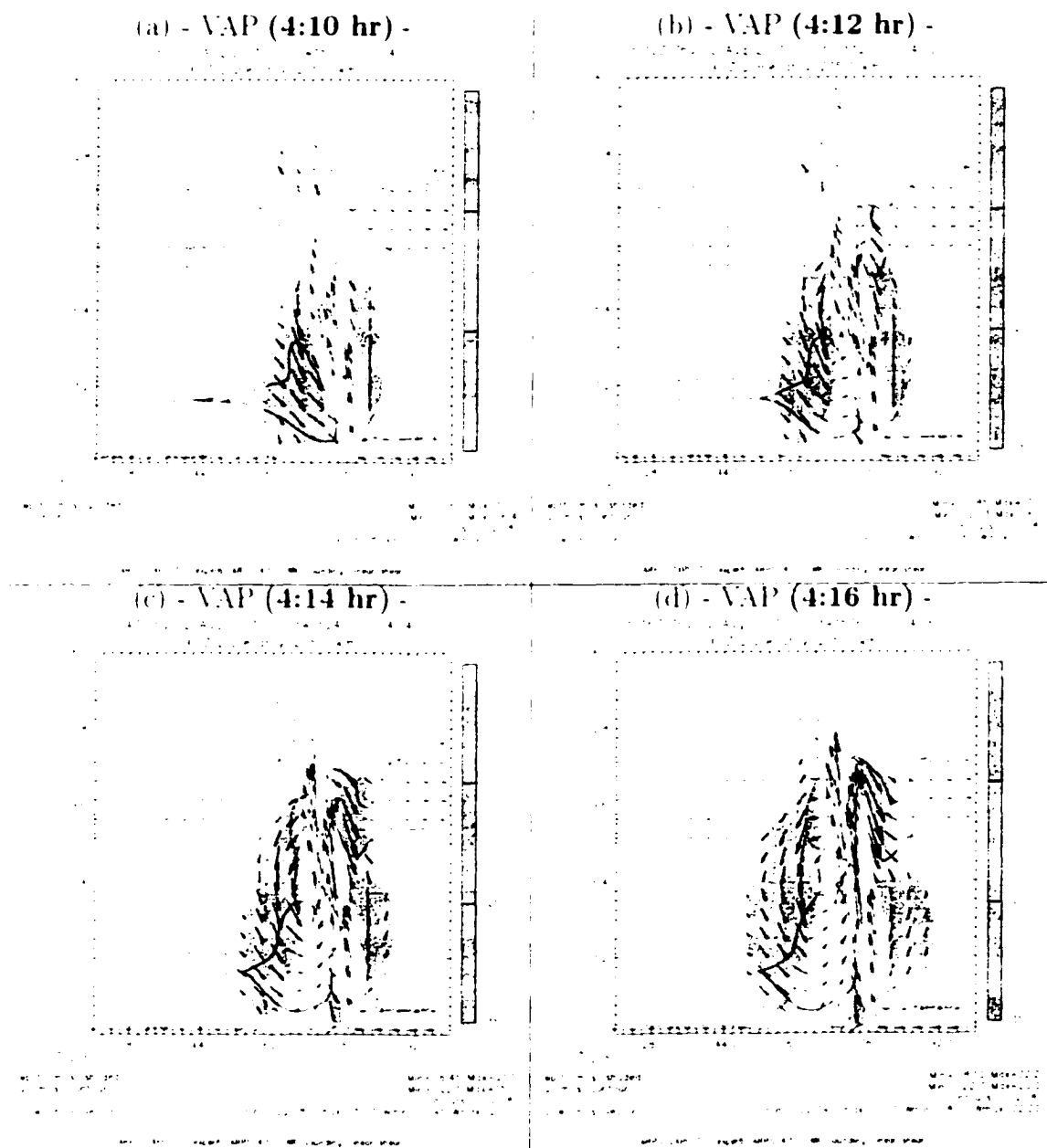


Figure 7.37: As in Fig. 7.21, but for experiment VAP, from $t = 4:10$ -hr to 4:20-hr.

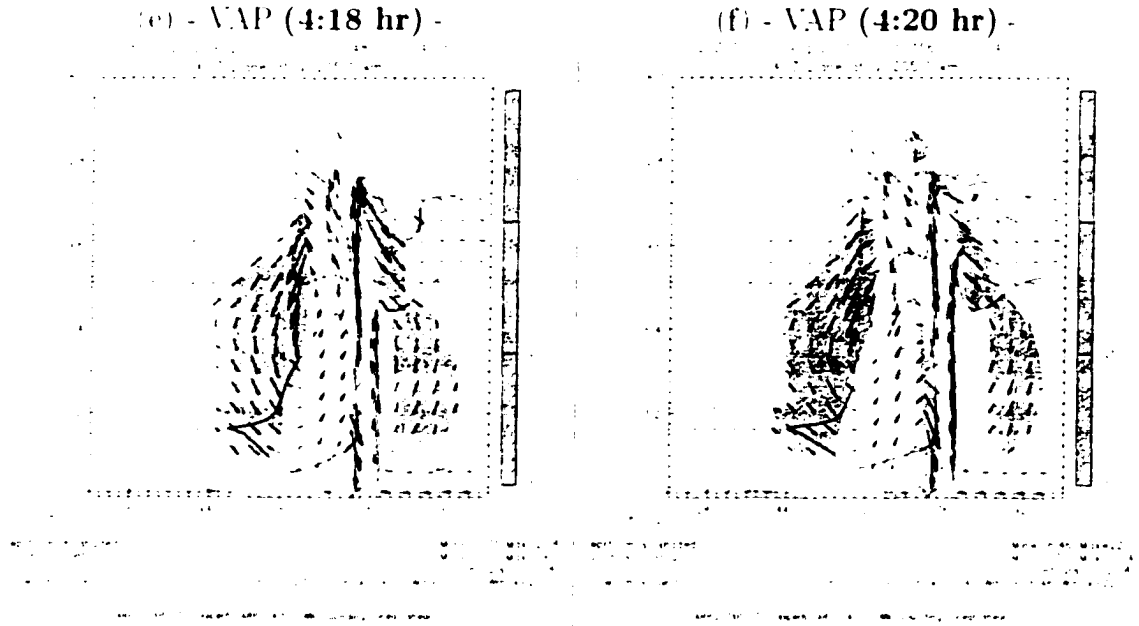


Figure 7.37 (continuation)

of the deep downdraft becomes more evident, the horizontal extent of the RIJ and trailing upper-level outflow shows some redevelopment consistent with the structure of the buoyant plume. Thus, it seems that the sequence shown in Fig. 7.37 captures the triggering of a HIGW pulse that propagates upstream at c_{HIGW} , and this coincides with the time when the heating source becomes considerably deeper (see Figs. 7.34c-f), in agreement with the relatively long λ_2 estimated from Eq. (7.7). Recall that in the first 10-min of integration in VAP, no clear evidence of rearward propagation of the buoyant plume exists.

Therefore, to a certain extent, the evolution of the simulated MCS aloft in experiment VAP is similar to that in THETA, though delayed. However, *important differences between the two withdrawal experiments are clear*. The trailing mid-level buoyant plume in VAP, after 10-min of integration, becomes *stronger* than in THETA and CNTRL, as shown from Fig. 7.34¹⁷. Because thermal buoyancy dominates the

¹⁷In the analysis that follows we refer specifically to the **propagating** branch of the buoyant plume which detaches

total buoyancy (e.g., Fig. 7.15), stronger positive temperature perturbations at mid levels exist in VAP to maintain a relatively intense buoyant plume even as it moves away from the main heating source (in contrast with CTRL and THETA). Diabatic and adiabatic processes may be responsible for such a response concomitantly.

To qualitatively investigate these processes, it is interesting to consider a simplified form of the thermodynamic equation, given by (e.g., Houze 1993):

$$\frac{1}{\theta_0} \left[\frac{\partial \theta'}{\partial t} + \vec{V} \cdot \nabla \theta' \right] = -w \frac{\partial \ln \theta_0}{\partial z} + \frac{\dot{Q}}{(c_p T)} \quad (7.8)$$

where θ_0 is the base state potential temperature (which is function only of height), θ' is the perturbation potential temperature, \vec{V} is the 3D wind vector, w is the vertical component of the wind, \dot{Q} is the rate of diabatic heating/cooling per unit mass (in $\text{J kg}^{-1} \text{s}^{-1}$) (note that, for our qualitative analysis, the effects of radiation, molecular diffusion and frictional heating are disregarded), c_p is the specific heat at constant pressure and T is temperature. The first term on the right-hand-side of (7.8) is the contribution from *adiabatic* heating (cooling) due to compression (expansion) in a statically stable atmosphere during subsidence (ascent). The second term represents the *diabatic* contribution associated with phase changes.

Adiabatic compression will dominate the response if strong (subsaturated) downdrafts are present in the trailing sector in VAP. Figure 7.38 compares the magnitude of the subsident motion in THETA and VAP at 4:08-hr and 4:16-hr, respectively. Different times are chosen for comparison because of the delayed evolution of the buoyant plume in VAP. The solutions at these times contain well defined deep downdrafts in both runs. From Figure 7.38 it is clear that experiment VAP displays stronger mid-level downdrafts. The trailing vertical motion in both runs is mostly subsaturated, with well defined dry layers accompanying the subsidence. This is further indicated

from the main convective region, clearly seen in Figs. 7.34e-f. The reason why we focus in such feature, is because its presence eventually leads to a behavior in the wind field that deviates substantially from CTRL and THETA.

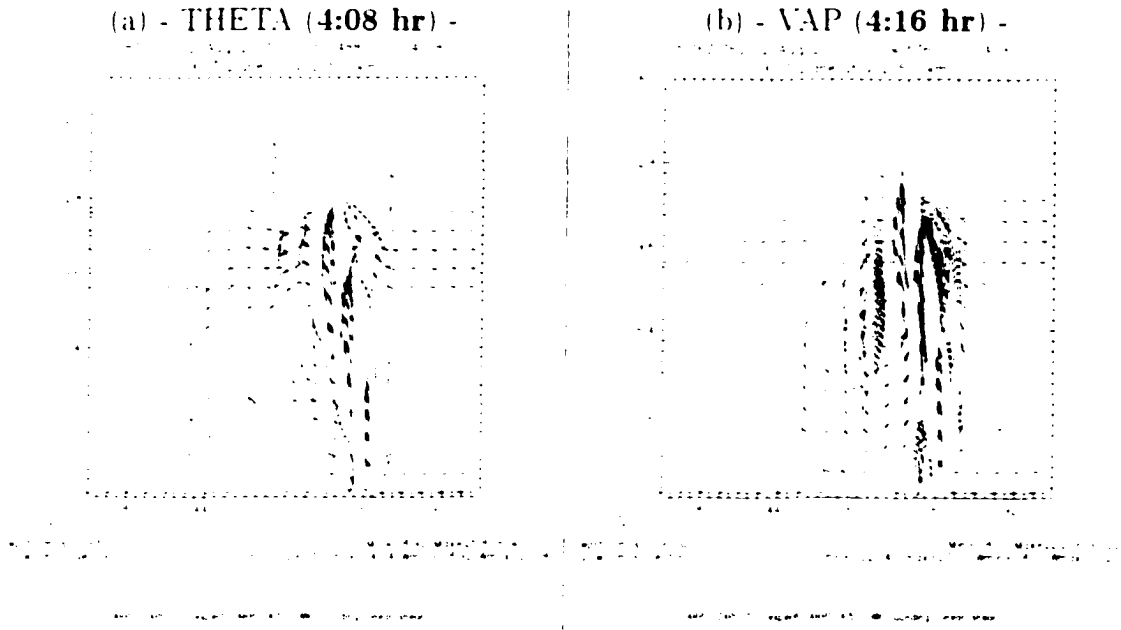


Figure 7.38: Vertical cross sections of the magnitude of downward motion (dashed lines) and storm-relative winds (vectors) in m s^{-1} for (a) experiment THETA at 4:08-hr, and (b) experiment VAP at 4:16-hr. Contour interval is 2 starting at $\pm 2 \text{ m s}^{-1}$. The domain shown is the same as in Fig. 7.14.

in Figure 7.39, which compares the ratio q_e/q_c , for the two withdrawal runs (THETA at 4:08-hr and VAP at 4:16-hr). In both THETA and VAP, an area of maximum q_e/q_c is evident in the center of the domain shown, associated with the saturated updrafts. Upstream of the convective activity, a broad dry layer (with q_e/q_c less than 0.6) is found in THETA from low to mid levels, associated with the rear-to-front flow and the propagating downdraft (Fig. 7.39a). In VAP, the corresponding dry layer is confined to leading edge of the system, where downward motion straddles the updrafts.

Therefore, enhanced adiabatic compression in VAP plays a significant role in generating a stronger propagating branch in the buoyant plume. On the other hand, the possible role played by diabatic effects in the generation of such feature may be less straightforward. As discussed earlier, diabatic cooling is enhanced at mid levels *early* in experiment VAP, which contrasts with the development of a stronger buoyant

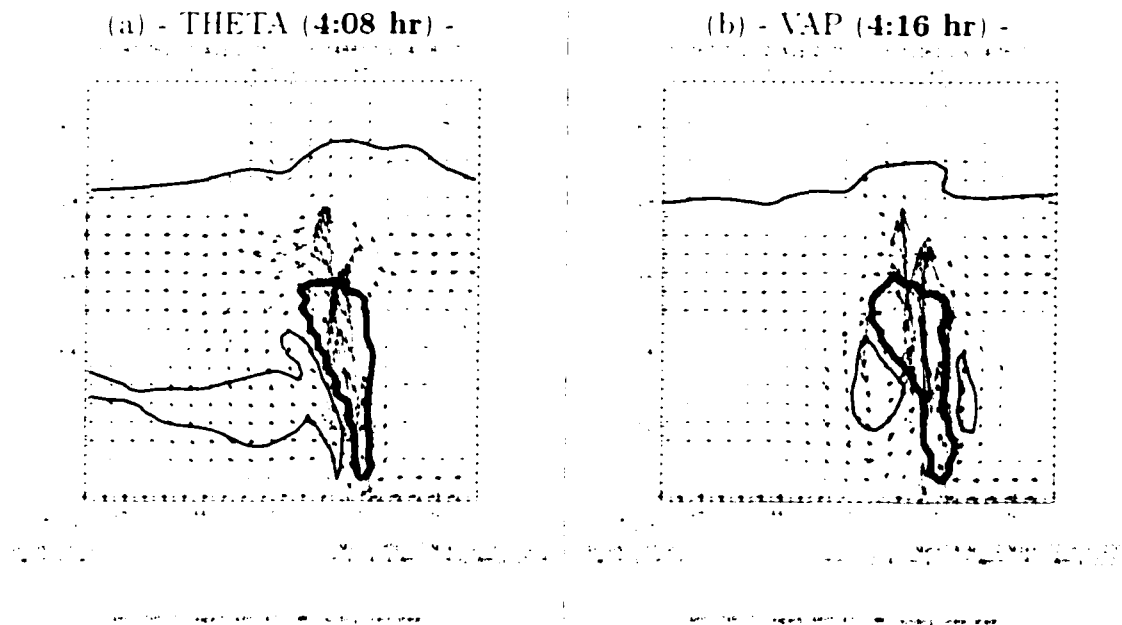


Figure 7.39. Vertical cross sections of the ratio q_e/q_s at 0.2 dimensionless intervals. Thick solid line in the center of the domain encloses areas with q_e/q_s equal to 1, while thin solid line indicates areas with q_e/q_s equal to or less than 0.6. Vectors are storm-relative winds in m s^{-1} . The domain shown is the same as in Fig. 7.14.

plume. Nevertheless, condensate loading is reduced in VAP (Fig. 7.32) in response to a drier mid-level atmosphere at restart time. (This process accounts for the increase in q'_e at mid-levels shown in Fig. 7.11c for the first 10-min of experiment VAP (dotted line in Fig. 7.11c)). Thus, with the reduced concentration of hydrometeors later in the integration, one may conjecture that the rate of detrainment of cloud elements (which leads to cooling by evaporation–sublimation) on the upshear side of the convective circulation is weakened due to a more rapid depletion of condensate. If this is the case, air parcels within downdrafts on the trailing side of the MCS become subsaturated earlier, and adiabatic warming may occur in a deeper layer than in THETA and CNTRL.

Figure 7.40 compares the total water mixing ratio q_{te} (where $q_{te} = q_e + q_r + q_i + q_s + q_h$) for experiments THETA and VAP. In THETA, the broad area of downward

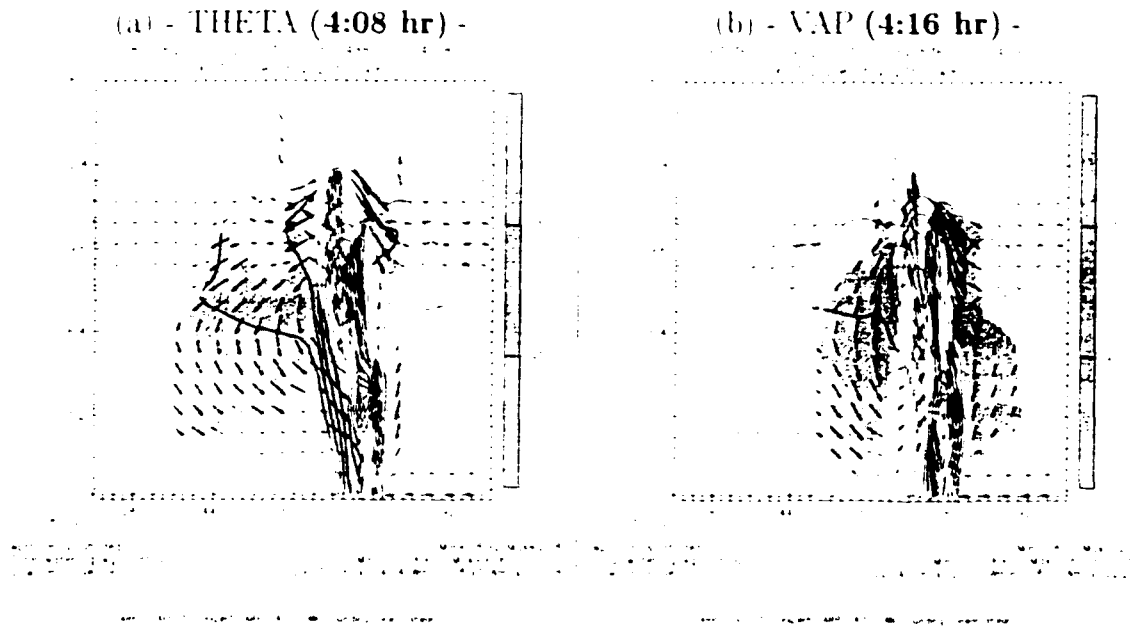


Figure 7.40: Vertical cross sections of total water mixing ratio (solid lines) along $y = 295 \text{ km}$ for (a) experiment THETA at $t = 4:08\text{-hr}$, and (b) experiment VAP at $t = 4:16\text{-hr}$. Contour interval is 1 g kg^{-1} . Vectors are storm-relative winds in m s^{-1} , and shading indicates areas with downward motion equal to or stronger than -1 m s^{-1} . Domain shown is the same as in Fig. 7.14.

motion is evident with intense outflow at upper levels, which advects cloudy air horizontally forming the anvil (Fig. 7.38a). The maximum q_k in the upper levels of the convective region reaches 7 g kg^{-1} at this time. In VAP at 4:16-hr, a trailing downdraft already shows signs of upstream propagation. The area with condensate is shallower compared to THETA, and q_k at upper levels reaches 5 g kg^{-1} , which is less than in THETA at 4:08-hr. However, as depicted in Fig. 7.39, this does not imply that a deeper layer of subsaturated subsidence is present in VAP, because the *depth* of the dry layers in both runs is comparable. Thus, there exists no clear evidence that (potentially) weaker detrainment from the convective region, hypothesized above, plays any significant role in differentiating the two runs at this stage.

The *origin* of the stronger mid-level downdrafts is associated with the regeneration of the buoyant plume itself, especially between 4:08-hr and 4:14-hr (Figs. 7.31f-g and

7.34b-c). Intense latent heating occurs at mid levels during this stage in VAP as saturated updrafts regain strength. Figure 7.41 shows time series of domain-maximum updrafts (DMUs) for simulations CNTRL, THETA and VAP. In VAP, the DMU is considerably reduced shortly after restart, as discussed earlier. As the originally shallow surface-based updrafts (forced by lifting over the gust front) become deeper after approximately 8-min (e.g., Figs. 7.33f-g and 7.35b-c), the DMU is restored. Note that *the strengthening of the DMU in VAP is more abrupt than early in experiment THETA* (Fig. 7.41) because, in THETA, the mid-level updrafts are simply *enhanced*, rather than *regenerated*. The behavior of the buoyancy field at the leading edge of the bow echo in VAP is consistent with the general evolution in vertical motion. Therefore, the corresponding BPGA induced around the buoyancy source (e.g., Fig. 7.18) should respond accordingly, leading to stronger downdrafts on the sides of the developing buoyant plume.

To address this process, Figure 7.42 depicts vertical cross sections of areas with downdrafts (shading) and negative A_{vpqB} (as defined in 5.7; dashed lines) for experiment VAP from $t = 4:08$ -hr to 4:12-hr (Figs 7.42b-d). The solution from CNTRL at $t = 4:10$ -hr also is shown for comparison (Fig. 7.42a). In VAP, the *magnitude* of A_{vpqB} at the *upper levels* of the convective region (or overshooting top; above $z = 9.6$ km) is less than in CNTRL, owing to a weaker downward VPGA at this time. However, at mid to upper levels, negative VPGA develops on the *sides* of the buoyancy source, where downdrafts are initiated. Note that the region of stronger A_{vpqB} at mid levels follows closely the evolution of the buoyant plume (refer to Figs. 7.31f-g and 7.34b), and by 4:12-hr (Fig. 7.42d) its magnitude is larger than its counterpart early in experiment THETA (Fig. 7.19b). This agrees with the time when the buoyant plume in VAP is strongest in the cross section being analyzed (Fig. 7.34b). This result links the generation of more intense mid-level downdrafts in VAP to a more active buoyancy

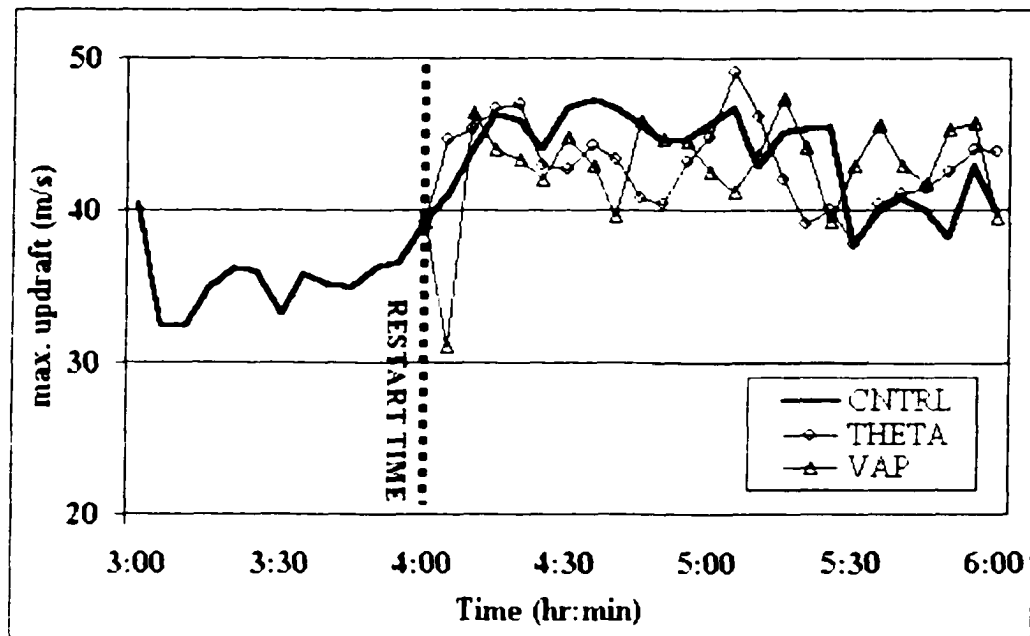


Figure 7.4f: Time series, from 3 to 6-hr, of domain maximum updrafts (m s^{-1}) sampled at 5-min intervals. Comparison between simulations CNTRL, THETA and VAP.

source at a given time — later in the simulation the intensity of the buoyant plume at *the leading edge of the MCS* is reduced and becomes comparable to that in CNTRL and THETA (e.g., 7.34f) — accounting for a more efficient adiabatic warming found on both upstream and downstream sides of the leading convection. This is essentially the mechanism that generates a relatively strong propagating branch of the buoyant plume and stronger pre-squall low mentioned before.

7.5.3 Impact upon the RIJ, inclination of the convective cells, and IGW and acoustic wave activity

In the previous section we showed that enhanced subsaturated downdrafts in VAP favor a trailing buoyant plume that is stronger than in CNTRL and THETA. As a result, just east of the propagating downdraft (on the upstream side of the bow echo), conditions become favorable for the generation of *strong upward motion*, which

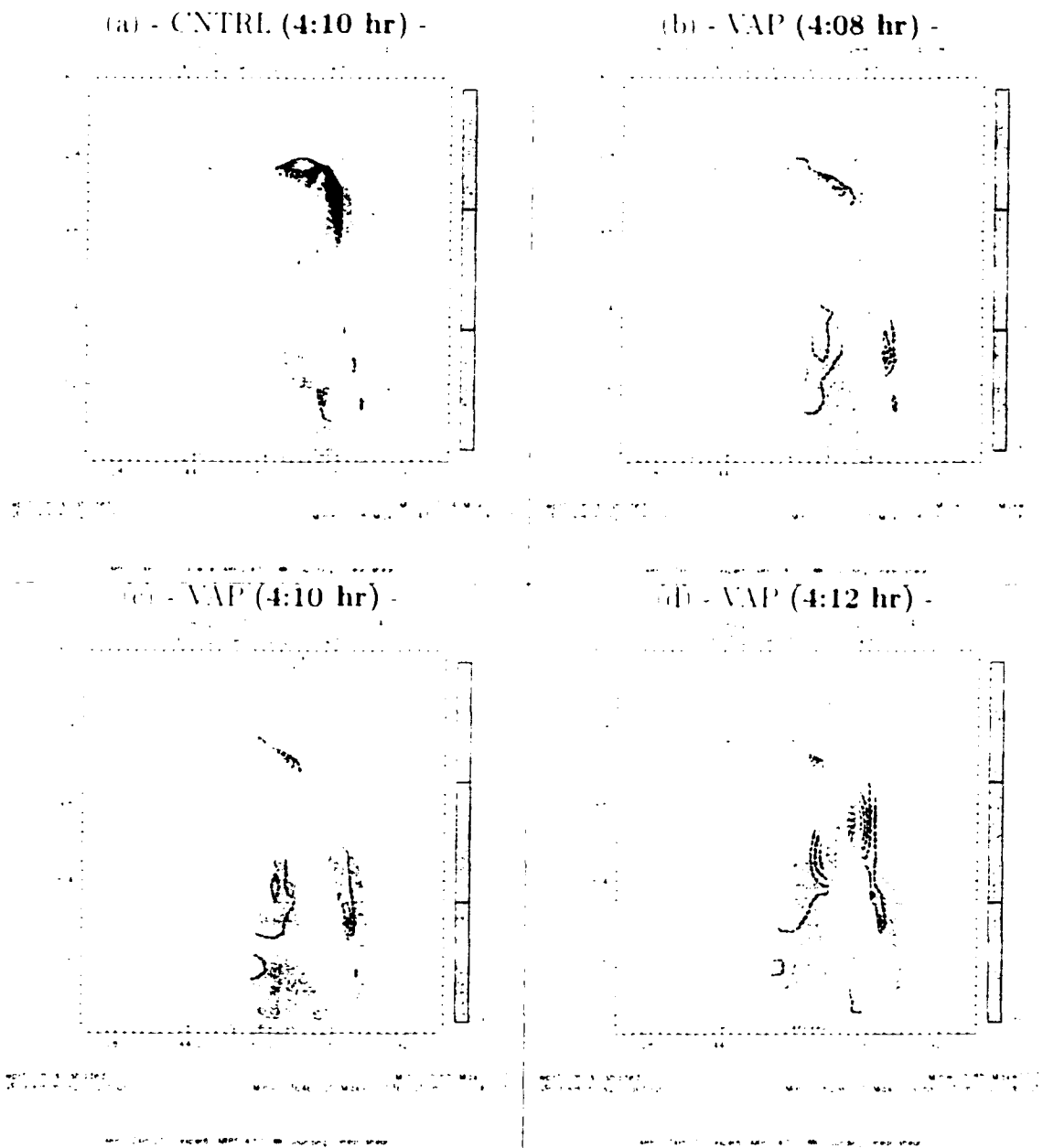


Figure 7.42: As in Fig. 7.19, but comparing solutions from simulation CNTRL at $t = 4:10$ -hr (panel (a)) and simulation VAP at $t = 4:08$ -hr, $4:10$ -hr and $4:12$ -hr (panels (b)-(d)).

is evident in Figs. 7.35d-f, because the trailing buoyancy source in VAP is intense enough to induce a significant positive A_{tpqB} , as illustrated in Figure 7.43. Note the presence of two regions of positive A_{tpqB} at low to mid levels in Fig. 7.43: the one to the east is associated with the leading surface-based updrafts, and the western one is associated with the propagating buoyant plume. The trailing updrafts *have no relation with the advancing gust front*, and their behavior represents an IGW-type response to the upstream buoyancy perturbation. Before addressing IGWs specifically, it is important to assess the influence of the trailing updrafts on the behavior of the simulated MCS in the region of study.

Figure 7.39b shows that the strong trailing updrafts generated in VAP are mostly subsaturated, especially at lower levels (west of $x = 176$ km). This indicates that subsaturated lift is present, which favors adiabatic cooling and, thus, erosion of the positively buoyant air within the trailing buoyancy source. This process explains the formation of a local minimum in buoyancy just behind the leading convection, evident in Figs. 7.34d-f, and *accounts for a major disruption in the structure of the MCS*. Not only is the buoyant plume eroded locally, but the trailing updrafts also advect moist air from the (artificially moister) boundary layer to higher levels, as indicated in Fig. 7.30d for $t = 4:30$ -hr. Such a circulation pattern does not agree with the structure of a mature bow echo for which a *descending* RIJ transporting *drier* air should be present. This result helps explain why the restoration of a low- to mid-level dry layer is slower in VAP (Fig. 7.11c). In addition, in the absence of a descending RIJ that transfers momentum to the surface, the low-level outflow becomes less intense and convergence at the gust front is reduced (Fig. 7.8g-i). Hence, the triggering of new surface-based updrafts at the leading edge of the system is weakened, as evident in Fig. 7.30d. The significant impact described above influence the behavior of IGWs as well.

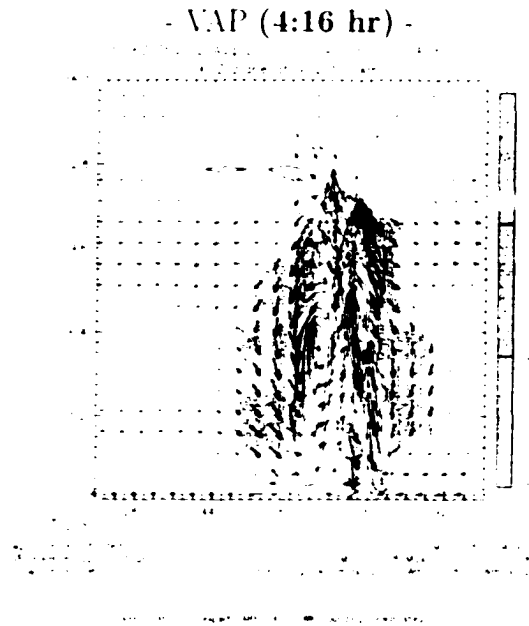


Figure 7.43: As in Fig. 7.19, but for experiment VAP at $t = 416$ -hr. Positive (solid lines) and negative (dashed lines) values of $A_{\theta, \theta}$ are plotted at 0.02 m s^{-2} intervals. Storm-relative winds (m s^{-1}) are indicated by vectors.

In experiment THETA, we discussed that the triggering of a HIGW with vertical wavelength comparable to that of the convective heating source is accompanied by a response from the horizontal wind field that maintains the *correct* structure of the RIJ and the upper-level outflow (PD96). In VAP, some evidence of a propagating HIGW (represented by the trailing buoyant plume and mid-level downdraft themselves) is also found after 10-min of simulation, as described in Fig. 7.37. However, the re-establishment of the RIJ is jeopardized by the generation of strong subsaturated updrafts following the propagation of the buoyancy source aloft. Applying PD96's reasoning, this suggests that an effective change in the aggregate structure of the heating source in the convective region occurs in VAP. In fact, we describe above how the (delayed) formation of a stronger mid-level buoyancy field in VAP affects the response from temperature, pressure and wind fields in such a way that leads to a significant alteration of the convective circulation.

Another important implication regarding IGW activity concerns the vertical inclination of convective cells. Several studies have shown that IGW activity tends to be favored in the direction of the tilt of the convective heating source (e.g., Fovell et al. 1992, PD96, Nachamkin and Cotton 2000), as confirmed in experiment THETA. The formation of relatively strong updrafts trailing the convective activity in VAP does affect the inclination of the convective cells. Figure 7.34f, for example, shows a buoyant plume (leading the MCS) that displays less upshear tilt than its counterpart in CNTRL (7.34a) and in THETA (7.14g).

To better illustrate the vertical tilt of convective flow, it is desirable to examine the solution with the correct aspect ratio. Figure 7.44 depicts a close-up view of the wind field across the gust front in vertical cross sections showing the correct aspect ratio of the flow in experiment VAP, from $t = 4:14$ -hr to $4:20$ -hr (when the trailing updrafts are evident). Note that the updrafts at the leading edge of the system become more vertically oriented as the rear-to-front flow acquires an upward-oriented vertical component. Thus, in the correct aspect ratio, the updrafts formed *upstream* of the gust front actually represent an “ascending RLJ”, that favors a gradual *downshear* leaning of the convective cells.

The presence of more erect convective circulation (and, therefore, more erect heating source) appears to be in agreement with enhanced disturbances (IGWs) *ahead* of the MCS in VAP. This becomes more clear in Figure 7.45, which compares the vertical motion field at $z = 4.8$ km for experiments VAP and THETA, 30-min after restart. In THETA, an asymmetric pattern of IGW activity is evident, with preferential activity on the upstream side of the system (Fig. 7.45a). This behavior is often associated with MCSs displaying upshear-tilted convective cells (e.g., PD96). In contrast, experiment VAP at $4:30$ -hr displays quite active disturbances on both sides of the simulated MCS. For instance, a broad subsidence area leads and trails the bow

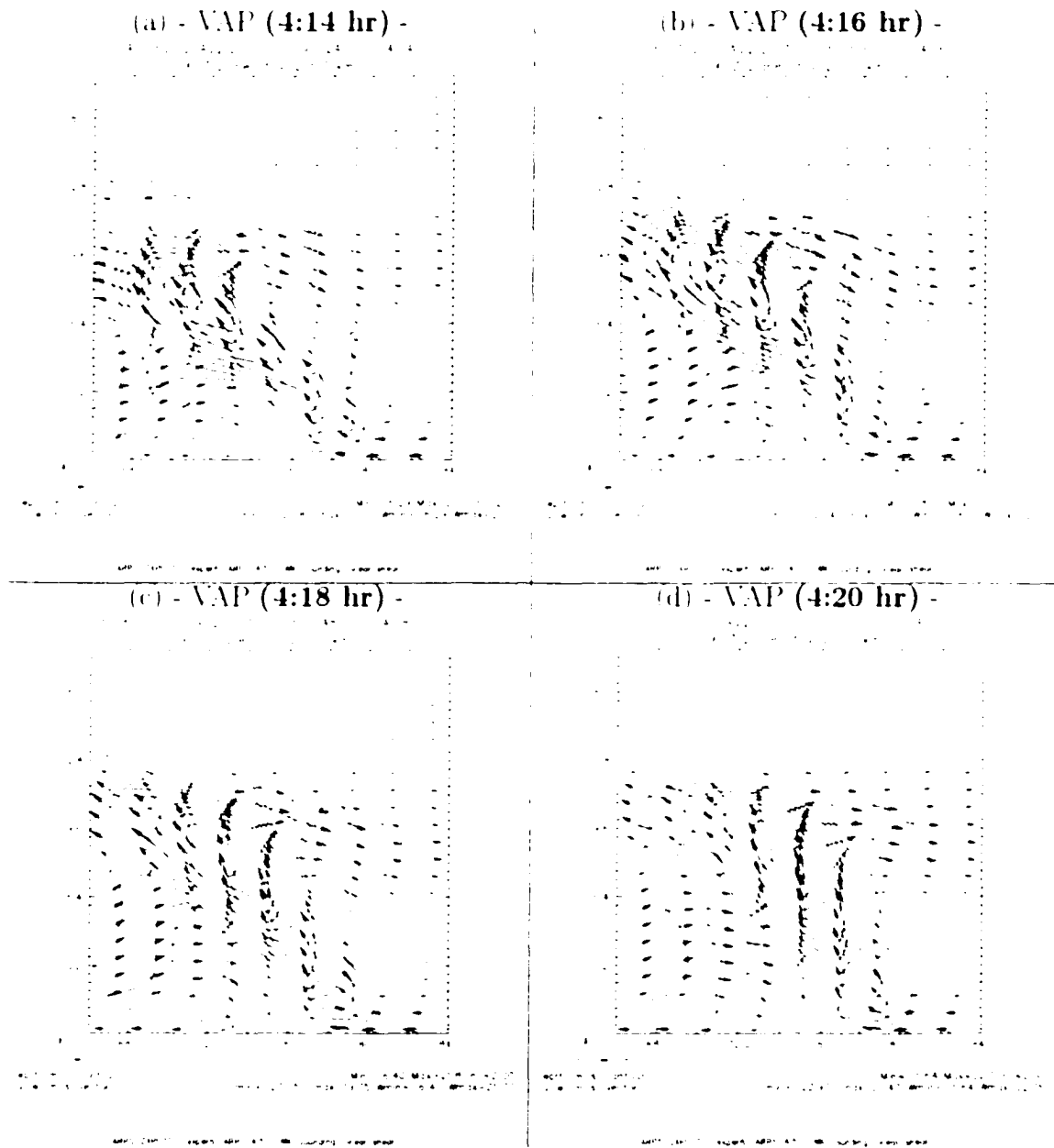


Figure 7.44: Vertical cross sections in the xz-plane along $y = 205 \text{ km}$ for the storm-relative wind field across the gust front in experiment VAP, from $t = 4:14\text{-hr}$ to $4:20\text{-hr}$. The domain shown is $18 \text{ km} \times 18 \text{ km}$. Vectors represent system-relative winds in m s^{-1} , and contours indicate magnitude of the vertical velocity in m s^{-1} (contoured at 2 m s^{-1} increments, with the zero line being suppressed). Solid (dashed) lines indicate updrafts (downdrafts).

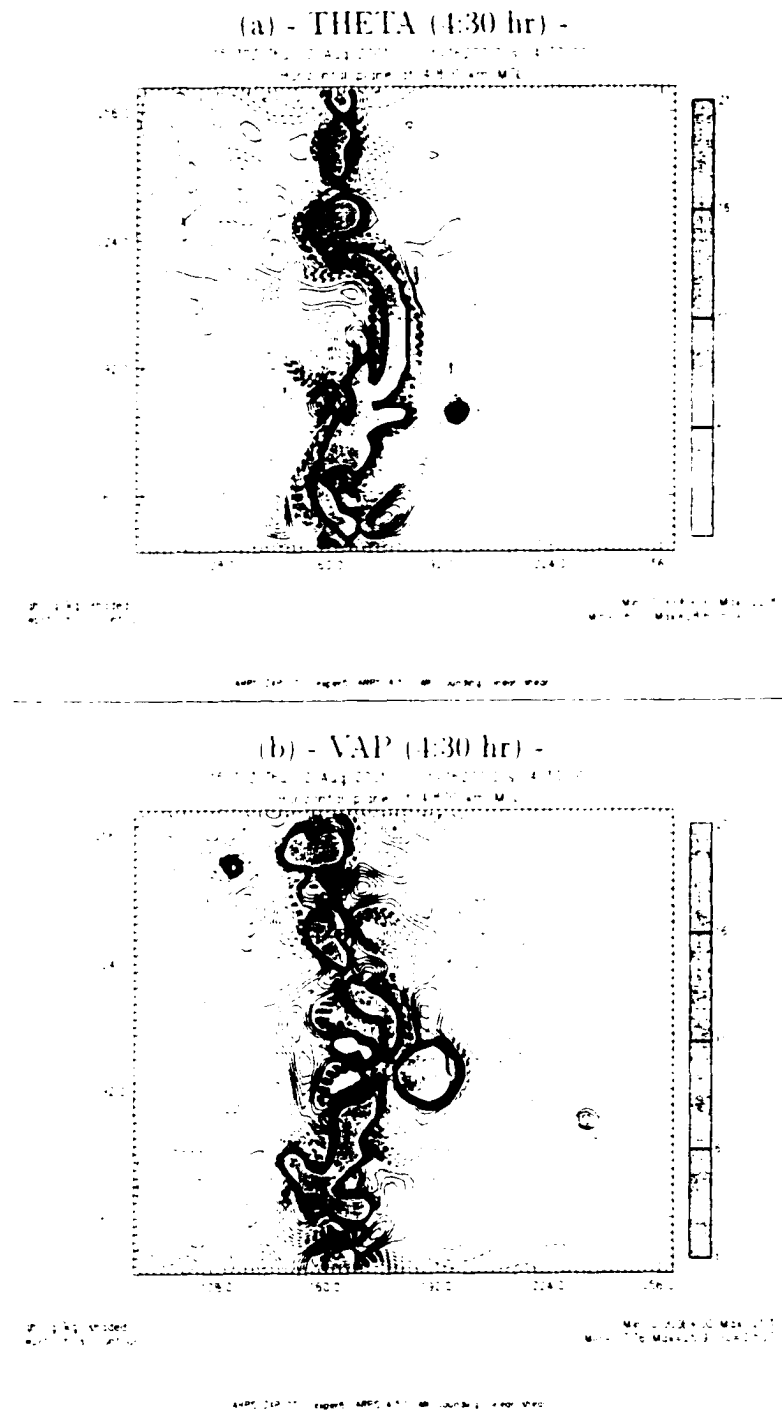


Figure 7.45: As in Fig. 7.24, but for THETA (panel (a)) and VAP (panel (b)) at $t = 4:30$ -hr.

echo in experiment VAP. It is important to note that, at restart, the IGW activity in VAP is the same as in simulation CNTRL, with more disturbances occurring on the upshear flank of the system (as in THETA), not shown. Therefore, an alteration occurs in VAP also in terms of the behavior of IGWs.

In previous analysis we mentioned that the solution in VAP shares some characteristics with that in THETA, though with a delay. While the buoyant plume in THETA is restored shortly after restart, in VAP it takes around 10 to 15-min for the buoyant plume (or, in a more general way, the heating source) to regenerate considerable depth and a maximum buoyancy perturbation at mid-levels (e.g., Fig. 7.34c). Interestingly, *only after restoring this basic structure does the mid-level downdraft and buoyancy source propagate rearward*, most probably associated with a HGW (Fig. 7.37).

Figure 7.46 shows time series of vertical motion at three different levels in experiment VAP at the same grid point analyzed for experiment THETA, i.e., at a location just upstream of the main bow echo segment at 4-hr. Recall that in THETA vertical motion at this grid point indicates the presence of *propagating* disturbances starting as soon as the run is started (Fig. 7.27). This is not the case in VAP. The early evolution depicted in Figure 7.46 simply describes the weakening of the main updraft in the first 10-min, followed by its gradual restoration starting at low levels. Note in Fig. 7.46 that the lower the level, the earlier the upward motion is regenerated (after 10-min of simulation), in accordance with the evolution described in Figs. 7.33 and 7.35. Although this cycle may be interpreted as the manifestation of IGWs (Yang and Houze 1995a), it does not represent a truly propagating disturbance in a storm-relative sense, which contrasts with experiment THETA. Our results indicate that a delayed regeneration of the full structure of the heating source sink in VAP is the main process accounting for such behavior.

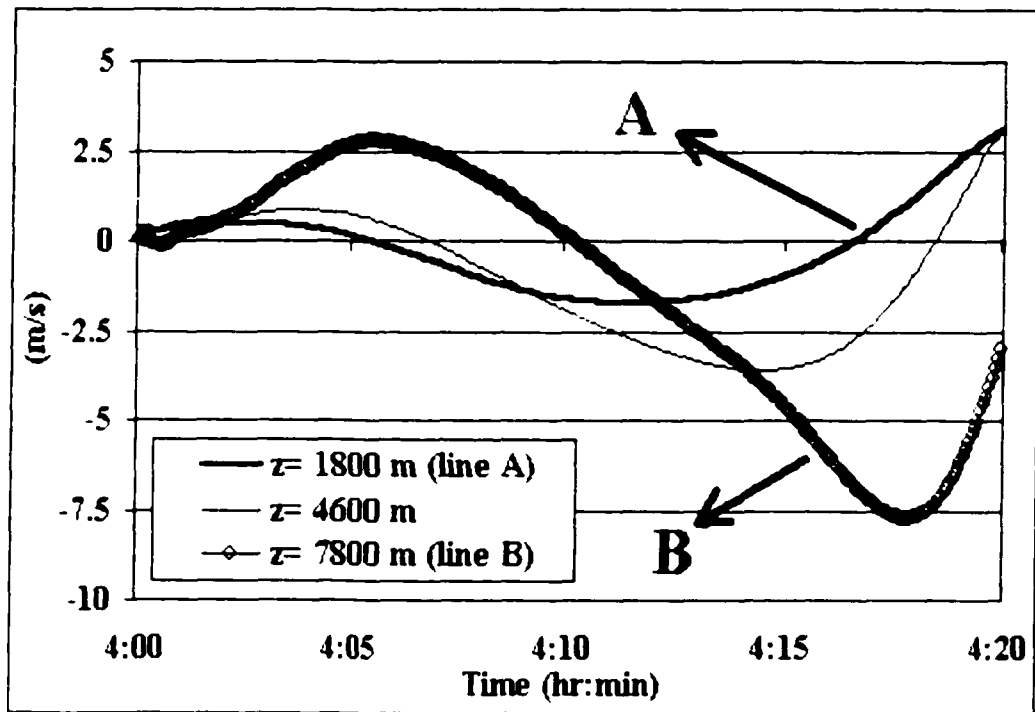


Figure 7.46 As in Fig. 7.27, but for experiment VAP.

Another interesting difference between THETA and VAP involves the behavior of acoustic modes. Figure 7.46 shows no clear indication of high-amplitude acoustic waves superimposed in the “gravity wave” evolution. This is also evident in terms of the pressure field, indicated in the time series in Figure 7.47. Instead of high frequency sound waves, the pressure field is dominated by a response to variations in the buoyancy field. Higher frequency oscillations are present, but with very low amplitude. It is not entirely clear why this is the case, but in experiment VAP, large areas of enhanced diabatic cooling at mid levels are present, which weakens the convective circulation. In THETA, enhanced mid-level diabatic *heating* associated with “impulsive” expansion occurs. This different response at the very early stages of the withdrawal seems to be the main cause for the distinct behavior of the acoustic modes.

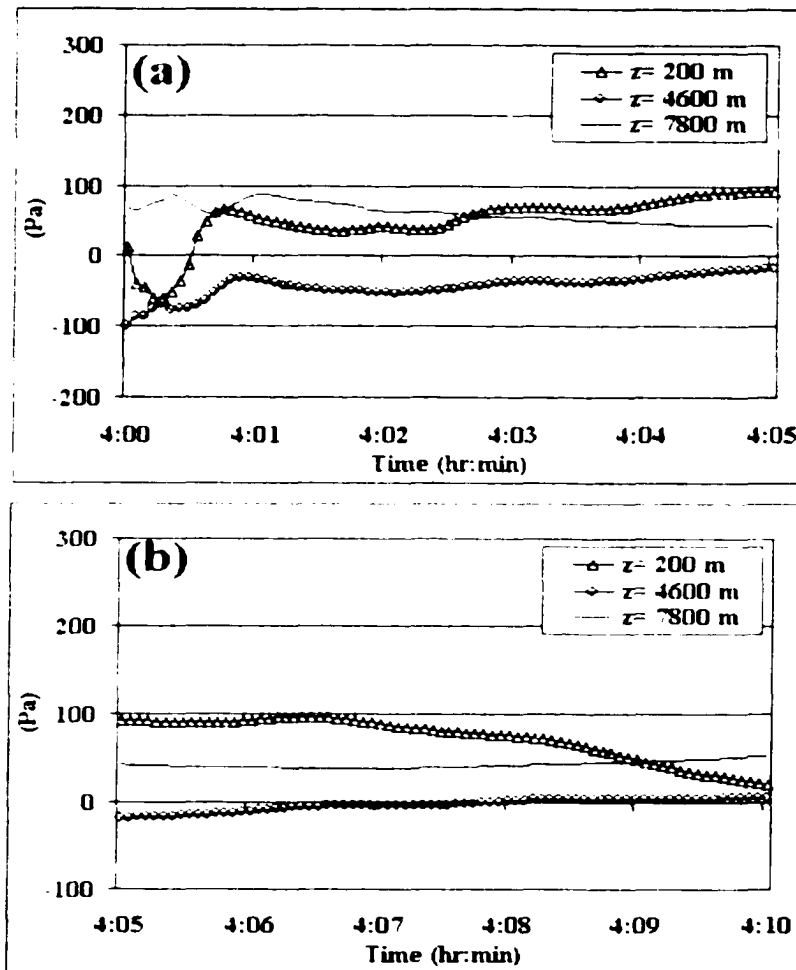


Figure 7.47: As in Fig. 7.29 but for the first 10-min in experiment VAP.

7.6 Impact of the Coriolis force

Because Earth's rotation is included in the simulations, it is important to assess the extent to which the Coriolis force plays a discernible role in the evolution of the first 30-min of experiments THETA and VAP. This is the time it takes to the buoyant plume in THETA to restore most of its structure, as indicated in the comparison in Figure 7.48. Moreover, it is within the first 30-min of simulation in experiment VAP that most processes leading to a different solution from CNTRL occur (see section 7.5).

Among the various formulations for the Rossby radius of deformation λ_R , the one that provides the most reasonable estimate for our purposes involves the distance traveled by a density current (i.e., a cold pool) before its propagation is completely deflected by the Coriolis force, given by:

$$\lambda_R = \frac{(gH\Delta\theta/\theta_0)^{1/2}}{f} \quad (8.6)$$

where g is the acceleration due to gravity, H is the initial depth of the density current, $\Delta\theta$ is the absolute change in potential temperature across the density current, θ_0 is the potential temperature of the warm air ahead of the density current, and f is the Coriolis parameter.

From experiment CNTRL (Fig. 4.7) we estimate that $H = 2.5$ km and $\Delta\theta = 8$ K, and from the background sounding $\theta_0 = 300$ K. Thus, with $g = 9.81 \text{ m s}^{-2}$ and $f = 0.7 \times 10^{-4} \text{ s}^{-1}$ (Table 4.2), $\lambda_R \approx 365$ km. This result is consistent with the Rossby radius of deformation usually associated with MCSs (Cotton et al. 1989). The surface cold pool propagates at approximately 22 m s^{-1} , such that in the absence of continuous forcing (but hypothetically maintaining its speed), the propagation would be completely deflected after 4.6-hr, which is a considerably long time compared to the 30-min

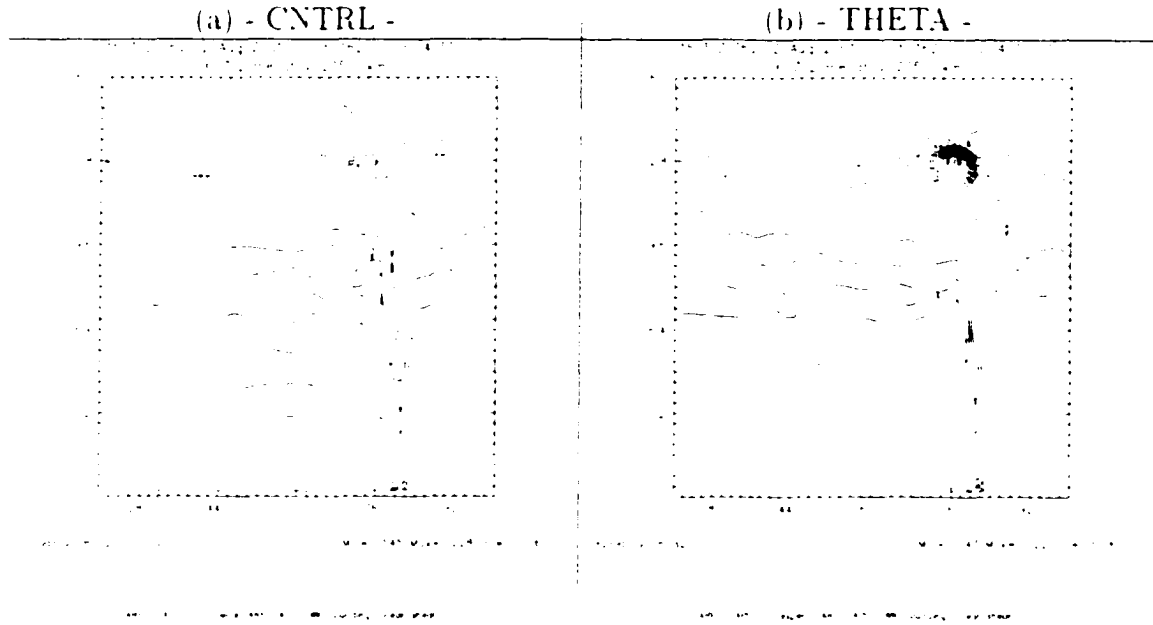


Figure 7.48. As in Fig. 7.44, but comparing the solutions from simulations CNTRL and THETA at 4.30-hr.

adjustment time noted above. While it is reasonable to expect the Coriolis force to affect the solution in a significant way even before 4-hr of integration, in the first 30-min following restart the effects of Earth's rotation are not important.

7.7 Summary

The results from experiments THETA and VAP highlight the relevance of specifying the thermal structure of MCSs, which includes the specification of regions of saturation and subsaturation. In VAP, perfect information about the temperature field is provided at the restart. However, *the information content in temperature alone is not sufficient to maintain the correct thermal structure of the bow echo during the simulation*, whereas latent heating and cooling play a crucial role in effectively determining the temperature field within the MCS. This is confirmed in experiment THETA, where the “perfect” information about water vapor and condensate allowed

the restoration of the temperature field, consistent with a mature MCS. Our results suggest that if a choice must be made among specifying the temperature, moisture and condensate species within an MCS, greater effort should be focused on the latter two fields. In essence, this result confirms the importance of diabatic initialization for convective-scale flows (e.g., Zhang 1999).

Among all variables, pressure is the one with larger degree of redundant information due to its strong response to buoyancy. A correct specification of the pressure field is useless if the buoyancy field is not adequately initialized.

Low frequency IGWs play a discernible role in dynamic adjustment in THETA and VAP, and are associated with the propagation of the mid-level buoyant plume which is an important feature the bow echo. The kinematic field trailing the MCS is also sensitive to the low frequency IGWs. Because the behavior of such waves is controlled by the evolution of the heating source-sink at the front of the system, the results suggest that most attention should be focused on initializing the thermal field in the leading convective cells of a squall line.

Chapter 8

Summary and Conclusions

8.1 Summary

The main goal of this research was to investigate the mechanisms that control the mutual adjustment among specific meteorological variables when an impulsive perturbation is applied in the 3D stormscale simulation of an idealized bow echo. This work was motivated by studies of atmospheric adjustment processes (e.g., geostrophic adjustment), which emphasize the importance of understanding the dynamic response of meteorological fields to the specification of ICs that do not satisfy a given balance relation (e.g., Blumen 1972, Bannon 1995). By examining such response, it is possible to identify variables that contain the most relevant information about atmospheric flow (i.e., the variables that *induce* a response from other fields), and which, in turn, should be given higher priority when initializing numerical models.

Motivation for this work also came from the development of data assimilation techniques specific for stormscale models involving the use of Doppler radar data. Studies in this area indicate that the capability to estimate/retrieve information about the inner structure of convective systems does exist (e.g., Sun and Crook 1997, Weygandt

et al. 2002a,b), but further investigation is necessary to address the question of which fields *must* be observed and best initialized in models.

It is relevant to mention that Shapiro et al. (1995b), Sun and Crook (2001b), Weygandt et al. (2002b), among others, conducted sensitivity tests in numerical simulations of convective storms initialized with Doppler radar data retrieved fields in order to assess the relative importance of specific meteorological fields in the simulations. These sensitivity tests were performed in the context of *specific* radar data retrieval techniques. *In the present research, we chose to address the sensitivity of the convective-scale simulation of an idealized bow echo to different atmospheric fields from a more general perspective (i.e., without the employment of a given model initialization technique), and to analyze the main physical processes driving the response among meteorological variables.* Our approach allowed not only the identification of potentially important meteorological fields but also the understanding of *why* they are important in storm-scale simulations. This is a relevant distinction between our study and the sensitivity tests performed in the investigations mentioned above.

Because no simple balance relation is known on the convective scale, our approach consisted of defining an artificial IC that violates the governing equations. This artificial IC was obtained from a 6-hr long control simulation of an idealized bow echo after resetting selected variables (one at a time) to their unperturbed base state values during the mature stage of the convective system ($t = 4$ -hr). By doing so, we generated three-dimensional fields containing incomplete information about the inner structure of the bow echo which were used to restart the numerical simulations at 4-hr. These were called *withdrawal experiments*.

Four withdrawal experiments were analyzed, which included resetting the following variables to their unperturbed base state: horizontal wind field (experiment UVEL), vertical wind field (WVEL), potential temperature (THETA) and water vapor mixing

ratio (VAP). Below we summarize the main findings:

1. The evolution and morphology of the simulated convective storm is modified substantially after withdrawing the perturbation horizontal winds. The information contained in the horizontal divergence field is crucial for forcing the correct vertical motion.
2. Elimination of the vertical velocity has virtually no impact on the bow echo simulation, since the horizontal divergence field restores updrafts and downdrafts quite efficiently.
3. Simulation THETA generates a strong MCS that shares several of the characteristics of bow echoes. Water vapor and condensate fields restore the thermal structure of the system through latent heating and cooling.
4. Withdrawal of perturbation water vapor mixing ratio leads to a simulated storm that deviates considerably from a bow echo MCS, particularly during the first 1-hr of simulation. The regeneration of the thermal field is delayed and the rates of latent heating and cooling are significantly altered, affecting the storm evolution.
5. Incomplete specification of the 3D divergence induces a strong VPGA that plays an important role in controlling the response of the vertical motion to the horizontal velocities in experiments UVVEL and WVEL.
6. High frequency sound waves and AGWs of large amplitude are triggered in experiments UVVEL and WVEL, characterizing a "transient evolution" consistent with acoustic adjustment. The response of the vertical motion to the horizontal wind field indicates that the bow echo behaves as a low aspect ratio convective flow from an acoustic adjustment standpoint.

7. Hydrostatic and non-hydrostatic IGWs are present in simulations THETA and VAP. Because non-hydrostatic IGWs are ubiquitous to MCSs they do not characterize a “transient evolution” clearly (i.e., high frequency IGWs do *not* represent a *special* feature of dynamic adjustment in simulations THETA and VAP), but the detection of a low-frequency IGW pulse provides an indication of redevelopment of the main thermal structure of the bow echo that does represent an important component of dynamic adjustment induced by thermodynamic fields.
8. Dynamic adjustment induced by the kinematic fields has a characteristic time-scale that is relatively short (less than 10-min), associated with fast-moving acoustic modes. Dynamic adjustment induced by the thermodynamic fields is dominated by IGWs, and has a longer time-scale (around 30-min). The Coriolis force does not play a significant role within these time-scales.

In experiments UVVEL and WVEL we examined the prognostic pressure equation and showed that the specification of an incomplete 3D divergence field induces an artificially strong VPGA within the convective system which, in turn, influences the response from the vertical motion. This adjustment is summarized in Figure 8.1a. In UVVEL, horizontal convergence and divergence patterns were withdrawn, and the modified 3D divergence field generated a VPGA that *weakened* the updrafts and downdrafts, with serious impact to the bow echo simulation. In WVEL, vertical divergence and convergence patterns were eliminated. In this case, the modified 3D divergence field induced a VPGA that favored a rapid *restoration* of the vertical motion. Essentially, this response accounted for a poor (good) simulation of the bow echo in UVVEL (WVEL) and represents a different way to address acoustic adjustment.

The thermal field was adequately recovered in experiment THETA. At low levels

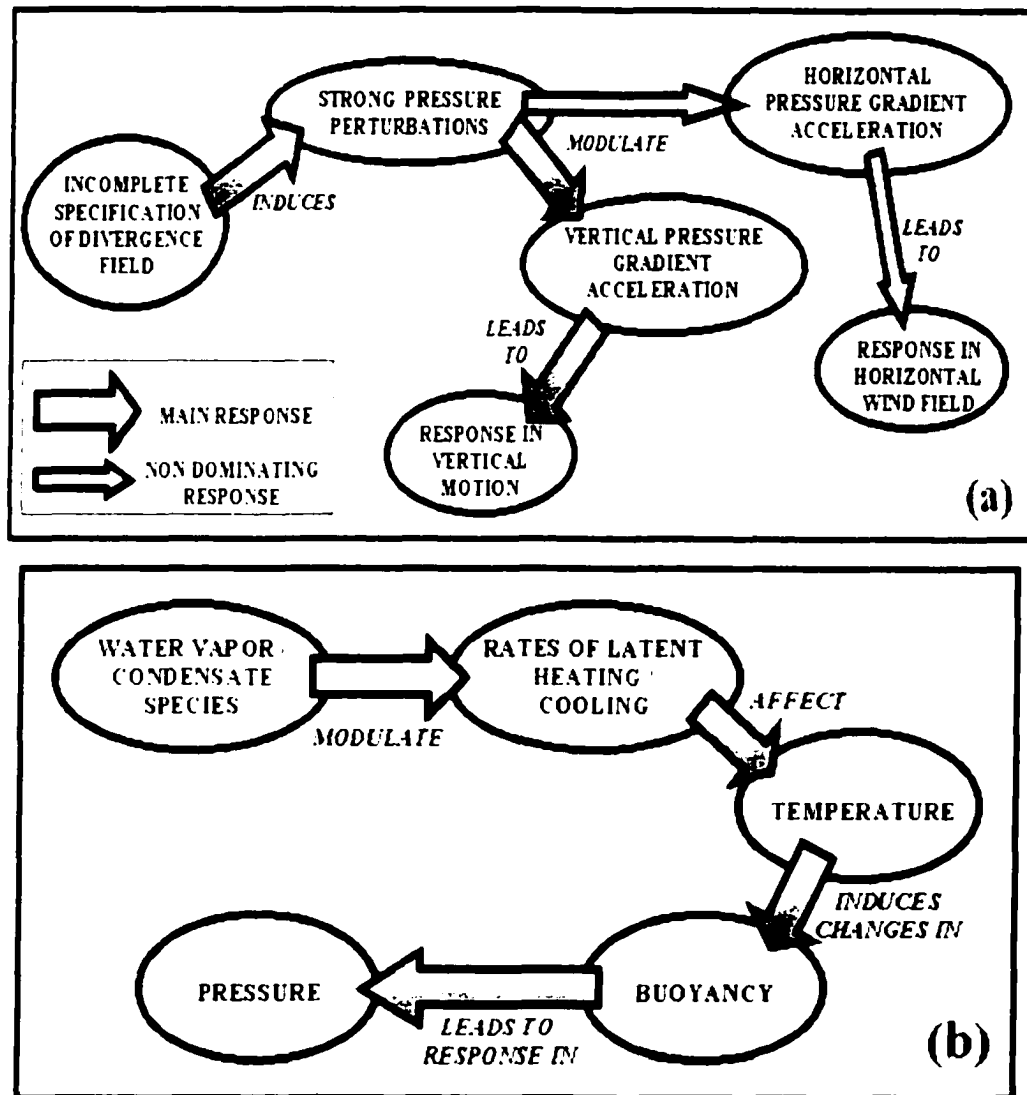


Figure S 1. Diagrams summarizing the response among meteorological fields early in the withdrawal experiments (i.e., during “transient evolution”). Panel (a) indicates the response in simulations WVCL and UVCL (dynamic adjustment induced by kinematic fields). Violation of mass conservation, associated with incomplete specification of the three-dimensional divergence field, leads to strong (but short-lived) pressure perturbations. In turn, the induced pressure gradient acceleration (PGA) leads to responses in the velocity field. The response from the vertical component of the wind is stronger due to a more intense PGA in the vertical during the adjustment process, which translates into the vertical motion adjusting to the horizontal wind field specified in the initial condition. Panel (b) indicates the response in simulations THETA and VAP (dynamic adjustment induced by the thermodynamic fields). Water vapor and condensate fields modulate the rates of latent heating and cooling, which, in turn, affect the temperature field. Variations in temperature affect buoyancy, while the pressure field responds to the distribution of buoyancy. This overall response emphasizes the importance of an adequate specification of the meteorological variables that control the magnitude of latent heating and cooling within convective storms.

its restoration was induced by enhanced evaporative cooling, while at mid levels latent heating regenerated a buoyant plume. With the recovered thermal structure, a strong MCS was generated after 2-hr of simulation. In VAP, reduced evaporative cooling weakened the surface cold pool and the accompanying outflow. Aloft, subsaturated updrafts were weakened by enhanced latent cooling (evaporation and sublimation) and adiabatic cooling (lifting of subsaturated air parcels) induced by the drying of the atmosphere at the restart time. These combined effects delayed the recovery of the thermal structure of the bow echo. In both experiments THETA and VAP, diabatic effects regulated the temperature field which, in turn, affected buoyancy, while pressure responded to changes in buoyancy (Figure 8.1b).

8.2 Conclusions and final remarks

8.2.1 Relative importance of specific meteorological fields

Our results suggest that horizontal winds, water vapor content and condensate species are the most relevant fields in describing the structure of bow echoes (and squall lines) and, thus, should receive particular attention in model initialization on the convective scale. Pressure, temperature and vertical motion, on the other hand, contain redundant information about the MCS. (Here we assign the expression “redundant” to the variables that respond to the atmospheric fields described by other variables, implying that a good initialization of a redundant variable does not necessarily imply in a good description of the relevant structure of the convective storm).

These results are encouraging for two main reasons: first, among the meteorological variables retrieved from Doppler radar data, the horizontal wind field is one of the most accurate (e.g., Gao et al. 2001, Weygandt et al. 2002b). Second, the relevance of water vapor and condensate fields for the storm simulation resides on the

fact that they modulate rates of latent heating/cooling which determine the thermal structure of the MCS. This ratifies the importance of efforts in developing diabatic initialization techniques specific for convective-scale models. In diabatic initialization, latent heating rates estimated from observations of clouds and precipitation are used to force a consistent vertical wind field in precipitation areas (i.e., including convective systems). Only recently has diabatic initialization been attempted on the stormscale (e.g., Zhang 1999, Brewster 2002). Our results provide further support in this direction. For instance, in experiment VAP, the sharp redevelopment of vertical motion along the leading edge of the bow echo induced an overestimation of the latent heating rate which resulted in a response from the wind field trailing the MCS that is inconsistent with the typical structure of a bow echo/squall line. This suggests that if latent heating were adequately estimated and used to retrieve the corresponding vertical motion (i.e., to “correct” the magnitude of the leading updrafts), the storm simulation could be significantly improved.

On the other hand, our results also point to some challenges faced in developing adequate observing systems for the stormscale. Water vapor field within convective systems is only roughly estimated from radar and satellite data (e.g., Zhang and Carr 1998), and regions of saturation and subsaturation are commonly parameterized in terms of rather arbitrary thresholds of radar reflectivity and Doppler-radar retrieved vertical motion (e.g., Weygandt et al. 2002b). Thus, water vapor content is probably one of the less accurately specified meteorological variables within numerically-simulated convective storms. Because water vapor mixing ratio is one of the fields influencing the rate of latent heating and cooling in MCSs, the initialization of such systems in convective-scale models would profit significantly from an improved estimation of the moisture field within thunderstorms.

8.2.2 Wave regime during dynamic adjustment

High-amplitude sound waves are present early in experiments WVFL and UVVFL (particularly within the first 5-min of simulation), being consistent with the main concept behind acoustic adjustment (Fiedler 2002). Although such waves have frequency well above the acoustic-cutoff frequency, we found that the environmental stratification has some influence upon the oscillatory regime (chapter 6). Thus, the effects of gravity cannot be neglected, suggesting that the acoustic modes excited in experiments WVFL and UVVFL consist of high-frequency AGWs (i.e., they are close to the pure sound wave regime, but not quite satisfying the condition of negligible gravitational effects that characterize such waves).

In the context of experiments THETA and VAP, it is important to recall the study by B95 which indicates that the gravity wave regime associated with an impulsive heating source of high aspect ratio (representative of convective storms) is dominated by non-hydrostatic IGWs. In agreement with this statement, results from THETA and VAP do show the presence of high frequency IGWs. However, an important response found in these withdrawal experiments consisted of a mid-level convective-scale downdraft that propagates away from the main heating source at the phase speed of a *hydrostatic* IGW. Rather than representing a contradiction with respect to B95's discussion (which focuses on *impulsive* heating sources), this result actually is consistent with the response expected from heating sources of *long duration* embedded in a statically-stable atmosphere (e.g., Bretherton and Smolarkiewicz 1989, PD96).

These important results indicate that the gravity wave component of dynamic adjustment in experiments THETA and VAP is composed of both hydrostatic and non-hydrostatic IGWs. Based on the results by PD96 and similar studies addressing the impact of long-lasting heating sources in a stably stratified environment (Bretherton

and Smolarkiewicz 1989, Nicholls et al. 1991, Mapes 1993, Fovell 2002), we postulate that the hydrostatic IGWs present in our simulations are associated with the restoration of the aggregate thermal structure of the bow echo (i.e., its low frequency thermal structure). The non-hydrostatic IGWs, on the other hand, are associated with the intermittent nature of discrete convective elements being regenerated along the leading edge of the bow echo. This process represents the high frequency component of the thermal structure of the MCS, and is more closely related to the concept of impulsive heating sources discussed in B95.

B95 also described acoustic modes displaying preferential horizontal propagation as part of the atmospheric response to impulsive heating sources of high aspect ratio. NP94a,b studied TCWs induced by idealized two-dimensional mesoscale circulations, and showed that they behave as Lamb waves, which propagate exclusively in the horizontal. In experiment THETA, high amplitude acoustic modes are present during dynamic adjustment. However, evidence of vertical propagation exists (section 7.4.3) and, thus, it is not clear that these waves behave as true or pure TCWs. On the other hand, because the heating source associated with the simulated bow echo does display vertical structure (e.g., Fig. 7.14a) — for which the vertical wavenumber m is different from zero — it is reasonable to expect acoustic modes with some vertical propagation based on the linear theory explored by B95 (Fig. 2.7).

8.2.3 Representativeness of the results and future work

Results from experiments UVVEL and WVEL agree with findings from Weygandt et al. (1999) for a simulated supercell, and with acoustic adjustment considerations addressed in Fiedler (2002). *We consider the processes controlling dynamic adjustment induced by the withdrawal of kinematic fields (discussed in this research) as representative of other modes of convection, particularly in the presence of vertical wind*

shear.

The possible role played by vertical wind shear in lowering the effective aspect ratio of the flow — by favoring horizontally-oriented divergence patterns — was discussed. However, no definite conclusion can be drawn regarding the sensitivity of the results to the presence of vertical wind shear without further investigation. Future work should address this topic.

Factors other than wind shear also may account for the behavior of the bow echo as a low aspect ratio flow (from an acoustic adjustment standpoint). The vertical motion field within bow echoes (and other storm systems) do not represent well-behaved sinusoidal patterns, as considered in the analytical approach to acoustic adjustment (Fiedler 2002). Regions of strong updrafts tend to be confined to localized regions in the cross-line dimension, while displaying significant horizontal extent in the along-line direction. In addition, compensating subsidence does propagate several tens of kilometers from the heating source, covering larger areas than those dominated by updrafts (e.g., Fig. 7.16f). Therefore, the vertical motion around MCSs displays complex patterns, with several of them possibly favoring an effective low aspect ratio flow.

Dynamic adjustment induced by thermodynamic fields may be sensitive to the environmental thermodynamic profile and/or convective mode. The atmospheric sounding utilized in this research is idealized, and moist throughout the troposphere. Weygandt et al. (2002b) found a different result regarding the importance of the specification of the water vapor mixing ratio when studying a numerically-simulated supercell (initialized with Doppler radar-derived fields) which evolves in a more realistic environment. They indicated that setting the water vapor field equal to that in the environmental sounding did not affect significantly the evolution of the surface cold pool. The sounding in their study displayed a low- to mid-level dry layer

that potentially favored the generation of stronger downdrafts and, thus, transport of low- θ_e air to the surface, allowing a good representation of the cold pool. Therefore, future work on dynamic adjustment must address sensitivity to the thermodynamic profile.

As indicated in chapter 4, the simulated bow echo in the present research does not display an extensive trailing stratiform precipitation area which is a feature often observed in actual bow echoes. This is essentially because of the choice of switching on ice microphysics in our simulations. Nevertheless, several of the important features that characterize dynamic adjustment in experiments THETA and VAP, such as the propagation of a low frequency IGW pulse trailing the bow echo, is also found in previous works studying MCSs with extensive trailing stratiform precipitation areas (e.g., PD96). This suggests that the structure of the *leading edge* of the bow echo contains the main mechanisms driving the response of atmospheric fields within and around the MCS. Future work may address such topic by examining whether the extent of the trailing stratiform precipitation area has any significant influence upon the response of the meteorological fields to perturbations within the convective storm.

The withdrawal of perturbation fields at different stages of evolution of the convective storm is also an interesting approach to assess if the relative importance of distinct meteorological variables for dynamic adjustment changes during the life cycle of the storm.

Another important point is that our simulations were conducted in a horizontally-homogeneous environment. In chapter 3 we briefly reviewed the atmospheric conditions conducive to long-lived bow echoes and described that well defined surface boundaries are always present. It is not clear the extent to which the results from experiments THETA and VAP may be affected by the specification of more realistic surface atmospheric conditions, and therefore follow-up studies on dynamic adjust-

ment in MCSs should gradually increase the degree of complexity of the atmospheric environment.

Despite some possible limitations discussed above, *we consider that the main result from experiments THETA and VAP, which emphasizes the role played by latent heating and cooling in determining the thermal structure of the convective storm which, in turn, drives the pressure field (Fig. 8.1b), is robust, being in conceptual agreement with previous studies investigating a broad spectrum of storm systems.*

As a continuation of this research, additional withdrawal experiments addressing the impact of the elimination of condensate species (i.e., ice and water mixing ratios) on the bow echo simulation should be conducted. Simulations THETA and VAP emphasized the importance of latent heating and cooling rates, which are affected by the distribution of hydrometeors. Also, numerical experiments withholding more than one variable—especially the “redundant” ones, e.g., potential temperature *and* vertical wind field; vertical wind field *and* pressure; etc...—should provide further insight regarding the minimum information necessary for a good simulation—numerical prediction of MCSs.

Moreover, because the rear-to-front flow (or RLJ) and the surface cold pool represent important mesoscale features in long-lived bow echoes (chapter 3), it is desirable to design withdrawal experiments in which atmospheric fields are withdrawn *within* these mesoscale features. The idea is to assess how important is the specification of the RLJ and cold pool for the stormscale simulation of bow echoes and squall lines. In particular, surface cold pools are often not well sampled by weather radars (e.g., Doviak and Zrnic 1993), reducing the amount of observations available to describe atmospheric conditions at low levels. Can a good specification of meteorological fields aloft “spin-up” a surface cold pool that is consistent with the parent MCS? Future studies should address this question.

The aspect ratio issue, extensively explored in this research, deserves a more detailed attention in future investigations. It may be desirable to refer to the aspect ratio of the convective flow in terms of measurable quantities with clear physical meaning. This approach should provide further insight into the processes controlling adjustment processes in convective storms.

Bibliography

- [1] Adlerman, E. J., and K. K. Droegemeier, 2002: The sensitivity of numerically simulated cyclic mesocyclogenesis to variations in model physical and computational parameters. *Mon. Wea. Rev.*, **130**, 2671-2691.
- [2] Atlas, R., 1997: Atmospheric observations and experiments to assess their usefulness in data assimilation. *J. Met. Soc. Japan*, **75**, 111-130.
- [3] Bannon, P. R., 1995a: Hydrostatic adjustment: Lamb's problem. *J. Atmos. Sci.*, **52**, 1743-1752.
- [4] Bannon, P. R., 1995b: Potential vorticity conservation, hydrostatic adjustment, and the anelastic approximation. *J. Atmos. Sci.*, **52**, 2302-2312.
- [5] Bannon, P. R., 1996a: Nonlinear hydrostatic adjustment. *J. Atmos. Sci.*, **53**, 3606-3617.
- [6] Bannon, P. R., 1996b: On the anelastic approximation for a compressible atmosphere. *J. Atmos. Sci.*, **53**, 3618-3628.
- [7] Barnes, S. L., and C. W. Newton, 1986: Thunderstorms in the synoptic setting. *Thunderstorm Morphology and Dynamics*, 2nd Edition, E. Kessler, Ed.,
- [8] Bartels, D. L., J. M. Brown, and E. I. Tollerud, 1997: Structure of a midtropospheric vortex induced by a mesoscale convective system. *Mon. Wea. Rev.*, **125**, 193-211.
- [9] Barwell, B., and Bromley, R., 1988: The adjustment of numerical weather prediction models to local perturbations. *Quart. J. Roy. Meteor. Soc.*, **114**, 665-684.
- [10] Bentley, M. L., and S. R. Cooper, 1997: The 8 and 9 July 1993 Nebraska derecho: an observational study and comparison to the climatology of related mesoscale convective systems. *Wea. Forecasting*, **12**, 678-688.
- [11] Bielli, S., and F. Roux, 1999: Initialization of a cloud-resolving model with airborne Doppler radar observations of an oceanic tropical convective system. *Mon. Wea. Rev.*, **127**, 1038-1055.

- [12] Biggerstaff, M. L., and R. A. Houze Jr., 1993: Kinematics and microphysics of the transition zone of the 10-11 June 1985 squall line. *J. Atmos. Sci.*, **50**, 3091-3110.
- [13] Blumen, W., 1972: Geostrophic adjustment. *Rev. Geophys. Space Phys.*, **10**, 485-528.
- [14] Bohren, C. F., and B. A. Albrecht, 1998: *Atmospheric Thermodynamics*, Oxford University Press, 402pp.
- [15] Braun, S. A., R. A. Houze Jr., 1994: The transition zone and secondary maximum of radar reflectivity behind a midlatitude squall line: results retrieved from Doppler radar data. *J. Atmos. Sci.*, **51**, 2733-2755.
- [16] Bretherton, C. S., and P. K. Smolarkiewicz, 1989: Gravity waves, compensating subsidence, and detrainment around cumulus clouds. *J. Atmos. Sci.*, **46**, 740-759.
- [17] Brewster, K. A., 2002: Recent advances in the diabatic initialization of a non-hydrostatic numerical model. *Preprints, 15th Conf. on Numerical Weather Prediction*, San Antonio, Amer. Meteor. Soc.
- [18] Bryan, G. H., and J. M. Fritsch, 2002: What is appropriate resolution for simulations of thunderstorms? An answer from a turbulence perspective. *Preprints, 21st Conf. on Severe Local Storms*, San Antonio, Amer. Meteor. Soc., 255-258.
- [19] Burgess, D. W., and B. F. Smull, 1990: Doppler radar observations of a bow echo associated with a long-track severe windstorm. *Preprints, 16th Conf. on Severe Local Storms*, Canada, Amer. Meteor. Soc., 203-208.
- [20] Chagnon, J. M., and P. R. Bannon, 2001: Hydrostatic and geostrophic adjustment in a compressible atmosphere: initial response and final equilibrium to an instantaneous localized heating. *J. Atmos. Sci.*, **58**, 3776-3792.
- [21] Charney, J., R. Fjortoft, and J. von Neumann, 1950: Numerical integration of the barotropic vorticity equation. *Tellus*, **7**, 22-26.
- [22] Charney, J., M. Halem, and R. Jastrow, 1969: Use of incomplete historical data to infer the present state of the atmosphere. *J. Atmos. Sci.*, **26**, 1160-1163.
- [23] Clark, T. L., 1979: Numerical simulations with a three-dimensional cloud model: Lateral boundary condition experiments and multicellular severe storm simulations. *J. Atmos. Sci.*, **36**, 2191-2215.
- [24] Coniglio, M. C., and D. J. Stensrud, 2001: Simulation of a progressive derecho using composite initial conditions. *Mon. Wea. Rev.*, **129**, 1593-1616.
- [25] Cortidi, S. F., 2002: MCS mode and motion: an updated forecast technique. *Submitted to Wea. Forecasting*.

- [26] Cotton, W. R., M. S. Lin, R. L. McAnelly, and C. J. Tremback, 1989: A composite model of mesoscale convective complexes. *Mon. Wea. Rev.*, **117**, 765-783.
- [27] Cram, T. A., M. F. Montgomery, and R. F. A. Hertenstein, 2002: Early evolution of vertical vorticity in a numerically simulated idealized convective line. *J. Atmos. Sci.*, **59**, 2113-2127.
- [28] Crook, N. A., 1996: Sensitivity of moist convection forced by boundary layer processes to low-level thermodynamic fields. *Mon. Wea. Rev.*, **124**, 1767-1785.
- [29] Crook, A., and J. D. Tuttle, 1994: Numerical simulations initialized with radar-derived winds. Part II: forecasts of three gust-front cases. *Mon. Wea. Rev.*, **122**, 1204-1217.
- [30] Daley, R., 1980: On the optimal specification of the initial state for deterministic forecasting. *Mon. Wea. Rev.*, **108**, 1719-1735.
- [31] Daley, R., 1991: *Atmospheric Data Analysis*. Cambridge University Press, 457pp.
- [32] Das, P., 1979: A non-Archimedean approach to the equations of convection dynamics. *J. Atmos. Sci.*, **36**, 2183-2190.
- [33] Davies-Jones, R., R. J. Trapp, and H. B. Bluestein, 2001: Tornadoes and tornadoic storms. *Severe Convective Storms*, C. A. Doswell III (Ed.), Amer. Meteor. Soc., 167-221.
- [34] Davis, C. A., and M. L. Weisman, 1994: Balanced dynamics of mesoscale vortices produced in simulated convective systems. *J. Atmos. Sci.*, **51**, 2005-2030.
- [35] Doviak, R. J., and D. S. Zrnic, 1993: *Doppler Radar and Weather Observations* 2nd edition, Academic Press, 562pp.
- [36] Droegemeier, K. K., 1990: Towards a science of storm-scale prediction. *Preprints, 16th Conf. on Severe Local Storms*, Canada, Amer. Meteor. Soc., 256-262.
- [37] Droegemeier, K. K., 1997: The numerical prediction of thunderstorms: challenges, potential benefits, and results from real-time operational tests. *W.M.O. Bulletin*, **46**, 324-336.
- [38] Droegemeier, K. K., and R. B. Wilhelmson, 1987: Numerical simulation of thunderstorm outflow dynamics. Part I: Outflow sensitivity experiments and turbulence dynamics. *J. Atmos. Sci.*, **44**, 1180-1210.
- [39] Ducrocq, V., J.-P. Lafore, J.-L. Redelsperger, and F. Orain, 2000: Initialization of a fine-scale model for convective-system prediction: a case study. *Quart. J. R. Met. Soc.*, **126**, 3041-3065.

- [10] Duke, J. W., and J. A. Rogash, 1992: Multiscale review of the development and early evolution of the 9 April 1991 derecho. *Wea. Forecasting*, **7**, 623-635.
- [11] Durran, D. R., 1986: Mountain waves. *Mesoscale Meteorology and Forecasting*, P.S. Ray (Ed.), Amer. Meteor. Soc., 472-492.
- [12] Durran, D. R., 1999: *Numerical Methods for Wave Equations in Geophysical Fluid Dynamics*. Springer-Verlag, 465pp.
- [13] Durran, D. R., and J. B. Klemp, 1983: A compressible model for the simulation of moist mountain waves. *Mon. Wea. Rev.*, **111**, 2341-2361.
- [14] Elmore, K. L., D. J. Stensrud, and K. C. Crawford, 2002a: Ensemble cloud model applications to forecasting thunderstorms. *J. Appl. Meteor.*, **41**, 363-381.
- [15] Elmore, K. L., D. J. Stensrud, and K. C. Crawford, 2002b: Explicit cloud-scale models for operational forecasts: a note of caution. *Wea. Forecasting*, **17**, 873-884.
- [16] Emanuel, K. A., 1994: *Atmospheric Convection*. Oxford University Press, 580pp.
- [17] Errico, R. M., and T. Vukicevic, 1992: Sensitivity analysis using an adjoint of the PSU-NCAR mesoscale model. *Mon. Wea. Rev.*, **120**, 1644-1660.
- [18] Evans, J. S., and C. A. Doswell III, 2001: Examination of derecho environments using proximity soundings. *Wea. Forecasting*, **16**, 329-342.
- [19] Fiedler, B. H., 2002: A wind transformation for acoustic adjustment in compressible models. *Mon. Wea. Rev.*, **130**, 741-746.
- [20] Fovell, R. G., 2002: Upstream influence of numerically simulated squall line storms. *Quart. J. R. Met. Soc.*, **128**, 893-912.
- [21] Fovell, R. G., and Y. Ogura, 1988: Numerical simulation of a midlatitude squall line in two dimensions. *J. Atmos. Sci.*, **45**, 3846-3879.
- [22] Fovell, R. G., D. Durran, and J. R. Holton, 1992: Numerical simulation of convectively generated stratospheric gravity waves. *J. Atmos. Sci.*, **49**, 1427-1442.
- [23] Fritsch, J. M., and G. S. Forbes, 2001: Mesoscale convective systems. *Severe Convective Storms, Meteor. Monogr.*, Vol. 28, No. 50, C. A. Doswell III, Ed., Amer. Meteor. Soc., 323-357.
- [24] Fujita, T. T., 1959: Precipitation and cold air production in mesoscale thunder-storm systems. *J. Meteor.*, **16**, 454-466.
- [25] Fujita, T. T., 1971: Proposed characterization of tornadoes and hurricanes by area and intensity. SMRP Research Paper 91, University of Chicago, 42pp.

- [56] Fujita, T. T., 1978: Manual of Downburst Identification for Project NIMROD. SMRP Research Paper 156, University of Chicago, 104pp.
- [57] Fujita, T. T., 1981: Tornadoes and downbursts in the context of generalized planetary scales. *J. Atmos. Sci.*, **38**, 1511-1534.
- [58] Fulton, S. R., W. H. Schubert, and S. Hausman, 1994: Dynamical adjustment of cumulonimbus anvils. *Preprints, 6th Conf. on Mesoscale Processes*, Portland, OR, Amer. Meteor. Soc., 424-427.
- [59] Funk, T. W., K. E. Darmofal, J. D. Kirkpatrick, V. L. DeWald, R. Przybylinski, G. Schmocker, and Y.-J. Lin, 1999: Storm reflectivity and mesocyclone evolution associated with the 15 April 1994 squall line over Kentucky and southern Indiana. *Wear Forecasting*, **14**, 976-993.
- [60] Gal-Chen, T., 1978: A method for initializing the anelastic equations: implications for matching models with observations. *Mon. Wea. Rev.*, **106**, 587-606.
- [61] Gao, J., M. Xue, A. Shapiro, Q. Xu, and K. K. Droegemeier, 2001: Three-dimensional simple adjoint velocity retrievals from single-Doppler radar. *J. Atmos. Oceanic Technol.*, **18**, 26-38.
- [62] Gill, A. E., 1982: *Atmosphere-Ocean Dynamics*, Academic Press, 662pp.
- [63] Gilmore, M. S., and L. J. Wicker, 1998: The influence of midtropospheric dryness on supercell morphology and evolution. *Mon. Wea. Rev.*, **126**, 943-958.
- [64] Granger, R. A., 1995: *Fluid Mechanics*, Dover Publications, 896pp.
- [65] Hamilton, R. E., 1970: Use of detailed intensity radar data in mesoscale surface analysis on the 4 July 1969 storm in Ohio. *Preprints, 14th Conf. on Radar Meteorology*, Tucson, AZ, Amer. Meteor. Soc., 339-342.
- [66] Henderson, H. W., and R. Wells, 1988: Obtaining attractor dimensions from meteorological time-series. *Advances in Geophysics*, Vol. 30, Academic Press, 205-237.
- [67] Hinrichs, G., 1888: Tornadoes and derechos. *Amer. Meteor. J.*, **5**, 306-317, 341-349.
- [68] Holton, J. R., 1992: *An Introduction to Dynamic Meteorology*, Academic Press, 3rd Edition, 507pp.
- [69] Hooke, W. H., 1986: Gravity waves. *Mesoscale Meteorology and Forecasting*, P.S. Ray (Ed.), Amer. Meteor. Soc., 272-288.
- [70] Hou, D., E. Kalnay, and K. K. Droegemeier, 2001: Objective verification of the SAMEX '98 ensemble forecasts. *Mon. Wea. Rev.*, **129**, 73-91.

- [71] Houze, R. A., Jr., 1993: *Cloud Dynamics*. Academic Press, 573pp.
- [72] Houze, R. A., Jr., S. A. Rutledge, M. I. Biggerstaff, and B. F. Smull, 1989: Interpretation of Doppler weather radar displays of midlatitude mesoscale convective systems. *Bull. Amer. Meteor. Soc.*, **70**, 608-619.
- [73] Hoxit, L. R., C. F. Chappell, and J. M. Fritsch, 1976: Formation of mesolows or pressure troughs in advance of cumulonimbus clouds. *Mon. Wea. Rev.*, **104**, 1419-1428.
- [74] Igau, R. C., M. A. LeMone, and D. Wei, 1999: Updraft and downdraft cores in TOGA COARE: Why so many buoyant downdraft cores? *J. Atmos. Sci.*, **102**, 521-544.
- [75] Jacobson, M. Z., 1999: *Fundamentals of Atmospheric Modeling*. Cambridge University Press, 656pp.
- [76] Jewett, B. F., R. B. Wilhelmson, J. M. Straka, and L. J. Wicker, 1990: Impact of ice parameterization on the low-level structure of modeled supercell thunderstorms. *Preprints, 16th Conf. on Severe Local Storms*, Canada, Amer. Meteor. Soc., 277-280.
- [77] Johns, R. H., 1993: Meteorological conditions associated with bow echo development in convective storms. *Wea. Forecasting*, **8**, 294-299.
- [78] Johns, R. H., and W. D. Hirt, 1983: The derecho: a severe weather producing convective system. *Preprints, 13th Conf. on Severe Local Storms*, Tulsa, OK, Amer. Meteor. Soc., 178-181.
- [79] Johns, R. H., and W. D. Hirt, 1987: Derechos: widespread convectively induced windstorms. *Wea. Forecasting*, **8**, 294-299.
- [80] Johns, R. H., and C. A. Doswell, 1992: Severe local storms forecasting. *Wea. Forecasting*, **7**, 588-612.
- [81] Johns, R. H., and J. A. Hart, 1993: Differentiating between types of severe thunderstorm outbreaks: a preliminary investigation. *Preprints, 17th Conf. on Severe Local Storms*, St. Louis, MI, Amer. Meteor. Soc., 46-50.
- [82] Johns, R. H., K. W. Howard, and R. A. Maddox, 1990: Conditions associated with long-lived derechos: an examination of the large-scale environment. *Preprints, 16th Conf. on Severe Local Storms*, Canada, Amer. Meteor. Soc., 408-412.
- [83] Johnson, D. E., P. K. Wang, and J. M. Straka, 1993: Numerical simulations of the 2 August 1981 CCOPE supercell storm with and without ice microphysics. *J. Appl. Meteor.*, **32**, pp. 745-759.

- [84] Johnson, R. H., 2001: Surface mesohighs and mesolows. *Bull. Amer. Meteor. Soc.*, **82**, 13-31.
- [85] Johnson, R. H., and P. J. Hamilton, 1988: The relationship of surface pressure features to the precipitation and air flow structure of an intense midlatitude squall line. *Mon. Wea. Rev.*, **116**, 1444-1472.
- [86] Johnson, R. H., and B. E. Mapes, 2001: Mesoscale processes and severe convective weather. *Severe Convective Storms, Meteor. Monogr.*, Vol. 28, No. 50, C. A. Doswell III, Ed., Amer. Meteor. Soc., 71-122.
- [87] Kessler, E., 1969: On the Distribution and Continuity of Water Substance in Atmospheric Circulation. *Meteor. Monogr.*, No. 32, Amer. Meteor. Soc., 84pp.
- [88] Klazura, G. E., and D. A. Imy, 1993: A description of the initial set of analysis products available from the NEXRAD WSR-88D system. *Bull. Amer. Meteor. Soc.*, **74**, 1293-1311.
- [89] Klemp, J. B., 1987: Dynamics of tornadic thunderstorms. *Annu. Rev. Fluid Mech.*, **19**, 369-402.
- [90] Klemp, J. B., and R. B. Wilhelmson, 1978: The simulation of three-dimensional convective storm dynamics. *J. Atmos. Sci.*, **35**, 1070-1096.
- [91] Klemp, J. B., and D. R. Durran, 1983: An upper boundary condition permitting internal gravity wave radiation in numerical mesoscale models. *Mon. Wea. Rev.*, **111**, 430-444.
- [92] Knupp, K. R., and W. R. Cotton, 1985: Convective cloud downdraft structure: An interpretive survey. *Rev. Geophys.*, **23**, 183-215.
- [93] Krishnamurti, T. N., J. Xue, H. S. Bedi, K. Ingles, and D. Oosterhof, 1991: Physical initialization for numerical weather prediction models over the tropics. *Bull.*, **43AB**, 73-81.
- [94] Kundu, P. K., and I. M. Cohen, 2001: *Fluid Mechanics*. Academic Press, 2nd Edition, 700pp.
- [95] Lafore, J.-P., and M. W. Moncrieff, 1989: A numerical investigation of the organization and interaction of the convective and stratiform regions of tropical squall lines. *J. Atmos. Sci.*, **46**, 521-544.
- [96] Lamb, H., 1932: *Hydrodynamics*. Dover Publications, 738pp.
- [97] Laroche, S., and I. Zawadzki, 1994: A variational analysis method for the retrieval of three-dimensional wind field from single-Doppler radar data. *J. Atmos. Sci.*, **51**, 2664-2682.

- [98] Lazarus, S., A. Shapiro, and K. K. Droegemeier, 2001: Application of the Zhang-Gal-Chen single-Doppler velocity retrieval to a deep convective storm. *J. Atmos. Sci.*, **58**, 998-1016.
- [99] Leary, C. A., and R. A. Houze Jr., 1979: Melting and evaporation of hydrometeors in precipitation from the anvil clouds of deep tropical convection. *J. Atmos. Sci.*, **36**, 669-679.
- [100] Leith, C., 1980: Nonlinear normal mode initialization and quasi-geostrophic theory. *J. Atmos. Sci.*, **37**, 958-968.
- [101] Li, Q., R. L. Bras, and S. Islam, 1995: Growth and decay of error in a numerical cloud model due to small initial perturbations and parameter changes. *J. Appl. Meteor.*, **34**, 1622-1632.
- [102] Liepman, H. W., and A. Roshko, 1957: *Elements of Gasdynamics*. John Wiley and Sons Inc., 439pp.
- [103] Lilly, D. K., 1962: On the numerical simulation of buoyant convection. *Tellus*, **XIV**, 148-172.
- [104] Lilly, D. K., 1990: Numerical prediction of thunderstorms - has its time come? *Quart. J. R. Met. Soc.*, **116**, 779-798.
- [105] Lin, Y.-L., and S. Li, 1988: Three-dimensional response of a shear flow to elevated heating. *J. Atmos. Sci.*, **45**, 2987-3002.
- [106] Lin, Y.-H., R. D. Farley, and H. D. Orville, 1983: Bulk parameterization of the snow field in a cloud model. *J. Climate Appl. Meteor.*, **22**, 1065-1092.
- [107] Lindzen, R. S., and D. Blake, 1972: Lamb waves in the presence of realistic distributions of temperature and dissipation. *J. Geophys. Res.*, **77**, 2166-2176.
- [108] Mapes, B. E., 1993: Gregarious tropical convection. *J. Atmos. Sci.*, **50**, 2026-2037.
- [109] McCaul, E. W., and C. Cohen, 2002: The impact on simulated storm structure and intensity of variations in the mixed layer and moist layer depths. *Mon. Wea. Rev.*, **130**, 1722-1748.
- [110] Moncrieff, M. W., and C. Liu, 1999: Convection initiation by density currents. Role of convergence, shear, and dynamical organization. *Mon. Wea. Rev.*, **127**, 2455-2464.
- [111] Nachamkin, J. E., and W. R. Cotton, 2000: Interactions between a developing mesoscale convective system and its environment. Part II: Numerical simulation. *Mon. Wea. Rev.*, **128**, 1225-1244.

- [112] Nascimento, E. L., and K. K. Droegemeier, 2002: Dynamic adjustment within an idealized numerically-simulated bow echo: implications for data assimilation. *Preprints, Symposium on Observations, Data Assimilation, and Probabilistic Prediction*, Orlando, FL, Amer. Meteor. Soc., 29-34.
- [113] Nicholls, M. E., and R. A. Pielke, 1994a: Thermal compression waves. I: Total energy transfer. *Quart. J. R. Met. Soc.*, **120**, 305-332.
- [114] Nicholls, M. E., and R. A. Pielke, 1994b: Thermal compression waves. II: Mass adjustment and vertical transfer of total energy. *Quart. J. R. Met. Soc.*, **120**, 333-359.
- [115] Nicholls, M. E., R. A. Pielke, and W. R. Cotton, 1991: Thermally forced gravity waves in an atmosphere at rest. *J. Atmos. Sci.*, **48**, 1869-1884.
- [116] Nolen, R. H. 1959: A radar pattern associated with tornadoes. *Bull. Amer. Met. Soc.*, **40**, 277-279.
- [117] Ogura, Y., 1963: A review of numerical modeling research on small scale convection in the atmosphere. *Severe Local Storms, Meteor. Monogr.*, No. 27, Amer. Meteor. Soc., 65-75.
- [118] Ogura, Y., and T. Takahashi, 1971: Numerical simulation of the life cycle of a thunderstorm cell. *Mon. Wea. Rev.*, **99**, 895-911.
- [119] Orlanski, I., 1975: A rational subdivision of scales for atmospheric processes. *Bull. Amer. Met. Soc.*, **56**, 527-530.
- [120] Pandya, R. E., and D. R. Durran, 1996: The influence of convectively generated thermal forcing on the mesoscale circulation around squall lines. *J. Atmos. Sci.*, **53**, 2924-2951.
- [121] Pandya, R. E., D. R. Durran, and M. L. Weisman, 2000: The influence of convective thermal forcing on the three-dimensional circulation around squall lines. *J. Atmos. Sci.*, **57**, 29-45.
- [122] Park, S. K., and K. K. Droegemeier, 2000: Sensitivity analysis of a 3D convective storm: implications for variational data assimilation and forecast error. *Mon. Wea. Rev.*, **128**, 184-197.
- [123] Phillips, N., 1960: On the problem of the initial data for the primitive equations. *Tellus*, **12**, 121-126.
- [124] Phillips, N., 1963: Geostrophic motion. *Rev. Geophysics*, **1**, 123-176.
- [125] Przybylinski, R. W. 1995: The bow echo: observations, numerical simulations, and severe weather detection methods. *Wea. Forecasting*, **10**, 203-218.

- [126] Przybylinski, R. W., and W. J. Gerv. 1983: The reliability of the bow echo as an important severe weather signature. *Preprints, 13th Conf. on Severe Local Storms*, Tulsa, OK, Amer. Meteor. Soc., 270-273.
- [127] Przybylinski, R. W., and D. M. DeCaire. 1985: Radar signatures associated with the derecho, a type of mesoscale convective systems. *Preprints, 14th Conf on Severe Local Storms*, Indianapolis, IN, Amer. Meteor. Soc., 228-231.
- [128] Qin, C.-J., and Q. Xu. 1996: Least squares retrieval of microburst winds from single-Doppler radar data. *Mon. Wea. Rev.*, **124**, 1132-1144.
- [129] Raymond, D. J., and R. Rotunno. 1989: Response of a stably stratified flow to cooling. *J. Atmos. Sci.*, **46**, 2830-2837.
- [130] Richardson, Y., 1999: The influence of horizontal variations in vertical shear and moisture on numerically-simulated convective storms. Ph.D. Dissertation, University of Oklahoma, 236 pp.
- [131] Rotunno, R., and Klemp, J. B., 1982: The influence of the shear-induced pressure gradient on thunderstorm motion. *Mon. Wea. Rev.*, **110**, 136-151.
- [132] Rotunno, R., and Klemp, J. B., 1985: On the rotation and propagation of simulated supercell thunderstorms. *J. Atmos. Sci.*, **42**, 271-292.
- [133] Rotunno, R., J. B. Klemp, and M. L. Weisman, 1988: A theory for strong, long-lived squall lines. *J. Atmos. Sci.*, **45**, 463-485.
- [134] Ryan, B. F., and J. C. Carstens, 1978: A comparison between a steady-state downdraft model and observations behind squall lines. *J. Appl. Meteor.*, **17**, 395-400.
- [135] Sawyer, J. S., 1946: Cooling by rain as the cause of the pressure rise in convective squalls. *Quart. J. Roy. Meteor. Soc.*, **72**, 168.
- [136] Schlesinger, R. E., 1975: A three-dimensional numerical model of an isolated deep convective cloud: preliminary results. *J. Atmos. Sci.*, **32**, 934-957.
- [137] Schmidt, J. M., and W. R. Cotton, 1990: Interactions between upper and lower tropospheric waves on squall line structure and maintenance. *J. Atmos. Sci.*, **47**, 1205-1222.
- [138] Scorer, R., 1949: Theory of waves in the lee of mountains. *Quart. J. Roy. Meteor. Soc.*, **75**, 41-56.
- [139] Shapiro, A., S. Ellis, and J. Shaw, 1995a: Single Doppler velocity retrievals with Phoenix II data: clear air and microburst wind retrievals in the planetary boundary layer. *J. Atmos. Sci.*, **52**, 1265-1285.

- [140] Shapiro, A., K. K. Droegemeier, S. Lazarus, and S. Weygandt, 1995b: Forward variational four-dimensional data assimilation and prediction experiments using storm-scale numerical model. *International Symposium on Assimilation of Observations in Meteorology and Oceanography*, Tokyo, Japan.
- [141] Skamarock, W. C., and J. B. Klemp, 1992: The stability of time-split numerical methods for the hydrostatic and the nonhydrostatic elastic equations. *Mon. Wea. Rev.*, **120**, 2109-2127.
- [142] Skamarock, W. C., M. L. Weisman, and J. B. Klemp, 1994: Three-dimensional evolution of simulated long-lived squall lines. *J. Atmos. Sci.*, **51**, 2563-2584.
- [143] Smagorinski, J., 1969: Problems and promises of deterministic extended range forecasting. *Bull. Amer. Met. Soc.*, **50**, 286-311.
- [144] Smagorinski, J., K. Mivakoda, and R. Strickler, 1970: The relative importance of variables in initial conditions for dynamical weather prediction. *Tellus*, **22**, 141-154.
- [145] Soong, S.-F., and Y. Ogura, 1973: A comparison between axis-symmetric and slab-symmetric cumulus cloud models. *J. Atmos. Sci.*, **30**, 879-883.
- [146] Sotack, F., and P. R. Bannon, 1999: Lamb's adjustment for heating of finite duration. *J. Atmos. Sci.*, **56**, 71-81.
- [147] Srivastava, R. C., 1987: A model of intense downdrafts driven by the melting and evaporation of precipitation. *J. Atmos. Sci.*, **44**, 1752-1773.
- [148] Steiner, J. F., 1973: A three-dimensional model of cumulus cloud development. *J. Atmos. Sci.*, **30**, 414-434.
- [149] Stensrud, D. J., R. A. Maddox, and C. L. Ziegler, 1991: A sublimation-initiated mesoscale downdraft and its relation to the wind field below a precipitating anvil cloud. *Mon. Wea. Rev.*, **119**, 2124-2139.
- [150] Straka, J. M., and J. R. Anderson, 1993: Numerical simulations of microburst-producing storms: some results from storms observed during COHMEX. *J. Atmos. Sci.*, **50**, 1329-1348.
- [151] Straka, J. M., Y. Liu, and L. Wicker, 1993: The influence of ice-phase microphysics on convective storm structure and evolution. *Preprints, 17th Conf. on Severe Local Storms*, St. Louis, MO, Amer. Meteor. Soc., 178-183.
- [152] Sun, J., and N. A. Crook, 1997: Dynamical and microphysical retrieval from Doppler radar observations using a cloud model and its adjoint. Part I: Model development and simulated data experiments. *J. Atmos. Sci.*, **54**, 1642-1661.

- [153] Sun, J., and N. A. Crook, 1998: Dynamical and microphysical retrieval from Doppler radar observations using a cloud model and its adjoint. Part II: Retrieval experiments of an observed Florida convective storm. *J. Atmos. Sci.*, **55**, 835-852.
- [154] Sun, J., and N. A. Crook, 2001a: Real-time low-level wind and temperature analysis using single WSR-88D data. *Wea. Forecasting*, **16**, 117-132.
- [155] Sun, J., and N. A. Crook, 2001b: Assimilation and forecasting experiments on supercell storms: Part I: experiments with simulated data. *Preprints, 14th Conf. on Numerical Weather Prediction*, Ft. Lauderdale, FL, Amer. Meteor. Soc., 142-146.
- [156] Sun, J., D. W. Flicker, and D. K. Lilly, 1991: Recovery of three-dimensional wind and temperature fields from simulated single-Doppler radar data. *J. Atmos. Sci.*, **48**, 876-890.
- [157] Sun, J., S. Braun, M. I. Biggerstaff, R. G. Fovell, and R. A. Houze Jr., 1993: Warm upper-level downdrafts associated with a squall line. *Mon. Wea. Rev.*, **121**, 2919-2927.
- [158] Talagrand, O., 1997: Assimilation of observations: an introduction. *J. Met. Soc. Japan*, **75**, 191-209.
- [159] Tao, W.-K., J. Simpson, and M. McCumber, 1989: An ice-water saturation adjustment. *Mon. Wea. Rev.*, **117**, 231-235.
- [160] Thunis, P., and R. Bornstein, 1996: Hierarchy of mesoscale flow assumptions and equations. *J. Atmos. Sci.*, **53**, 380-397.
- [161] Frier, S. B., W. C. Skamarock, and M. A. LeMone, 1997: Structure and evolution of the 22 February squall line: Organization mechanisms inferred from numerical simulation. *J. Atmos. Sci.*, **54**, 386-407.
- [162] Tuttle, J. D., and G. B. Foote, 1990: Determination of the boundary-layer airflow from a single Doppler radar. *J. Atmos. Oceanic Technol.*, **7**, 218-232.
- [163] Verlinde, J., and W. R. Cotton, 1993: Fitting microphysical observations of nonsteady convective clouds to a numerical model: an application of the adjoint technique of data assimilation to a kinematic model. *Mon. Wea. Rev.*, **121**, 2776-2793.
- [164] Wakimoto, R. M., 2001: Convectively driven high wind events. *Severe Convective Storms, Meteor. Monogr.*, Vol. 28, No. 50, C. A. Doswell III, Ed., Amer. Meteor. Soc., 255-298.
- [165] Wei, D., A. M. Blyth, and D. J. Raymond, 1998: Buoyancy of convective clouds in TOGA COARE. *J. Atmos. Sci.*, **55**, 3381-3391.

- [166] Weisman, M. L., 1992: The role of convectively generated rear-inflow jets in the evolution of long-lived meso-convective systems. *J. Atmos. Sci.*, **49**, 1827-1847.
- [167] Weisman, M. L., 1993: The genesis of severe, long-lived bow echoes. *J. Atmos. Sci.*, **50**, 645-670.
- [168] Weisman, M. L., 2001: Bow echoes: A tribute to T. T. Fujita. *Bull. Amer. Meteor. Soc.*, **82**, 97-116.
- [169] Weisman, M. L., and C. A. Davis, 1998: Mechanisms for the generation of mesoscale vortices within quasi-linear convective systems. *J. Atmos. Sci.*, **55**, 2603-2622.
- [170] Weisman, M. L., W. C. Skamarock, and J. B. Klemp, 1997: The resolution dependence of explicitly modeled convective systems. *Mon. Wea. Rev.*, **125**, 527-548.
- [171] Weygandt, S. S., J. M. Straka, and Kelvin K. Droegemeier, 1993: Sensitivity of storm-scale predictions to initialization with simulated Doppler radar data. *Preprints, 26th Conf. on Radar Meteorology*, Norman, OK, Amer. Meteor. Soc., 193-195.
- [172] Weygandt, S. S., A. Shapiro, and K. K. Droegemeier, 2002a: Retrieval of model initial fields from single-Doppler observations of a supercell thunderstorm. Part I: single-Doppler velocity retrieval. *Mon. Wea. Rev.*, **130**, 433-453.
- [173] Weygandt, S. S., A. Shapiro, and K. K. Droegemeier, 2002b: Retrieval of model initial fields from single-Doppler observations of a supercell thunderstorm. Part II: thermodynamic retrieval and numerical prediction. *Mon. Wea. Rev.*, **130**, 454-476.
- [174] Weygandt, S. S., P. Nutter, E. Kalnay, S. K. Park, and K. K. Droegemeier, 1999: The relative importance of different data fields in a numerically-simulated convective storm. *Preprints, 8th Conf. on Mesoscale Processes*, Boulder, CO, Amer. Meteor. Soc., 310-315.
- [175] Wicker, L. J., M. P. Kay, and M. P. Foster, 1997: STORMTIPe-95: Results from a convective storm forecast experiment. *Wea. Forecasting*, **12**, 388-398.
- [176] Wilhelmsen, R. B., and L. J. Wicker, 2001: Numerical modeling of severe local storms. *Severe Convective Storms, Meteor. Monogr.*, Vol. 28, No. 50, C. A. Doswell III, Ed., Amer. Meteor. Soc., 255-298.
- [177] Williamson, D., and C. Temperton, 1981: Normal mode initialization for a multi-level grid-point model. Part II: non-linear aspects. *Mon. Wea. Rev.*, **109**, 745-757.
- [178] Wilson, J. W., N. A. Crook, C. K. Mueller, J. Sun, and M. Dixon, 1998: Now-casting thunderstorms: a status report. *Bull. Amer. Met. Soc.*, **79**, 2079-2099.

- [179] Xu, Q., H. D. Gu, and C. Qiu, 2001: Simple adjoint retrievals of wet-microburst winds and gust-front winds from single-Doppler radar data. *J. Appl. Meteor.*, **40**, 1485-1499.
- [180] Xue, M., K. K. Droegemeier, and V. Wong, 2000: The Advanced Regional Prediction System (ARPS) - A multi-scale nonhydrostatic atmospheric simulation and prediction model. Part I: model dynamics and verification. *Meteor. Atmos. Physics*, **75**, 161-193.
- [181] Xue, M., K. K. Droegemeier, V. Wong, A. Shapiro, and K. Brewster, 1995: *Advanced Regional Prediction System, Version 4.0: User's Guide*. Center for Analysis and Prediction of Storms, University of Oklahoma, 380pp.
- [182] Xue, M., K. Brewster, K. K. Droegemeier, F. Carr, V. Wong, Y. Liu, A. Sathye, G. Bassett, P. Jamsh, J. Levit, and P. Bothwell, 1996: Real time prediction of storm-scale weather during VORTEX-95. Part II: operation summary and example cases. *Preprints, 18th Conf. on Severe Local Storms*, San Francisco, CA, Amer. Meteor. Soc., 178-182.
- [183] Yang, M.-J., and R. A. Houze Jr., 1995a: Multicell squall-line structure as a manifestation of vertically trapped gravity waves. *Mon. Wea. Rev.*, **123**, 641-661.
- [184] Yang, M.-J., and R. A. Houze Jr., 1995b: Sensitivity of squall-line rear inflow to ice microphysics and environmental humidity. *Mon. Wea. Rev.*, **123**, 3175-3193.
- [185] Yuter, S. E., and R. A. Houze Jr., 1995a: Three-dimensional kinematic and microphysical evolution of Florida cumulonimbus. Part I: Spatial distribution of updrafts, downdrafts, and precipitation. *Mon. Wea. Rev.*, **123**, 1921-1940.
- [186] Yuter, S. E., and R. A. Houze Jr., 1995b: Three-dimensional kinematic and microphysical evolution of Florida cumulonimbus. Part II: Frequency distributions of vertical velocity, reflectivity, and differential reflectivity. *Mon. Wea. Rev.*, **123**, 1941-1963.
- [187] Zhang, J., 1999: Moisture and diabatic initialization based on radar and satellite observations. Ph.D. Dissertation, University of Oklahoma, 194 pp.
- [188] Zhang, J., and F. H. Carr, 1998: Moisture and latent heating rate retrieval from radar data. *Preprints, 12th Conf. on Numerical Weather Prediction*, Phoenix, AZ, Amer. Meteor. Soc., 185-188.
- [189] Zipser, E. J., 1977: Mesoscale and convective-scale downdrafts as distinct components of squall line circulation. *Mon. Wea. Rev.*, **105**, 1568-1589.